UNIVERSITY OF LIVERPOOL

A Tale of Four Seasons: Investigating the seasonality of physical structure and its biogeochemical responses in a temperate continental shelf sea

Thesis submitted in accordance with the requirements of the
University of Liverpool
for the degree of

Doctor in Philosophy

by

Juliane Uta Wihsgott

January 2018

in the

Faculty of Science and Engineering
School of Environmental Sciences
Department of Earth, Ocean and Ecological Sciences

ABSTRACT

A Tale of Four Seasons:
Investigating the seasonality of physical structure and its biogeochemical responses in a temperate continental shelf sea

Juliane Uta Wihsgott

Due to their high biological productivity, continental shelf seas are significant sinks of anthropogenic carbon. To better understand the cycling of carbon within them, an accurate prediction of their vertical density stratification is required, as this is a critical control on the carbon drawdown. While the dominant controls on density structure are boundary driven mixing and seasonal heating, internal waves have been shown to play a small but critical role in both open ocean and shelf sea physical and biogeochemical cycles. Current knowledge on the spatial and temporal variability in internal mixing is however still severely limited.

The aim of the work in this thesis was to develop new insight into the seasonal variability of physical controls on the vertical density structure and examine its biogeochemical responses in a temperate shelf sea.

This thesis presents and examines new results that test the impact of boundary layer and internal wave forcing on stratification and vertical density structure in continental shelves. A new series of continuous measurements of full depth density and velocity structure, meteorological and wave forcing, surface nitrate and surface chlorophyll a spanning 17 months (March'14 − July'15) provide unprecedented coverage over a full seasonal cycle at a station 120 km north-east from the continental shelf break.

Work within this thesis showed that the controls on vertical density structure at the mooring site were largely analogous to that of open-ocean environments with tidal mixing only playing a minor role. This result contrasts with the well-known tidally controlled frontal systems described by Simpson and Hunter (1974). Since a large proportion of continental shelf regions are away from tidal mixing fronts this result suggest the requirement for an adjusted third regime that bridges the gap between open-ocean environments and frontal regions, to accurately predict the vertical density structure within them.

The long-term observations presented in this thesis reveal a seasonality within the internal wave energy, which suggest internal mixing varying relative to the seasonal cycle of stratification, represented by N^2. By investigating the representation of this seasonality by three commonly used internal wave parameterisations it was shown that each predicted a seasonality that directly contradicted that observed within the internal wave energy. It was suggested that the reason for this was most likely due to

their failure to introduce the enhanced S^2 that is attributable to internal waves, which have been shown in this work to have a strong seasonal cycle with maximum energy levels during the summer. In an attempt to provide realistic scaling of turbulence an adjusted iteration of the MacKinnon and Gregg (2003a) scaling of turbulence was employed using an observed close relationship between N^2 and S^2 to introduce a state of marginal stability in the pycnocline, thus introducing a seasonally varying level of internal mixing that follows the observed seasonality in internal wave energy.

Examining the biogeochemical response to the seasonal change in vertical density structure also highlighted the importance of the autumn phytoplankton bloom within the annual cycle of primary production. By putting the autumn phytoplankton bloom within the context of the seasonal cycle it was shown that it has the potential to be as productive as the well-studied spring phytoplankton bloom and the summer subsurface chlorophyll maximum and thus has the capacity to significantly contribute to the drawdown of atmospheric carbon dioxide.

Contents

List of Figures

List of Tables

Nomenclature

Acronyms

0D	0-dimensional
1D	1-dimensional
ACP	acoustic current profiler
ADCP	acoustic Doppler current profiler
$_b$	sea bed
$_{BG}$	background internal wave mixing parameterisation
BML	bottom mixed layer
$_{CA}$	Canuto *et al.* (2001) internal wave mixing parameterisation
CCS	central Celtic Sea
Cefas	Centre for Environment, Fisheries and Aquaculture Science
chl a	chlorophyll-a fluorescence
CO_2	carbon dioxide
CTD	conductivity-temperature-depth
CTG	Chelsea Technology Group
Defra	Department of Environment, Food & Rural Affairs
DY	RRS Discovery
ECMWF	European Centre for Medium-Range Weather Forecasts
ERA	European Reanalysis
FFT	fast Fourier transform
GEBCO	General Bathymetric Chart of the Oceans
$_{GM}$	Garrett and Munk (1979)
GPS	Global Positioning System
GSW	Gibbs-SeaWater
$_h$	high
$_{int}$	internal

$_{iw}$	internal wave
JC	RRS James Cook
$_{KC}$	Kantha and Clayson (1994) internal wave mixing parameterisation
KE	kinetic energy
$_{l}$	low
$_{m}$	medium (when not unit of length, metres)
mab	metres above bed
$_{MG}$	MacKinnon and Gregg (2003a)
MOC	meridional overturning circulation
NaN	non-value
NEODAAS	NERC Earth Observation Data Acquisition and Analysis Service
NERC	Natural Environment Research Council
NW	North West
$_{obs}$	observations
ODAS	Ocean Data Acquisition System
PAR	photosynthetically active radiation
PDF	probability density function
PE	potential energy
PEA	potential energy anomaly
PML	Plymouth Marine Laboratory
POLCOMS	Proudman Oceanographic Laboratory Coastal Ocean Modelling System
POLPRED	Proudman Oceanographic Laboratory Predictions
PSD	power spectral density
RDI	RD Instruments
RMSE	root mean square error
RRS	Royal Research Ship
RV	research vessel
$_{s}$	sea surface (when not unit of time, seconds)
S2P3	Shelf Sea Physics and Primary Production model described in Simpson and Sharples (2012)
SB84	1D PE model derived by Simpson and Bowers (1984)
SBE	Sea-Bird Electronics
SCD	Sverdrup's 1953 critical depth theory
SCM	subsurface chlorophyll maximum
SCF	Seapoint Chlorophyll Fluorometer
$_{sh}$	shear

SH74	0D PE model derived by Simpson and Hunter (1974)
SML	surface mixed layer
SSB	Shelf Sea Biogeochemistry
SST	sea surface temperature
std	standard deviation
$_{t2}$	semi-diurnal
TC	1D turbulence closure model, S2P3
TC2	1D turbulence closure model described in Simpson and Sharples (1994)
TKE	turbulent kinetic energy
TS	temperature - salinity

Greek Symbols

α	thermal expansion coefficient of seawater
Γ	mixing efficiency
γ_s	slippage factor
δ	wind mixing efficiency
ε	turbulent kinetic energy dissipation rate
κ	von Kármán's constant
σ	Stefan's constant
σ_t	density of seawater - 1000 kg m^{-3}
ϕ	phases of sea surface slope oscillations
Φ	potential energy anomaly
Φ_0	Simpson and Bowers (1981) constant
ρ	density of seawater
$\overline{\rho}$	depth averaged density
ρ_a	density of air
ρ_b	density at the sea bed
ρ_s	surface density
τ_b	tidal stress
τ_s	wind stress
χ	Simpson and Hunter (1974) parameter
ω	angular frequency
ω_a	annual frequency

Roman Symbols

A	amplitudes of the oscillating sea surface slopes
a_C	conductivity accuracy
a_T	temperature accuracy
$\boldsymbol{B}$	buoyancy production of turbulence
B	buoyancy force per unit area
B_0	buoyancy flux
c	phase speed of internal waves
C	length of the semi-major axis of the tidal ellipse
$c_{1\text{-}3}$	constants within Canuto *et al.* (2001) internal wave mixing parameterisation
c_{CA}	constant within Canuto *et al.* (2001) k-ε turbulence closure scheme
c_D	surface drag coefficient
c_e	Dalton number
c_h	Stanton number
$\mathrm{c_{KC}}$	constant within Kantha and Clayson (1994) internal wave mixing parameterisation
c_p	specific heat capacity of seawater
c_{pa}	specific heat capacity of air
d	bottom boundary layer
D	absolute RMSE
e	tidal mixing efficiency
e_a	vapour pressure of water
e_m	emissivity
e_w	saturated vapour pressure
f	Coriolis parameter
F_{bt}	body force
g	acceleration due to gravity
g'	reduced g
h	water depth
H_s	significant wave height
i	tidal constituent
I_0	surface irradiance
I_c	compensation irradiance
$_{\mathrm{int}}$	internal
k	thermal exchange coefficient
k_b	bottom drag coefficient

k_s	product of c_d and γ_s
K_z	vertical eddy diffusivity
L	turbulent length scale
L_{OB}	Obukhov length
La_t	turbulent Langmuir number (McWilliams *et al.*, 1997)
n	vertical levels
N^2	Brunt Väilsälä or buoyancy frequency squared
n_c	cloud cover
ns	sample size
N_z	vertical eddy viscosity
$\boldsymbol{P}$	shear production of turbulence
p_a	air pressure
P_l	polarity
Pr	Prandtl number
P_T	stirring power of the tide
P_W	stirring power of the wind
R^2	coefficient of determination
q_a	specific humidities of air at air temperature
q_w	specific humidity at sea temperature
Q_{lw}	longwave heat flux
Q_{net}	net heat flux
Q_{s}	solar radiation at the top of the atmosphere
Q_{sen}	sensible heat flux
Q_{sw}	shortwave heat flux
Q_{u}	$Q_{\mathrm{lw}} + Q_{\mathrm{sen}} + Q_{\mathrm{lat}}$
r_h	relative humidity
r_T	temperature resolution
Ri	Richardson number
Ri_{cr}	critical Richardson number
Ri_g	gradient Richardson number
S^2	vertical shear of horizontal velocities squared
S_0	Stokes drift
S_M	momentum stability function
S_H	heat stability function
T_0	initial temperature profile
T_a	air temperature
T_d	dew point temperature
t_J	Julian day
t_l	latent heat of vaporisation of water

T_p	wave period
T_s	sea surface temperature
u, v	horizontal velocities in the E-W and N-S direction
$\hat{u}$	depth averaged velocity
$\langle u \rangle$	barotropic velocity
u'	baroclinic velocity
v_{bt}	barotropically induced vertical velocity
q_a	specific humidities of air at air temperature
q_w	specific humidity of air at sea temperature
w	wind speed
w_*	friction velocity
x, y	horizontal direction
z_0	roughness length
z_{cr}	critical depth

Acknowledgements

First and foremost I wish to thank my supervisors Jonathan Sharples, Jo Hopkins and Mattias Green for their patient guidance, support and motivation throughout this thesis. Jonathan and Jo, thank you both for lots of thought provoking discussions that have always led on to interesting avenues to explore, but thanks also for keeping me on track. Thanks also go to Matthew Palmer for great discussions about the nitty-gritty aspects of turbulence and mixing. Jo and Matthew, thank you both for all your knowledge and expertise of working with observational data that you have shared and taught me over the years.

I am also grateful to the crew and officers of the RRS Discovery, RRS James Cook and RV Cefas Endeavour, without whom the observations and research presented in this thesis would not have been possible. I also thank Chris Balfour and Emlyn Jones for their technical support in processing the long-term mooring data.

Thanks also go to my many collaborators, who shared their excellent data with me and never tired of my questions: Tom Hull, Naomi Greenwood, Dave Sivyer, Malcolm Woodward, Tom Bell, Jon Turton and the ECMWF team.

I would also like to thank my PhD colleagues whom became good friends and created a great working environment. Carl and Calum, thanks for many great Friday nights in the Pen.

I am also grateful to my family, who have supported me throughout my education.

And finally, Matthew, you have been the greatest support of all. Thank you for all your love and encouragement throughout this journey.

Declaration

I certify that the work described in this thesis is my own except where otherwise stated, and has not previously been submitted for any degree at this or any other University.

Juliane Uta Wihsgott

Chapter 1

Introduction

1.1 Background and motivation

Continental shelf seas connect the deep ocean with our coasts. They are typically less than 500 metres deep and extend all the way from the coast to the continental shelf break, where the sea bed dramatically drops to the average open-ocean depth of approximately 4 km. These regions of rapid changes in depth are known as the continental slopes or shelf edges, and are responsible for dramatic changes in physical processes between the deep ocean and the shelf seas. Shelf seas are typically described by ocean depths $\leq$ 500 metres, and it is evident in Figure 1.1 that they only account for $\sim$ 9% of the global ocean surface area (Liu, 2010) and less than 0.5% of its volume. However, shelf seas have an influence and importance that is vastly underrepresented by these numbers.

As open ocean tides cross onto the continental shelf they undergo a process of amplification (Simpson, 1998). This subsequent increase in available mechanical energy results in between 60 - 70% of the global tidal energy dissipation occurring within shelf sea environments (Egbert and Ray, 2000), causing vigorous turbulent mixing at the sea bed. With the addition of less regular inputs of energy from wind and waves, the

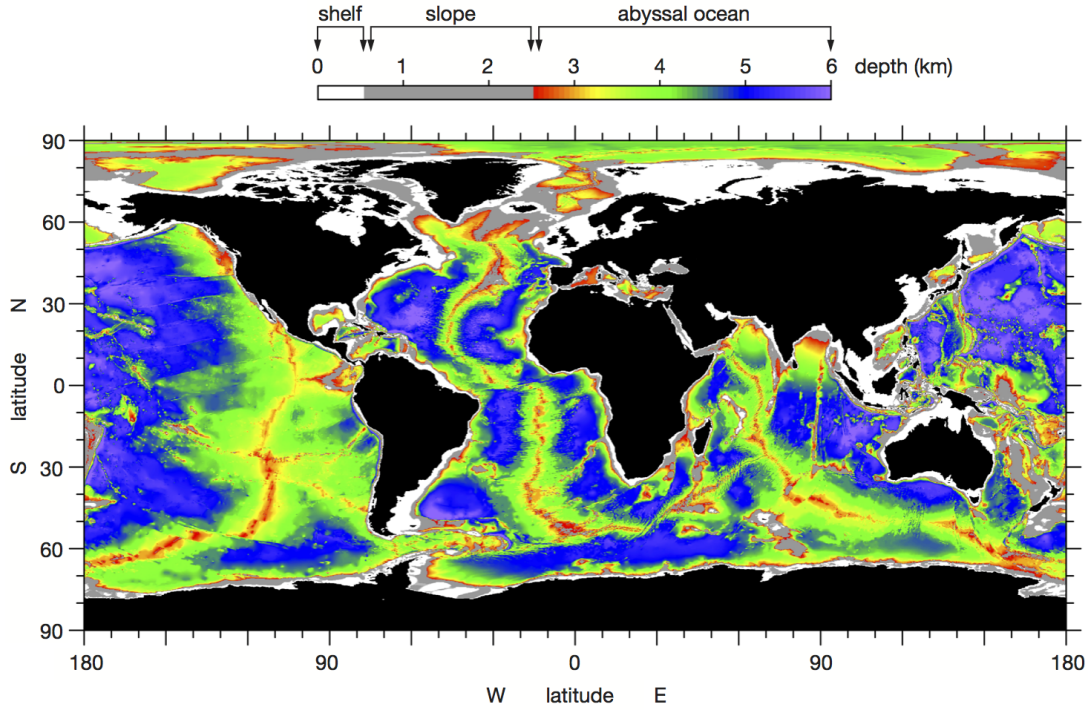

FIGURE 1.1: Global ocean depths [km] based on General Bathymetric Chart of the Oceans (GEBCO) bathymetry, split by shelf (white), slope (grey) and deep-ocean (colours). Adapted from Simpson and Sharples (2012).

shelf sea environment is significantly more energetic than open ocean environments. Combined with strong gradients in physical, biological and chemical properties, shelf seas are typically complex environments that are difficult to predict.

The relatively shallow depths of shelf seas results in tight coupling with cycles in solar radiation, which act to alter their density structure horizontally and vertically throughout the year. While the buoyancy input in the majority of mid-latitude shelf seas is temperature controlled, driven by the seasonal cycle of solar radiation (Pingree, 1975), large amounts of freshwater (from rivers) can also become the dominant control on density in regions near the coast (Simpson, 1997), or during particularly heavy rainfall (Pingree *et al.*, 1976).

This dynamic nature results in shelf seas supporting relatively high levels of biological productivity. Despite only accounting for $\sim$ 9% of the global ocean surface area

(Figure 1.1) they perform a disproportionately important role within the global carbon cycle and marine ecosystem (Liu, 2010). Shelf seas support up to a third of all oceanic primary productivity (Wollast, 1998; Bauer *et al.*, 2013), and at least 40 % of oceanic particulate organic carbon (POC) is sequestered on continental margins of depth < 200 metres (Muller-Karger *et al.*, 2005; Dunne *et al.*, 2007; Regnier *et al.*, 2013). Temperate shelf seas have also been highlighted as being substantial sinks for atmospheric carbon dioxide (CO_2) (Thomas *et al.*, 2004; Borges *et al.*, 2005; Cai *et al.*, 2006; Cai, 2011), and they provide an important link between terrestrial, oceanic and atmospheric carbon reservoirs. Atmospheric CO_2 concentrations have been observed to rise to levels unprecedented within the last 800,000 years (Stocker, 2014), increasing by 40% since pre-industrial times. As a result, the ocean has taken up approximately 30% of this anthropogenic CO_2 (Doney and Schimel, 2007; Stocker, 2014), understanding the shelf seas' role in the oceanic carbon sink is thus of growing importance.

The global significance of these biogeochemical processes arises from the vertical density structure (Thomas *et al.*, 2004; Bianchi *et al.*, 2005) due to the dependence of biological productivity on the cycle of stratification, which in temperate regions has a strong annual seasonality.

The often quoted first-order paradigm of vertical density structure in shelf seas is a competition between the stratifying influence of seasonally varying surface solar irradiance and boundary driven turbulent mixing that has been reported to be dominated by tidal bed stress, with minor contributions from wind stress acting on the sea surface and convective overturning (Simpson and Hunter, 1974; Simpson *et al.*, 1978; Simpson and Bowers, 1984). While shallow regions with high tidal velocities remain vertically mixed all year round, the majority (≈ 70 %) of the North-West European shelf stratifies seasonally (Pingree *et al.*, 1978). In these regions the water column is fully mixed during the winter months, as solar radiation is insufficient to overcome the dissipation of energy from wind and tides and heat loss at the surface provides regular periods of convection. In spring, solar radiation eventually becomes strong enough to

out-compete the combined mixing effects of the tide, wind and convection to allow the water column to stratify. The developing stratification acts to divide the water column into a well mixed surface and bottom mixed layer separated by a region of a sharp temperature/density gradient (thermocline/pycnocline). This interface acts to restrict the diapycnal transfer of momentum, heat and tracers such as nutrients and oxygen. The common hypothesis is that stratification persists until heat losses in autumn destabilise the water column sufficiently to return to a fully mixed winter state. (Edinger *et al.*, 1968; Nielsen and St. John, 2001; Townsend *et al.*, 2010).

This seasonal cycle of stratification has strong implications on primary production as the vertical density structure affects the light and nutrient availability to phytoplankton throughout the year. In a year-round well mixed water column, primary production is limited as phytoplankton are constantly mixed throughout the water column, thereby decreasing their average light intake, despite nutrient replete conditions (Holligan *et al.*, 1984).

In a seasonally stratifying water column however, phytoplankton are split into two separate communities, each of them trapped within a new mixed layer. As long as the pycnocline developed above the critical depth (here phytoplankton losses balance gains) the community in the surface layer will receive enough light to outcompete losses from grazing and respiration and rapid growth occurs (Sverdrup, 1953). This transition is known as the spring phytoplankton bloom, which is generally thought to be the most important event within the annual cycle of primary production in shelf seas (e.g. Holligan, 1989; Pingree *et al.*, 1976) and the open-ocean (e.g. Siegel *et al.*, 2002; Waniek, 2003; Brody and Lozier, 2014). During the spring bloom, nutrient concentrations become quickly depleted O(weeks) (Pingree *et al.*, 1976; Sieracki *et al.*, 1993; Birchill *et al.*, 2017) in the surface layer, the phytoplankton community becomes nutrient limited and the biomass reduces. During the following summer months, the majority of the phytoplankton biomass is concentrated in the thermocline region. This narrow region enhanced growth is often termed the subsurface chlorophyll maximum

(SCM) has recently been identified as a significant contributor to the total annual production within shelf sea environments (Hickman *et al.*, 2012). Figure 1.2 shows vertical profiles of temperature, chlorophyll and nitrate typical of a summer stratified shelf sea. Clearly evident are the depleted nitrate concentrations in the surface layer, which result in near background levels of chlorophyll.

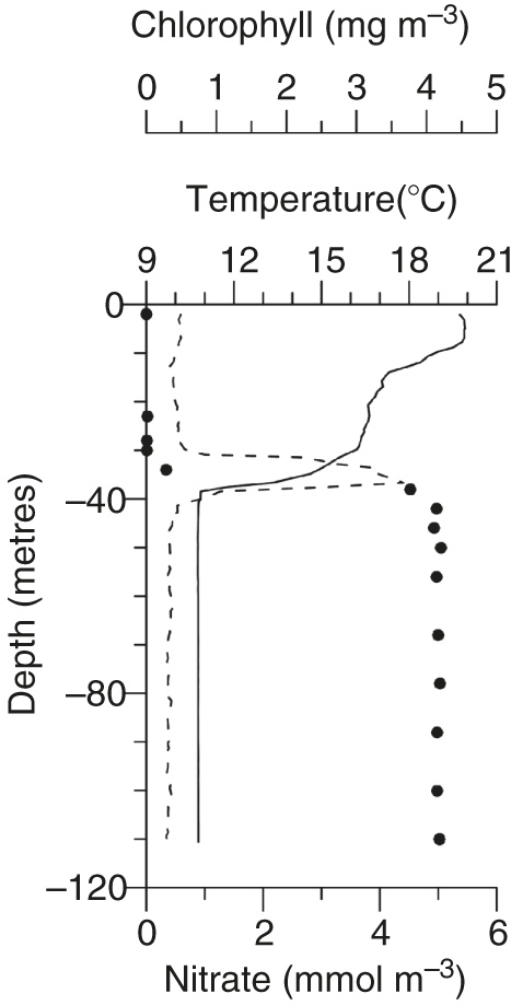

FIGURE 1.2: Vertical profiles of temperature (solid line), chlorophyll (dashed line) and nitrate (dots) during summer. Collected at the western English Channel. Adapted from Simpson and Sharples (2012).

The existence of the SCM suggests the availability of sufficient light for photosynthesis and a diapycnal flux of nutrients from the light limited, nutrient rich bottom layer. This diapycnal flux of nutrients is often thought to be a direct consequence and indicator of

midwater mixing that sustains this upward flux in combination with a strong nutrient gradient (Sharples *et al.*, 2001; Williams *et al.*, 2013; Lee *et al.*, 2016). Loss of heat in autumn results in convective overturning of the water column, which often results in an autumnal phytoplankton bloom. Due to their relatively small surface signature, short duration, and spatial and temporal variability (Colebrook and Robinson, 1961; Hu *et al.*, 2011; Chiswell, 2011; Song *et al.*, 2011), autumn phytoplankton blooms have been less well studied than the spring phytoplankton bloom or the summer SCM (Findlay *et al.*, 2006; Painter *et al.*, 2016).

One of the key mechanisms contributing to interior mixing in shelf sea thermoclines is the dissipation of turbulent kinetic energy by internal waves (e.g. Sandstrom and Elliott, 1984; Sharples *et al.*, 2007, 2009; Inall *et al.*, 2011).

In the deep ocean internal waves also play a key role in the heat budget of the ocean and in maintaining the meridional overturning circulation (e.g. Munk and Wunsch, 1998; Wunsch and Ferrari, 2004; Nikurashin and Ferrari, 2013). In an oversimplified view, the zonally averaged meridional overturning circulation (MOC) is formed by cold waters sinking at the poles, which is balanced by upwelling of deep water at lower latitudes. In order to transform this deep water into lighter water diapycnal mixing with the overlying water masses is required. Breaking of internal waves are thought to provide this mixing (Gregg, 1989; Polzin *et al.*, 1997; Garrett and Kunze, 2007).

Internal waves are generated by baroclinic conversion of energy from the barotropic flow. Energy is typically extracted either directly by wave breaking, or through the introduction of enhanced vertical shear in the horizontal flow, which acts to help destabilise the water column. Despite generally having far lower energy levels than other mixing mechanisms, such as boundary driven mixing by wind and tide, internal waves propagate along density interfaces and so are able to introduce mixing directly into the pycnocline/thermocline, which typically exists at or beyond the limit of boundary forcing.

Internal waves are typically generated by the interaction of stratified flow with topography (e.g. Kunze *et al.*, 2002; Naveira Garabato *et al.*, 2004; Nash *et al.*, 2006). In shelf seas, the most obvious source of internal waves is the continental shelf break (Baines, 1982; Stigebrandt and Aure, 1989; Simpson, 1998; Rippeth and Inall, 2002), which forces the oscillating barotropic flow to generate internal waves through the elevation and depression of the pycnocline (Figure 1.3). As a result of this periodic perturbation a wave at the tidal frequency then radiates both onto the shelf and into the deep ocean. Due to their period these internal waves are also called internal or baroclinic tides.

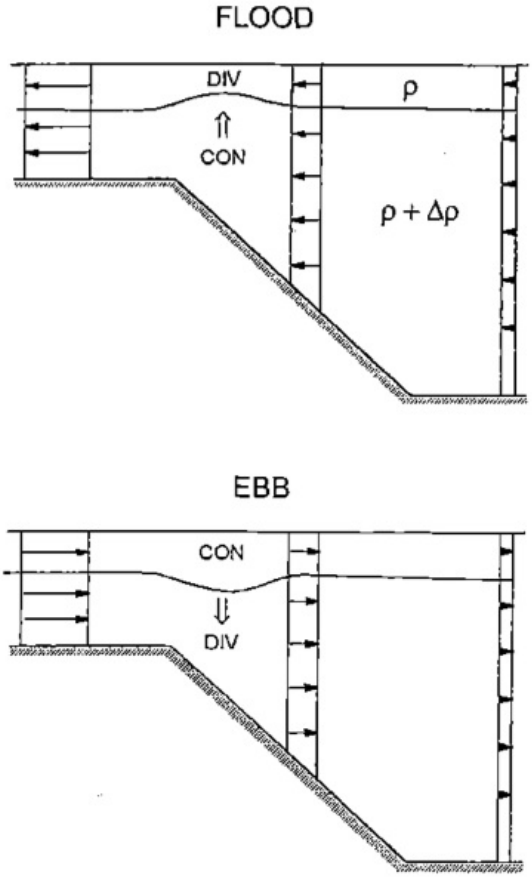

FIGURE 1.3: Generation of the internal tide at the continental shelf edge. Taken from Simpson (1998)

Inertial oscillations are another baroclinic oscillatory mechanism by which interior mixing can occur in the thermocline (e.g. van Haren *et al.*, 1999; Waterhouse *et al.*, 2014; Rumyantseva *et al.*, 2015). Inertial oscillations are periodic motions with a

frequency $I = f/2\pi$, where f is the Coriolis parameter. They are generated by sudden changes in wind forcing, either changes in direction or magnitude. As the direct forcing from the wind is removed or changed the only force acting on the flow is the Coriolis force, which sets the resulting frequency of the oscillation. During stratified conditions, such flows are triggered in the upper layer and permitted to continue until its energy is dissipated. The proximity of the coast in shelf seas can result in these oscillations being $\sim 180^{\circ}$ out of phase within the surface and bottom layers, due to continuity, which promotes shear within the pycnocline (Rippeth *et al.*, 2002).

While numerous studies have attempted to provide thorough understanding of the contribution that internal waves, including inertial oscillations, make to interior mixing, there is no general solution and so internal mixing remains poorly represented in global ocean or regional scale models. The primary reason for this is that internal waves are simply not resolvable by the majority of ocean models, and so either direct mixing or that attributable to enhanced shear is not accurately introduced.

1.2 Thesis aims

From this brief review it is evident that the vertical density structure provides a key control on the biogeochemical cycle. It is therefore critical to accurately predict and reproduce this density structure to assess the contribution that temperate shelf seas make to global carbon budgets and Earth's climate.

While the dominant controls on vertical density structure are boundary driven mixing and seasonal heating, internal waves have been shown to play a small but significant role in both open ocean and shelf sea physical and biogeochemical cycles. The current knowledge on the spatial and temporal variability in internal mixing is however still severely limited. The aims of this thesis are therefore to develop new insight into,

(1) physical controls on the seasonal cycle of vertical density structure in temperate shelf seas

(2) the contribution from internal waves to internal mixing throughout the seasonal cycle of stratification

(3) the capabilities of current turbulence models and empirically derived parameterisations replicating the observed internal wave characteristics

(4) the biogeochemical response to the change in vertical density structure

1.2.1 Thesis structure

Chapter 2 provides a more complete review of the current state of knowledge in processes controlling stratification in shelf sea environments and introduces three models of increasing complexity.

In Chapter 3 the instrumentation used to collect the observational data presented in this thesis is introduced, along with the analytical methods employed.

Chapter 4 presents a new, high-resolution, long-term observational time series, which is used throughout this thesis. These data are then used to provide an overview of the seasonal cycle of vertical density structure and its main controls throughout the observational campaign.

Chapter 5 examines the capability of heating-stirring approaches in replicating the observed stratification. Any discrepancies between the predicted and observed water column structure will be used to identify missing or poorly parameterised processes within these models.

Chapter 6 investigates the observed internal wave field in detail. Three commonly used internal wave parameterisations are tested to see whether they replicate the mixing induced by the observed internal wave field. By examining the relationship between the

predicted and observed stratification a new internal wave parameterisation is suggested and implemented within the heating-stirring framework.

Chapter 7 provides a first attempt at examining the biogeochemical response to the observed seasonal cycle of stratification, with a particular focus on the breakdown of stratification in autumn 2014. This aim of this chapter is to establish the role the autumn phytoplankton bloom plays within the seasonal cycle of primary production.

This thesis concludes in Chapter 8 by summarising the key findings of this thesis and assessing their wider implications.

Chapter 2

Modelling stratification and mixing in shelf seas

Introduction

This chapter will provide the theoretical background to the work presented in this thesis, as well as introductions to the three numerical approaches of increasing complexities, which will be used later in Chapter 5 to investigate the seasonal cycle of internal wave mixing in a temperate shelf sea.

This chapter first considers the physical principles of stratified fluids due to changes in potential energy, and how the strength of stratification can be quantified using these principles (Section 2.1). This is then followed by the introduction of three models and their assumptions in Section 2.2, 2.3 and 2.4. The model described in Section 2.2 provides the most basic approach considering stratification as a simple 0-dimensional (0D) balance of competing potential energy sink and source terms, i.e. heating vs. stirring (by tide and wind). In Section 2.3 these energy considerations are applied to a 1-dimensional (1D) framework, but similar to the 0D approach, the supply of potential energy to the water column, i.e. mixing, is still prescribed. The final model

introduced in Section 2.4 is fundamentally different to the former two, as it employs a turbulence closure scheme (Section 2.4.1) and is thus able to regulate the amount of turbulence based on the stability of the water column. This results in an improved representation of turbulent processes, which is illustrated in Section 2.4.5. Another key difference between the former prescriptive mixing models and the final model is the representation of internal mixing processes in the latter.

2.1 Energetics of stratification

Energetically the water column's potential energy (PE) is at its highest relative level during vertically mixed conditions, as the centre of mass is at its highest vertical position. Vertical stratification lowers the centre of mass, and as a result PE levels decrease compared to the mixed reference state. When turbulent mixing erodes stratification the water column's PE increases until the water column becomes vertically mixed again.

2.1.1 Measuring stratification

Based on the principles of PE source and sinks, Simpson (1981) developed a method to quantify the strength of stratification by calculating the potential energy anomaly (PEA) Φ [J m^{-3}],

$$\Phi = \frac{1}{h}\int_{-h}^{0} (\overline{\rho} - \rho(z))\; gz\; dz \qquad \overline{\rho} = \frac{1}{h}\int_{-h}^{0} \rho(z)\; dz \tag{2.1}$$

where h [metre] is the water column depth, $\rho(z)$ [kg m^{-3}] is the density profile and $\overline{\rho}$ is the depth-average density, $g = 9.81$ m s^{-2} is the acceleration due to gravity, and z [metre] is the depth. Φ is calculated from observations of the vertical density structure and is a quantitative measure of stratification. It represents the difference in PE between a vertically mixed and stratified water column for a thermodynamically

closed system, i.e.;

$$\Phi = \frac{1}{h}[\mathrm{PE(mixed)} - \mathrm{PE(stratified)}] = \frac{\Delta \mathrm{PE}}{h} \tag{2.2}$$

Hence Φ is a measure of the energy that needs to be supplied as mixing in order to restore vertically homogeneous conditions. Φ can therefore be defined as the amount of mechanical work per unit volume (J m^{-3}) required to completely mix the water column with a given initial density stratification. By definition, when $\Phi = 0$ J m^{-3} the water column is completely vertically mixed.

2.2 Heating-stirring competition: 0D approach

Knowledge about the physical forcing underpinning shelf sea stratification was first developed to better predict the locations of strong discontinuities observed in SST over relatively short horizontal distances (≥ 1°C km^{-1}, Figure 2.1 and Figure 2.2b), known as tidal mixing fronts (hereafter fronts) e.g. Simpson and Hunter (1974). Fronts, within the shelf sea context, are transitional regions separating stratified ($\Phi > 0$ J m^{-3}) and vertically mixed ($\Phi = 0$ J m^{-3}) parts of shelf seas (Figure 2.2), such as the St. Georges Channel Front between the Celtic and Irish Sea (Figure 2.1). They have also been linked to high biological activity, often being characterised by enhanced surface chlorophyll *a* concentrations (Holligan, 1981).

In order to predict the locations of these features, Simpson and Hunter (1974) proposed a simple model using only the dominant PE terms controlling stratification. They argued that stratification is to first-order controlled by the seasonal cycle of solar radiation competing against turbulent mixing processes at the sea bed, namely tidal mixing.

Away from the influence of freshwater on density and during positive heat input from the atmosphere, an amount of heat per unit area ΔQ [J m^{-2}] acts as the sole term

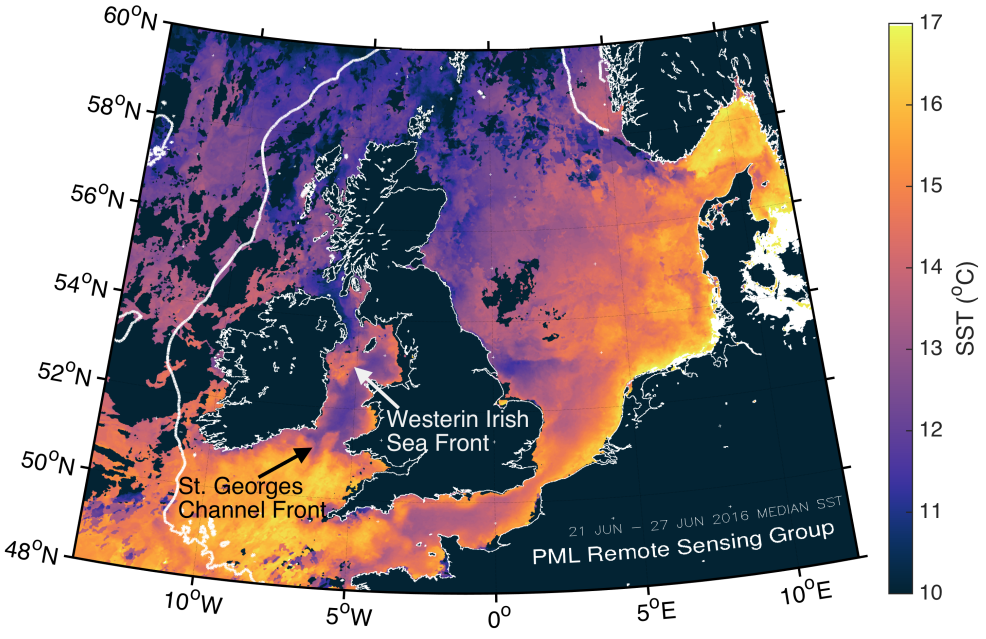

FIGURE 2.1: Summer 2016 sea surface temperature (SST, °C) on the NW European shelf. Away from coastal boundaries, warmer SSTs represent seasonally stratified regions and colder SSTs the year-round vertically mixed regions. The arrows mark two prominent fronts. The thick, white line denotes the 200 metre bathymetry contour, which marks the edge of the NW European continental shelf. This satellite image is a 1 week median SST composite, 21st - 27th June 2016, courtesy of NEODAAS Plymouth Marine Laboratory, UK.

supplying positive buoyancy by increasing the temperature by:

$$\Delta T = \frac{\Delta Q}{c_p \rho_0 h_1} \qquad [^\circ C], \tag{2.3}$$

where $c_p = 3985$ J kg $^{-1}$ °C^{-1} is the specific heat capacity of sea water, ρ_0 [kg m^{-3}] is a reference density, h_1 [metre] is the thickness of thin mixed surface layer that the incoming heat. The increase in temperature due to positive ΔQ (Equation 2.3) imposes a reduction in density $\Delta\rho$, which implies a total force of positive buoyancy per unit area of:

$$B \;=\; g\Delta\rho h_1 \;= g\alpha\rho_0 \Delta T h_1 = \frac{\alpha g \Delta Q}{c_p} \qquad [\mathrm{N\ m^{-2}}] \tag{2.4}$$

where, α [°C^{-1}] is the thermal expansion coefficient of seawater. Since the density

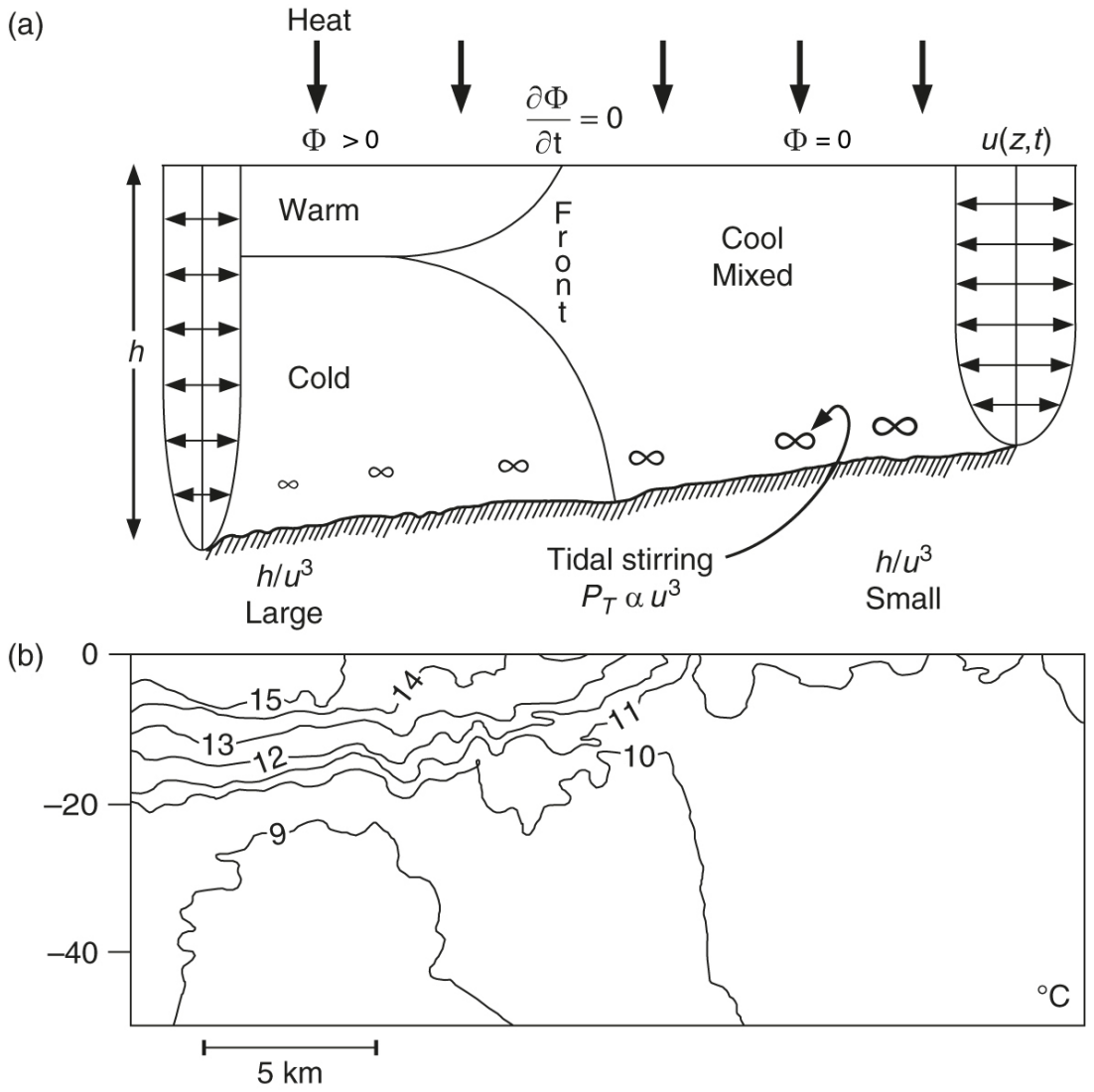

FIGURE 2.2: Tidal mixing fronts. a) Model and b) temperature observations illustrating the partitioning of shelf seas into stratified and mixed regimes, separated by a tidal mixing front. P_T represents the tidal stirring power, which is proportional to the tidal velocity profile, here depicted by $u(z,t)$. Adapted from Simpson and Sharples (2012).

change is distributed over the entire water depth, h [metre], the average work that is being done is therefore $Bh/2$. If the heat is supplied over a short period, Δt at a rate Q_{net} [W m^{-2}], then the change of Φ is:

$$h\Delta\Phi \;=\; \Delta PE \;=\; \frac{\alpha g h}{2c_p}\, Q_{\text{net}}\Delta t. \tag{2.5}$$

Here Q_{net} [W m^{-2}] is the surface net heat flux, which is generally considered to be the sum of all in- and outgoing heat fluxes:

$$Q_{\text{net}} = Q_{\text{sw}} + Q_{\text{lw}} + Q_{\text{sen}} + Q_{\text{lat}}, \tag{2.6}$$

where Q_{sw} [W m^{-2}] represents shortwave radiation due to solar irradiance, Q_{lw} [W m^{-2}] is the longwave heat flux due to approximate black body radiation, Q_{sen} [W m^{-2}] is the sensible heat flux due to convection and conduction of heat, and Q_{lat} [W m^{-2}] is the latent heat flux and represents heat transfer due to evaporation and transpiration.

As $\Delta t \to 0$ in the absence of any stirring, and only considering surface net heat fluxes as the sole source for positive stratification, Φ increases at a rate given by

$$\left(\frac{d\Phi}{dt}\right)_{heat} = \frac{\alpha g Q_{\text{net}}}{2c_p} \qquad [\text{W m}^{-3}], \tag{2.7}$$

Equation 2.7 only considers the local heat exchange with the atmosphere and no horizontal processes such as diffusion and/or advection of heat.

The energetics model (Section 2.1) further states that in order to vertically mix the water column, ($\Phi \to 0$), a source must supply sufficient levels of mechanical energy to the water column. Simpson and Hunter (1974) proposed that the tidal flow exerting stress on the seabed is the dominant source of this energy on the NW European Shelf. This stress on the seabed, τ_b [N m^{-2}], can be quantified by:

$$\tau_b = k_b \rho_0 \hat{u}^2 \qquad [\text{N m}^{-2}], \tag{2.8}$$

Here, $k_b \sim 0.0025$ and is the bottom drag coefficient in the assumed quadratic drag law and $\hat{u}$ denotes the depth average of the velocity profile $u(z,t)$ [m s^{-1}] (direction is not important). The turbulent energy production by the tide can then be quantified

as

$$P_T = -\tau_b \hat{u} = k_b \rho_0 |\hat{u}|^3 \qquad [\text{W m}^{-2}], \tag{2.9}$$

where $|\hat{u}|$ is the modulus (magnitude) of $\hat{u}$. Combining the two competing mechanisms Simpson and Hunter (1974) established the overall change in Φ as a balance of heating vs. stirring (by the tide):

$$\frac{\partial \Phi}{\partial t} = \underbrace{\frac{\alpha g Q_{\text{net}}}{2 c_p}}_{\text{heating}} - \underbrace{\frac{e k_b \rho_0 |\hat{u}|^3}{h}}_{\text{stirring}} \qquad [\text{W m}^{-3}] \tag{2.10}$$

While most of the turbulent energy is dissipated and transformed into heat, it is assumed that a fixed fraction, e, of P_T is available to decrease Φ. Hence, the factor e acts as a *mixing efficiency* of tidal stirring and was initially taken to be constant.

By using this basic 0D, energy-based argument one can determine whether a shelf sea region will become thermally stratified ($\frac{\partial \Phi}{\partial t} > 0$) or vertically mixed ($\frac{\partial \Phi}{\partial t} < 0$) during periods of positive buoyancy input. Between these two conditions, where PE gains from stirring balance PE losses from heating $\frac{\partial \Phi}{\partial t} = 0$ and Equation 2.10 simplifies to

$$\frac{\alpha g Q_{\text{net}}}{2 c_p} = \frac{e k_b \rho_0 |\hat{u}|^3}{h}. \tag{2.11}$$

This state marks the position of fronts (Figure 2.2). At either side of these fronts the competing forces are imbalanced, which results in the partitioning observed on the NW European Shelf (Figure 2.1 and Figure 2.2): If the buoyancy input is greater than vertical mixing by the tide, shelf seas stratify. Regions that are either shallow or have strong tides will overcome the stratifying influence and stay vertically mixed all year round.

Considering that most terms in Equation 2.11 are held constant, frontal positions are predominantly controlled by

$$\frac{Q_{\text{net}} h}{|\hat{u}^3|} \tag{2.12}$$

where if it is further assumed that Q_{net} is spatially uniform within a certain region, at least relative to tidal mixing, the locations of fronts can now simply be determined by (Simpson and Hunter, 1974):

$$\chi = \frac{h}{|\hat{u}^3|} \tag{2.13}$$

For known stratification, heating and tidal amplitude, the tidal *mixing efficiency*, e, can be calculated by rearranging Equation 2.10. Typical values for e are $\sim\ 0.002 - 0.006$ (e.g. Simpson *et al.*, 1978; Garrett *et al.*, 1978; Simpson and Bowers, 1981; Bowers and Simpson, 1987). These small values indicate that the majority of the available stirring energy is transformed into heat, and only a fraction of $\sim 0.5\%$ is utilised to perform vertical mixing and raise the system's PE. The reason for the low efficiency of tidal mixing is that tidal current shear, and hence turbulence, is concentrated in the region near the sea bed, i.e within the bottom boundary layer. In order to be more effective in reducing Φ, turbulent kinetic energy needs to be injected closer the pycnocline, which will be nearer to the surface because of the rapid absorption of heat.

2.2.1 Mixing at the sea surface

In a typical summer situation the pycnocline is usually located closer to the sea surface than to the sea bed, especially in depths exceeding 100 metres. Therefore it is useful to consider additional sources of PE that act at the sea surface, such as the wind stress. Similarly in shelf seas with weak tidal flows, wind stirring can be the dominant mixing mechanism.

Similar to the tidal stress on the seas bed, τ_b (Equation 2.8), the wind stress on the sea surface, τ_s [N m^{-2}] can be quantified as:

$$\tau_s = c_D \rho_a w^2 \qquad [\text{N m}^{-2}], \tag{2.14}$$

Here, $c_D \approx 0.0012$ is the drag coefficient of the wind over the sea surface, ρ_a [kg m^{-3}] is the density of air and w [m s^{-1}] is the wind speed. The stirring power of the wind, P_W, can be defined as:

$$P_W = k_s \rho_a w^3 \qquad [\text{W m}^{-2}], \tag{2.15}$$

where k_s is the product of c_D multiplied by the slippage factor ($\gamma_s \approx 0.02$). Simpson *et al.* (1978) extended the traditional boundary mixing theory by adding the effect of the wind stress at the sea surface. Now energy was supplied by tidal and wind stirring and the energy balance could be defined as

$$\begin{aligned} \frac{\partial \Phi}{\partial t} &= \frac{\alpha g Q_{\text{net}}}{2 c_p} - \frac{e k_b \rho_0 |\hat{u}|^3}{h} - \frac{\delta k_s \rho_a w^3}{h} \qquad [\text{W m}^{-3}] \\ \frac{\partial \Phi}{\partial t} &= \frac{\partial \Phi}{\partial t}_{\text{heat}} + \frac{\partial \Phi}{\partial t}_{\text{tide}} + \frac{\partial \Phi}{\partial t}_{\text{wind}} \qquad [\text{W m}^{-3}] \end{aligned} \tag{2.16}$$

where δ is the constant mixing efficiency of wind stirring. Although Simpson *et al.* (1978) noted that the addition of wind mixing improved the fit of the predictions with the observations, they concluded that mixing by tidal currents remains the dominant control on influencing the location of fronts, due to a greater spatial homogeneity of the wind across shelf areas.

Further additions to the traditional boundary mixing theory have been developed since particularly to investigate the physical processes affecting stratification in regions of freshwater influence and in the presence of strong horizontal density gradients (e.g. van Aken, 1986; Simpson *et al.*, 1990; Ranasinghe and Pattiaratchi, 1999; De Boer *et al.*, 2008; Hofmeister *et al.*, 2009).

2.2.2 0D model operation

To illustrate the model operation, Equation 2.16 was solved at regular time steps for one year using idealised forcing terms (Figure 2.3a) for a hypothetical site with a water

depth of $h = 90$ metres, and then integrated.

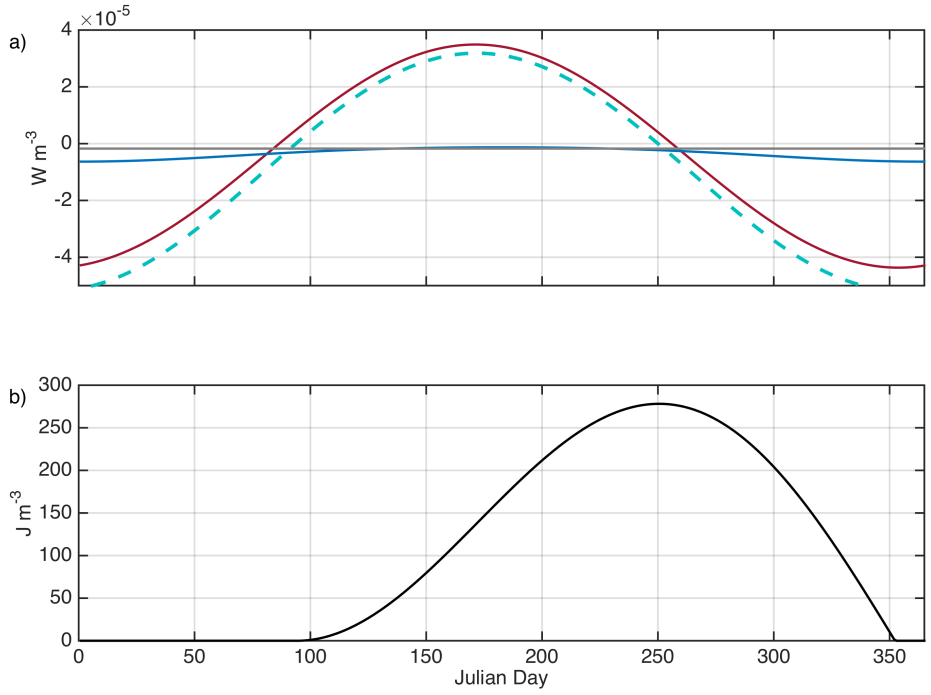

FIGURE 2.3: Energetics model: Idealised run for typical seasonally stratifying shelf sea site. a) forcing terms of Equation 2.16: $\frac{\partial \Phi}{\partial t}_{\text{heat}}$ (red), $\frac{\partial \Phi}{\partial t}_{\text{wind}}$ (blue) and $\frac{\partial \Phi}{\partial t}_{\text{tide}}$ (grey) and their sum, $\frac{\partial \Phi}{\partial t}$ (dashed cyan) [W m^{-3}] b) 0D model result: Φ [J m^{-3}]

Here, both $\frac{\partial \Phi}{\partial t}_{\text{heat}}$ and $\frac{\partial \Phi}{\partial t}_{\text{wind}}$ are characterised by a seasonal cycle typical for the NW European Shelf (James, 1977). The tidal stirring term, $\frac{\partial \Phi}{\partial t}_{\text{tide}}$, is kept constant here. When winds speeds are low in the summer months, $\frac{\partial \Phi}{\partial t}_{\text{tide}}$ becomes the dominant negative term in Equation 2.16. Once integrated over the entire year, the seasonal cycle of Φ (Figure 2.3b) suggests that this hypothetical water column was stratified ($\Phi > 0$ J m^{-3}) between early-April and mid-December. As can be seen from the sum of all forcing terms, $\frac{\partial \Phi}{\partial t}$ (cyan in Figure 2.3a), which is the left hand side term of Equation 2.16, Φ is increasing for $\frac{\partial \Phi}{\partial t} > 0$ W m^{-3} and decreasing for the opposite.

2.2.3 Note on mixing efficiencies

As already mentioned, both stirring terms in Equation 2.16 are scaled by an efficiency constant. Mixing efficiency is the ratio of energy available to mixing to the total amount of dissipated kinetic energy (KE). Using Equation 2.16 and observations of frontal positions from the Irish and Celtic Sea collected in May 1978, Simpson and Bowers (1981) found efficiency values of $e \simeq 0.0037$ and $\delta \simeq 0.023$. The higher efficiency of the wind mixing, δ, compared to e can be explained by the closer proximity of wind stirring to the location of the strongest density gradient (pycnocline).

2.2.4 Performance - model validation at tidal mixing fronts

The success of the energetics model predicting the observed state of the water column, i.e. either vertically stratified or fully mixed, has been widely tested using data from in-situ (Garrett *et al.*, 1978; Pingree and Griffiths, 1978) and remote sensing observations (Simpson *et al.*, 1977; Simpson and Bowers, 1979). Both approaches have largely found good agreement for the averaged partitioning of shelf seas. In principle, the energetics model might therefore also be capable of describing the shelf seas in response to varying PE sinks and source terms, and in particular the tidal spring-neap cycle. Simpson and Bowers (1981) found, however, that the model overestimated the erosion of stratification, as the predicted movement of the frontal position between neap and spring tides was more than typically observed in satellite images. This overestimation was attributed to the fixed mixing efficiency e, which in reality becomes modulated by the existing level of stratification. In order for stratified areas to become mixed, the stirring has to overcome two sources of buoyancy. Firstly mixing has to counteract any buoyancy input from surface heating, and secondly it needs to remove any stored buoyancy that was established during neap periods. This had been previously shown using tank experiments by Linden (1979). Simpson and Bowers (1981) therefore suggested the introduction of a feedback constraint, where mixing efficiencies were stability dependent. Hence, they proposed to multiply the efficiency factors e and δ by a factor

F:

$$F = \left(\frac{\Phi_0}{\Phi_0 - \Phi} \right)^{\frac{1}{2}}, \tag{2.17}$$

where Φ_0 [J m $^{-3}$] is a constant. Using this stability criterion Simpson and Bowers (1981) found that the magnitude of the inferred mixing could be reduced close to the observations using a value of $\Phi_0 = 5$ J m $^{-3}$ and choosing 0.25 as a lower limit for F. While Yanagi and Tamaru (1990) successfully used the variable efficiency model proposed by Simpson and Bowers (1981), relating mixing efficiencies to stability (as proposed in Equation 2.17), has been argued to be a somewhat arbitrary parameterisation (Sharples and Simpson, 1996; Simpson and Sharples, 2012).

2.2.5 Summary: 0D heating-stirring model

In summary, the 0D heating-stirring model (hereafter referred to as SH74), introduced in Section 2.2, is based on a simple energy criterion, where stratification is a vertical exchange process balanced by heating vs. stirring at the boundaries (Equation 2.16, Figure 2.3). It is a powerful tool to predict the state of the water column using only a single variable, Φ. However, Φ is only a quantitative measure of the strength of the vertical density stratification and is unable to inform about the vertical density profile, important for biological processes and thus air-sea gas exchange (e.g. Thomas *et al.*, 2004). The following Section 2.3 therefore expands this framework into the vertical dimension.

2.3 Heating-stirring competition: 1D approach

Mixing efficiencies are not the only aspects of the heating-stirring competition that are affected by stored buoyancy. Pingree (1975) noted that the vertical heat exchange of a system is similarly affected by its existing heat storage. Due to the 0D approach, the surface heat flux used by Simpson and Hunter (1974) and Simpson and Bowers (1981) was independent of the water column's depth, h, and its energetic state i.e. its potential

energy anomaly (Φ, Equation 2.1). However this is physically incorrect, as heat losses are proportional to sea surface temperatures (SST); a shallow surface layer of warm water (such as a stratified water column) will be warmer but will absorb less heat overall than an adjacent fully mixed water column. As a result, Simpson and Bowers (1984) proposed to mediate the heat flux by the existing SST. This naturally led on to the question how heat is vertically distributed in the water column due to vertical mixing. In order to answer this question, the original heating-stirring framework needed to be extended to a 1D model (Simpson and Bowers, 1984).

In order to vertically distribute energy/heat, Simpson and Bowers (1984) developed a 1D model based on the heating-stirring approach developed in earlier work (Simpson and Hunter, 1974; Simpson *et al.*, 1978; Simpson and Bowers, 1981). This new framework was able to directly model the sea surface temperature, and thus able to influence the heat flux at the surface. As in previous models, horizontal processes of heat transfer (such as advection and diffusion) were ignored, as they were considered small compared to the vertical flux of heat. Furthermore, mixing efficiencies were kept constant throughout the seasonal cycle. The 1D heating-stirring model is hereafter referred to as SB84.

2.3.1 SB84 description and operation

Figure 2.4 demonstrates the operation of the SB84. The SB84 initiation consists of setting values representative of the study area, i.e. the total depth, h [metre], which is split into evenly spaced bins of thickness Δz [metre], which then determines the number of vertical bins, n (Figure 2.4). The total duration of the model run [days] is split into evenly spaced time steps, Δt [hours]. As the model directly modelled the vertical temperature structure it also required an initial temperature profile, T_0. In order to calculate Φ from a vertical density profile, SB84 assumed a constant salinity profile.

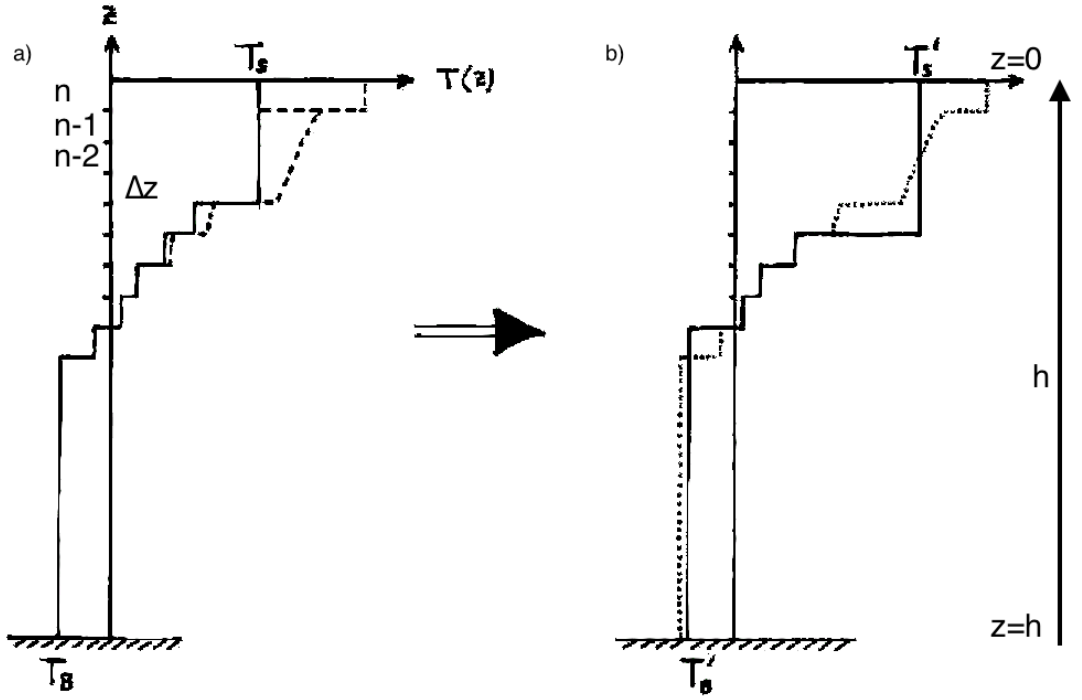

FIGURE 2.4: SB84 operation: distribution of heat at each time step of the model. a) heating phase: here heat is distributed in the surface layers (dashed line) Solid lines denotes the temperature profile at T_n. b) mixing phase: the new temperature profile (dashed line) is altered by boundary stresses, distributing heat in the vertical. The final temperature profile at T_{n+1} (after heating and stirring has taken place) is denoted by the solid black line in b). Adapted from Simpson and Bowers (1984).

In contrast to SH74, within SB84 the net heat flux term Q_{net} [W m^{-2}] (Equation 2.6), was split into an incoming (net heat gain, which generally comes from the shortwave radiation) component, Q_{sw} [W m^{-2}], and an outgoing (net heat loss) component, Q_{u} [W m^{-2}], i.e.:

$$Q_{\text{net}} = Q_{\text{sw}} + Q_{\text{u}}. \tag{2.18}$$

Here, Q_{u} is equivalent to the sum of all other main heat flux terms i.e.

$$Q_{\text{u}} = Q_{\text{lw}} + Q_{\text{sen}} + Q_{\text{lat}}, \tag{2.19}$$

Rather than estimating each heat flux component separately, Q_{u} was simply parameterised as:

$$Q_{\text{u}} = k(T_d - T_s) \tag{2.20}$$

Here, $k(T_d, T_s, w)$ [W m^{-2} °C^{-1}] is a thermal exchange coefficient (Brady *et al.*, 1969; Edinger *et al.*, 1974), and T_d and T_s [°C] are the dew point and sea surface temperate, respectively.

Seasonal values of Q_{sw} [W m^{-2}], T_d [°C] and w [m s^{-1}] were taken from sinusoidal fits to observational data in the Celtic Sea (Simpson and Sharples, 2012):

$$Q_{\mathrm{sw}} = 136.1 \; + \; 109.34 \; \sin(\omega_a t_J - 1.378) \tag{2.21}$$

$$T_d = 8.65 \; + \; 5.07 \; \sin(\omega_a t_J - 1.4612) \tag{2.22}$$

$$w = 7.35 \; + \; 1.94 \; \sin(\omega_a t_J + 1.569) \tag{2.23}$$

Here, ω_a is the annual frequency and t_J the Julian day.

At the beginning of each time step, the heat terms are applied to the surface layers (Figure 2.4a): After the heat loss, $\mathrm{Q_u}$, is applied to the surface grid cell only, the incoming heat flux, $\mathrm{Q_{sw}}$, is distributed in the near surface according to a typical vertical distribution of shortwave radiation in coastal areas (Ivanoff, 1977). Here, 55% of $\mathrm{Q_{sw}}$ were input to the top layer, which represents the rapid attenuation of the red end of the spectrum. The remaining 45% are distributed exponentially with depth (dashed line in Figure 2.4a). The new temperature profile is then stirred due to the input of wind and tidal energy at the sea surface and bed, respectively. In order to stir the profile, SB84 takes the following steps: A density profile is calculated using the new temperature profile and a constant salinity profile. For each energy input (wind and tidal) the model then iteratively loops from the respective boundary through the vertical profile as long as the available energy from either wind, P_W or tide, P_T is greater or equal to the amount of PE required to mix the water column to this point. Once these levels are found for each energy input, SB84 then homogenises the temperature profile up to this point. This process of stirring is illustrated in Figure 2.4b as the change from the dashed to the bold temperature profile. Hence depending on the source of the energy,

the stirring either takes place from the bottom upwards (tidal) or from the top down (wind stirring). The amount of PE gained by the water column at each time step is equivalent to the effective stirring energy input by tide ($e\mathrm{P}_T$, Equation 2.9) and wind ($\delta\mathrm{P}_W$, Equation 2.15). If less than the available PE was used for mixing at each time step, Δt, than the remaining PE is carried over to the next time step, unless the water column is already fully mixed. Similar to SH74, and of relevance to the implications of the results presented later in this thesis, SB84 was solely driven by forces acting on the boundaries (sea surface and sea bed) and therefore lacked any representation of processes supplying PE in midwater, such as mixing due to internal waves.

To illustrate the model operation and output, SB84 was run for one year for a hypothetical site with a water depth of $h = 90$ metres. The time step used here was $\Delta t = 24$ hrs, the vertical resolution was set to $\Delta z = 1$ metre and the initial temperature profile was set to $T_0 = 8°\mathrm{C}$. This run was forced using the idealised forcing terms shown in Figure 2.5.

The heat flux terms, Q_{sw} and Q_{u} (Figure 2.5a), and the dew point temperature T_d (Figure 2.5b) were obtained by evaluating Equations 2.21 - 2.22. Here T_s was taken from the model output at each time step (Figure 2.4b). Figure 2.5c shows the wind stirring term, $\delta\mathrm{P}_W$ [W m^{-2}], which was calculated using a seasonal cycle of wind speed (not shown) obtained by evaluating Equation 2.23. A typical time series of the tidal stirring term, $e\mathrm{P}_T$ [W m^{-2}] is shown in Figure 2.5d. Here $e\mathrm{P}_T$ was based on a constant tidal amplitude of ~ 0.4 m s^{-1}.

Since SB84 operates over a 1D domain, i.e. depth, the forcing terms (Figure 2.5) of SB84 have units of W m^{-2} rather than W m^{-3}, as was the case for SH74 (Figure 2.3a), where PE sources and sinks were scaled by the depth, h, of the water column (Equation 2.16).

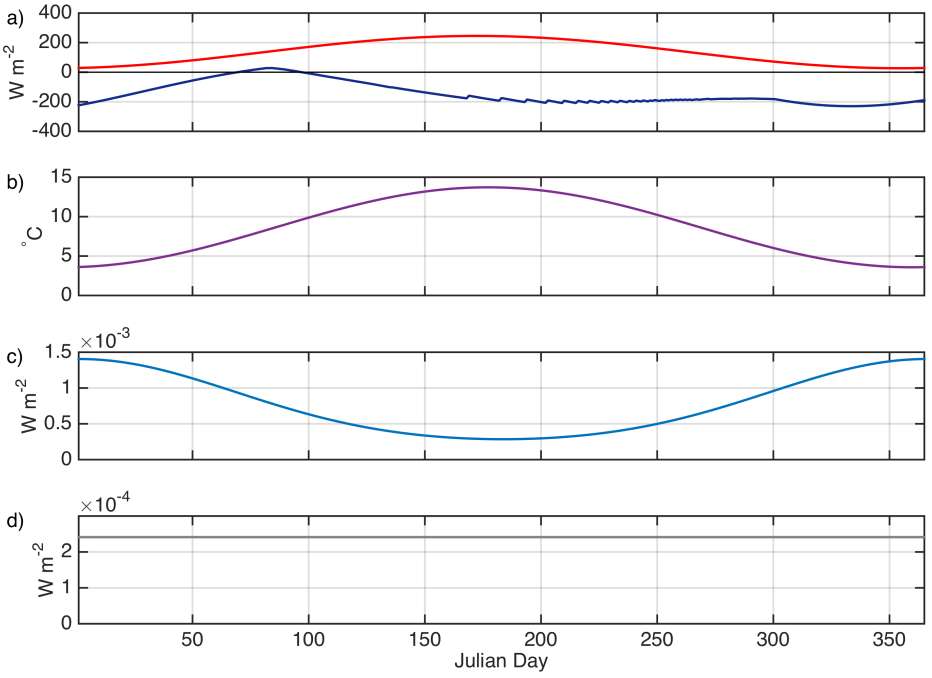

FIGURE 2.5: SB84 forcing terms. a) heat fluxes: Q_{sw} (red) and Q_{u} (blue) [W m^{-2}] b) dew point temperature, T_d, [°C] c) $\delta \mathrm{P}_W$ [W m^{-2}] d) $e\mathrm{P}_T$ [W m^{-2}].

Figure 2.6 illustrates the SB84 model output, over the entire time domain (Figure 2.6a). Using the constant salinity profile set at the start to calculate density profiles (not shown), Φ (Equation 2.1) was then evaluated (Figure 2.6b).

This hypothetical water column was fully mixed until late March and stratification broke down at the end of November (Figure 2.6). Both the surface and bottom layer temperature increased, until they equilibrated when stratification became completely eroded in November (Figure 2.6a).

2.3.2 Seasonal heat storage

In order to investigate how vertical stirring and depth affects the seasonal heat storage of a water column, Simpson and Bowers (1984) ran SB84 using several setups (Figure 2.7).

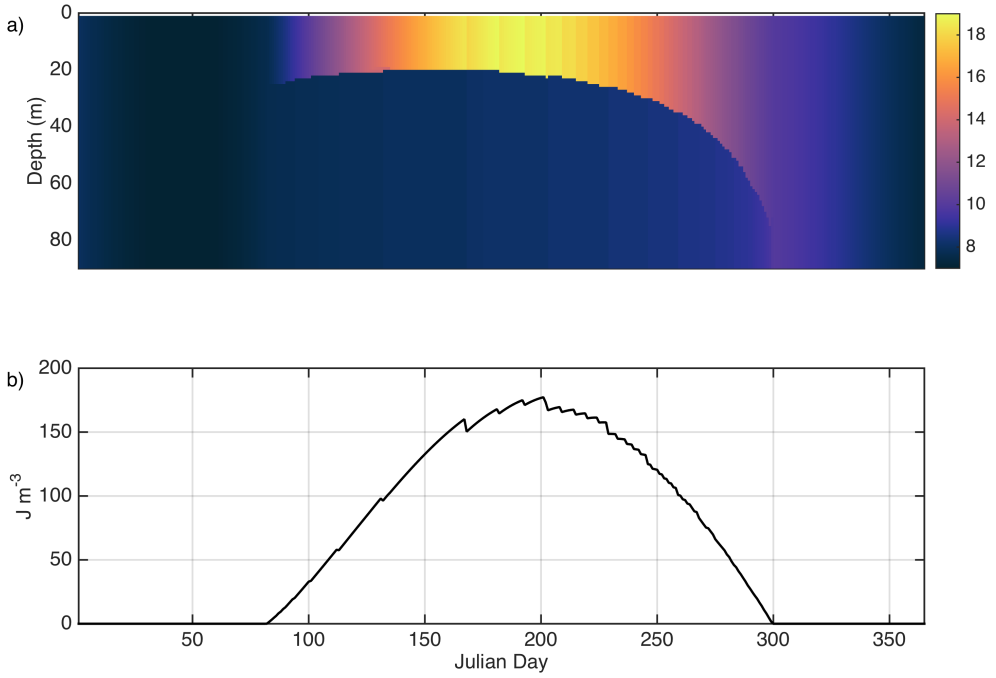

FIGURE 2.6: SB84 output. a) Temperature [°C] b) Φ [J m^{-3}]

They found that for depths of $h < 50$ metres the amplitude of the seasonal heating cycle increased with increasing depth (Figure 2.7). However, for $h > 50$ metres, the amount of tidal stirring (here denoted by χ, Equation 2.13) became the dominant control on the seasonal heat storage of a water column (Figure 2.7). In fact, high levels of tidal mixing, i.e. low χ, resulted in the highest heat storage. In a stratified water column, the lack of vertical heat distribution concentrates incoming heat in the top layer, hence why stratified areas are associated with higher SSTs (Figure 2.1, Figure 2.2). This leads to an increased heat flux back to the atmosphere and an overall reduced amount of stored heat. Whereas in mixed water columns, high levels of tidal mixing result in heat being uniformly distributed, lower SSTs and less heat loss, and therefore a higher heat storage overall. The difference in amplitude of seasonal heat storage between mixed and stratified regimes was predicted to be of factor ~ 2 and agreed well with observations (Simpson and Bowers, 1984, 1990).

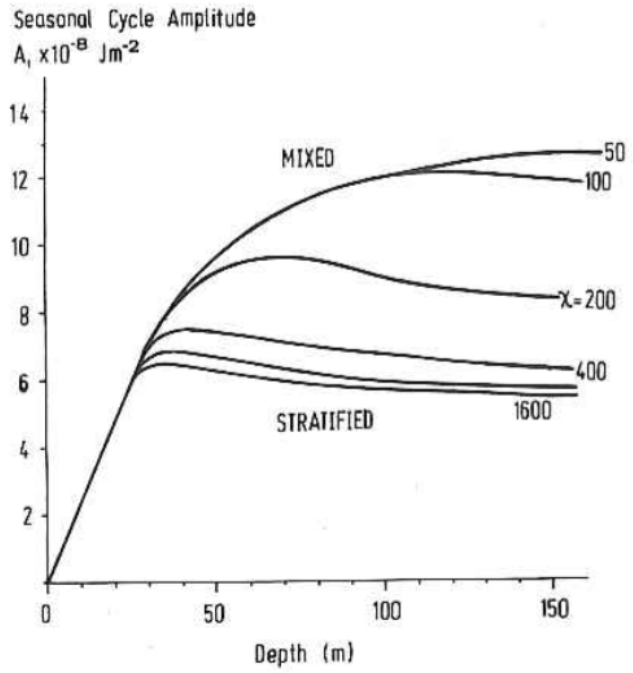

FIGURE 2.7: Amplitude of seasonal heat storage [J m^{-2}] for typical shelf sea depths [metre] and levels of tidal stirring, χ [m^2 s^{-3}]. Taken from Simpson and Bowers (1984).

2.3.3 Summary: 1D heating-stirring model

The 1D SB84, introduced in Section 2.3, uses the same energy criterion (Equation 2.16) and assumptions regarding the efficiency of mixing as the SH74 (Section 2.2). Due to its additional dimension it is able to distribute heat more realistically, and thereby give a quantitative (Φ) and qualitative ($T(z)$) estimate of the vertical water column structure, and it has been shown to predict the seasonal cycle of surface and bottom temperatures well in stratified regions (Bowers and Simpson, 1987; Elliott and Clarke, 1991). However, similar to SH74 it only considers the mixing driven at the boundaries and thus lacks any internal mixing mechanisms. While the model's prescriptive nature of mixing processes makes it cheap and easy to run, the boundary-driven nature of the model could limit it in simulating the vertical density structure correctly (Simpson and Sharples, 2012). The SB84 also neglects the modification of mixing efficiencies due to varying stratification (Turner, 1973; James, 1977).

In order to avoid these aforementioned limitations (lack of internal mixing mechanism, prescribing mixing without modification due to varying stratification) imposed by the prescriptive models (SH74 and SB84), introduced in Sections 2.2 and 2.3, respectively, the following Section 2.4 will introduce a simple 1D turbulence closure (TC) model.

2.4 TC model

The TC model used in this thesis is the Shelf Sea Physics and Primary Production (S2P3) model available in Simpson and Sharples (2012). This TC model is similar to the one previously used and described in Sharples *et al.* (2006), but differs by the inclusion of 3 possible internal mixing parameterisations that the TC model can employ. By employing a turbulence closure scheme (Section 2.4.1) and a choice of three internal wave mixing schemes (Section 2.4.3) the TC model should be able to represent turbulent mixing processes throughout the water column more accurately than the prescriptive models (SH74 and SB84), as the turbulence closure scheme enables to link the stability of the water column to the amount of mixing that is taking place. While an attempt had been made within SH74 to take account of the effect stability of the water column has on the mixing efficiencies (Equation 2.17), the description seemed rather arbitrary (Section 2.2.4). In contrast, the TC model is based on theory and knowledge gained in laboratory experiments. The implications of the improved representation of turbulence within the TC model compared to using prescriptive mixing models will be illustrated in Section 2.4.5. Figure 2.8 demonstrates the operation of the 1D TC model. Similar to the SB84, the TC model consists of n vertical levels (grid cells) spread evenly over the total depth h [metre], of thickness $\Delta z = h/n$ [metre], with z the vertical co-ordinate positive upwards (Figure 2.8).

Rather than prescribing the effects of mixing as done by SH74 (Simpson and Hunter, 1974) and SB84 (Simpson and Bowers, 1984), this numerical model simulates vertical profiles of currents, turbulence and temperature. The core component of this model

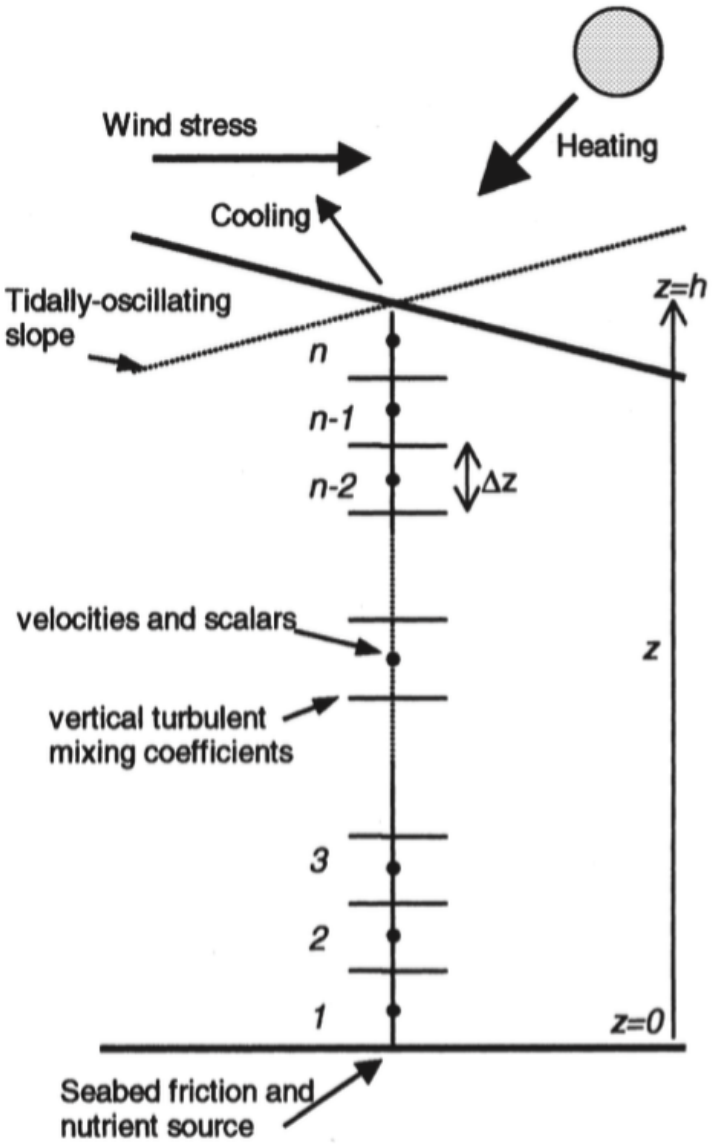

FIGURE 2.8: TC model grid and operation of physical processes. Velocity and scalar values are representative of the centre of the grid cells, however turbulent processes act on the lower boundary of the grid cell. Taken from Sharples (1999).

uses an implicit scheme to integrate the Navier Stokes equations (equations of motion). The linearised momentum equations for the horizontal x and y velocity components, u and v [m s^{-1}], in the absence of horizontal density gradients, are given by:

$$\frac{\partial u}{\partial t} = -g \sum_{i=1}^{m} A_{ix} \cos(\omega_i t - \phi_{ix}) + fv + \frac{\partial}{\partial z}\left(N_z \frac{\partial u}{\partial z}\right) \tag{2.24}$$

$$\frac{\partial v}{\partial t} = -g\sum_{i=1}^{m} A_{iy}\ \cos(\omega_i t - \phi_{iy}) - fu + \frac{\partial}{\partial z}\left(N_z \frac{\partial v}{\partial z}\right) \tag{2.25}$$

Here, the first term of of the right hand side of Equations (2.24) and (2.25) represents the total barotropic tidal forcing of m tidal constituents. For the i^{th} tidal constituent, $A_{ix,\ iy}$ are the surface slope amplitudes, $\phi_{ix,\ iy}$ are the tidal slope phases in the x and y directions and ω_i [s^{-1}] is the angular frequency of tidal constituent i. Tidal slope amplitudes are calculated as:

$$A_{ix} = \frac{C_i}{g}(\omega_i + P_{il} f); \qquad A_{iy} = \frac{C_i}{g}(\omega_i P_{il} + f) \tag{2.26}$$

Here, C_i [$\mathrm{m\ s}^{-1}$] is the length of the semi-major axis of the tidal ellipse, f is the Coriolis parameter and P_l is the polarity, which is sometimes also referred to as polarisation (Simpson and Tinker, 2009) or ellipticity (Pugh, 1996; Souza and Simpson, 1996). Both C_i and P_{il} were derived from results of harmonic analysis on the u and v component of the observed flow following Souza and Simpson (1996).

The Coriolis term is the second term on the right hand side of Equations (2.24) and (2.25). This term describes the force exerted on a moving parcel of water on Earth due to Earth's rotation.

The final term on the right hand side of Equations (2.24) and (2.25) is the frictional term. This term represents the vertical transfer of momentum by relating the stress to a vertical gradient of horizontal velocity through the vertical eddy viscosity, N_z [m^2 s^{-1}].

At the sea surface ($z = h$), surface stresses are equal to the wind stresses, which are driven by the x and y component of the wind velocity, w_x and w_y [$\mathrm{m\ s}^{-1}$]. The

horizontal components of these surface stresses are calculated as:

$$\tau_{sx} = -\rho N_z \frac{\partial u}{\partial z} = -c_D \rho_a \sqrt{\left(w_x^2 + w_y^2\right)}\ w_x$$
$$\tau_{sy} = -\rho N_z \frac{\partial v}{\partial z} = -c_D \rho_a \sqrt{\left(w_x^2 + w_y^2\right)}\ w_y \tag{2.27}$$

Here, $\rho_a = 1.3$ kg m^{-3} is the air density, and the surface drag coefficient c_D is related to the wind speed, w, following Smith and Banke (1975):

$$c_D = (0.63 + 0.066\mathrm{w})\rho_s^{-1} \tag{2.28}$$

Here, ρ_s is the density of the top grid cell.

At the bottom boundary ($z = 0$), a quadratic stress law (see also Equation 2.9) is applied in both horizontal directions, x and y:

$$\tau_{bx} = -k_b \rho_b \sqrt{\left(u_1^2 + v_1^2\right)}\ u_1; \qquad \tau_{by} = -k_b \rho_b \sqrt{\left(u_1^2 + v_1^2\right)}\ v_1 \tag{2.29}$$

Here, ρ_b is the density of the lowest grid cell, and u_1 and v_1 are the velocity components 1 metre above the sea floor.

In the absence of horizontal gradients and rotation, the vertical distribution of heat and salt due to turbulent mixing is controlled by

$$\frac{\partial (T,S)}{\partial t} = \frac{\partial}{\partial z}\left(K_z \frac{\partial (T,S)}{\partial z}\right) \tag{2.30}$$

where K_z [m^2 s^{-1}] is the vertical eddy diffusivity, and is taken to be equal for salt and heat.

In order to solve and integrate the momentum equations (2.24) and (2.25), and the diffusion equation (2.30) forward in time values for the vertical mixing coefficients, N_z and K_z, need to be found. These variables represent the vertical transport of scalar and

momentum due to turbulent processes, and thus depend on the amount of turbulence within the flow. To derive them, the TC model employs a $k-\varepsilon$ turbulence closure scheme developed by Canuto *et al.* (2001), which will be introduced in Section 2.4.1.

2.4.1 $k-\varepsilon$ turbulence closure scheme

Like other turbulence closure schemes, the $k-\varepsilon$ scheme uses several expressions to relate fluctuations of a scalar to properties of the mean flow (e.g. Mellor and Yamada, 1982; Burchard *et al.*, 1998; Canuto *et al.*, 2001). Firstly, it assumes that turbulent kinetic energy (TKE) is in local equilibrium, i.e. TKE is produced and dissipated in the same location (Equation 2.31):

$$\begin{aligned} \frac{\partial \mathrm{TKE}}{\partial t} &= N_z S^2 - K_z N^2 - \varepsilon \\ &= \boldsymbol{P} - \boldsymbol{B} - \text{TKE dissipation} \end{aligned} \tag{2.31}$$

Here, S^2 [s^{-2}] is the vertical shear of horizontal velocities squared:

$$S^2 = \frac{dU}{dz}^2 = \left(\frac{du}{dz}^2 + \frac{dv}{dz}^2\right) \tag{2.32}$$

and $\boldsymbol{P}$ represents the shear production of turbulence. $\boldsymbol{P}$ is always positive, as kinetic energy from shear flows is transformed into TKE. The term, $\boldsymbol{B}$ represents buoyancy production of TKE, where N^2 [s^{-2}] (Equation 2.33) is the Brunt Väilsälä, or buoyancy frequency squared. N depicts the frequency of oscillation of a vertically displaced water parcel when displaced within a stably stratified fluid.

$$N^2 = -\frac{g}{\rho}\frac{\partial \rho}{\partial z} \tag{2.33}$$

For unstable density stratification, $\boldsymbol{B}$ is negative (promotion of convective mixing), whereas during stable conditions, TKE is used to work on buoyancy, hence $\boldsymbol{B}$ becomes

positive. The final term, ε [m^2 s^{-3}], on the right hand side of Equation 2.31 represents the TKE dissipation.

During stratified conditions ($\boldsymbol{B}$>0), turbulence becomes a balance of shear production ($\boldsymbol{P}$) working against buoyancy production ($\boldsymbol{B}$) and dissipation (ε). For turbulence to develop in stably stratified fluids, shear production must therefore outweigh the buoyancy production. This ratio of supply and demand of TKE production is known as the *flux Richardson number*:

$$Ri_f = \frac{K_z}{N_z} \frac{-\frac{g}{\rho}\frac{\partial \rho}{\partial z}}{\left(\frac{du}{dz}^2 + \frac{dv}{dz}^2\right)} = \frac{K_z}{N_z}\frac{N^2}{S^2} \tag{2.34}$$

The ratio of K_z and N_z is called the *Prandtl number*:

$$Pr = \frac{K_z}{N_z} \tag{2.35}$$

If it is further assumed that the transfer of turbulence (N_z) is equal to energy that mixes vertical gradients of scalars (K_z), $Pr = 1$, and thus Equation 2.34 simplifies to:

$$Ri_g = \frac{N^2}{S^2} = \frac{-\frac{g}{\rho}\frac{\partial \rho}{\partial z}}{\left(\frac{du}{dz}^2 + \frac{dv}{dz}^2\right)} \tag{2.36}$$

This is known as the *gradient Richardson number*, Ri_g. Ri_g or its inverse, $1/Ri_g$, have been used widely as an indicator for the likelihood of shear driven instability to occur (e.g. van Haren *et al.*, 1999; MacKinnon and Gregg, 2005b; Moum *et al.*, 2008). Miles (1961) and Howard (1961) used stability analysis of shear flows to show that the critical threshold for instabilities to occur and the generation of excess TKE to erode stratification is $Ri_{cr} \leq 0.25$.

The $k-\varepsilon$ turbulence closure scheme by Canuto *et al.* (2001) is based on two governing equations for the local rate of change of TKE and ε:

$$\frac{\partial \mathrm{TKE}}{\partial t} - \frac{\partial}{\partial z}\left(N_z \frac{\partial \mathrm{TKE}}{\partial z}\right) = N_z S^2 - K_z N^2 - \varepsilon \tag{2.37}$$

$$\frac{\partial \varepsilon}{\partial t} - \frac{\partial}{\partial z}\left(N_z/1.08\ \frac{\partial \varepsilon}{\partial z}\right) = \frac{\varepsilon}{\mathrm{TKE}}\left[c_1 N_z S^2 - c_3 K_z N^2 - c_2 \varepsilon\right] \tag{2.38}$$

Here, c_{1-3} are constants (Canuto *et al.*, 2001), and ε is related to TKE via a turbulent length scale, L [metre], by

$$\varepsilon = 0.5562^3 \frac{\mathrm{TKE}^{3/2}}{L} \tag{2.39}$$

Once TKE, ε and L are known, N_z and K_z can be derived from:

$$N_z = S_M \sqrt{\mathrm{TKE}}\ L; \qquad K_z = S_H \sqrt{\mathrm{TKE}}\ L \tag{2.40}$$

S_M and S_H are momentum and heat stability functions (Galperin *et al.*, 1988), which relate N_z and K_z to the gradient Richardson number Ri_g (Equation 2.36, Figure 2.9).

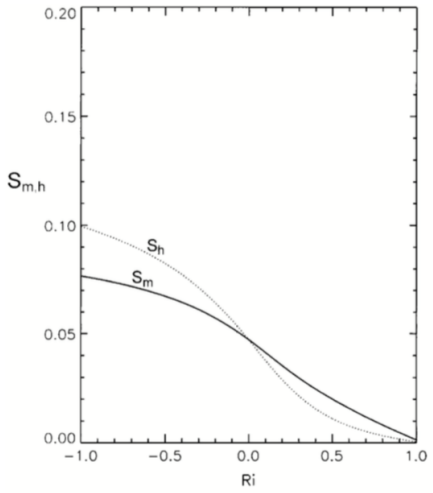

FIGURE 2.9: Predicted variations of stability functions, S_H and S_M, to changes in Ri_g (here denoted as Ri). Taken from Canuto *et al.* (2001).

For unstable stratification ($Ri_g < 0$) S_H and S_M are greatest, and they reduce as water column stability increases, until a critical point, $Ri_{cr} = 0.85$, where turbulence is arrested.

2.4.2 Heat flux calculations

Instead of parameterising the heat flux terms Q_{sw} and Q_{u}, as was done in SB84 (Equations 2.21 and 2.20), here the individual heat flux terms that make up Q_{net} (Equation 2.6) are calculated from bulk parameterisations (Gill, 1982). In order to derive the shortwave radiation term Q_{sw}, the solar radiation at the top of the atmosphere, $Q_{\mathrm{s}} = 1368$ W m^{-2}, is modified by cloud cover, Earth's albedo, and solar declination, which depends on the time of year, latitude and time of day. Daily variation of the of solar irradiance is then calculated as a half-sinusoid variation between sunset and sunrise times, which were based on latitude and time of year. Similarly to the SB84 model, 55% of $\mathrm{Q_{sw}}$ are input to the top layer and the remaining 45% were distributed exponentially with depth.

The remaining heat flux terms that make up Q_{u} (Equation 2.19) were calculated as outlined in Gill (1982) and Sharples *et al.* (2006):

The longwave heat flux, Q_{lw}, is the radiative heat flux due to cooling of earth's surface is usually calculated as a product of black body radiation and the fraction of cloud cover n_c:

$$Q_{\mathrm{lw}} = e_m \sigma (T_s + 273.15)^4 \ (0.39 - 0.05 \ e_a^{1/2})(1 - 0.6 \ n_c^2) \tag{2.41}$$

The emissivity, $e_m = 0.985$, is a correction factor for the departure of the ocean's surface from blackbody behaviour, σ is Stefan's constant (5.67×10^{-8} W m^{-2} K^{-4}), and e_a [mbar] is the vapour pressure of water calculated as:

$$e_a = 0.01 r_h e_w \tag{2.42}$$

where r_h [%] is relative humidity and e_w [mbar] is the saturated vapour pressure calculated as a function of air temperature T_a:

$$\log_{10} e_w = \frac{0.7859 + 0.03477 \ T_a}{1 + 0.00412 \ T_a} \tag{2.43}$$

The sensible heat flux, Q_{sen}, is representative for the exchange of heat due to conduction or convection, and was calculated as:

$$Q_{\text{sen}} = c_h \rho_a c_{pa} w (T_s - T_a) \tag{2.44}$$

Here, c_h is the Stanton number (1.45×10^{-3}), and c_{pa} is the specific heat capacity of air (1004 J kg^{-1} K^{-1}).

The latent heat flux, Q_{lat}, is associated with phase changes of water and therefore represents the heat flux due to evaporation or condensation. This was calculated as:

$$Q_{\text{lat}} = c_e t_l \rho_a w (q_w - q_a) \tag{2.45}$$

Here, c_e is the unitless Dalton number (1.5×10^{-3}), t_l is the latent heat of vaporisation of water (2.5×10^6 - 2.3×10^3 T_s J kg^{-1}), and q_w and q_a are the specific humidities of air at sea and air temperature, respectively:

$$q_w = \frac{0.62\ e_w}{p_a - 0.38 e_w} \qquad q_a = \frac{0.62\ e_a}{p_a - 0.38 e_a} \tag{2.46}$$

where p_a [mbar] is air pressure.

2.4.3 Internal wave mixing parameterisation

While the TC model itself can be considered a boundary driven model like SH74 and SB84, it is the inclusion of internal mixing parameterisations that enable the TC model to include the influence of internal mixing at the thermocline. The way these schemes parameterise the influence of shear driven mixing at the thermocline due to internal mixing processes such as internal waves will be outlined below:

2.4.3.1 Simple background viscosity and diffusivity – BG

The first parameterisation is the most basic approach, as it simply limits the minimum values of N_z and K_z, as a representation of background mixing taking place as a result on non-resolved processes, i.e.

$$N_z^{\min} = K_z^{\min} = \text{background} \tag{2.47}$$

Within this thesis, these background values were set to $N_z^{\min} = K_z^{\min} = 1 \times 10^{-5}$ m^2 s^{-1} to represent typical background values of weak internal wave mixing away from large topographic features (Townsend, 1991; Benitez-Nelson *et al.*, 2000; Sharples *et al.*, 2001, 2009). Results of the TC model that employed this background based internal mixing parameterisation will be identified by using the subscript $_{\mathrm{BG}}$.

2.4.3.2 Kantha & Clayson – KC

The second scheme parameterises shear-induced mixing as a decreasing function of Ri_g as is it increases towards a critical value, $Ri_{KC} = 0.7$ (Kantha and Clayson, 1994). Within the thermocline region, which is identified by the value of TKE falling below a threshold of $\mathrm{TKE}_{\min} = 1 \times 10^{-6}$ m^2 s^{-2}, the following three scenarios are possible:

If $Ri_g > Ri_{KC}$, diffusivity and viscosity are internal wave ($^{\mathrm{iw}}$) driven, here:

$$N_z = N_z^{\mathrm{iw}}; \qquad\qquad K_z = K_z^{\mathrm{iw}}; \tag{2.48}$$

where $N_z^{\mathrm{iw}} = 1 \times 10^{-4}$ m^2 s^{-1} and $K_z^{\mathrm{iw}} = 5 \times 10^{-5}$ m^2 s^{-1}. This is similar to the BG parameterisation described in Section 2.4.3.1.

If $Ri_g < 0$ (convectively unstable) diffusivity and viscosity are elevated to rapidly mix the fluid.

$$N_z = 5 \times 10^{-3} \text{ m}^2 \text{ s}^{-1} \qquad K_z = 5 \times 10^{-3} \text{ m}^2 \text{ s}^{-1}. \tag{2.49}$$

In an unstable fluid the effect of internal waves on mixing is small, and the dominant effect is vigorous mixing from increased shear driven mixing ($^{\mathrm{sh}}$), i.e. convection.

If $0 < Ri_g < Ri_{KC}$, diffusivity and viscosity are derived according to:

$$N_z = N_z^{\mathrm{iw}} + c_{KC}\ N_z^{\mathrm{sh}}; \qquad K_z = K_z^{\mathrm{iw}} + c_{KC}\ K_z^{\mathrm{sh}}; \tag{2.50}$$

where c_{KC} is a scaling factor:

$$c_{KC} = \left[1 - \left(\frac{Ri_g}{Ri_{KC}}\right)^2\right]^3 \tag{2.51}$$

Results of the TC model that employed this Kantha and Clayson (1994) based internal mixing parameterisation will be identified by using the subscript $_{\mathrm{KC}}$.

2.4.3.3 Canuto – CA

For the third parameterisation Canuto *et al.* (2001) argues that critical *Richardson number* for internal wave mixing is of the form

$$Ri_{iw} = \frac{N^2}{S_{iw}^2} \tag{2.52}$$

where S_{iw}^2 is the shear due to internal waves. In an attempt to avoid overmixing due to internal waves, Canuto *et al.* (2001) suggests a constant Ri_{cr}-factor, $c_{\mathrm{CA}} = 0.88$, by which the turbulence closure schemes Ri_{cr} is scaled by to get Ri_{iw}:

$$Ri_{iw} = c_{\mathrm{CA}}\ Ri_{cr} = 0.88\ Ri_{cr} \tag{2.53}$$

Using the predicted N^2, S_{iw}^2 can then be found by rearranging Equation 2.52:

$$S_{iw}^2 = \frac{N^2}{Ri_{iw}} \tag{2.54}$$

Results of the TC model that employed the Canuto *et al.* (2001) based internal mixing parameterisation will be identified by using the subscript $_{\mathrm{CA}}$.

2.4.4 TC model operation

To illustrate the model operation and demonstrate the typical model output, the TC model was run for one year for a hypothetical site in the Celtic Sea using the background (BG) scheme described in Section 2.4.3.1. The model's default values were set to a water depth of $h = 80$ metres, $n = 40$ vertical levels, thus $\Delta z = 2$ metres, $N_z^{\min} = K_z^{\min} = 1 \times 10^{-5}$ m^2 s^{-1}, latitude = 50°N. Except for $A_{\mathrm{M}_2 u} = 0.4$ m s^{-1}, all other values of $A_{iu,\,iv}$ and $\phi_{iu,\,iv}$ were kept constant at 0. The time step, Δt was calculated by the model based on the vertical resolution, Δz, and the maximum value for N_z and K_z using:

$$\Delta t < \frac{\Delta z^2}{2N_z^{\max}} \tag{2.55}$$

For default settings of h, n and $N_z^{\max} = K_z^{\max} = 1 \times 10^{-1}$ m^2 s^{-1}, $\Delta t = 37.5$ seconds.

In order to evaluate Equations 2.41 - 2.46, the TC model required daily meteorological data of wind speed, w, [m s^{-1}], wind direction [°N], cloud cover, n_c, [%], air temperature, T_a [°C], air pressure, p_a [mbar] and relative humidity, r_h [%]. If these were not available, the TC model defaulted to using sinusoidal fits (Equations not shown) to UK Met Office data representative of the grid cell 50°N and 7 °W instead. The default meteorological data are shown in Figure 2.10.

Except for the wind direction (purple in Figure 2.10a) and air pressure (green in Figure 2.10c) all other meteorological variables display a typical seasonal cycle. The wind direction was rotated by 72° every day, due to observations of wind direction not displaying a seasonal cycle in the Celtic Sea (Simpson and Sharples, 2012). Air pressure was kept constant for practical reasons, as Sharples (2008) noted that the annual variability of p_a was weak in the Celtic Sea.

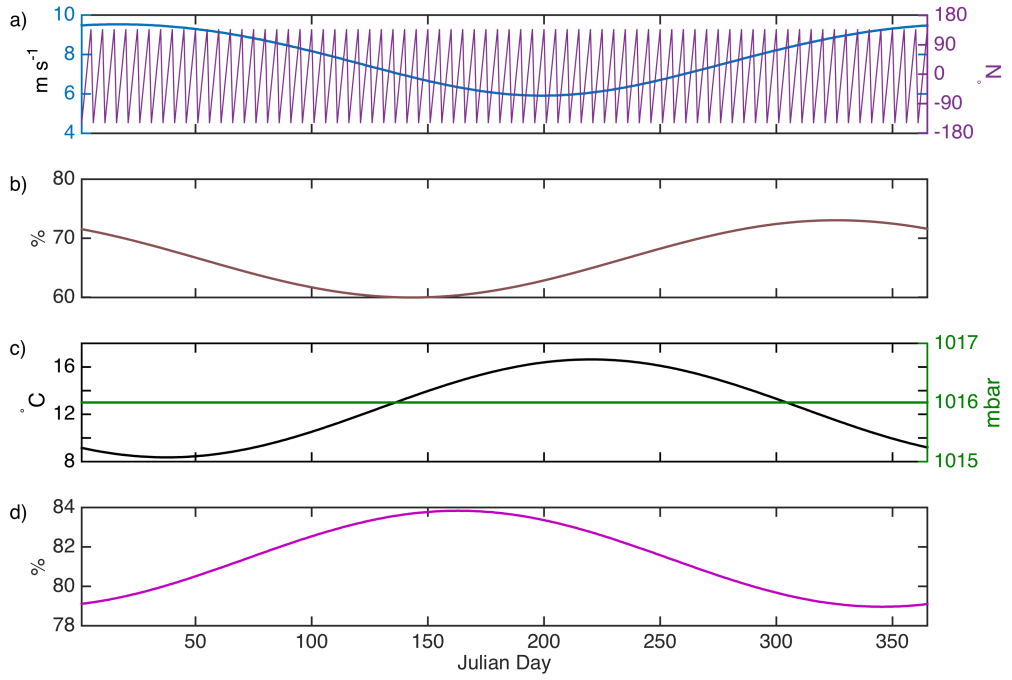

FIGURE 2.10: Smoothed daily meteorological input a) wind speed, w [m s^{-1}] and direction [°N] b) cloud cover, n_c [%] c) air temperature, T_a [°C] and air pressure, p_a [mbar] d) relative humidity, r_h [%].

The typical hourly TC data output includes vertical profiles of temperature [°C], σ_t [kg m^{-3}], E-W (u) and N-S (v) velocity component [m s^{-1}], $\log_{10} K_z$ [m^2 s^{-1}] and $\log_{10} \varepsilon$ [m^2 s^{-3}]. Here, the values of temperature, σ_t, u and v are instantaneous representative of the centre of the grid cell, whereas the values of the turbulent parameters are averages of the previous hour located at the boundaries of the grid cell (Figure 2.8).

Figure 2.11 shows some of the hourly output data produced by TC$_{\mathrm{BG}}$ when run with the above described default input settings and forcing terms. This hypothetical water column was stratified between March and early November (Figure 2.11a-b). By only setting one tidal constituent of the u velocity component, this site experienced rectilinear currents, which displayed a strong M$_2$ tidal cycle (Figure 2.11c). This strong M$_2$ tide results in ε values exhibiting a strong M$_4$ in the bottom boundary layer (Figure 2.11d), as the tide flows back and forth twice a day. This is in good agreement

with observations of many other shelf sites with similarly strong tidal currents, e.g. Simpson *et al.*, 2002; Palmer *et al.*, 2008

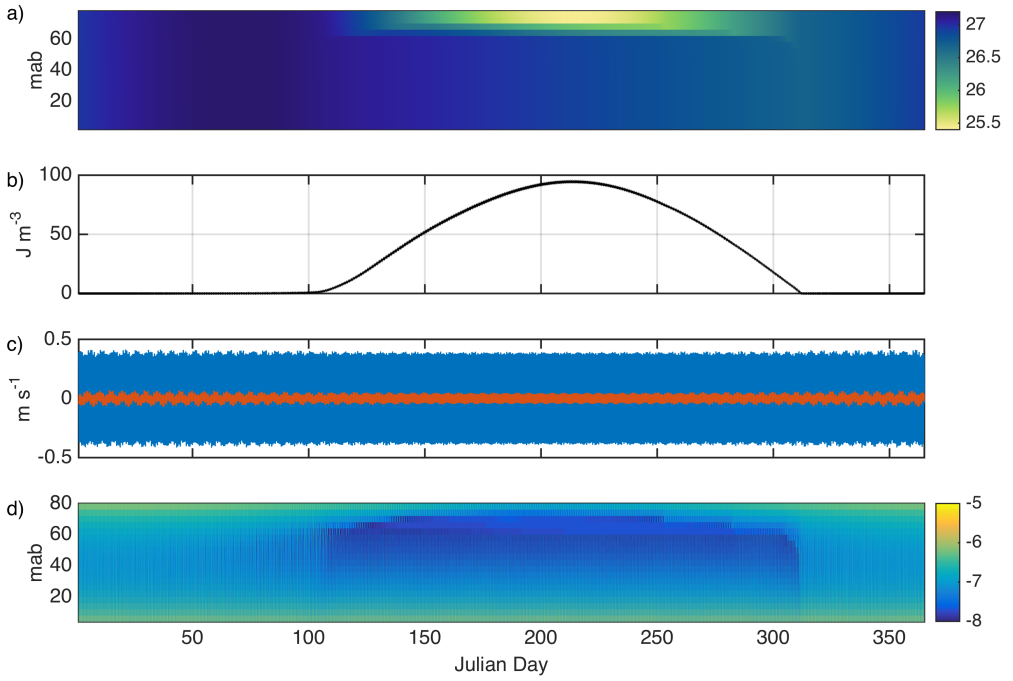

FIGURE 2.11: TC_{BG} run with default settings a) σ_t [kg m^{-3}] b) Φ [J m^{-3}] c) depth averaged u (blue) and v (red) velocity components [m s^{-1}] d) $\log_{10}\varepsilon$ [m^2 s^{-3}].

2.4.5 Prescribing vs. parameterising turbulent processes

To illustrate the effect the improved representation of dynamical and turbulent processes within the TC model has on reproducing the vertical water column structure, this section will review studies investigating an alternative constraint on stratification. While the prescriptive models, SH74 and SB84, provided strong evidence (Section 2.2.4, Section 2.3.2) that stratification is to first order controlled by the heating-stirring competition (Equation 2.16). Garrett *et al.* (1978) first proposed that the influence of Earth's rotation provides an alternative control on stratification. They argued that assuming a constant eddy diffusivity, N_z, which is a prerequisite for prescribing mixing

within SB74 and SB84, is only valid for areas where

$$h \leq h_{bl} \tag{2.56}$$

where h is the full water depth and h_{bl} the sum of the boundary layer thickness. Consequently in areas where the water depth exceeds h_{bl}, i.e. in stratified areas, rotation may need to be taken into account.

Earth's rotation limits the vertical extent of mixing to an Ekman layer near the boundaries. Here, the influence of friction is restricted to a thickness layer, d [metre], which can be approximated by

$$d \approx \left(\frac{2N_z}{f}\right)^{1/2} \tag{2.57}$$

At 49°N and a typical eddy viscosity, N_z, of O(10^{-2}) m^2 s^{-1} , $d \sim 14$ metres. If the stress, τ, is known, d can also be approximated using:

$$d \approx \frac{cu_*}{f}. \tag{2.58}$$

where $u_* = (\tau/\rho)^{1/2}$ is the friction velocity [m s^{-1}], and c a constant. Usually $c \sim 0.4$, although Stigebrandt (1988) has suggested a lower value of $c \sim 0.2$ with a corresponding decrease of the depth that is affected by friction.

For tidal flow confined to the horizontal dimensions, the particle trajectories can be described as ellipses. This elliptical motion can be decomposed into cyclonic (anticlockwise in northern hemisphere) and anticyclonic (clockwise in northern hemisphere) circular components (Prandle, 1982). Soulsby (1983) then derived the corresponding

boundary thicknesses as:

$$d_+ \approx \frac{cu_*}{\omega + f} \qquad \text{for cyclonic (anticlockwise) and}$$
$$d_- \approx \frac{cu_*}{\omega - f} \qquad \text{for anticyclonic (clockwise) motion} \tag{2.59}$$

Here, ω is the frequency of oscillation such as the semidiurnal tidal constituent, M_2. Due to the differing effect of tidal rotation compared to Earth's rotation, the boundary layers of these two circular components differ in height. In mid-latitudes f is close to ω_{M_2}, and here $d_+ \ll d_-$, which means that the anticyclonic component penetrates much further into the interior of the water column. This would imply that stratification is not merely dependent on the strength of the tidal velocities but also on the polarity, P_l of the currents. Polarity is defined as

$$P_l = \pm \frac{\text{minor axis}}{\text{major axis}} \tag{2.60}$$

with a positive/negative value indicating cyclonic/anticyclonic rotation.

Following this, Stigebrandt (1988) suggested that a frontal position is not controlled by an energy balance. Instead he suggested that fronts are located where the frictional boundary layer, d, is equal to the depth of the water column, h.

In response to this alternative explanation, attempts have been made at verifying either method by using observations of frontal positions (Loder and Greenberg, 1986; Bowers and Simpson, 1987). Yet studies found that both criteria result in predictions that are rather similar and hard to distinguish, when compared to the available observational data.

In order to test the problem numerically, Simpson and Sharples (1994) investigated the effect of rotation by simulating the seasonal cycle of stratification and frontal positions

using a 1D turbulence closure (TC2) model, and compared it to the above described prescriptive model, SB84 (Section 2.3), by Simpson and Bowers (1984). The TC2 model used by Simpson and Sharples (1994) is similar to the TC model described in Section 2.4, but used a Mellor-Yamada (level 2) turbulence closure scheme (Mellor and Yamada, 1974; Simpson and Sharples, 1994).

While both models predicted a similar seasonal cycle of surface and bottom temperatures, the timing of onset in spring and breakdown of stratification in autumn were delayed in the TC2 model (Figure 2.12a). These phase lags were associated with the inverse relationship of N_z to Φ implemented by the turbulence closure scheme (Simpson and Sharples, 1994). The variable mixing efficiency in the TC2 model was also evident in the seasonal cycle of the net heat flux (Figure 2.12b). High surface temperatures in late summer inhibited heat gain in the TC2 model, but not in the SB84 model.

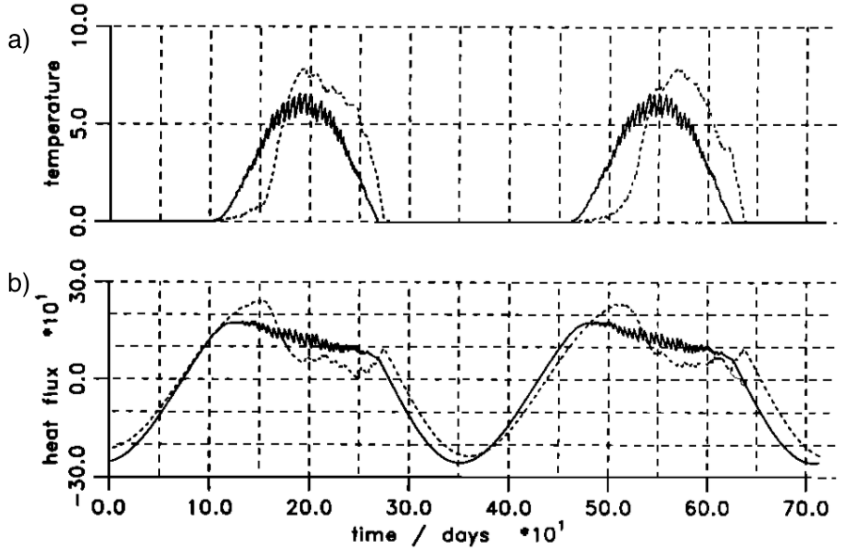

FIGURE 2.12: Comparison of TC2 (dotted line) and SB84 (solid line) model results over two seasonal cycles. a) Surface-bottom temperature difference [°C] b) net heat flux [W m^{-2}]. Taken from Simpson and Sharples (1994).

Figure 2.13 shows the effect polarity (Equation 2.60) has on frontal positions in midsummer for a water depth of $h = 100$ metres. Here, the frontal positions were denoted by $\log(\chi)$ (Equation 2.13). For an anticyclonic site ($P_l < 0$) both models were in

agreement (Figure 2.13a, d) with observed values of frontal positions (Simpson and James, 1986). Since anticyclonic boundary layers penetrate further into the water column, an omission of rotational effects in SB84 was therefore unlikely to deteriorate the prediction. For rectilinear tidal ellipses ($P_l = 0$, equal cyclonic and anticyclonic components), the TC2 model predicted frontal positions at lower values of $\log(\chi)$ (Figure 2.13c) compared to the SB84 model (Figure 2.13d), due to a reduced boundary layer thickness, d. This effect was further accentuated for the cyclonic site ($P_l > 0$). Here, the TC2 model was predicting a significant frontal displacement of $\Delta \log(\chi) \sim 1.5$ due to the shallower bottom boundary layer (Figure 2.13b), which was not captured by the descriptive model SB84 (Figure 2.13d).

In summary, Simpson and Sharples (1994) concluded that the influence of rotation was small for anticyclonic sites but increased as the polarity of the currents became positive. They also noted that the effect of rotation on the boundary layers increased with increasing water depth, h.

In relation to the northwest European shelf, Simpson and Sharples (1994) argued that the shelf-wide influence of rotation on stratification is limited however, as the majority (95 %) of this shelf has a polarity of $P_l < 0.3$ (Flather, 1976). Here, the changes in stratification should be sufficiently captured by the prescriptive SB84 model. Yet in areas where $P_l \geq 0.3$, rotation considerably thins the bottom boundary layer thickness, d, and therefore also shifts the location of fronts to shallower depths. Here, using prescriptive mixing models could significantly overestimate the bottom boundary layer and thus underestimate the strength of stratification.

Simpson and Tinker (2009) tested these earlier conclusions using observations collected in the Celtic Sea, choosing a cyclonic and an anticyclonic site. As expected, they found a significant difference in the thickness of the bottom boundary layer, d, and vertical extent of turbulent kinetic energy dissipation, ε [W kg^{-1}], between the two sites (Figure 2.14). The observed difference in water column structure between both sites

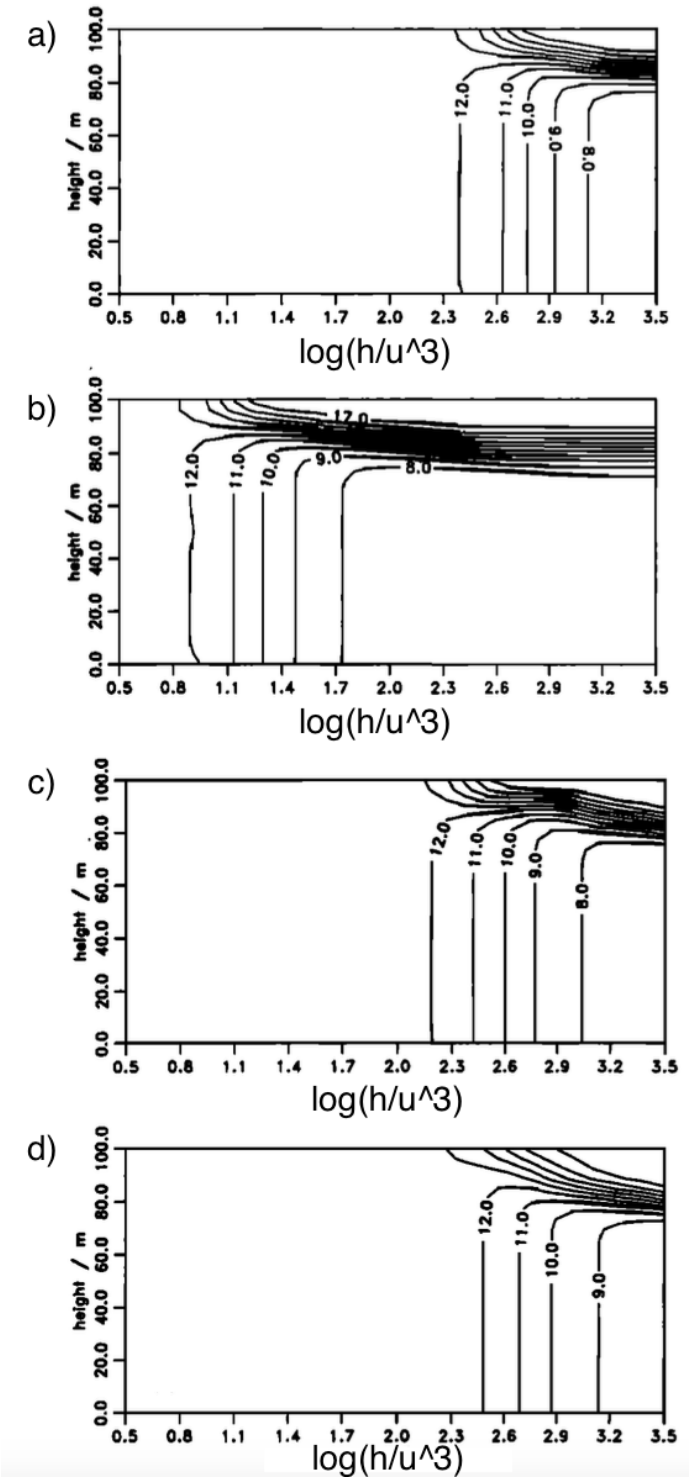

FIGURE 2.13: Contours of temperature as a function of depth and $\log(h/u^3)$. TC2 model results for tidal currents with a) $P_l < 0$ b) $P_l > 0$ c) $P_l = 0$. d) SB84 model results. Taken from Simpson and Sharples (1994).

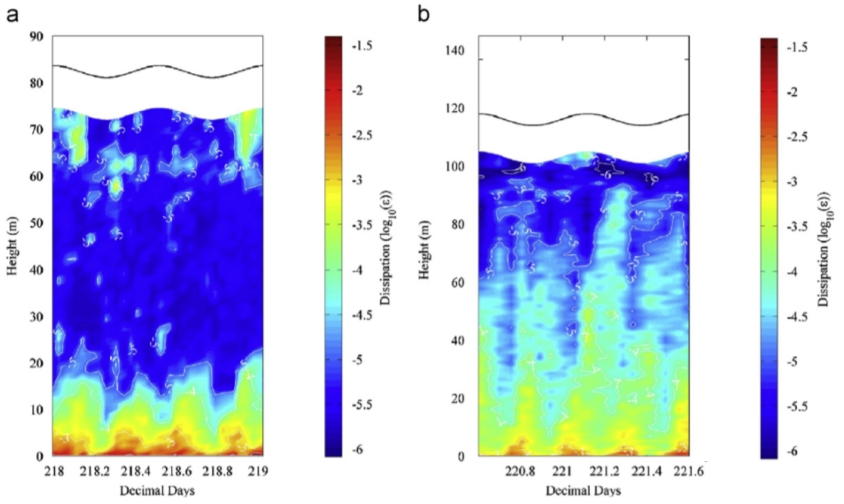

FIGURE 2.14: Effect of tidal ellipse rotation on d. Observations of TKE dissipation rate, $\log_{10}\varepsilon$ [W m^{-3}]. a) Cyclonic site b) anticyclonic site. Adapted from Simpson and Tinker (2009).

was attributed to a combination of rotation and positive feedback through the effects of stratification itself. Positive rotation reduces the upward penetration of mixing, which allows strengthening of stratification, which itself inhibits further mixing, due to reduced eddy viscosity restricting vertical transfer of momentum.

2.4.6 Summary: TC model

The TC model introduced in Section 2.4 significantly differs from the prescriptive models, SH74 and SB84 described in Section 2.2 and Section 2.3, respectively, due to its application of a turbulence closure scheme (Section 2.4.1) and the representation of internal mixing processes (Section 2.4.3). Out of the three numerical approaches, the TC model thus constituted the most complex one. Section 2.4.5 highlighted the implications an improved representation of turbulent processes within the TC model has on studying the dominant controls on stratification. Here, particularly for sites with cyclonic rotating tidal ellipses, it is important for turbulent processes to be scaled by the existing stratification in order to replicate the vertical water column structure realistically (Simpson and Tinker, 2009).

2.5 Summary: Modelling stratification and mixing in shelf seas

In summary, this chapter has provided the theoretical background of stratified fluids and introduced three models of increasing complexity. The first two models were based on basic PE considerations of the water column: To first-order stratification is considered a vertical exchange processes driven by the competition of PE sink and source terms at the boundaries (sea bed and sea surface). Namely, buoyancy input from solar heating competes against wind and tidal mixing. Both SH74 and SB84 are solely driven by forces at the boundaries (sea bed and sea surface), and hence they do not describe the generally weaker mixing found around the pycnocline. In contrast to to this, the TC model is able to represent interior mixing by employing internal wave mixing parameterisations to act on the pycnocline.

In Chapters 5 and 6, the performance of these three models will be tested by comparing their results to the observations. The failures of each model will then be used to better understand any missing or poorly parameterised physics within them.

The following Chapter 3 will however first introduce the instruments and methodologies used in this thesis to process the observations, which will be presented and examined in Chapter 4.

Chapter 3

Data collection, processing and quality control procedures

Introduction

To meet the aims of this thesis, the objectives of the observational component were:

1. Observe the transition of the vertical density and velocity structure throughout a typical seasonal cycle in a temperate continental shelf sea.
2. Observe and quantify the critical processes shaping the observed changes in physical structure
3. Observe and quantify the biogeochemical response driven by the change in vertical density structure throughout the year.

This chapter presents a detailed description of the instruments and methods used to collect, process and quality control the observational and reanalysis data interpreted in this thesis.

This chapter starts with a brief overview of the research site in Section 3.1. This is followed by an introduction of all observational platforms, outlining the instruments and data channels used, along with their profiling setups. For each platform, a comprehensive account of the processing and quality control methods applied to those data channels is given.

Since the focus of this research deals with the seasonality, the long-term temperature-salinity (TS) logger mooring, introduced in Section 3.3, and acoustic current profiler (ACP) time series, introduced in Section 3.4, provide the core datasets of this thesis. Two additional surface buoys provided invaluable long-term, near-surface observations of oceanographic, meteorological and biogeochemical variables. These were the SmartBuoy, maintained by Centre for Environment, Fisheries and Aquaculture Science (Cefas) (Section 3.3.2 and Section 3.6) and, an Ocean Data Acquisition System (ODAS) buoy maintained by the UK Met Office (Section 3.3.2 and Section 3.5). The observed meteorological field was further complemented by the addition of meteorological data from the extended-range European Reanalysis Interim product of gridded meteorological fields (Dee et al., 2011) from the European Centre for Medium-Range Weather Forecasts.

While the conductivity-temperature-depth (CTD) data (Section 3.2) provided primary calibration data for the TS mooring, its vertical profiles of chlorophyll-a fluorescence and nitrate+nitrite values, derived from its bottle samples (Section 3.7), were crucial in better understanding the depth variation of the biogeochemical environment throughout the observational campaign.

Where data channels were supplied processed or quality controlled by other contributors than the author, this is acknowledged at the end of each section.

3.1 Rationale and overview of the central Celtic Sea site

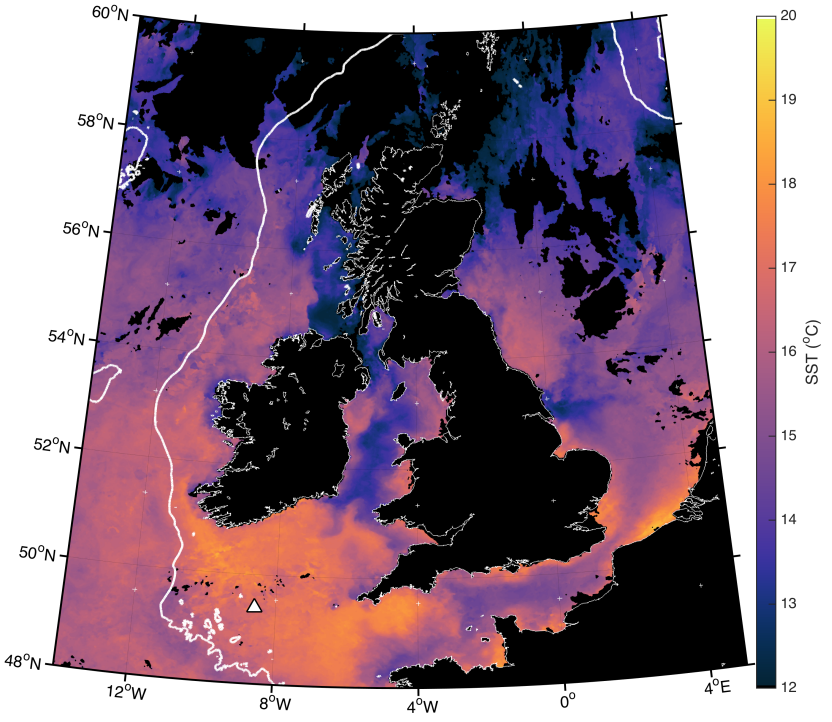

FIGURE 3.1: Summer 2014 sea surface temperature (SST) [°C] around the British Isles. Overlaid are the central Celtic Sea (CCS) mooring array location (white triangle, 49.4°N, 8.6°W) and the 200 metres bathymetry contour (thick, white line). This satellite image is a 1 week median SST composite, 25th June - 1st July 2014, courtesy of NEODAAS (Plymouth Marine Laboratory, UK).

All observations presented in this thesis were collected as part of the **UK Shelf Sea Biogeochemistry (SSB)** programme. SSB was a large strategic programme jointly funded by the UK Natural Environment Research Council (NERC) and Department of Environment, Food & Rural Affairs (Defra) researching the carbon and nutrient dynamics and fluxes within and across temperate continental shelf seas.

The sampling location was at the centre of the Celtic Sea, which is part of the North-west European Shelf (Figure 3.1). Depths in the Celtic Sea typically range from 50 to 200 metres and descend quickly beyond the 200 metre contour of the continental shelf

edge (black contour in Figure 3.1) to over 4000 metres. The central Celtic Sea mooring site (CCS) was located on the continental shelf, ∼120 km northeast of the continental shelf break and ∼ 200 km south-west from the British Isles. Its nominal location was 49.4°N and 8.6°W, in a mean water depth of 145.4 metres, this is marked by the white triangle in Figure 3.1. The relatively warm sea surface temperatures (SSTs) surrounding the CCS site (orange in Figure 3.1), represent seasonally stratified regions (away from coastal boundaries). Colder SSTs (e.g. in the Irish Sea) represent the year-round vertically mixed regions. The site was located well away from any tidal mixing fronts, which can be inferred by the sharp gradients from warm to cold SSTs e.g. between the Irish and the Celtic Sea. Its central location within this seasonally-stratifying region, and its distance to tidal mixing fronts, as well as a lack of large topographic features such as banks or the shelf edge, made CCS an ideal location to represent the background state of a temperate, seasonally stratifying continental shelf sea. Due to this quiescent nature, CCS is characterised of minimal fishing activity (Sharples *et al.*, 2013), which significantly improved the chances of a successful observational campaign, without substantial losses due to collision or trawling.

At CCS, a long-term mooring array collected continuous measurements spanning 17 months (March 2014 − July 2015). A full-depth temperature-salinity logger mooring collected hydrographic data. A bottom mounted, upward facing, narrowband 150 kHz acoustic current profiler (ACP) recorded horizontal velocities. A SmartBuoy, maintained by Cefas, collected surface nitrate+nitrite (hereafter nitrate), photosynthetically active radiation (PAR), surface chlorophyll-*a* fluorescence (hereafter chl *a*) and near-surface temperature data. An ODAS buoy, maintained by the UK Met Office, supplied meteorological forcing and near-surface sea temperature observations.

The SSB field campaign was supported by nine process cruises; their names and dates can be found in Table 3.1. In addition to the mooring array, full-depth profiles of CTD including chl *a* and nitrate data collected during these nine process cruises were also used.

Cruise	Dates
DY008	18.03. – 13.04.2014
JC105	15.06. – 24.06.2014
DY026a	03.08. – 15.08.2014
DY026b	15.08. – 25.08.2014
DY018	09.11. – 03.12.2014
DY021	01.03. – 26.03.2015
DY029	01.04. – 30.04.2015
DY030	04.05. – 25.05.2015
DY033	11.07. – 03.08.2015

TABLE 3.1: SSB process cruises. Here, DY stands for RRS Discovery and JC for RRS James Cook.

The following sections will explain the setup, processing and quality control procedures applied to the data streams used on each of those platforms.

3.2 CTD data

During each cruise a Sea-Bird Electronic (SBE) 911*plus* CTD and a Chelsea Technology Group (CTG) Aquatracka fluorometer mounted on a 24-bottle rosette system collected vertical profiles of temperature, salinity, and chl *a* fluorescence at CCS. The following methods were employed to quality control the raw data: The raw 24 Hz profiles were extracted, filtered and corrected for thermal inertia using SBE Data processing Software (Seasave V 7.23.2). The data were subsequently screened and anomalous data removed, averaged onto a 1 db grid and calibrated against samples of chl *a* concentration and salinity.

These data were supplied quality controlled by Jo Hopkins (National Oceanography Centre).

3.3 Long-term temperature-salinity mooring

The long-term hydrographic time series data were collected by the full-depth temperature - salinity (TS) logger mooring. Five continuous deployments recorded data for 17 consecutive months, which span from March 26th 2014 to July 25th 2015. The TS mooring was designed to capture the vertical structure of the whole water column and had a vertical resolution of 2.5 metres in the pycnocline and 5 - 20 metres resolution in the surface and bottom layer. The instruments temporal sampling resolution was 5 minutes.

The exact set-up of instruments changed during every deployment: see TS mooring Table A.2 - Table A.6 for details in Appendix A. Table 3.2 summarises the general mooring setup, and Figure 3.2 shows the technical mooring diagram for the first deployment period.

Instrument type	Typical deployment depths
SBE 16*plus* SeaCAT CTD	10, 45, 129, 145 metres
SBE 37 MicroCAT CTD	30, 49, 69, 99 metres
16 temperature loggers (mixture of Star Oddi DST Centi Temperature, Star Oddi Starmon mini underwater temperature & RBRsolo T | Temperature Logger)	15, 20, 25, 35, 37,40, 42, 47, 54, 59, 64, 74, 79, 89, 109, 120 metres

Table 3.2: General instrument setup of long-term TS mooring

While the lowest SBE16*plus* instrument (at 145 metres) was not physically attached to the TS mooring (Figure 3.2) its data were included as part of the full-depth hydrographic time series. The instrument was attached to an alongside bed frame housing the acoustic current profiler (Section 3.4), which was deployed at the same nominal location as the TS mooring. The separation distance of both platforms was always $<$ 1 km.

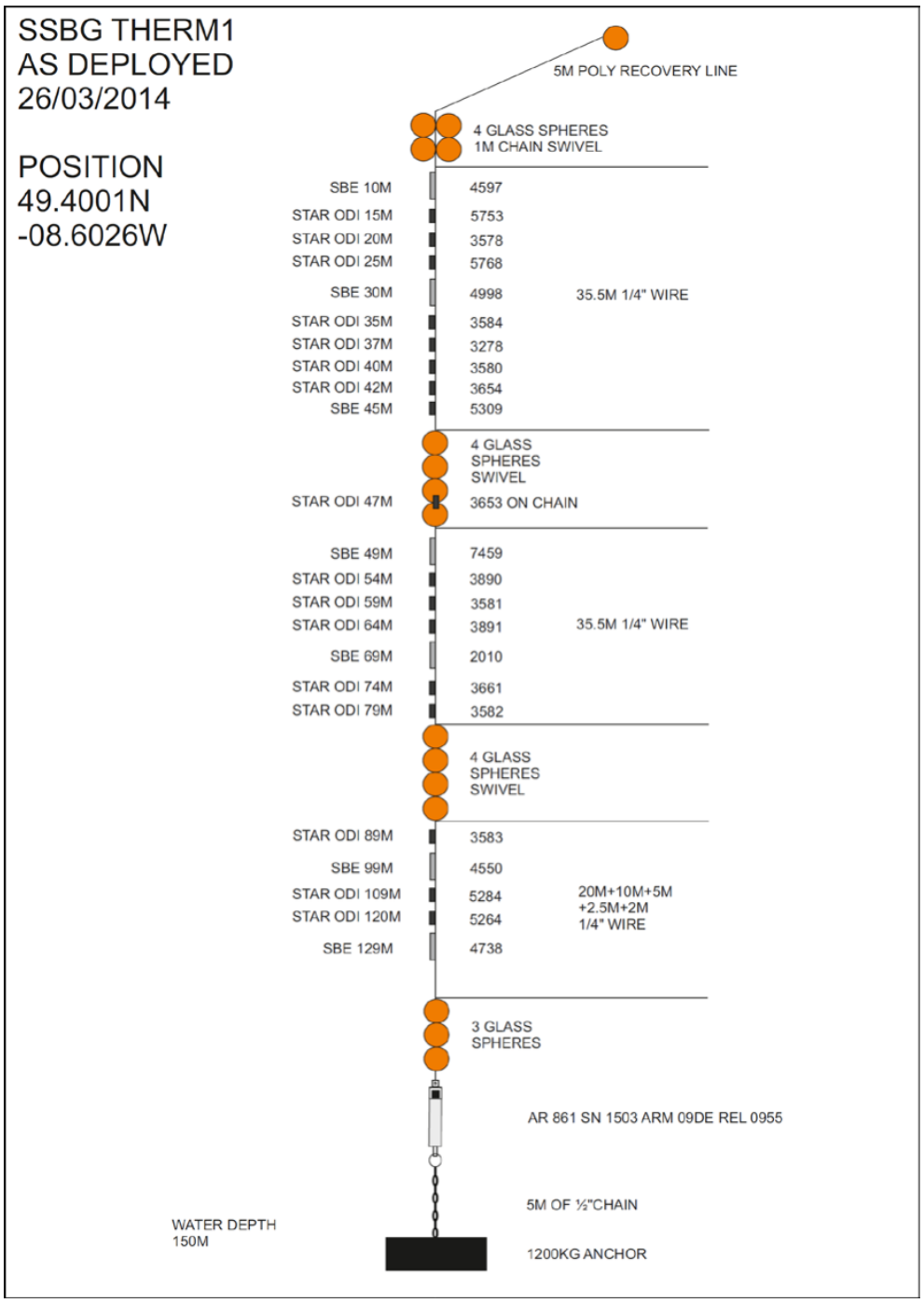

FIGURE 3.2: Diagram of first CCS TS logger mooring deployed on March 26th 2014.

3.3.1 TS mooring quality control

3.3.1.1 Linear offset and de-spiking

In order to quality control the TS mooring instruments, all temperature and salinity observations were calibrated using post-deployment and pre-recovery CTD profiles to find linear offsets, which could then be applied to the entire instrument deployment time series.

Once casts were identified, mooring instrument time stamps were matched to coincide with the CTD downcast profile times. Similarly, pressure records of the mooring were used to match the CTD data to the instruments on the mooring. Only the SBE instruments, however, recorded pressure themselves. The pressure of the remaining instruments was estimated based on a) the pressure record from the nearest or most appropriate SBE instrument and b) the separation distances to those reference instruments converted into pressure using the Gibbs-SeaWater (GSW) Oceanographic Toolbox gsw_p_from_z.m routine (McDougall and Barker, 2011). These distances were taken from mooring diagrams (e.g. Figure 3.2) or engineers' log sheets. If pressure data of the SBE instruments were missing or suspect, they have been blanked with non values (NaNs) and subsequently reconstructed using harmonic analysis of the M_2, S_2, N_2, O_1 and K_1 tidal constituents, which were obtained from the remaining pressure record.

The final correction was taken as the average offset for each instrument relative to the post-deployment and pre-recovery CTD profiles. Figure 3.3 demonstrates this process using data from the first mooring deployment: Here, the mean offset is the difference between the raw temperature data, shown as red crosses, and the CTD profiles, shown as a continuous blue line. The black stars already have the offset applied, and therefore match both the post-deployment and pre-recovery cast well.

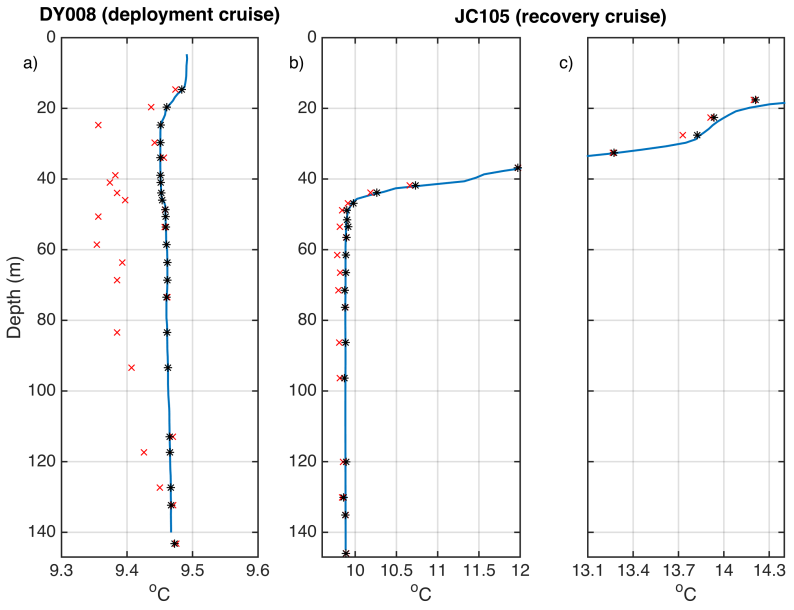

FIGURE 3.3: Temperature calibration using CTD casts. a) post-deployment b-c) pre-recovery (note different axes). CTD casts in blue, raw temperature observations (red crosses), temperature observations with corrections applied (black stars).

To avoid over-correcting the TS observations, the calculated offsets were only applied if the average offset > temperature/conductivity accuracy, (a_T [°C], a_C [S m^{-1}]) of each instrument. Otherwise the deviation to the CTD data were considered to be caused by instrument inaccuracies, rather than a consistent offset throughout the instrument's deployment time. The accuracies of the different temperature/conductivity sensors differed between a_T = ± 0.1 - 0.002°C and a_C = ± 0.0003-0.0005 S m^{-1} depending on instrument type and make (Star Oddi, 2015a,b; RBR, 2015; Sea-Bird Electronics, 2015a,b).

If necessary, the temperature and salinity data have also been de-spiked using appropriate windows, depending on the length of the deployments (Figure 3.4).

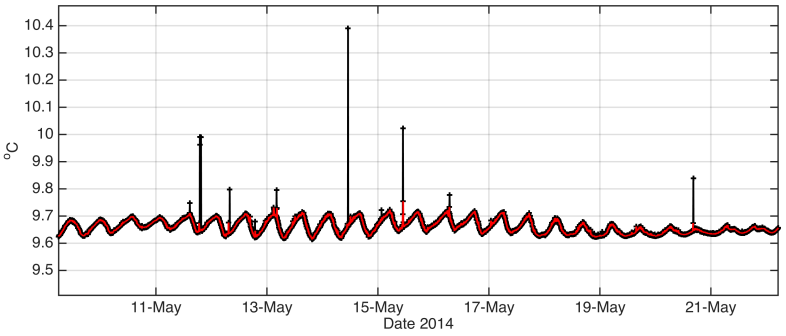

FIGURE 3.4: De-Spiking. Raw (black) compared to de-spiked (red) temperature data.

3.3.1.2 Full-depth salinity and density fields

Similarly to pressure observations, conductivity/salinity observations were only taken by 8 SBE instruments situated throughout the water column (Table 3.2, Figure 3.2). In order to construct full-depth profiles of salinity, a salinity surface of the form *salinity = function(time, salinity, temperature)* was fitted to all simultaneous observations of salinity, temperature and time. This was constructed using a nearest neighbour, three-dimensional interpolation function, similar to the methods employed by Hopkins *et al.*, 2014. Delaunay triangulation was then used to evaluate salinity for all available temperature measurements. Here, a new salinity surface was calculated for each TS mooring deployement. Potential density [kg m^{-3}] was derived using the GSW Oceanographic Toolbox (McDougall and Barker, 2011).

During periods of little or no stratification (March 2014, November 2014 - April 2015) the temperature resolution, r_T [°C], of the Star Oddi DST Centi Temperature logger (r_T = 0.032 °C, Star Oddi, 2015a) appeared insufficient to resolve small scale temperature changes with depth. While the blue and yellow lines in Figure 3.5 denote SBE instruments that have temperature resolutions of $r_T = 0.0001$°C (Sea-Bird Electronics, 2015a,b), the step changes notable in the red line mark the $r_T = 0.032$°C temperature resolution of the Star Oddi DST centi logger.

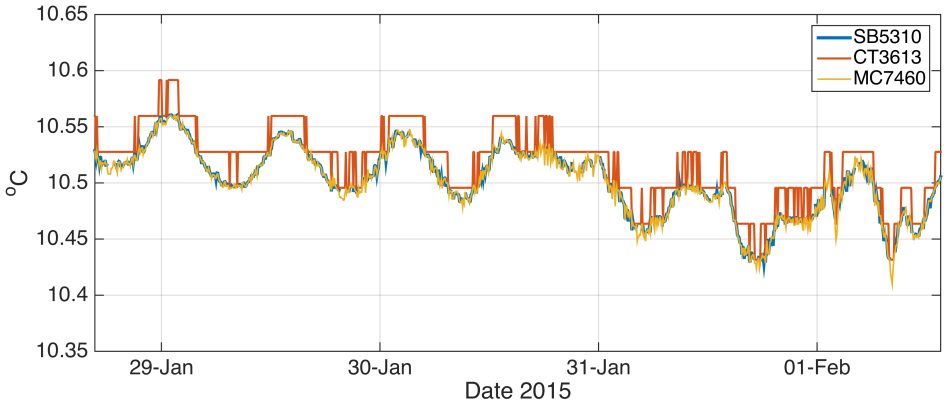

FIGURE 3.5: Temperature resolution in vertically mixed conditions. Colours denotes temperature observations of 3 instruments located at 45-49 metres below the sea surface.

Without accounting for these comparatively low resolutions, an interpolation onto a regular depth grid resulted in temperature, and ultimately density inversions that persisted for O(hours) and were deemed unrealistic. It was therefore checked whether the absolute temperature difference between two adjacent SBE instruments was less than the temperature resolution of all instruments physically situated between these two reference points. If this was the case, the relevant data were excluded from the salinity surface triangulation, and the final interpolation onto the regularly spaced temporal and spatial grid.

3.3.1.3 Further processing and quality control

The depths of the TS mooring instruments were derived using the GSW Oceanographic Toolbox gsw_z_from_p.m routine (McDougall and Barker, 2011).

While time drift data were available for some instruments (taken from engineers' log sheets), these were not applied as they were O(sec) and therefore considered negligible compared to the sampling resolution of 5 minutes and deployment periods of O(months).

For the majority of the analysis the TS data were interpolated onto a regular 5 min x 2.5 metres resolution grid.

These quality controlled data have been published and are available through the British Oceanographic Data Centre (Wihsgott *et al.*, 2016).

3.3.2 Near-surface temperature observations

To complement near-surface observations of the TS mooring, temperature data collected by instruments tethered to the Cefas SmartBuoy and the Met Office ODAS buoy were also incorporated into the main TS mooring time series.

The SmartBuoy collected near-surface temperature observations at 2.5 and 5.0 metres below the sea surface tethered from a surface buoy. These data were available between 19th June 2014 and 26th August 2015 and had a temporal sampling resolution of 5 minutes. Instruments used on this platform were Star Oddi DST Centi Temperature recorders at 5.0 metres and Star Oddi Starmon mini underwater temperature recorders at 2.5 metres below the sea surface. From October 2014 onwards all except one Star Oddi DST Centi Temperature recorder were replaced with RBRsolo T | Temperature Loggers. The instruments were supplied by the National Oceanography Centre and processed data were supplied by Dave Sivyer (Cefas).

Between 21st August 2014 and 26th August 2015, 5 SBE 56 Temperature Loggers were suspended from the SmartBuoy at 0.3, 0.6, 1.6, 3.5 and 7.0 metres below the sea surface (in addition to the instruments at 2.5 and 5 metres). These instruments had a temporal sampling resolution of 15 seconds, and the data were supplied processed by Tom Bell (Plymouth Marine Laboratory, PML).

The Met Office ODAS buoy also collected near-surface temperature observations at 1 metre below the sea surface with a temporal resolution of 1 hour. Due to their comparatively low temporal resolution, but also coarse temperature resolution of $r_T = 0.1°C$ (J. Turton, personal communication, 02.09.2014) these observations were only incorporated into the TS mooring data between March and June 2014, when no other near-surface data were available. These data were supplied quality controlled by Jon Turton (Met Office) as part of the Met Office ODAS buoy data further described in Section 3.5.

3.3.2.1 Quality control of near-surface temperature observations

Initially, the pressure data for all additional (SmartBuoy and ODAS buoy) near-surface thermistors (Section 3.3.2) were estimated using methods outlined in Section 3.3.1.1. Here, existing pressure records and log sheet data were used to generate corresponding pressure time series for each instrument.

In order to quality control the near-surface temperature sensors, it was initially attempted to calibrate these data using the same post-deployment and pre-recovery CTD used for the TS mooring (see Section 3.3.1.1). Yet, for most of the CTD casts, the top 5 metres (or more depending on sea state) of near-surface data were removed owing to the CTD surface soaking prior to the downcast profile (J. Hopkins, personal communication, 22.03.2015). As a result the CTD could have missed considerable fine-scale structure evident in the near-surface (Figure 3.6), and any calibration to the nearest available data point could have meant the loss of high-resolution data or the introduction of errors.

Instead, the near-surface data were cross-calibrated with the near-surface TS mooring observations. If, by combining the near-surface thermistor with the TS mooring data, temperature/density inversions persisted for O(hours), these data were deemed unrealistic and excluded from the final data product.

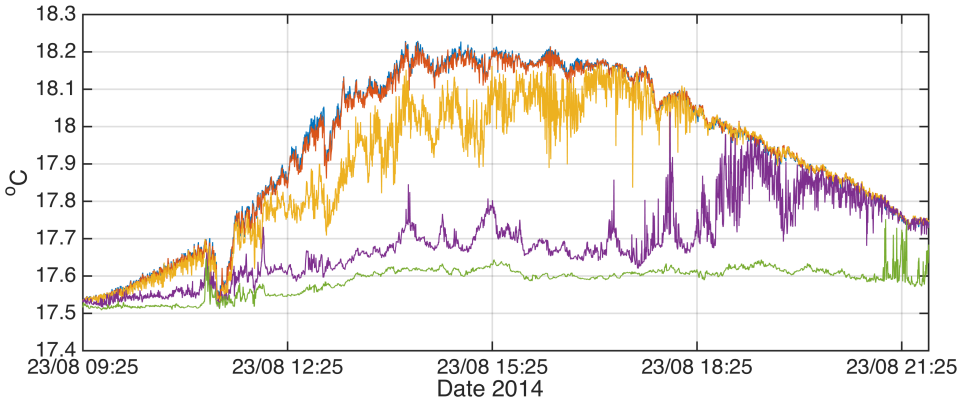

FIGURE 3.6: Selection of near-surface temperature loggers during August 2014. Loggers were located at 0.3 (blue), 0.6 (red), 1.6 (yellow), 3.5 (purple) and 7 (green) metres below the sea surface.

Since none of the near-surface thermistors took conductivity/salinity observations, salinity data were derived using the same methods used for the TS mooring data (Section 3.3.1.2). However, the lack of any near-surface salinity data required using the already fitted salinity functions, which were obtained using coincident measurements of time, salinity and temperature for each TS mooring deployment. These functions were then evaluated using the near-surface temperature data to derive a near-surface salinity field.

The quality controlled near-surface data were then interpolated onto the same 5 minutes x 2.5 metres resolution grid as the TS mooring. The combined and quality controlled full depth observations of vertical water column structure can be seen in Figure 3.7. For reference, the cruise times, during which CTD casts exist, have been overlaid to Figure 3.7.

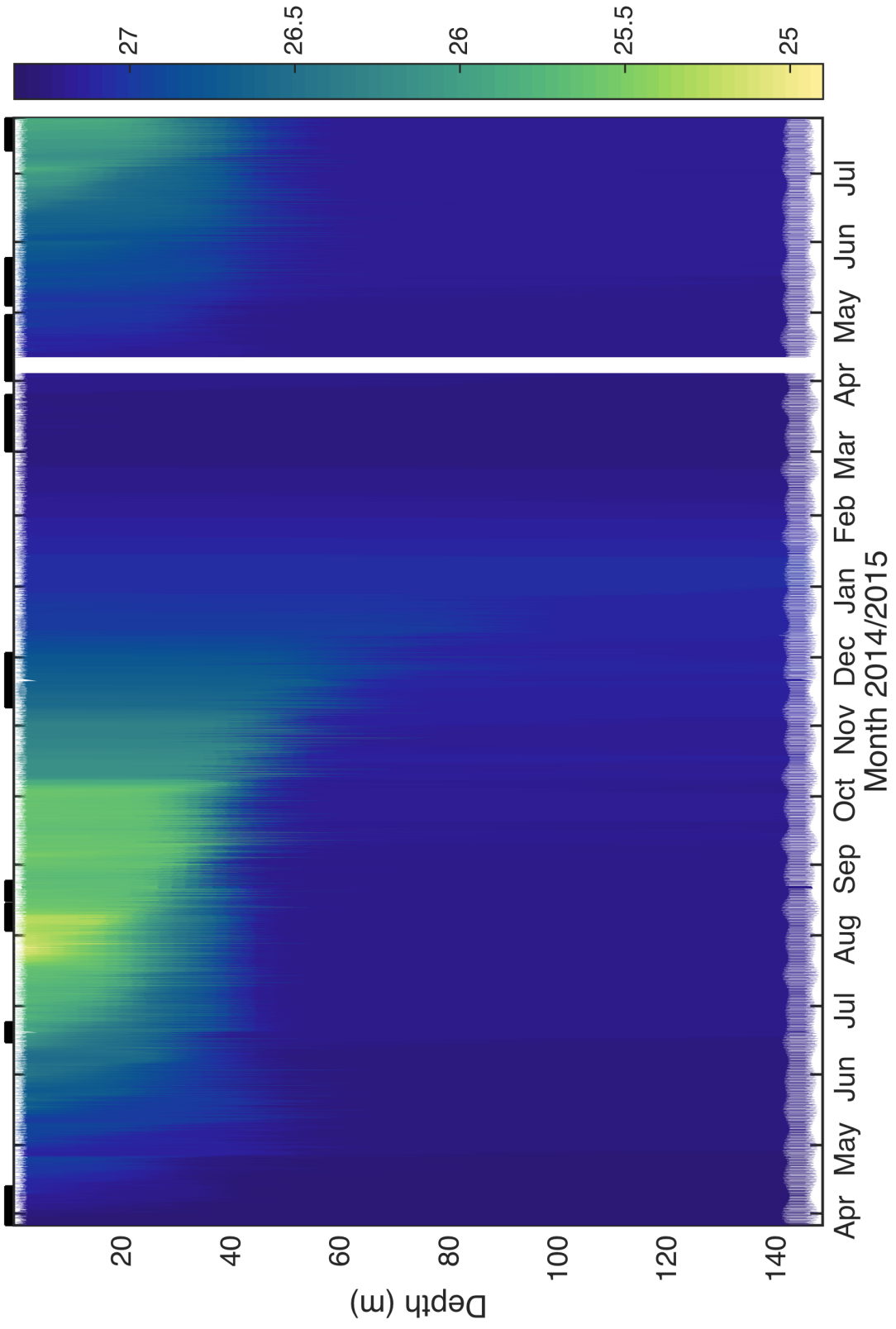

FIGURE 3.7: Full depth potential density [kg m^{-3}] over the entire 17 month observational period. Black bars above denote the cruise dates (Table 3.1).

3.4 Acoustic current profiler

A bottom mounted, upward facing, narrowband 150 kHz FlowQuest acoustic current profiler (ACP) recorded horizontal velocities between March 26th 2014 and July 31st 2015 throughout the whole water column using the setup found in Table 3.3.

Make	FlowQuest
Frequency	150 kHz (narrowband)
Beam angle	22°
Beam configuration	4 beam convex
Blanking distance	2.8 metres
Velocity accuracy	± 5 mm s^{-1}
Compass accuracy	± 2.0°
Bin size (vertical resolution)	2 metres
Temporal resolution	2 min 30 sec
Pings per ensemble	75

TABLE 3.3: ACP specification (LinkQuest Inc., 2013), and setup during deployments

3.4.1 ACP processing and quality control

The along beam velocities were averaged over each bin and then converted into horizontal (E-W, N-S) [m s^{-1}] using the FlowQuest software. In order to remove all data recorded above the sea surface, the sea surface elevation (or depth) was calculated using the pressure of an alongside SBE 16*plus* in addition to its height above the sea bed (taken from engineers' notes). All bins above the sea surface were blanked with non values (NaNs). After the sea surface was calculated, significant side lobe contamination was found in the first seven near-surface bins.

Side lobes are on an angle to the main acoustic lobes of each transducer (Figure 3.8) and are typically suppressed relative to the main lobe. Echoes from a relatively hard surface however, such as the sea surface, can overwhelm this suppression, which results in contaminated data near this 'hard' surface (RD Instruments, 2011).

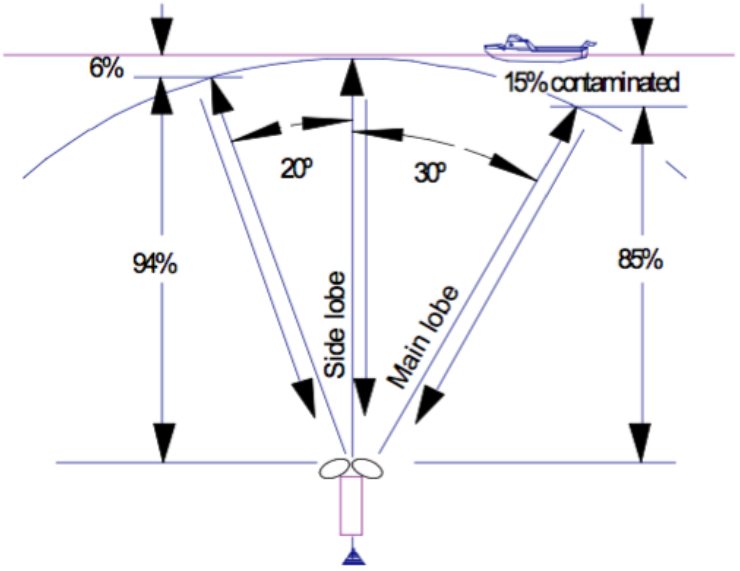

FIGURE 3.8: Relationship between transducer beam angle and the thickness of contaminated surface layer. RD Instruments (2011)

By examining the horizontal velocities within individual bins (Figure 3.9a) evidence of side lobe contamination within the first 6 near-surface bins (blue to light blue) manifested itself as deviations of up to 1.5 m s^{-1} from the lower bins (thick purple, turquoise and orange), which are in agreement. The 7^{th} near-surface bin (pink line in Figure 3.9a) only showed occasional small deviations of 0.2 m s^{-1} compared to the lower bins during the ebb tide. To verify whether the 7^{th} bin was unaffected by side lobe contamination, vertical shear of the horizontal velocities squared, S^2 [s^{-2}] (Equation 2.32) was calculated (Figure 3.9b). Since S^2 is representative of the TKE shear production term, $\boldsymbol{P}$ (Equation 2.31), elevated levels of S^2 are indicative of shear driven turbulence.

While it is expected to observe elevated levels of S^2 due to turbulent processes such as wind, or wave driven mixing near the sea surface (e.g. MacKinnon and Gregg, 2003a), it is rarely confined to particular bins for the entire mooring deployment period. The fact that elevated levels of S^2 ($S^2 > 1 \times 10^{-2}$ s^{-2} compared to S^2 values below 7^{th} bin of $\leq 3 \times 10^{-3}$ s^{-2}) persisted throughout the top seven bins below the sea surface (Figure 3.9b) suggested that all seven near-surface bins had been affected by side

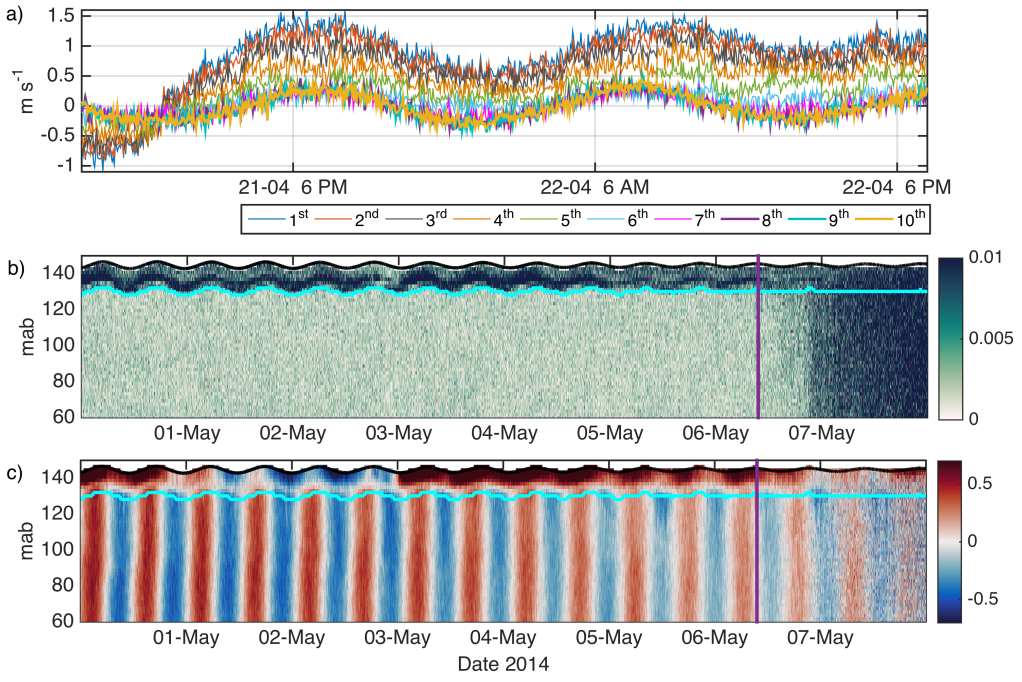

FIGURE 3.9: a) N-S horizontal velocities [m s^{-1}] of the ten topmost near-surface bins b) vertical shear of horizontal velocities squared, S^2 [s^{-2}]. c) Raw N-S horizontal velocity observations [m s^{-1}]. Overlaid to b and c are the sea surface elevation (black), the top of bins unaffected by side lobe contamination (cyan), and the cut-off point due to a battery failure in May 2014 (vertical purple line). Note b-c only show the top 80 metres of the water column.

lobe contamination. These were subsequently blanked with non values (NaNs). This resulted in a near full-depth coverage between 6.5 and 130 metres above the seabed.

The presence of noise within the horizontal velocities and strong S^2 signal that commenced around 10 am on May 6$^{\text{th}}$ 2014 seen in Figure 3.9b-c is indicative of reduced data quality, and has been linked to a battery failure of the first deployed ACP (SN11043). As a result, data recorded after May 6$^{\text{th}}$ 2014 at 09:35 were not recoverable and had to be blanked with non values (NaNs). The vertical purple lines in Figure 3.9b-c represent the chosen cut-off point based on increased levels of background S^2, which is used here to mark the beginning of reduced data quality due to battery failure.

After removal of near-surface data, horizontal velocity observations were corrected for compass and declination errors. Compass errors are caused by local magnetic fields of the surrounding batteries and metal frames affecting the inbuilt compass of the ACP. These errors manifest themselves as deviations to the true direction of the tidal currents (Figure 3.10). The direction of the semi-major or semi minor axis for a tidal constituent is usually measured positive cyclonically (anticlockwise) from east. This means the direction indicates the orientation of the maximum current induced.

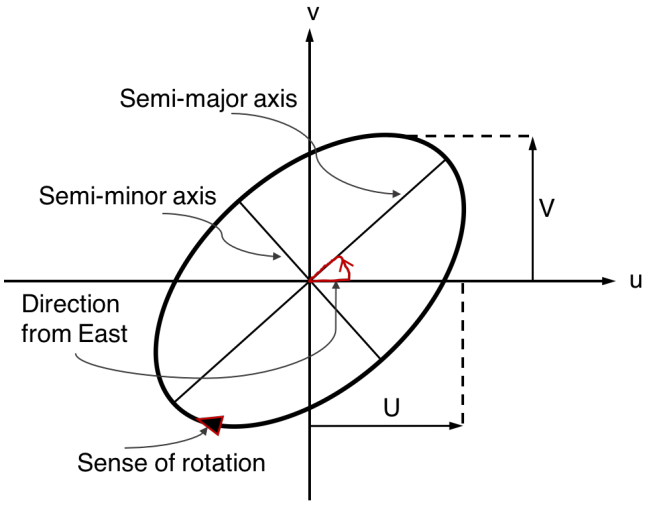

FIGURE 3.10: Basic parameters of a current ellipse. Example shows an anticyclonically rotating current ellipse with an ellipse orientation of 45° cyclonic from east. Adapted from Pugh (1996).

The true orientation of the M_2 tidal ellipse at CCS was found using independent horizontal velocity observations recorded by the ships' acoustic Doppler current profilers (ADCPs) at CCS during DY018 and DY033. Here, one 75 kHz and one 150 kHz RDI ADCP independently recorded horizontal velocities during each cruise. Since the ship's GPS corrected compass was used to orientate the velocities, these measurements are free of local magnetic field disturbances and therefore free of compass errors.

Applying a least squares fit method of harmonic analysis to the depth averaged horizontal velocities recorded by the ship's ADCPs revealed that the orientation of the

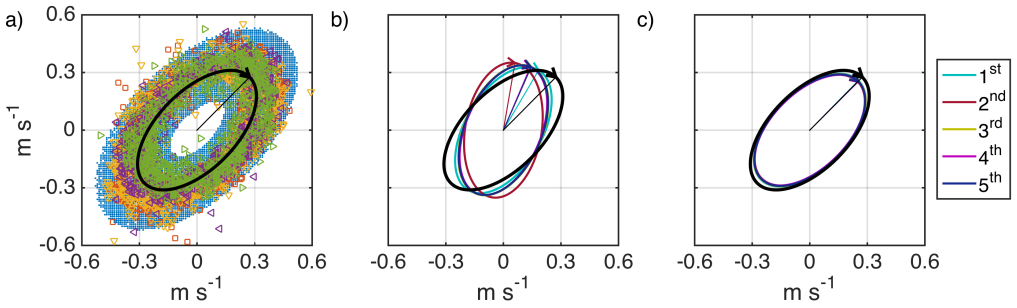

FIGURE 3.11: Ellipse orientations at CCS a) ship's ADCP observations during DY018 & DY033 (markers) compared to POLPRED model (blue dots). The overlaid black ellipse in a-c constitutes the true M_2 ellipse orientation of 45.2° (cyclonic from east). b) Uncorrected ACP M_2 ellipse orientations. c) Corrected ACP M_2 ellipse orientation. Colours denote different ACP deployments.

M_2 tidal ellipse, which is the major tidal constituent at CCS, was 44.5° ± 1.0° (cyclonic from east, black line in Figure 3.11). This was in good agreement with the Proudman Oceanographic Laboratory Predictions (POLPRED) software output (National Oceanography Centre, 2014) for CCS (blue markers in Figure 3.11a-c), which suggested a M_2 tidal ellipse orientation of 45.2° (cyclonic from east). The uncorrected ACP M_2 tidal ellipse orientations varied between deployments between 59.5° and 80.2° (cyclonic from east, Figure 3.11b). The resulting deviation to the true orientation was therefore beyond the compass accuracy of ± 2.0° (Table 3.3), and horizontal velocities were subsequently rotated accordingly (Figure 3.11c), using one angle per deployment.

Magnetic declination is the angle between magnetic and true north. It varies spatially and with time due to the change of earth's magnetic field. For each deployment, a declination was computed using Geomag 7.0 (International Association of Geomagnetism and Aeronomy *et al.*, 2010). Declinations found using this toolbox ranged between -3.6°N and -3.9°N during the observational campaign. However, since the final data were corrected using data based on the ship's GPS-corrected compasses, declinations did not need to be applied separately.

After the initial data quality control, the ACP data still showed signs of relatively high instrument noise, which resulted in comparatively high S^2 levels over the whole water column (Figure 3.12). Therefore a third-order low pass Butterworth filter with a low pass cut-off frequency of $\omega_n = \frac{1}{0.25}$ cycles m^{-1} was applied to each velocity profile to reduce noise (Figure 3.12c).

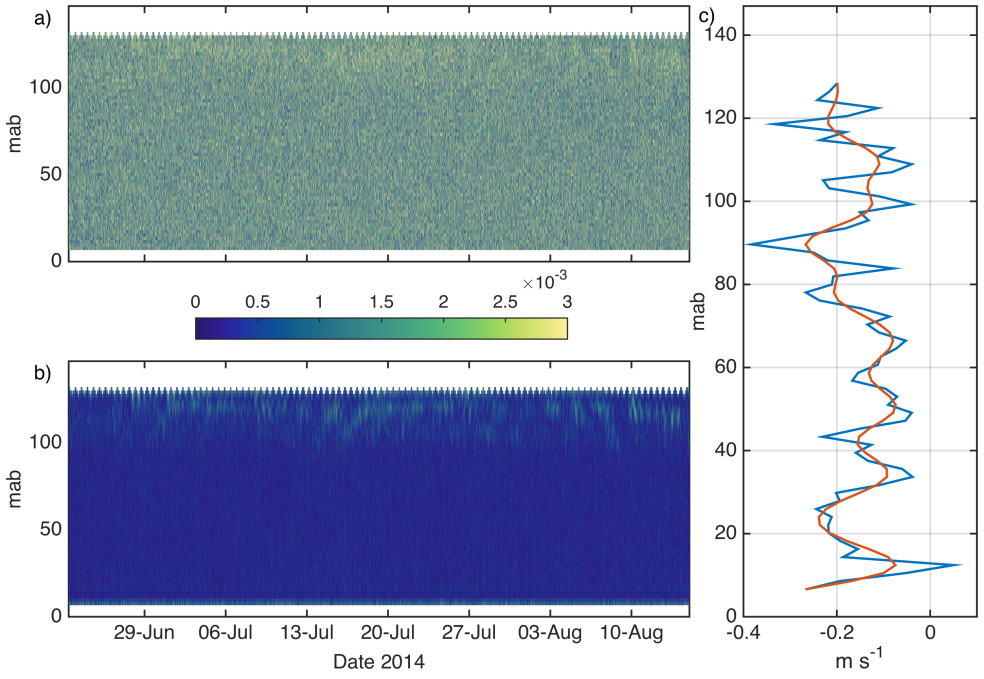

FIGURE 3.12: Butterworth filter. S^2 [s^{-2}] (Equation 2.32) of a) raw and b) smoothed horizontal velocities. c) Single profile: Smoothed (red) compared to raw (blue) velocity observations [m s^{-1}]

This removed high frequency variations in space in the horizontal velocities in order to isolate processes caused by large scale events (Figure 3.12b), while at the same time preserve the high temporal resolution, which would have been lost by taking time averages of profiles.

For the majority of the analysis, the velocity data were interpolated onto the same 5 minute x 2.5 metre resolution grid as the TS logger mooring to enable direct comparison to the temperature/density structure with the local current field.

These quality controlled data have been published and are available through the British Oceanographic Data Centre (Wihsgott *et al.*, 2018).

3.5 Meteorological data

In addition to near-surface temperature observations, T_s [°C], introduced in Section 3.3.2, the Met Office Ocean Data Acquisition Systems (ODAS) buoy provided the majority of the meteorological data as well as surface wave observations. It took hourly observations (10 min averages) of wind speed, w [knots] & direction [°N], relative humidity, r_h [%], air temperature, T_a [°C], air pressure, p_a [mbar], air density, ρ_a [kg m^{-3}], significant wave height, H_s [metre] and wave period, T_p [s]. Hourly observations from the ODAS buoy were available between March 26$^{\text{th}}$ 2014 to August 31$^{\text{st}}$ 2015.

The data were supplied quality controlled by Jon Turton (Met Office).

3.5.1 Wind data conversion

Due to the wind speed units being in knots, the observations were first converted from knots to m s^{-1}. Since the wind observations were taken at a height of at 3.75 metres above the sea surface (J. Turton, personal communication, 21.07.2015), these data were then converted to an equivalent height of 10 metres, as this is the international reference standard for surface wind observations. Within the atmospheric boundary layer, the vertical velocity profile, $w(z)$, is generally accepted to vary according to the logarithmic law:

$$w(z) = \frac{w_*}{\kappa} ln \frac{z}{z_0} \tag{3.1}$$

Here, $w(z)$ [m s^{-1}] is the wind speed measured by the anemometer at a height of z above the sea surface. w_* [m s^{-1}] is the friction velocity, $\kappa = 0.41$ is the von Kármán's constant and z_0 [metre] is the roughness length of the boundary.

In order to convert wind speeds to the 10 metre reference height, Equation 3.1 was rearranged and a roughness length generally representative for the ocean was chosen: $z_0 = 0.0002$ metres (Geernaert, 1987; Zhang and Mcphaden, 1995).

Hereafter, all wind observations and calculations were based on 10 metre wind speeds in m s^{-1}.

3.5.2 Heat flux calculations

In order to calculate heat fluxes, which were used to force the prescriptive models SH74 (Section 2.2) and SB84 (Section 2.3) in Chapter 5, ODAS buoy meteorological observations were complemented with shortwave radiation, Q_{sw} [W m^{-2}], and total cloud cover, n_c [%], data from the extended-range European Reanalysis (ERA) Interim product of gridded meteorological fields (Dee *et al.*, 2011) from the European Centre for Medium-Range Weather Forecasts (ECMWF). This product integrates observations to model the atmospheric fields across the globe to give 3-hourly datasets with 80 km spatial resolution. The time series used here has been interpolated onto the CCS mooring location. In order to verify the model data, they were compared to observations of the Met Office buoy and the overall fit for the wind speed was found to be good (R^2=0.9097, Figure 3.13).

Using these combined data, Q_{lw}, Q_{sen} and Q_{lat} [W m^{-2}] were calculated using Equations 2.41 − 2.46 (Gill, 1982; Sharples *et al.*, 2006). The sum of these derived fluxes and Q_{sw} [W m^{-2}] (Figure 4.2a), which was obtained from the ERA-Interim product (Dee *et al.*, 2011) made up Q_{net} [W m^{-2}] (Equation 2.6). All heat flux components will be investigated in Section 4.1.

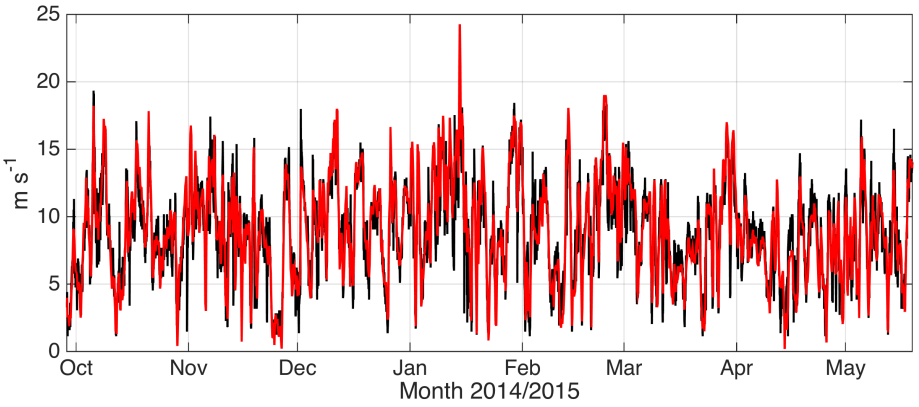

FIGURE 3.13: A comparison of 10 metres, hourly wind speed [m s^{-1}] observations by the Met Office ODAS buoy (black) and 3 hourly ERA-Interim reanalysis data (red).

3.6 Cefas SmartBuoy

In addition to near-surface temperature sensors mentioned in Section 3.3.2, the Centre for Environment, Fisheries and Aquaculture Science (Cefas) SmartBuoy sensor package (Figure 3.14) also consisted of a Seapoint Chlorophyll Fluorometer (SCF) [mg m^{-3}] and a quantum photosynthetically active radiation (PAR) [μE m^{-2} s^{-1}] meter (PAR; LiCor Inc., USA).

The data were stored using the ESM2 data logger, which was configured to sample for 10 min at 1 Hz every 30 min as outlined in Kröger *et al.* (2009); Hull *et al.* (2016). In order to correct for instrument drift, the SCF was standardised to arbitrary fluorometry units using fluorescent sulphate microspheres (FluoSpheres, Thermo Fisher Scientific Inc.) after each deployment at the Cefas laboratories.

While chl *a* is not a direct measure of cell abundance, it is used here as a proxy for chlorophyll biomass. In order to omit artefacts due to non-photochemical quenching, only chl *a* data that were collected when PAR < 10 μE m^{-2} s^{-1} (i.e. hours of darkness) were included here.

Observation of surface nitrate concentrations [μmol l^{-1}] were collected using automated water samplers operated by pumping samples into polyethylene bags pre-injected with

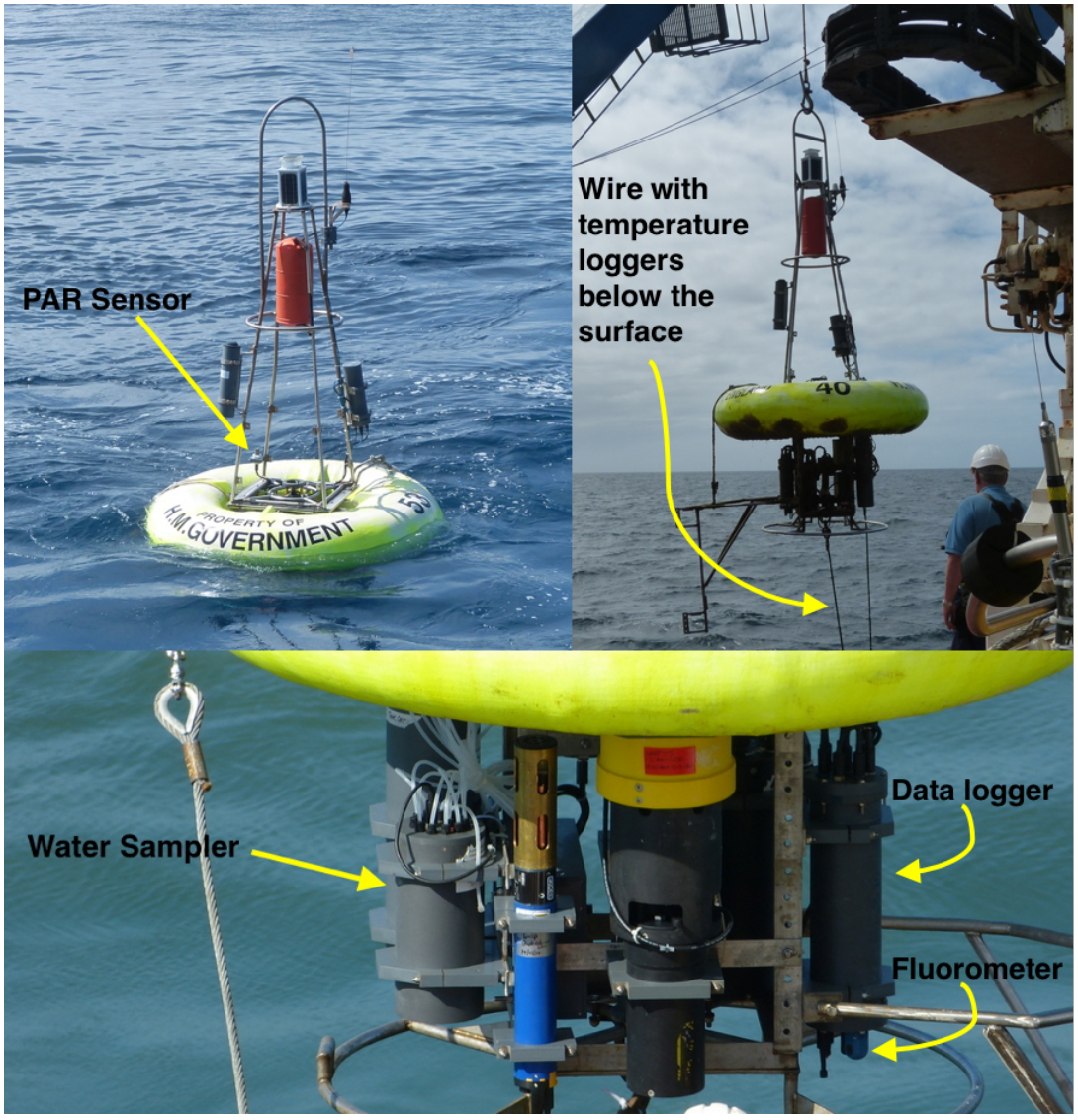

FIGURE 3.14: Cefas SmartBuoy setup. Photos supplied by Tom Hull (Cefas).

5 ml of 1.4 g l^{-1} mercuric chloride ($HgCl_2$ in ultrapure water) as a preservative. On return to shore bag samples were then filtered using 0.2 μm pore size Whatman Cyclopore polycarbonate filters and analysed using a Skalar SAN plus segmented flow autoanalyser, by standard spectrophotometric methods (Kirkwood, 1996).

With the exception of the near-surface temperature data, all SmartBuoy observations were supplied processed and quality controlled by Tom Hull (Cefas).

3.7 Nitrate derived from CTD bottle samples

Nitrate samples from the CTD bottle water samples, were all analysed on board the research ships using a Bran and Luebbe segmented flow colorimetric auto-analyser using classical analytical techniques as described in Woodward and Rees (2001). Clean sampling and handling techniques were employed during the sampling and manipulations within the laboratory, and where possible carried out according to the International GO-SHIP nutrient manual recommendations (Hydes *et al.*, 2010). Nutrient reference materials (KANSO Japan) were run each day to check analyser performance and to guarantee the quality control of the final reported data. The typical uncertainty of the analytical results was between 2-3%, and the limits of detection for nitrate were 0.02 μmol l^{-1} and nitrite 0.01 μmol l^{-1}.

All nitrate data derived from CTD bottle samples were supplied quality controlled by Malcolm Woodward (Plymouth Marine Laboratory).

Chapter 4

Observations: Physical environment

Introduction

This chapter will present the high-resolution, long-term observational data introduced in Chapter 3 to provide an overview of the physical conditions that prevailed at CCS throughout the 17-month observational campaign of the SSB programme. The length of the observational campaign provided an excellent opportunity to focus particularly on the seasonality, and the chance also to investigate the variability between 2014 and 2015.

This chapter first considers the surface observations of meteorology and the wave climate at CCS (Section 4.1). Section 4.2 introduces the velocity field and determines the dominant tidal constituents. Section 4.3 then combines findings from Sections 4.1 and 4.2, to investigate the evolution of the vertical water column structure in response to meteorological and tidal forcing throughout the seasonal cycle.

4.1 Meteorological and wave observations

Between 26th March 2014 and 31st August 2015 a Met Office Ocean Data Acquisition System (ODAS) buoy collected hourly meteorological and wave observations (Section 3.5). By complementing these data with European Reanalysis (ERA)-Interim data (Dee *et al.*, 2011) from the European Centre for Medium-Range Weather Forecasts (ECMWF), heat fluxes were calculated for CCS according to Equations 2.41 − 2.46 (Gill, 1982; Sharples *et al.*, 2006) and Equation 2.6.

Here, the data are presented using daily and monthly averages. Monthly averaged data for March 2014 were excluded from the analysis as the short data record did not warrant a representative value for the entire month.

4.1.1 Wind observations

Over the observational campaign, wind speeds averaged 7.9 ± 2.8 (1 standard deviation) m s^{-1} (Figure 4.1a). While wind speeds in spring months (April - May) 2014 averaged 7.8 ± 0.9 m s^{-1}, averaged wind speeds decreased during summer months (June - August) 2014 to 6.9 ± 1.1 m s^{-1}. During autumn months (September - November) 2014 and winter months (December - February) 2014/2015, wind speeds increased again, averaging 7.3 ± 3.6 and 9.1 ± 3.1 m s^{-1}, respectively. Wind speeds during spring (March - May) and summer months (June - August) 2015, were considerably higher compared to the similar periods in 2014, reaching averages of 9.5 ± 1.4 and 8.6 ± 3.7 m s^{-1}, respectively. Generally, the wind speed was characterised by a weak seasonal signal, with a winter maximum. Although short-term variability had a considerably larger range of values than that of the seasonal cycle.

The dominant wind direction was from the southwest (Figure 4.1b) in line with the large-scale North Atlantic weather systems driving westerlies in the mid-latitudes.

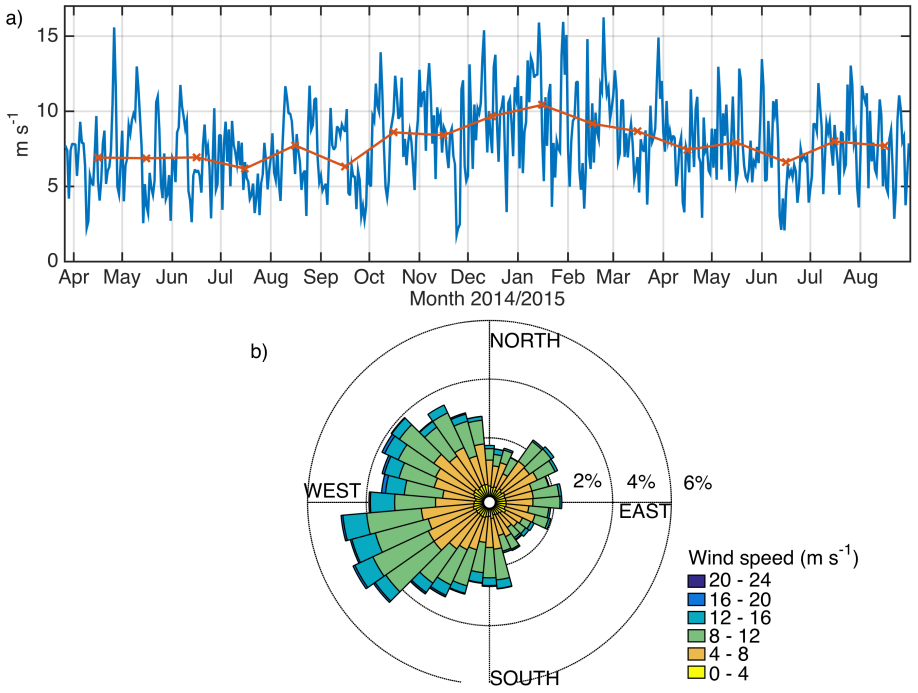

FIGURE 4.1: Wind observations. a) w [m s^{-1}], daily averaged (solid line), monthly averaged (red line with crosses). b) wind direction [°N], occurrence (%), and intensity [m s^{-1}].

4.1.2 Heat fluxes

As expected for any mid-latitude site, the incident solar radiation, Q_{sw}, which controls the succession of seasons throughout the year, showed a clear seasonal cycle at CCS (Figure 4.2a). Daily averaged shortwave fluxes reached 373 and 336 W m^{-2} in the summers of 2014 and 2015, respectively. While the lowest daily averaged values of 3.7 W m^{-2} occurred in December 2014. In contrast, the radiative heat flux, Q_{lw}, was relatively constant throughout the observational campaign (Figure 4.2b), radiating on average -54.5 $\pm$ 15.5 W m^{-2} to the overlying atmosphere. Q_{lw} (Equation 2.41) is primarily a function of the earth's temperature, here the sea surface temperature, T_s, and the earth's emissivity, e_m, due to the ocean not behaving as a perfect black body. The lack of seasonality observed in Q_{lw} (Figure 4.2b) might therefore be explained by the relatively constant T_s only varying 9.0°C over the seasonal cycle, compared to a

general surface temperature range in continental Europe of approximately 40°C over a seasonal cycle.

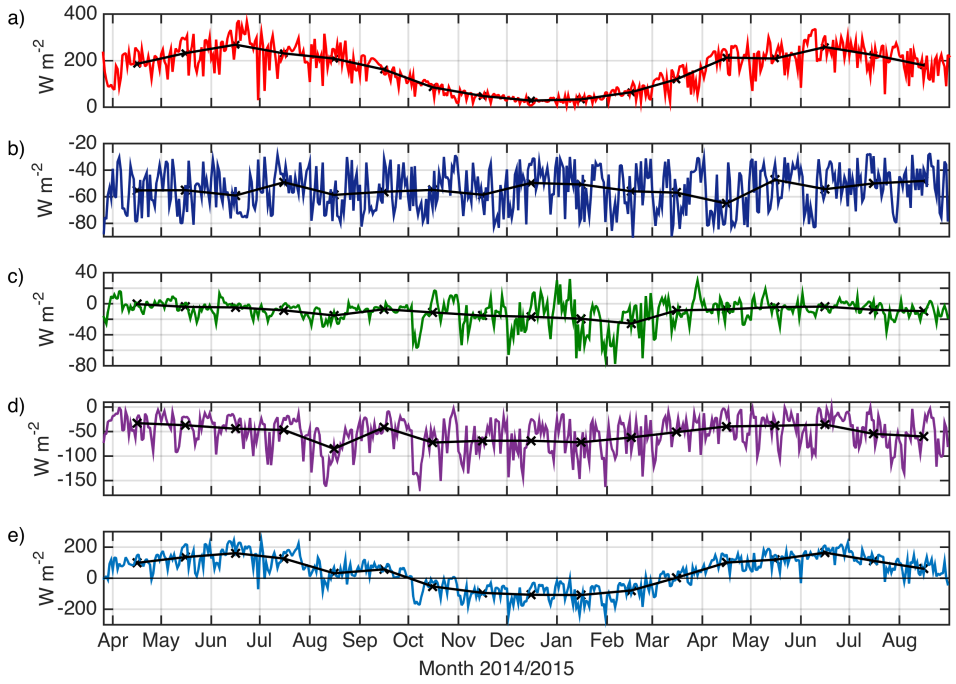

FIGURE 4.2: Heat fluxes at CCS [W m^{-2}] a) shortwave radiation, Q_{sw} b) longwave radiation, Q_{lw} c) sensible heat flux, Q_{sen} d) latent heat flux, Q_{lat} e) net heat flux, Q_{net}. Daily averaged values (solid line), monthly averaged values (black line with crosses). A positive sign denotes heat gain by the ocean, whereas a negative sign means the ocean is losing heat to the overlying atmosphere.

The sensible heat flux, Q_{sen} (Figure 4.2c) only made a relatively small contribution to the net heat flux, Q_{net} (Figure 4.2e, Equation 2.6) between April - September 2014. During this time, the sensible heat flux was on average -6.7 $\pm$ 8.5 W m^{-2}. Contributions between October - February 2014/2015 increased and showed a larger variability of -17.4 $\pm$ 21.9 W m^{-2}. From March to August 2015, average values of Q_{sen} increased again to -6.9 $\pm$ 10.9 W m^{-2}. Since Q_{sen} is a function of air-sea temperature difference and wind speed (Equation 2.44), the absolute magnitude of Q_{sen} was greatest (-77.6 W m^{-2}) and showed the largest range in values during autumn and winter months (October - February), when wind speeds were high but variable (Figure 4.1a), and a drop in air temperature increased the differential between the sea and air temperature.

The latent heat flux, Q_{lat} (Figure 4.2d) averaged -53.5 ± 33.8 W m^{-2} over the entire observational period. At times Q_{lat} became the dominant term in altering the polarity of the net heat flux (Figure 4.2e). Similar to Q_{sen}, Q_{lat} is a function of the wind speed (Equation 2.45) and was therefore strongest in winter months (Figure 4.2d).

The combined sum of all outgoing and incoming heat flux terms (Equation 2.6) denotes the net heat flux, Q_{net} (Figure 4.2e). Q_{net} at CCS was clearly dominated by the incoming solar radiation, Q_{sw} (Figure 4.2a) and follows a similarly evident seasonal cycle (Figure 4.2e). As a result, the ocean was gaining heat between the end of March to the end of September 2014. At the beginning of October 2014, the ocean started losing heat to the overlying atmosphere until March 2015, indicated by the sign of the net heat flux turning positive again (Figure 4.2e).

4.1.3 Air temperature and relative humidity

Air temperatures, T_a [°C], at CCS were on average 13.0 ± 3.1°C and varied seasonally between minimum values of 6.5°C in February 2015 and maximum values of 19.7°C in July 2015 (Figure 4.3a). While T_a was driven by the seasonal changes in solar radiation (Figure 4.2a), maximum and minimum T_a exhibited a phase lag of approximately one month compared to Q_{sw} (Figure 4.2a). Interestingly, monthly averaged air temperatures between April - August 2015 were all colder by 0.3°C (April) - 1.5°C (July) compared to their 2014 equivalent periods.

Relative humidity, r_h [%] (Figure 4.3b), is a function of air temperature (Figure 4.3a) and air pressure (not shown). Values of r_h maintained an average value of 85.2 ± 7.3 % between April - August 2014 and then declined as T_a started to decrease in October 2014. Between October - February 2014/2015, values of r_h averaged 79.2 ± 9.4 %. As soon as T_a increased again in March 2015, values of r_h responded, averaging 85.2 ± 8.6 % during March - August 2015. The monthly averaged value during August 2014 was

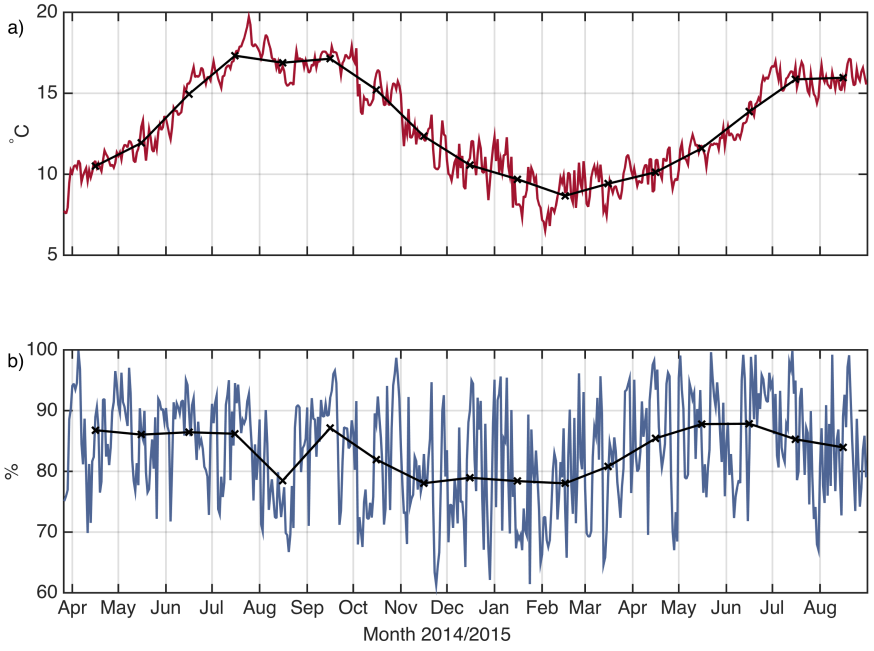

FIGURE 4.3: Meteorological observations. a) air temperature, T_a [°C] b) relative humidity, r_h [%]. Daily averaged values (solid line), monthly averaged values (black line with crosses).

similar to winter levels, averaging 78.9 ± 7.6 %. This corresponded to a decrease in T_a of 3.2°C throughout August 2014, which could be associated with a cold front, passing over the mooring location and thereby bringing cold, dry air to CCS. An example of this is shown in Figure 4.4.

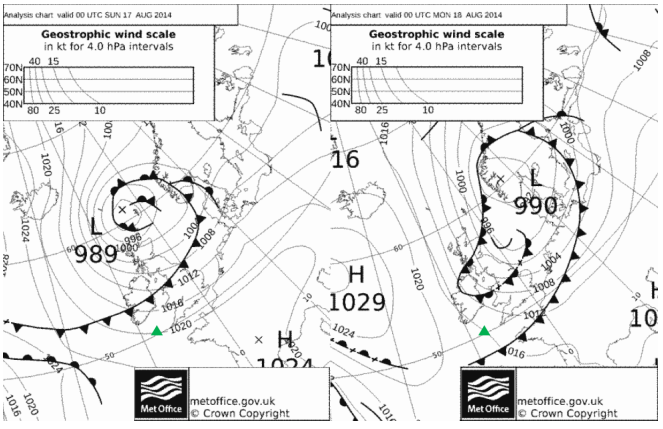

FIGURE 4.4: Synoptic weather charts of NE Atlantic centred on British Isles. Left: 17th and right: 18th August 2014. Green triangle shows the CCS location. Adapted from Met Office (2014).

4.1.4 Wave observations

Throughout the observational campaign, significant wave height, H_s [metre], which is the mean wave height of the highest $\frac{1}{3}$ of waves, was on average 3.2 $\pm$ 1.7 metres (Figure 4.5a). While lowest values of H_s were recorded in the summer months (June - August) 2014, averaging 2.0 $\pm$ 0.8 metres, they more than doubled during the winter months (December - February) 2014/2015 with peaks approaching 10 metres (Figure 4.5a). As might be expected from the signal seen in the wind speed observations (Figure 4.1a), values of H_s were higher during spring (April - May) and summer months (June - August) 2015 compared to their 2014 equivalent periods by 24 and 20 %, respectively.

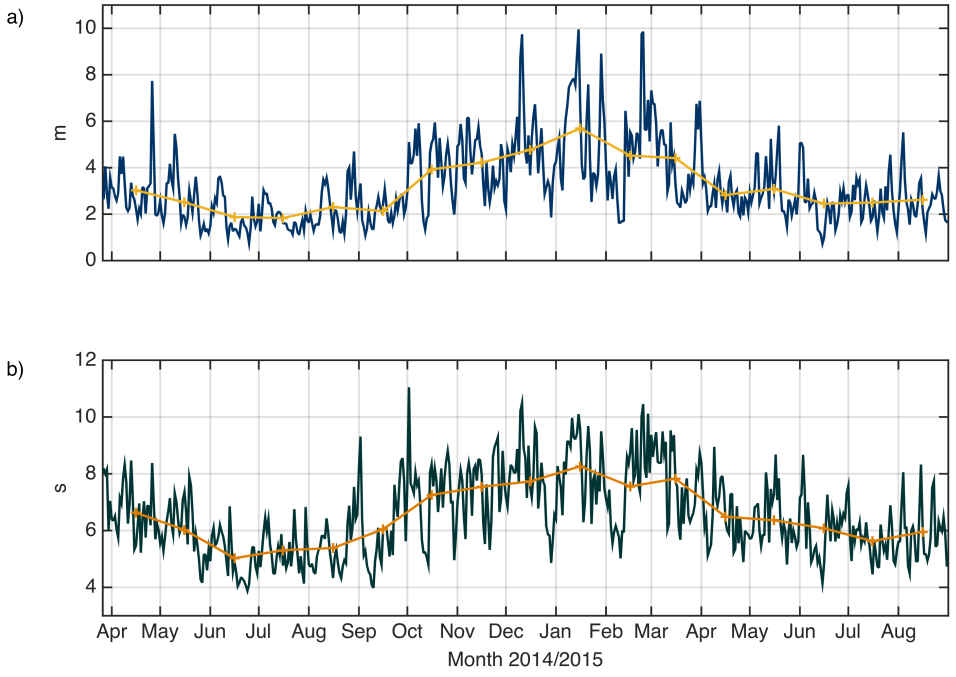

FIGURE 4.5: Wave observations. a) significant wave height, H_s [metre] b) wave period, T_p [s]. Daily averaged values (solid line), monthly averaged values (solid line with crosses).

Unsurprisingly the wave period, T_p [s], also showed a seasonal signal (Figure 4.5b) in parallel to H_s. The shortest wave periods were observed in the summer months (June

- August) 2014 averaging 5.3 ± 0.8 s. Whereas the longest wave periods were recorded during the winter months (December - February) 2014/2015 averaging 7.9 ± 1.4 s. The increase in wave period during spring (April - May) and summer months (June - August) 2015 compared to their 2014 equivalent periods, was 11 and 10 %, respectively and thus less pronounced than the increase seen in H_s.

The wave climate (Figure 4.5) observed at CCS portrayed an apparent stronger seasonal signal compared to the wind speed (Figure 4.1a). Values of H_s and T_p showed an increase from summer to winter values of 37 and 33%, respectively. While wind speeds only increased by 24% over the same period (Section 4.1.1). While the smaller, shorter period waves were likely locally generated, the larger, longer period waves, known as swell, typically required fetch distances in excess of 500 km (Bascom, 1964), so were most likely remotely generated by big storms in the NE Atlantic. This is likely due to an increased number of low-pressure systems in the NE Atlantic during winter months (Young, 1999), generating large swell that can propagate to CCS.

4.2 Currents

A bottom mounted, upward facing, narrowband 150 kHz FlowQuest acoustic current profiler (ACP) collected horizontal velocities [m s^{-1}], along the E-W (u) and N-S (v) direction, between 26th March 2014 and 31st July 2015 at CCS. After quality control (Section 3.4) the velocity data were interpolated onto the same 5 minute x 2.5 metre resolution grid as the TS logger mooring (Section 3.3) to enable direct comparison to the temperature/density structure with the local current field.

The full observational record of the E-W (u) velocity is shown in Figure 4.6a. The large gap of data between May and June 2014, was linked to a battery failure (Section 3.4), whereas the smaller, and often barely visible gaps in August and November 2014, and more notably in April 2015 in Figure 4.6, corresponded to servicing of the moorings.

Naturally, the same gaps will apply to all products derived from the velocity data here (e.g. Figure 4.6b) and later on in this thesis.

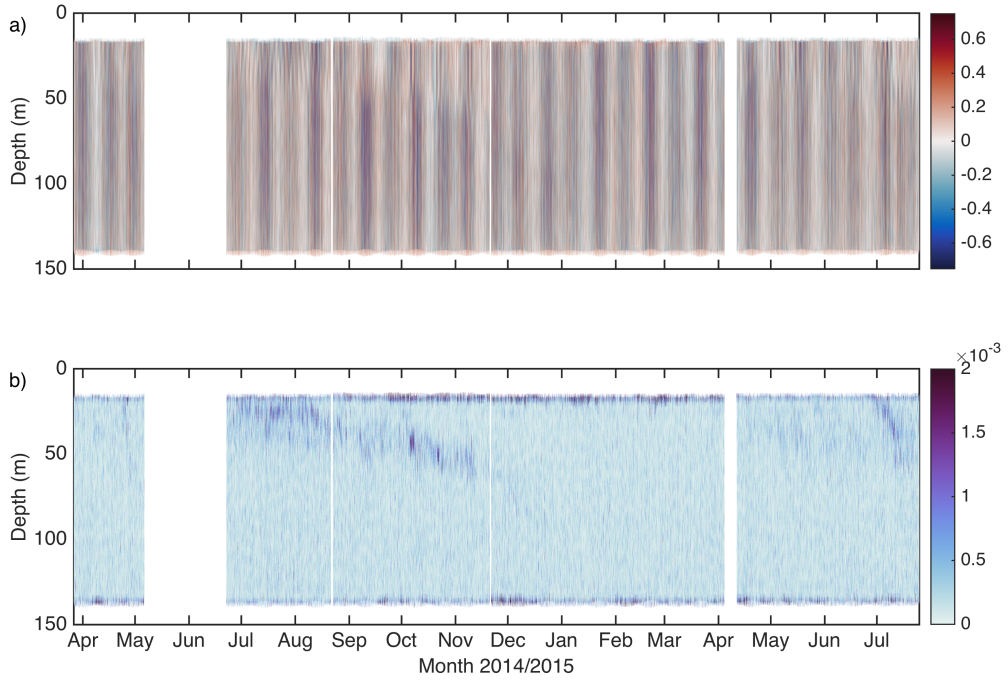

FIGURE 4.6: Full depth observations of the u (E-W) velocity component [m s^{-1}] b) total vertical shear squared of the horizontal velocities, S^2 [s^{-2}] (Equation 2.32).

During the observational campaign peak horizontal velocities reaching 0.88 and 0.50 m s^{-1} were observed during spring and neap tides, respectively. Figure 4.6b shows the instantaneous vertical shear of the horizontal velocities squared, S^2 [s^{-2}] (Equation 2.32), which is representative of the TKE shear production term, $\boldsymbol{P}$ (Equation 2.31). Throughout the observational period S^2 was high ($\approx 1 \times 10^{-2}$ s^{-2}) at the sea surface and sea bed. This is a result of stresses from wind (Equation 2.14) and tide (Equation 2.8), respectively. Elevated levels of S^2 of 2×10^{-3} s^{-2} were also present in midwater. These increased levels of shear started near the sea surface in both spring 2014 and 2015, and then continued to deepen throughout the seasonal cycle, clearly detaching itself from both boundary layers. These elevated levels of midwater shear are typically associated with density interfaces (Rippeth *et al.*, 2005), and

thus followed the deepening of the pycnocline throughout the seasonal cycle. Sources of this shear are likely to be interaction with boundary driven flows from wind and tide due to the local reduction in eddy viscosity (Section 2.4.5), and the pycnocline-focused opposing baroclinic velocity attributable to internal waves. Internal waves, including those generated by topographic interaction of stratified flow and wind-triggered inertial oscillations, have often been attributed to be the main source of internal shear and associated mixing in shelf seas (e.g. Rippeth, 2005; Shroyer *et al.*, 2011) and in the open ocean (e.g. Gregg, 1989; Garrett and Munk, 1979). The internal wave field at CCS will be investigated in-depth in Chapter 6.

In order to find the dominant harmonic constituents of the barotropic tide, rotary power spectral density (PSD) spectra were calculated for the complex form, $\hat{u} + i\hat{v}$, of the depth averaged horizontal velocities. This was done using a Welch's periodogram with a Hanning window of the size of 50% of the total data record of 123747 data points with windows overlapping by 50%. Here, the anticyclonic (clockwise) spectra are defined for frequencies, $F < 0$, and the cyclonic (anticlockwise) spectra for $F > 0$ (e.g. Thomson and Emery, 2014). The one-sided PSD spectra, where both rotary components are plotted as functions of $|F| \geq 0$, can be seen in Figure 4.7.

The spectra were dominated by three peaks at semi-diurnal frequencies (Figure 4.7b): the principal lunar component, M_2, the principal solar component, S_2 and the larger lunar elliptic component, N_2 (Figure 4.7a). An increase in energy was also observed at the local inertial frequency (Figure 4.7a), which at 49.4°N has a period of $T_f = 15.76$ hours. As expected for inertial currents in the northern hemisphere, this was confined to the anti-cyclonic rotating component. The spectra also showed significant peaks at the diurnal frequencies representative of the two lunar diurnal components, K_1 and O_1. Furthermore, there were two peaks at the M_4 and M_6 frequencies present (Figure 4.7a). Both are M_2 overtides, which are caused by the interaction of the M_2 frequency with itself due to the shallow bathymetry of continental shelves (depths up to 500 metres,

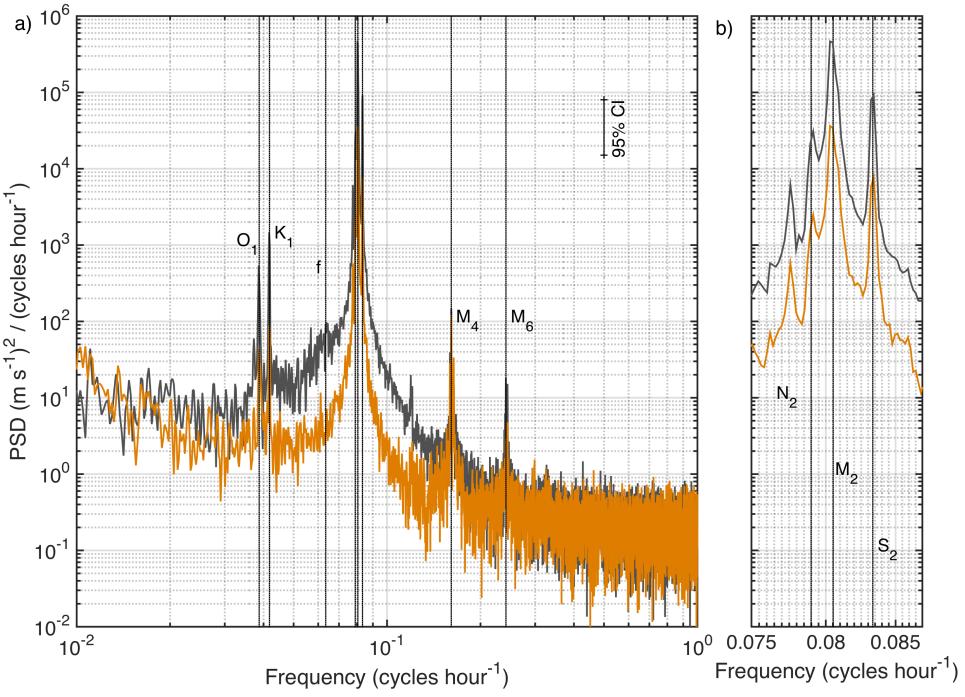

FIGURE 4.7: One-sided rotary PSD spectra [(m s^{-1})^2/ cycles $hour^{-1}$] of depth averaged rotary current components: anticyclonic (grey) and cyclonic (orange). a) full spectra b) focusing on the frequency range of the semi-diurnal tidal constituents. Vertical lines denote frequencies of dominant tidal constituents.

compared to the deep ocean where depth average 4 km). Hence these overtides are also referred to as shallow water constituents.

Using the dominant frequencies found through spectral analysis (Figure 4.7), a least squares fit method of harmonic analysis was then applied to the depth averaged horizontal velocities. This revealed the tidal ellipse properties of the dominant tidal constituents (Table 4.1).

The principal lunar component, M_2, dominated, however the S_2 and N_2 frequencies also showed moderate contribution (Table 4.1), which resulted in the horizontal velocities exhibiting a pronounced spring-neap cycle, which was modulated by the N_2 tide (Figure 4.8a). Due to this N_2 modulation, the spring-neap cycle was stronger (increased difference between peak spring and neap tides) in mid-August – mid October 2014

Constituent	Period [hr]	Semi-major axis [m s^{-1}]	P_l $\left(\frac{\text{minor}}{\text{major axis}}\right)$	Ellipse orientation [° anticlockwise from E]	Phase [°]
Semi-diurnal constituents					
M_2	12.42	0.357	-0.553	45	177.7
S_2	12	0.132	-0.556	44.3	121.7
N_2	12.66	0.068	-0.577	42.9	135.3
Diurnal constituents					
O_1	25.82	0.011	-0.515	160	129.6
K_1	23.98	0.015	-0.644	155	158.4
Shallow water constituents					
M_4	6.21	0.009	-0.078	46.2	306.5
M_6	4.14	0.002	-0.403	13.9	197.2

TABLE 4.1: Tidal ellipse properties for dominant tidal constituents at CCS

and mid January − mid-April 2015 than during the rest of the observational period (Figure 4.8a). The polarity, P_l (Equation 2.60), of all tidal constituents suggested anticyclonic (clockwise) rotation (Table 4.1) at CCS, as previously predicted by Simpson and Tinker (2009) using M_2 tidal velocities simulated with the POLCOMS regional scale ocean model (Holt and James, 2001). The semi-major axes of the semi-diurnal constituents were all roughly aligned, being orientated ≈45° cyclonic from east (Figure 4.8b). Depth averaged horizontal velocities reached speeds of typically 0.35-0.50 m s^{-1} during spring tides and up to 0.25 m s^{-1} during neap tides (Figure 4.8a). The tidal excursion distance, which represents the Lagrangian distance moved by a water particle during a single tidal cycle, ranged between ∼ 9 km during neap and ∼ 21 km during spring tides.

4.2.1 Barotropic and baroclinic velocities

While several studies have used the observed depth averaged velocity ($\hat{\boldsymbol{u}}$) to represent the barotropic component, $\langle \boldsymbol{u} \rangle$, of the flow (e.g. MacKinnon and Gregg, 2005b; Palmer *et al.*, 2008; Shroyer *et al.*, 2011). In this thesis barotropic velocities were estimated

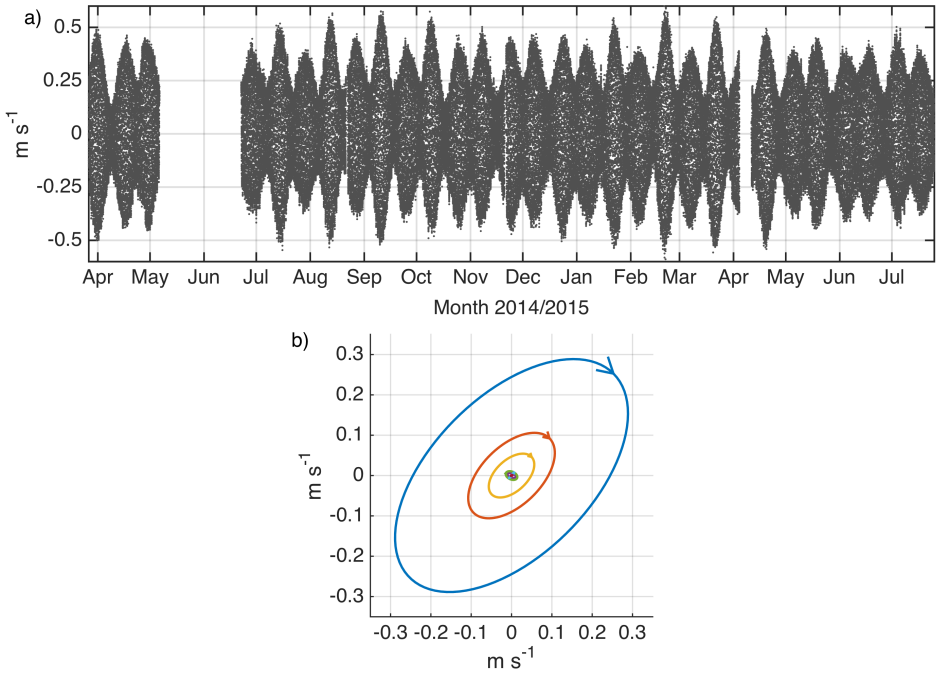

FIGURE 4.8: Tidal velocities. a) E-W depth averaged currents [m s^{-1}]. b) tidal ellipse of main tidal constituents: M_2(blue), S_2(red), N_2(yellow), O_1(purple), K_1(green), M_4(light blue) and M_6(pink).

as the predicted part of the depth averaged velocities, as these were considered more representative of the barotropic tidal forcing. An example of the error in estimating tidal velocities from the depth averaged current can occur due contamination of temporary mean flows, such as caused by persistent winds, or other non-tidal components of the observed velocity. These effects on the flow are visible as enhanced levels of S^2 in the surface and bottom boundary layers of the raw velocities (Figure 4.6b). Here, S^2 increased in the surface layer during autumn and winter months as wind speeds strengthened (Section 4.1).

In order to derive barotropic velocities from the raw velocities, a least squares fit method of harmonic analysis was performed to the depth averaged horizontal velocities using the frequencies of the five dominant tidal constituents, M_2, S_2, N_2, O_1 and K_1 (Table 4.1). Barotropic currents were then derived by reconstructing u and v velocity components using the amplitudes and phases found through the fit (Figure 4.9). For

completeness barotropic currents were also reconstructed for the duration of the ACP battery failure (May 6$^{\text{th}}$- June 19$^{\text{th}}$ 2014).

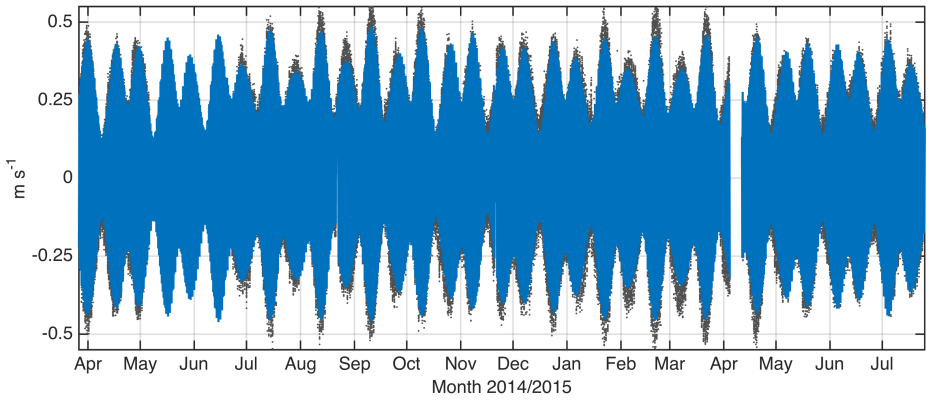

FIGURE 4.9: Depth averaged (grey) vs barotropic (blue) velocities [m s^{-1}].

Baroclinic velocities ($\boldsymbol{u}'$) were then derived according to

$$\boldsymbol{u}' = \boldsymbol{U} - \langle \boldsymbol{u} \rangle - \bar{\boldsymbol{u}} \tag{4.1}$$

Here, $\boldsymbol{U}(z,t)$ is the raw velocity, $\langle \boldsymbol{u} \rangle$ is the barotropic velocity and $\bar{\boldsymbol{u}}$ is the residual velocity. The residual velocities were calculated as the time average of the depth-averaged velocities using a window size of 4 M_2 periods. The observed baroclinic velocities will be discussed later as part of the investigation into the internal wave field at CCS in Chapter 6.

4.3 Vertical density structure

The seasonal change of the vertical water column density structure was captured by the long-term TS logger mooring (Wihsgott *et al.*, 2016) and the additional near-surface temperature sensors, described in Section 3.3. The observed evolution of potential density, potential temperature and absolute salinity (McDougall *et al.*, 2012) throughout the 17 months deployment period can be seen in Figure 4.10. Similar to the

current data presented in Section 4.2, the gaps of TS mooring data in June, August and November 2014, and most notably in April 2015 in Figure 4.10, corresponded to mooring servicing. Naturally, the same gaps will apply to all products derived from the TS logger data that will be analysed later in this thesis.

These data are currently the longest and best resolved time series of water column structure on the European Shelf and comparable to data collected during the North Sea Project (Simpson, 1994).

At CCS 99% of the variability in density was explained by the variability in temperature (Figure 4.10a-b), thus temperature plays the leading role in defining the density structure at CCS. This confirms previous findings that away from coastal boundaries, the leading control on density in the Celtic Sea is predominantly temperature, (e.g. Pingree, 1975; Simpson and Hunter, 1974; Simpson and Bowers, 1984). There is however occasional variability in the salinity field (Figure 4.10c) that may have a controlling effect on the density structure. Pingree *et al.* (1976) suggested that during the early part of the year, when the net heat gain of the ocean is weak, buoyancy input from precipitation could become a leading control over short time-scales.

The overall pattern in density structure observed at CCS shows a typical seasonal cycle of stratification. Throughout the winter months, CCS was fully mixed, while the positive net heat flux (Figure 4.2e) during spring and summer months resulted in the development of stratified conditions (Figure 4.10). The following Sections 4.3.1, 4.3.2 and 4.3.3 will explore the transition made throughout the observational campaign in more detail. Here, changes in density, stratification (Φ [J m^{-3}], Equation 2.1) and surface mixed layer (SML) depth will be investigated in response to the seasonal influences of heating and stirring (by wind and tide).

The mixed layer depth (MLD) describes the topmost layer of the ocean in contact and with the atmosphere, which is assumed to be homogeneous up to a certain depth

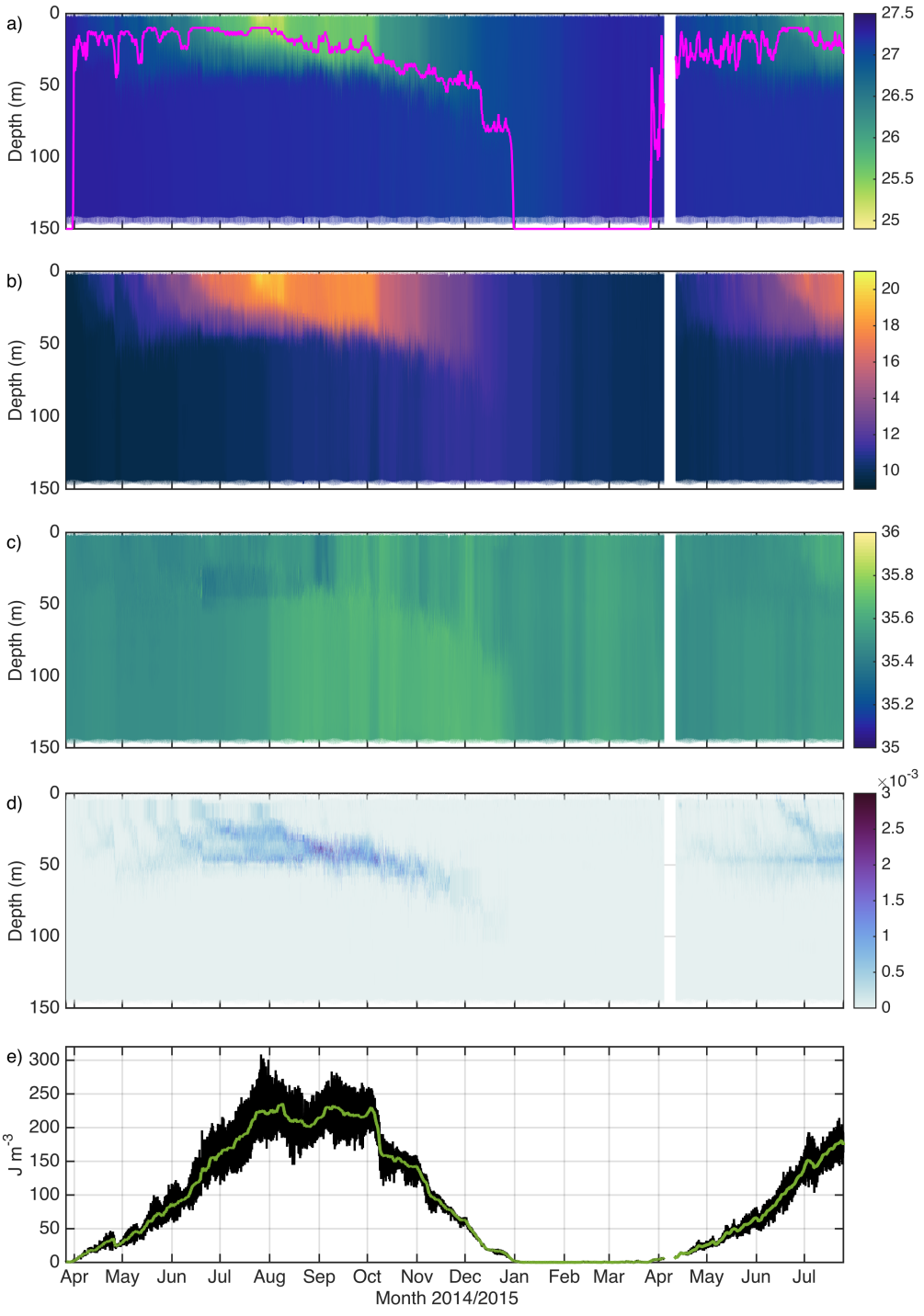

FIGURE 4.10: Full depth observation of a) potential density [kg m^{-3}] SML depth overlaid (pink) b) potential temperature [°C] c) absolute salinity [g kg^{-1}] d) N^2 [s^{-2}] e) Φ [J m^{-3}] (black - instantaneous, green - 25 hr running average)

owing its existence to turbulent processes such as wind stress, waves and convective overturning keeping it mixed. There are several methods to determine the depth of the mixed layer (e.g. de Boyer Montégut *et al.*, 2004; D'Ortenzio *et al.*, 2005; Holte and Talley, 2009; Mignot *et al.*, 2009). In this thesis, mixed layer depth estimates were derived using a fixed density threshold relative to the a near surface/bed value, as this most closely resembled the MLD when tested on individual profiles. The depth of the surface mixed layer (SML) was defined as a density change of +0.02 kg m^{-3} relative to the value at 10 metres depth and the depth of the bottom mixed layer (BML) as a density change of -0.02 kg m^{-3} relative to the value closest to the bed, as this was found to be consistently representative of the transitional points between the surface and bottom mixed layer and the seasonally stratified interfaces.

4.3.1 Onset of stratification in spring 2014

When the TS mooring was first deployed on 26$^{\text{th}}$ March 2014, the water column was still vertically mixed from the previous winter (Figure 4.11a). This is evident from the SML depth extending to the full depth (Figure 4.11a), and the potential energy anomaly (Φ [J m^{-3}], Equation 2.1) shown in Figure 4.11b. Here, $\Phi \approx = 0$ J m^{-3} indicates the water column was fully mixed. On 30$^{\text{th}}$ March 2014 a period of prolonged positive Q_{net} (Figure 4.11c) was observed, which resulted in the onset of stratification in 2014, indicated by SML $< h$ and $\Phi > 0$ J m^{-3} (Figure 4.11a, b). While the wind stress, τ_s (Equation 2.14), was low during this period, it is interesting to note that the onset of stratification coincided with waxing (increasing) spring tides (Figure 4.11d), during which barotropic velocities were increasing to 0.45 m s^{-1} (Figure 4.9). This suggests that even relatively strong tidal mixing was not sufficient to prevent stratification occurring at this time.

In the following days stratification continued to strengthen until April 26$^{\text{th}}$ 2014, when a storm passed over the mooring site (Figure 4.12). Wind speeds in excess of 18 m s^{-1}

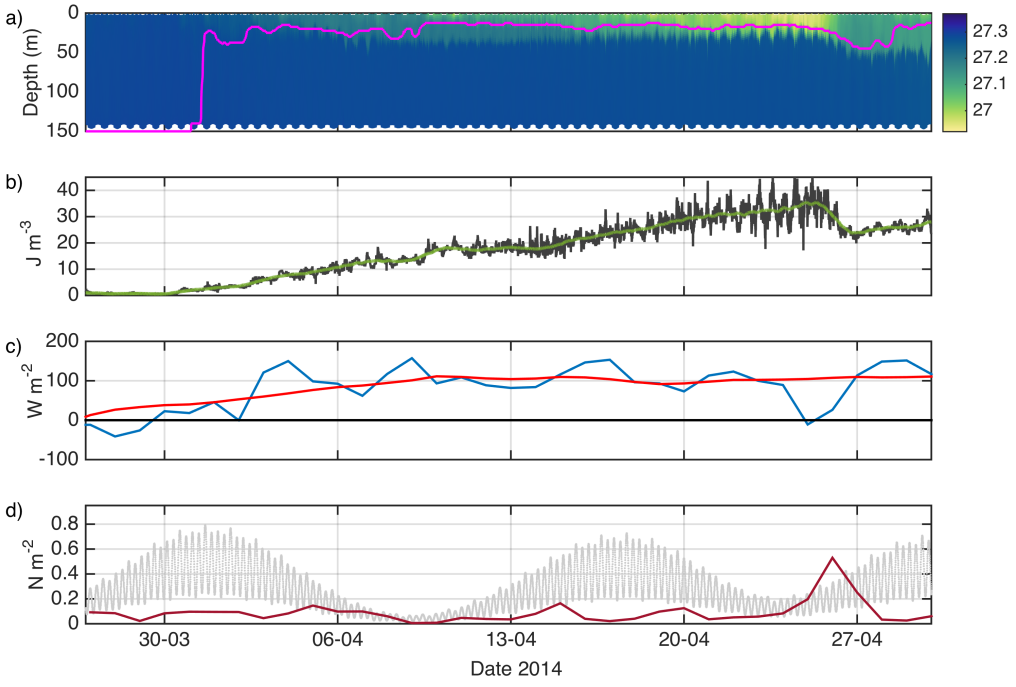

FIGURE 4.11: Onset of stratification 2014. a) potential density [kg m^{-3}] overlaid is the SML depth (pink) b) Φ [J m^{-3}] (grey - instantaneous, green - 25 hr running average) c) Q_{net} [W m^{-2}] (blue - daily averaged, red -15 day running average). d) daily averages of wind, τ_s, (red) and hourly averages of tidal, τ_b (grey) stresses [N m^{-2}] acting on the sea surface and bed, respectively.

(Figure 4.12b) resulted in surface stresses that exceeded tidal stresses (Figure 4.11d) on April 26$^{\text{th}}$ 2014. The combined effect of high winds and extreme wave conditions ($H_s > 9$ metres, Figure 4.11c) produced a significant increase in surface mixing, which is evident as a reduction in Φ of $\approx$ 11 J m^{-3} and a rapid deepening of the SML of $\approx$ 20 metres over a 36 hour period.

Following this stormy period a reduction in surface mixing permitted the formation of new stratification in the near surface layer (Figure 4.12a).

4.3.2 Return to a vertically mixed state in autumn 2014

In October 2014 Q_{net} changed from its mainly positive condition during summer, to a predominantly negative condition signifying the start of steady heat loss from the

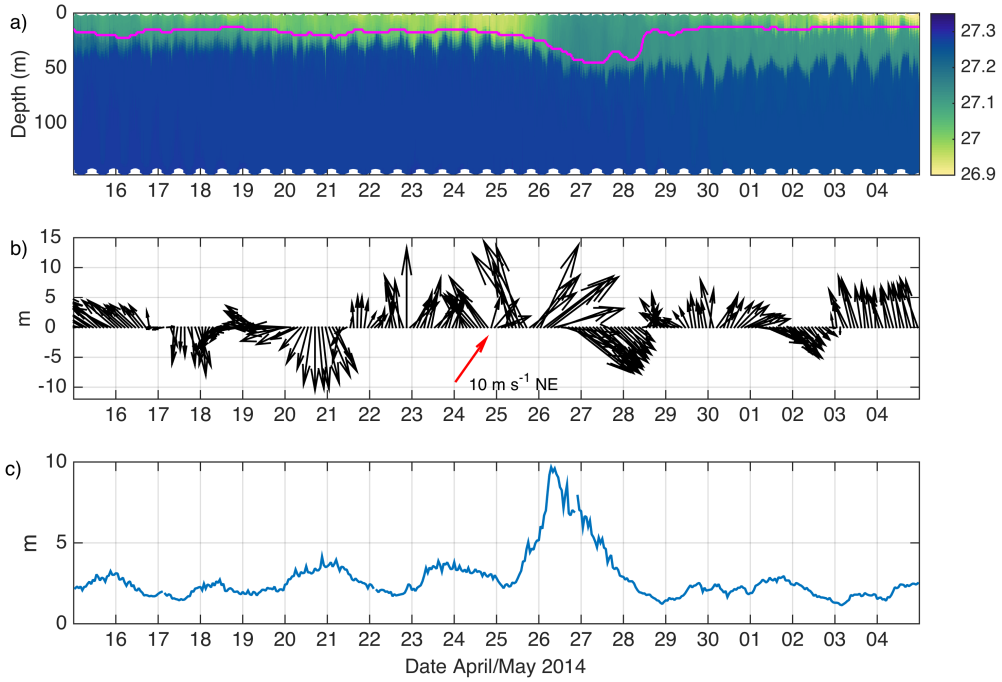

FIGURE 4.12: Spring storm 2014: a) potential density [kg m^{-3}], overlaid is the SML depth (pink) b) w [m s^{-1}] and direction [°N] c) H_s [metre]

ocean (Figure 4.2e and Figure 4.13c). At the same time wind speeds had increased to an average of 8.8 ± 3.3 m s^{-1} (October-December 2014) compared to an average of 6.8 ± 1.1 m s^{-1} during July - September 2014 (Figure 4.1a). This increase in mean wind speed resulted in the wind stress often exceeding tidal stresses to become the dominant mixing term during autumn and winter months. This was particularly evident during neap tides (Figure 4.13d).

The combination of strong winds and a predominantly negative Q_{net} led to persistent deepening of the SML depth (Figure 4.13a). This steady deepening of the pycnocline marked the beginning of the breakdown of seasonal stratification in 2014 (Figure 4.13a-b). The breakdown began with a sharp drop in stratification, Φ, of $\approx$ 70 J m^{-3} at the beginning of October 2014 (Figure 4.13b). Here, negative Q_{net}, high wind speeds (often exceeding 11 m s^{-1}) and waxing spring tides coincided (Figure 4.13c-d) to result in a peak in mixing through the combined contribution from the three mixing

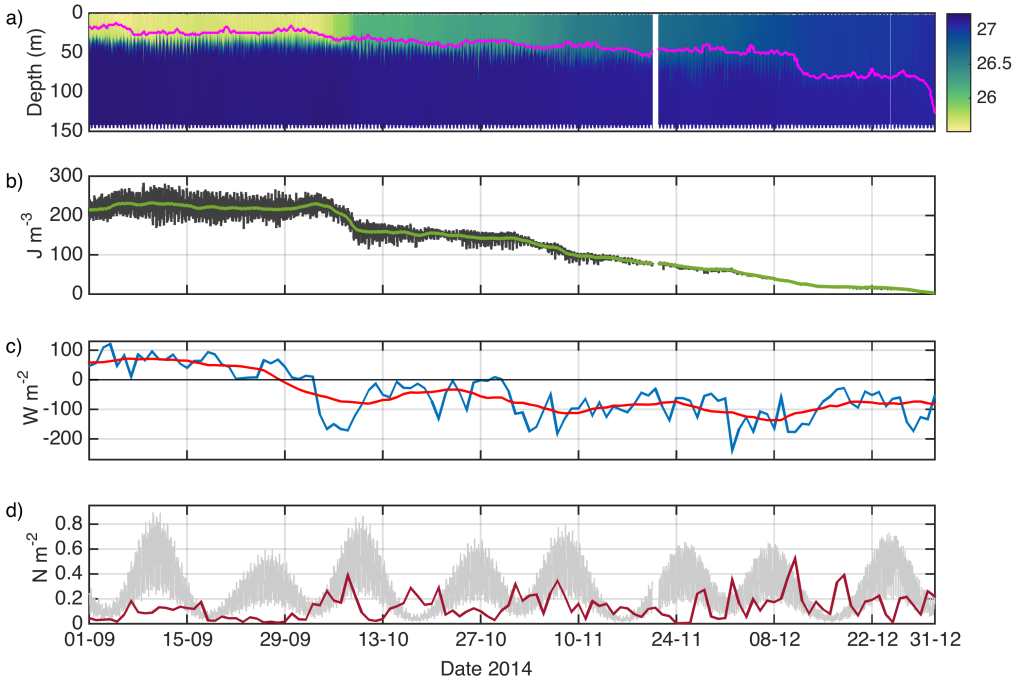

FIGURE 4.13: 4 month period including the breakdown of stratification in autumn 2014: a) potential density [kg m^{-3}] with SML depth overlaid (pink) b) Φ [J m^{-3}] (grey - instantaneous, green - 25 hr running average) c) net heat flux [W m^{-2}] (blue - daily averaged, red -15 day running average). d) daily averages of τ_s (red) and hourly averages of τ_b (grey) stresses [N m^{-2}].

mechanisms. While the SML depth was steadily increasing throughout autumn, a sharp increase of SML depth of 25 $\pm$ 3 metres was observed between 10$^{\text{th}}$ and 14$^{\text{th}}$ December 2014 (Figure 4.13a). This event coincided with strong wind speeds with maximum instantaneous values of 18 m s^{-1} that resulted in wind stresses exceeding tidal stresses at this time (Figure 4.13d). However, this change in SML depth did not result in a similarly dramatic response evident in Φ. Following this event, Φ remained near constant, despite high wind speeds often exceeding instantaneous values of 11 m s^{-1}. During the 7 day period (14$^{\text{th}}$ and 21$^{\text{th}}$ December 2014) Φ only decreased by $\approx$ 3 J m^{-3}. This period, however, also coincided with weak neap tides, which are a result of the N_2 modulation of the spring-neap cycle (Section 4.2). During this time depth-averaged horizontal velocities rarely exceeded 0.2 m s^{-1}, which potentially explains why stratification had not been sufficiently eroded during this time. It appears that

after the SML deepening had taken place in mid-December 2014, high wind stresses had little or no effect in reducing Φ. Only waxing spring tides at the end of December 2014 eroded stratification completely and the water column became fully mixed on December 31st 2014 (Figure 4.13a-b). The contribution of the dominant processes eroding stratification in autumn 2014, will be explored in more detail in Section 4.3.2.1.

Along with the heat gain at the sea surface through direct exchange with the atmosphere, the temperature at the sea bed also increased by 1.8 ± 0.02°C between April and December 2014 (Figure 4.14).

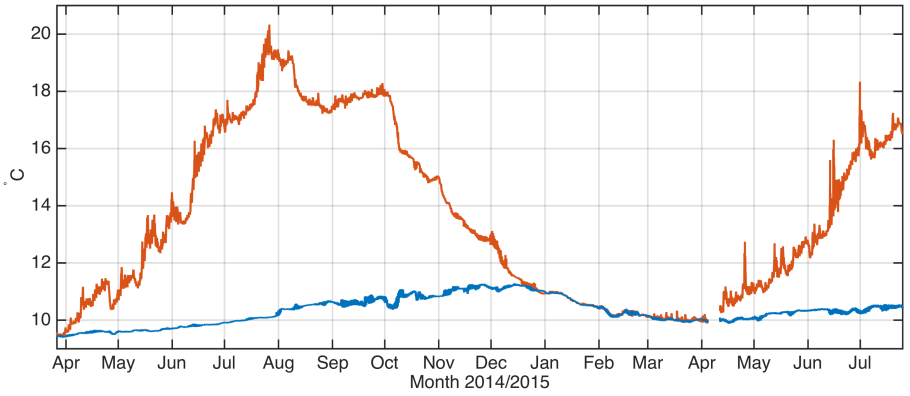

FIGURE 4.14: Evolution of near surface (red) near bottom (blue) temperature [°C].

Similar to observations made by Simpson and Bowers (1984) the maximum in sea bottom temperature of 11.2 ± 0.02°C (Figure 4.14a) coincided with the complete breakdown of stratification at the end of 2014 (Figure 4.13). During the winter months, January - March 2015, the water column was persistently losing heat to the overlying atmosphere and eventually cooling down to an average of 10.0 ± 0.05 °C during March 2015. Bed temperatures between April and July 2015 were consistently warmer between 0.1 and 0.5 °C warmer compared to the bed temperatures during the equivalent period in 2014 (Figure 4.14a).

4.3.2.1 Breakdown of stratification

During the autumn period negative heat fluxes rarely occurred in isolation from strong wind forcing at CCS (Figure 4.13c-d). In order to determine whether the breakdown of stratification in 2014 was driven by shear driven processes caused by wind stress, or by convective mixing due to buoyancy reduction initiated by negative heat fluxes, the Obukhov length scale, L_{OB} [metre], (Obukhov, 1946) was used to examine this competition:

$$L_{\mathrm{OB}} = -\frac{w_*^3}{\kappa B_0} \tag{4.2}$$

Where, w_* [m s^{-1}] is the water friction velocity and B_0 [m^2 s^{-3}] is the surface buoyancy flux. Here, w_* is a function of the wind stress:

$$w_* = \left(\frac{\tau_s}{\rho_0}\right)^{1/2} \tag{4.3}$$

τ_s [N m^{-2}] is the surface stress (Equation 2.14) and $\rho_0 = 1026$ kg m^{-3} is the reference density. The drag coefficient, c_D, within Equation 2.14 was here calculated as a function of the wind speed, w, (Garratt, 1977), according to:

$$c_D = (0.75 + 0.067w) \times 10^{-3} \tag{4.4}$$

Considering that temperature is the dominant control on density at CCS (Section 4.3) B_0 was estimated to be directly proportional to the surface net heat flux (Q_{net}) using

$$B_0 = \frac{\alpha g}{c_p \rho_0}\, Q_{\mathrm{net}} \tag{4.5}$$

Here, the thermal expansion coefficient of seawater, α [°C^{-1}], was calculated using the Gibbs-SeaWater (GSW) Oceanographic Toolbox (McDougall and Barker, 2011). Similar to the observed and calculated heat flux terms in Section 4.1, B_0 was defined to be positive downwards.

The $|L_{\mathrm{OB}}|$ specifies the vertical extent over which either convection or mechanical stirring (at the boundary) is the dominant surface mixing mechanism (Taylor and Ferrari, 2011). $L_{\mathrm{OB}} > 0$ occurs when there is strong surface cooling, and thus unstable stratification. $L_{\mathrm{OB}} < 0$ requires positive heat fluxes and hence indicates stable stratification. Following the framework developed by Brody and Lozier (2014), Table 4.2 defines three surface regimes/cases shaping the SML depth.

Convective mixing regime (case 1)	$\mathbf{\lvert L_{OB}\rvert < SML}$ while $Q_{\mathrm{net}} < 0$ and hence $B_0 < 0$ Here, the buoyancy/net heat flux is large and negative (ocean loses heat), and wind speeds are low. As a result the dominant surface deepening mechanism is convective mixing due to surface cooling.
Wind mixing regime (case 2)	$\mathbf{\lvert L_{OB}\rvert > SML}$ For surface deepening to be driven by wind mixing, wind speeds have to be moderate or large. The sign of the buoyancy/net heat flux is irrelevant on this occasion. In case of a small positive buoyancy/net heat flux (stable stratification, $L_{\mathrm{OB}} < 0$) the wind becomes the sole surface mixing mechanism by default.
Heating regime (case 3)	$\mathbf{\lvert L_{OB}\rvert < SML}$ while $Q_{\mathrm{net}} > 0$ and hence $B_0 > 0$ When the buoyancy/net heat flux becomes large and positive, vertical momentum transfer is inhibited. Here, stable stratification counteracts wind mixing and SML deepening is suppressed.

TABLE 4.2: Surface regimes shaping the SML depth, according to Brody and Lozier (2014).

Using hourly data of observed wind speed, w, and net heat flux, Q_{net}, L_{OB} was calculated for the entire time series. These hourly results of L_{OB} were then compared to the SML depth (Figure 4.13a) and categorised accordingly for each day, using the criteria in Table 4.2. Subsequently, a relative contribution was attributed to each regime on a daily basis, e.g. if $|L_{\text{OB}}| >$ SML for 12 hours during 10$^{\text{th}}$ October 2014, then wind forcing was considered the dominant SML shaping mechanism during 50% of that day. To filter out some of the short term variability owing to sporadic events in heating and wind forcing, the daily contributions were then smoothed using an 8 day running average (Figure 4.15a).

As might be expected from the observed Q_{net} (Section 4.1), the convective and heating regime (cases 1 & 3) displayed a clear seasonal cycle (Figure 4.15), with convection more dominant during winter and heating in the summer months. While the wind regime (case 2), was less seasonal, it dominated throughout the observational campaign (53% of the entire observational period). During the period of the active SML deepening (2$^{\text{nd}}$ October - 31$^{\text{st}}$ December 2014, grey bar Figure 4.15a), the contribution of both wind and convection (case 1 & 2) increased compared to the rest of the year, and the heating regime (case 3) was completely shut off at times. Despite several periods of sustained surface cooling occurring during autumn 2014 (Figure 4.13c), the wind regime further increased its control on the SML depth, being dominant 63% of the time the SML deepened (2$^{\text{nd}}$ October - 31$^{\text{st}}$ December 2014). Periods when the convective regime was dominant accounted for 32% of this time, which coincided with low wind speed/stresses. Periods when positive stratification counteracted wind mixing (heating regime) accounted for the least amount of time during the SML deepening period, of 5%. While shear stresses due to wind appear to be the dominant SML deepening mechanism, considerable variability between and within days was observed (Figure 4.15b & c). The main sources of this variability was the diurnal heat cycle and the relatively short duration of some wind events.

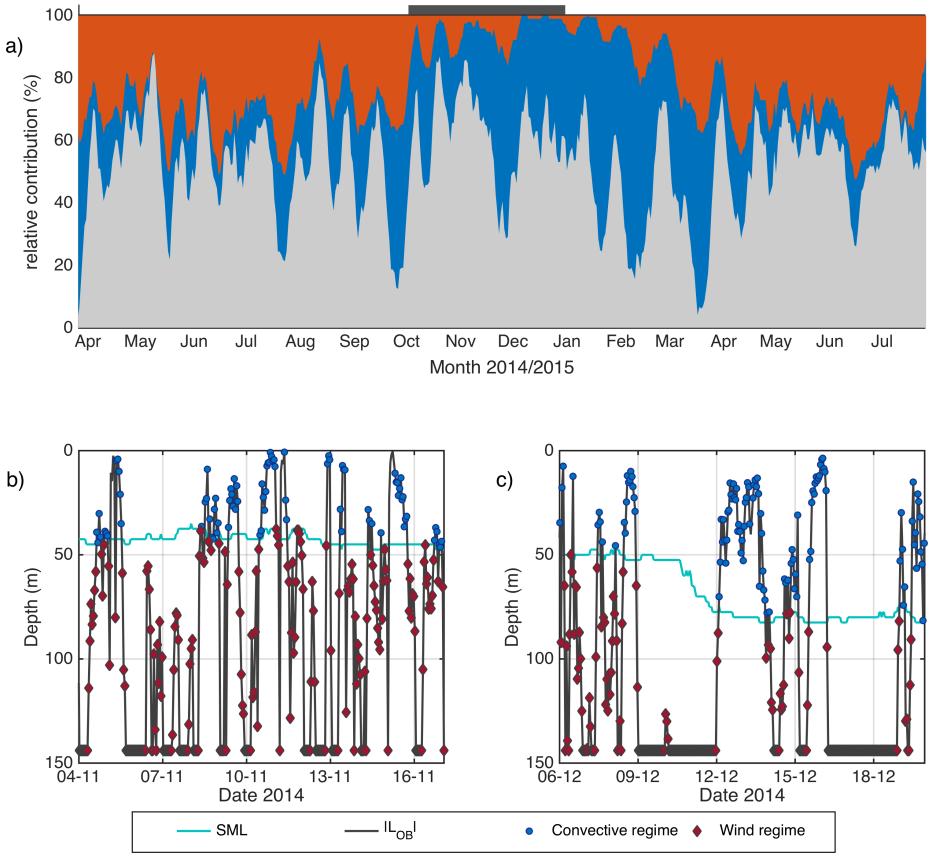

FIGURE 4.15: Dominant SML shaping mechanisms: 8 day running average of proportional control on SML: wind (grey), convective (blue) and heat (red) regime. The grey bar above marks the SML deepening period, 2nd October - 31st December 2014 b) & c) Two example periods during this period. Here, SML depth [metre] (turquoise), $|L_{\mathrm{OB}}|$ [metre] (dark grey), convective regime (blue circles) and wind regime (red diamonds). For plotting purposes all values of $|L_{\mathrm{OB}}| > 145$ metres were set equal to 145 metres.

Considering that convection has been suggested to dominate over wind driven mixing during the autumnal SML deepening period in shelf seas (Edinger *et al.*, 1968; Nielsen and St. John, 2001; Townsend *et al.*, 2010), as well as in open-ocean environments, (Kraus and Turner, 1967; Lacombe *et al.*, 1970; Marshall and Schott, 1999; Taylor and Ferrari, 2011), this was an interesting result. This should though be treated with some caution since the balance of terms that L_{OB} (Equation 4.2) represents, originated in atmospheric sciences (Obukhov, 1946), and hence does not consider secondary mixing mechanisms in the ocean surface boundary, such as wave induced turbulence, which

will be explored in more detail in Section 5.1.3. Secondly, the Obukhov length has no knowledge of the existing strength of stratification such as that from the seasonal thermocline, which would moderate any mixing and thus SML deepening that takes place by providing additional buoyancy for surface mixing to work against.

This is an interesting and potentially significant result as it challenges many previous assumptions that convection is the dominant mechanism driving seasonal breakdown of stratification. While an attempt has been made to separate the individual contributions from wind and convection, the observed mixing effects on density structure are difficult to distinguish as they both contribute to the same process. In an attempt to investigate each forcing mechanism in isolation, the 1-dimensional prescriptive mixing model, SB84, will be used explore the competition of wind and convection further in Section 5.2.3.2.

4.3.3 Onset of stratification in spring 2015

While the water column was fully mixed for most of the winter months, periods of transient stratification (defined here as $\Phi \geq 2$ J m^{-3}) occurred during winter months prior to the onset of stratification in 2015. These transient states rarely lasted more than one day but were observed to occur for four consecutive days between 11$^{\text{th}}$ - 15$^{\text{th}}$ and 17$^{\text{th}}$ - 21$^{\text{st}}$ March 2015 (Figure 4.16b). Such stratification typically only manifested itself in the top 10 metres of the water column (Figure 4.16a) and were typically eroded by night time convection. On the 26$^{\text{th}}$ March 2015 the buoyancy input of Q_{net} (Figure 4.16c) became strong enough to overcome the wind, tide and convective mixing and the water column began to restratify (Figure 4.16a-b).

The wind stress, τ_s, was low during the onset of stratification (26$^{\text{th}}$ March 2015) but then increased to > 0.4 N m^{-2} (Figure 4.16d), equivalent to a wind speed of ≈ 15 m s^{-1} (Figure 4.1a). This resulted in stratification staying at a constant strength of $\Phi = 5 \pm 1$

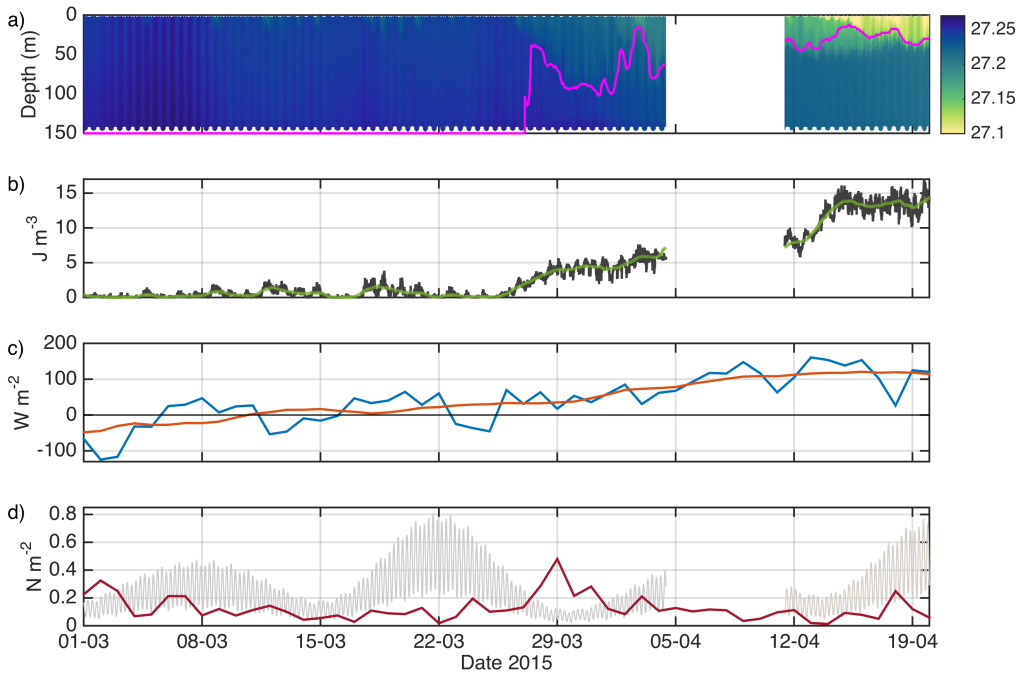

FIGURE 4.16: Onset of stratification 2015. a) potential density [kg m^{-3}] with SML depth overlaid (pink) b) Φ [J m^{-3}] (grey - instantaneous, green - 25 hr running average) c) Q_{net} [W m^{-2}] (blue - daily averaged, red -15 day running average). d) daily averages of τ_s, (red) and hourly averages of τ_b (grey) stresses [N m^{-2}].

J m^{-3}, despite increasing Q_{net} until the wind subsided again 2 days later (Figure 4.16b) and Φ continued to strengthen. In contrast to 2014, the onset of stratification in 2015 occurred during a waning spring tide, yet maximum observed current velocities were still significant, reaching 0.4 m s^{-1}.

4.3.4 2014 vs. 2015

While the timing of the onset of stratification in both years occurred during the end of March (Section 4.3.1 and Section 4.3.3), the rate at which stratification was strengthening was lower during 2015 (1.5 J m^{-3} d^{-1}) compared to the same time in 2014 (1.9 J m^{-3} d^{-1}). This resulted in the water column being less strongly stratified at any time during 2015 compared to the previous year (Figure 4.17a). At the end of the observational period, in July 2015, the difference in Φ was 42.4 $\pm$ 1.9 J m^{-3} or $\approx$ 20%

less than observed compared to July 2014 (Figure 4.17a). The change in vertical temperature distribution provides a reasonable explanation for the weakened stratification in spring/summer 2015: The combination of generally lower near-surface temperatures (peaking at 1.5 °C in July), and higher near bed temperatures (Section 4.3.2) during 2015 compared to 2014, resulted in a reduced mean top-bottom temperature difference that peaked at 3.4°C between the two years (Figure 4.17).

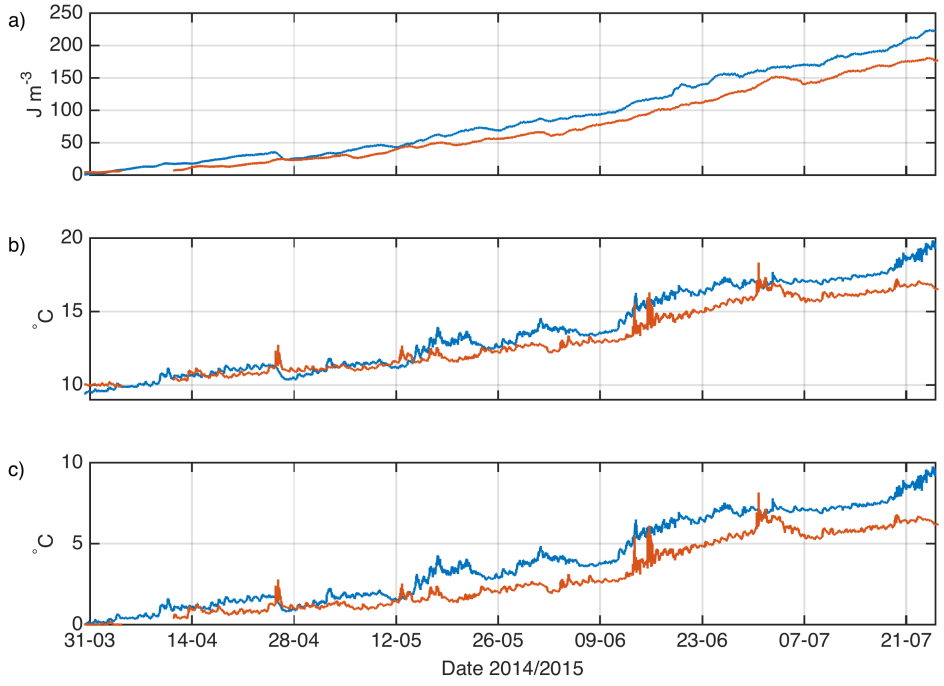

FIGURE 4.17: Stratification 2014 vs. 2015. a) 15 day running average of Φ [J m^{-3}] b) near surface temperature c) top bottom temperature difference. Blue and red lines denote observations taken in 2014 and 2015, respectively.

A potential candidate for this change in temperature distribution and thus strength of stratification in spring/summer 2015 is the increased wind and wave states in 2015 compared to 2014 mentioned in Section 4.1.1 and Section 4.1.4. This observed differences between 2014 and 2015 will be explored in more detail in Chapter 5.

4.4 Summary: Observations describing the physical environment at CCS

The aim of this chapter was to present the newly collected, long-term time series of observational data collected at CCS and to provide an overview of the physical environment during the 17-month observational campaign. The main findings of this chapter are summarised below.

Meteorological conditions intuitively displayed a strong seasonal cycle (Section 4.1), most evident in the solar radiation, which formed a key component of boundary forcing. This periodicity was less evident in wind speeds, which despite displaying winter maxima were highly variable throughout the observations and provided a constant source of energy with minimum monthly averages of around 7 m s^{-1} during summer 2014. Winds were predominantly coming from the southwest.

The seasonal cycle of surface net heat flux, Q_{net}, had maxima during June during both 2014 and 2015 and was at a minimum during December - January 2014/2015. Daily averaged Q_{net} reveals the ocean to be gaining heat between the end of March until the end of September and losing heat from October to March. While the seasonal cycle was the dominant signal in Q_{net}, other processes were observed to have limited control. Among other components, relative humidity (r_h) moderates the flux of heat between ocean and atmosphere (Equation 2.42) and was shown to be highly variable throughout the year, with only subtle differences between seasons. A passing cold front (Figure 4.4) was observed to have a dramatic effect on T_a and r_h (Figure 4.3) and subsequently SST (Figure 4.14).

Despite the close link between wind and wave fields, significant wave height (H_s) and period (T_p) were shown to exhibit a stronger seasonal cycle than wind (Figure 4.5). The largest waves were observed during winter months (December - February) 2014/2015 averaging $H_s \approx 5.0$ metres ($T_p \approx 7.9$ s). The summer (June - August) 2014 wave field

was significantly weaker averaging $H_s \approx 2.0$m ($T_p \approx 5.3$ s). While monthly averaged wave heights and periods were typical of locally generated waves, occasional larger magnitude, longer period swell waves were identified approaching H_s of 10 metres and T_p of 10 s that were likely generated remotely in the North Atlantic.

The long duration current observations at CCS enabled accurate calculation of the barotropic tide (Table 4.1) by harmonic reconstitution of the dominant tidal frequencies, identified by spectral analysis (Figure 4.7). Aside from the expected dominance of the M_2 and S_2 constituents, a strong N_2 contribution was identified resulting in a modulation of the spring-neap cycle (Figure 4.8a).

The impacts of meteorological seasonality is clearly evident in the vertical structure provided by the TS mooring at CCS (Section 4.3.1, Section 4.3.2 and Section 4.3.3). Spring stratification was seen to occur on the 30$^{\text{th}}$ March 2014 and 26$^{\text{th}}$ March 2015. Due to the 17 month duration of the observations only one breakdown period was observed, with the water column becoming fully mixed at the very end of 2014 on December 31$^{\text{st}}$.

Spring (Section 4.3.1 and Section 4.3.3) was characterised by increasing stratification (Figure 4.10e) and the depth of the SML was variable (Figure 4.10a). Unsurprisingly stratification was strongest in summer and early autumn (Figure 4.10e), here the SML depth was on average 16.7 $\pm$ 5.8 metres (Figure 4.10a). Instantaneous values of Φ reached maximum values of 308 J m^{-3} in late July. During this time, observed profiles of N^2 [s^{-2}] (Equation 2.33) had two midwater maxima (Figure 4.10d). Once these two maxima merged in September 2014, maximum values of N^2 were in excess of 3×10^{-3} s^{-2}. After which time the location of maximum N^2 and the SML depth started to deepen (Figure 4.10a, d), but Φ stayed relatively constant (Figure 4.10e), until the breakdown of stratification commenced in autumn (Section 4.3.2).

In an attempt to investigate the relative contributions to the vertical density structure from wind mixing, heating and convection, the Obukhov length scale (L_{OB}, Equation 4.2) was used, as it represents a balance between wind stress and buoyancy fluxes. The framework of Brody and Lozier (2014) provided a useful framework for this (Table 4.2). Wind mixing (case 2 conditions) was shown to be the dominant control on ocean structure making the largest contribution for 53% of the time. This influence was found to further increase during October - December 2014 prior to breakdown of stratification, wind being the dominant control for 63% during this period. This is a potentially significant result since convection is typically thought to dominate SML deepening in autumn. While contributions to mixing are difficult to distinguish using observational data, the competition of wind and convection driving the breakdown of stratification will therefore be further explored in Section 5.2.3.2.

During the winter months (January - March) 2015 transient periods of stratification were observed to last for short periods as daily increases in surface heating competed against wind, wave and convective mixing. As seasonal stratification was approached there was evidence of transient stratification occurring for four consecutive days.

In summary, the mooring site exhibited a response typical of seasonally stratifying mid-latitude shelf seas under the influence of net heat flux (Figure 4.2e), wind (Figure 4.1a) and tides (Figure 4.8) as it transitioned through the seasons (Section 4.3.1, Section 4.3.2 and Section 4.3.3). The system generally appeared to behave in response to the well-recognised heating-stirring framework (Simpson and Hunter, 1974; Simpson *et al.*, 1978) introduced in Section 2.2, however also exhibited behaviours when this relationship seemingly broke down. Examples of this are the onset of stratification in 2014 occurring during waxing tides (Section 4.3.1), and the dominance of wind mixing over buoyancy during the erosion of stratification (Section 4.3.2.1). This will be further investigated in Chapter 5.

The following Chapter 5 will now investigate how the models introduced in Chapter 2 perform at reproducing the observed stratification at CCS.

The TS mooring and ACP datasets that were quality controlled and used within this thesis are available freely from the British Oceanographic Data Centre under **doi:10/bqwf** (Wihsgott *et al.*, 2016) and **doi:10.5285/631ddd2a-48df-143b-e053-6c86abc0d49f** (Wihsgott *et al.*, 2018).

Chapter 5

Prescriptive mixing models

Introduction

In this chapter the prescriptive mixing models SH74 (Section 2.2) and SB84 (Section 2.3) are examined to test their capability in replicating the observed stratification at CCS. Any discrepancies between the predicted and observed water column structure will be used to identify missing or poorly parameterised processes within the models.

At the beginning of each section, the setup of each model is explained and the main forcing terms will be introduced. The results of each model will then be compared to the observations, introduced in Chapter 4. Here, the results show that the bulk of the seasonal cycle is replicated well by both models, and improves with complexity of the model. The failures within each model were similar, and linked to an overestimation of Φ due to a potential underestimation of mixing and an insufficient response to sudden meteorological forcing. The following discussion then explores possible explanations for the discrepancies seen in the models. A key result shows, that tidal stirring is a less dominant term in controlling the vertical water column structure than previously assumed. In fact, CCS seems to behave more like an open-ocean site, exhibiting a predominant surface-forcing control on stratification. It is also shown that both

wind and convection are necessary to fully mix the water column in autumn. This chapter finishes by demonstrating that an addition of a previously unaccounted source of internal mixing can improve the results significantly. It is hypothesised that the energetic internal wave field at CCS, which has been described in earlier studies and will be investigated in depth in Section 6.1, is the source of this 'missing mixing'. However, the discrepancy seen between the model and the observations highlights an apparent seasonality in the internal wave field, which will be further explored in Chapter 6.

5.1 0D approach - SH74

5.1.1 Model setup SH74

In order to test SH74 (Section 2.2) for the CCS location, Equation 2.16 was solved at regular time steps from January 1$^{\text{st}}$ 2014 to the end of 2015 and then integrated. The model started on January 1$^{\text{st}}$ 2014 as the water column in this region is usually fully mixed and hence $\Phi = 0$ J m^{-3}, which removed the requirement to estimate an integration constant.

During the dates when meteorological observations recorded by the Met Office ODAS buoy (Section 3.5) were available (March 26$^{\text{th}}$ 2014 to August 31$^{\text{st}}$ 2015), SH74 was forced using observed values of the parameters required to calculate the net heat flux, Q_{net} (Equations 2.6 and 2.41 − 2.46) and wind speed, w. Outside of this date range, Q_{net} and w data were complemented using data from the extended-range reanalysis ERA-Interim product of gridded meteorological fields (Dee *et al.*, 2011) from the European Centre for Medium-Range Weather Forecasts (ECMWF). Similarly, during the date range of the ACP frame deployment (March 26$^{\text{th}}$ 2014 to July 25$^{\text{th}}$ 2015) SH74 was forced using observed values of barotropic currents, $\langle \boldsymbol{u} \rangle$, while outside of this date range, the record of currents was extended by reconstructing the barotropic u and v

components from the results of least squares fit method of harmonic analysis to the observed currents.

Since this approach considers just the energetics of the water column, and the model has no knowledge of the water column's initial temperature and/or state, all remaining variables were held constant, yet representative for the CCS location: these were $\alpha = 1.77 \times 10^{-4}$ °C^{-1}, $c_p = 3985$ J kg $^{-1}$, $\rho_0 = 1027$ kg m^{-3}, $h = 145$ metres and $\rho_a = 1.3$ kg m^{-3}. Mixing efficiencies for wind and tidal mixing were held constant at $\delta = 0.023$ and $e = 0.0037$, respectively. This was done as CCS was located in the centre of the seasonally stratifying Celtic Sea, which corresponds to same location where the well validated mixing efficiencies were originally empirically derived from (Simpson and Hunter, 1974; Simpson and Bowers, 1981). Without further analysis, no reason was identified to significantly change these in order to test the performance of SH74 at CCS. Since the ECMWF data had the lowest temporal resolution, $\Delta t = 3$ hours, all other data were interpolated onto the same time grid.

Using these data and constants the three forcing terms on the right hand side of Equation 2.16, i.e. heat ($\frac{\partial \Phi}{\partial t}_{\text{heat}}$), wind ($\frac{\partial \Phi}{\partial t}_{\text{wind}}$) and tidal stirring ($\frac{\partial \Phi}{\partial t}_{\text{tide}}$) were calculated for the entire time domain of 2014 and 2015 (Figure 5.1).

Throughout 2014 and 2015, $\frac{\partial \Phi}{\partial t}_{\text{heat}}$ constituted the dominant forcing term (Figure 5.1). The second most dominant term was $\frac{\partial \Phi}{\partial t}_{\text{wind}}$. However, this was only the case during winter months November-February (Figure 5.1) when wind speeds were high (Section 4.1.1). $\frac{\partial \Phi}{\partial t}_{\text{tide}}$ was the smallest forcing term overall, except for periods with low wind speeds such as during the summer months. As might be expected from the observed meteorological forcing described in Section 4.1, both $\frac{\partial \Phi}{\partial t}_{\text{heat}}$ and $\frac{\partial \Phi}{\partial t}_{\text{wind}}$ were characterised by a strong seasonal cycle (Figure 5.1), due to their dependence on Q_{net} (Equation 2.7) and the cube of the wind speed (Equation 2.15), respectively. Similar to the barotropic velocities (Figure 4.9), the tidal stirring term showed a clear spring-neap cycle, which was modulated by the interaction with the N_2 tide (Figure 5.1).

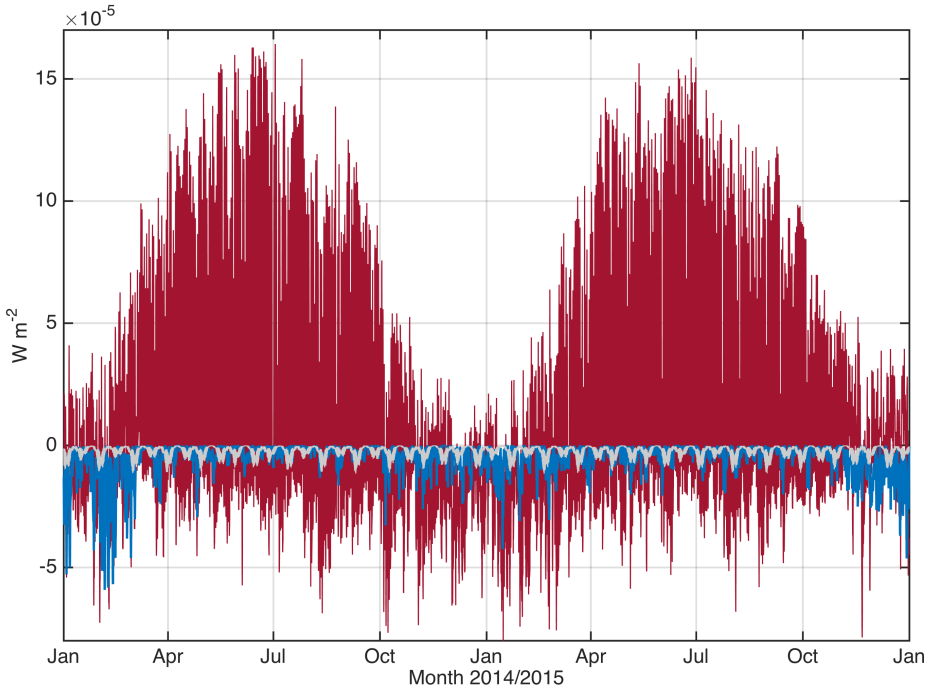

FIGURE 5.1: SH74 forcing terms [W m^{-3}]: $\frac{\partial \Phi}{\partial t}_{\text{heat}}$ (red), $\frac{\partial \Phi}{\partial t}_{\text{wind}}$ (blue) and $\frac{\partial \Phi}{\partial t}_{\text{tide}}$ (grey).

This modulation is accentuated by $\frac{\partial \Phi}{\partial t}_{\text{tide}}$ being dependent on the cube of the modulus of the complex barotropic velocities (Equation 2.9).

The additional modelled values introduced to SH74 for the meteorological forcing (ECMWF) and tidal forcing (obtained by harmonic analysis) provide further insight into conditions affecting CCS prior to and after the mooring deployment took place, which potentially explain some of the differences between the observed conditions in 2014 and 2015 (Section 4.3.4).

The period before observations began, winter 2013/2014, was classified as the stormiest within the last 20 years (Matthews *et al.*, 2014; Kendon and McCarthy, 2015). The period following the mooring recovery was characterised by particularly mild conditions, with winter 2015/2016 being reported as one of the warmest and wettest since records began in the UK (Barker *et al.*, 2016; McCarthy *et al.*, 2016). In good agreement with these UK wide observations, values of $\frac{\partial \Phi}{\partial t}_{\text{wind}}$ often exceeded 5×10^{-5} W

m^{-3} and averaged 1.3×10^{-5} W m^{-3} during January and February 2014, while values during January and February 2015 only averaged 7×10^{-6} W m^{-3} (Figure 5.1). The mild conditions in winter 2015/2016 resulted in $\frac{\partial \Phi}{\partial t}_{\text{heat}}$ being significantly higher during November and December 2015, than during the equivalent period in 2014. This suggests that the water column experienced fewer instances of convective instability at the end of 2015 than the year before.

5.1.2 Results SH74

Figure 5.2a shows the result of solving and integrating Equation 2.16 forward in time using the forcing terms shown in Figure 5.1 and a regular time step $\Delta t = 3$ hours. These model data are plotted alongside the observed strength in stratification at CCS (Φ_{obs}) for direct comparison. Overall, SH74 was able to predict the general behaviour of the seasonal cycle of stratification observed at CCS, however due to several failures the model only achieved a relatively low correlation coefficient of $R^2 = 0.5196$ (for the whole period). While this general behaviour of SH74 reflects the dominance of the vertical processes over horizontal processes, such as advection, which were not included in SH74, the model suffered from the following failures.

SH74 struggled to predict the timing of onset and breakdown of stratification accurately. The onset of stratification in 2014 was predicted to occur ~ 3 weeks earlier than observed, and stratification was eroded a month too late, compared to observations. In 2015, the timing of the onset of stratification was predicted accurately. However, SH74 suggested stratification would not have been broken down by the end of 2015. The magnitude of Φ_{SH74} at the end of 2015 was as strong as observed peak summer values of Φ in 2014. Even though winter 2015/2016 was considered anomalously warm (McCarthy *et al.*, 2016), such high stratification at the end of the year is unlikely.

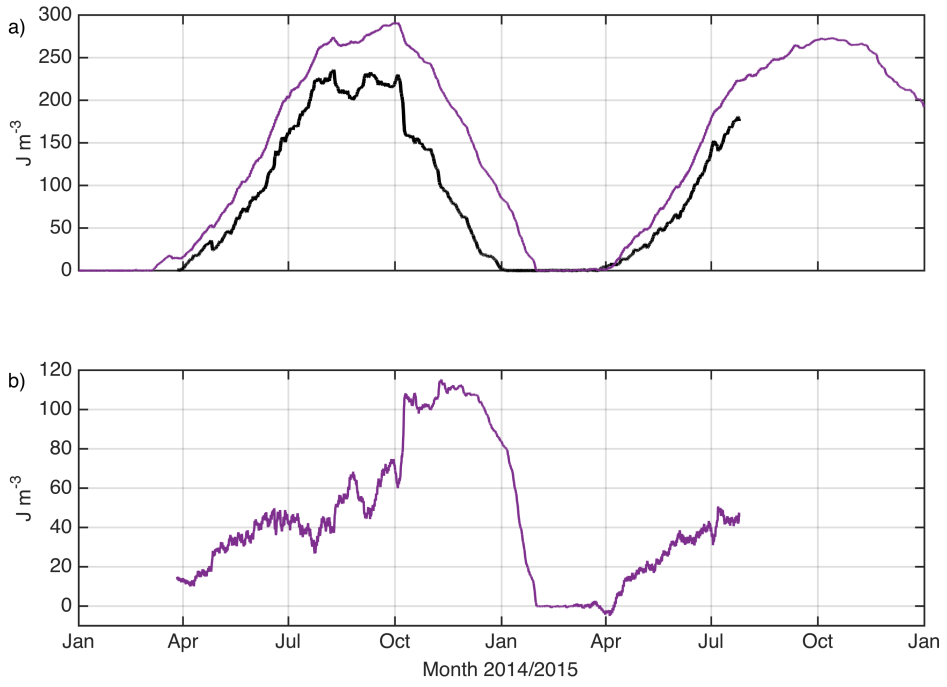

FIGURE 5.2: SH74 performance: a) 25 hr moving mean of Φ_{obs} (black) and Φ_{SH74} (purple) b) Φ_{SH74} - Φ_{obs} [J m^{-3}]

The model also appeared to perform poorly at capturing effects of short meteorological events. For instance, a spring storm in late April 2014 caused a decrease in Φ_{obs} of 12 J m^{-3} as a result of a strong wind event (Section 4.3.1), yet SH74 only predicted a decrease in Φ_{SH74} of 4 J m^{-3} (April 25th - 27th 2014). Another such event was the start of the breakdown of stratification in October 2014, when negative Q_{net}, high wind speeds and waxing spring tides coincided (Section 4.3.2). At this time, a decrease of $\approx$ 70 J m^{-3} was observed over a 7 day period, yet SH74 only predicted a decrease of 22 J m^{-3}.

It was also obvious that SH74 was unable to replicate the magnitude of Φ_{obs} correctly. The model overestimated Φ in both years during the summer months (Figure 5.2a) as stratification was gradually being accumulated at higher rates than was observed during this time. Figure 5.2b shows the difference in predicted and observed Φ, which accumulated steadily at a rate of 0.25 J m^{-3} d^{-1} (April 1st - September 30th 2014),

until it abruptly increased when the observed stratification started to break down in autumn 2014 (Section 4.3.2). In 2015, the difference between modelled to observed Φ (Figure 5.2b) increased at a rate of 0.34 J m^{-3} d^{-1} (April 1st - July 25th 2015). This increased rate potentially explains the high Φ_{SH74} at the end of 2015, compared to the predicted signal in 2014.

In summary, SH74 suffered from three major modes of failure: (1) Additional stratification was gradually being accumulated during the summer months. (2) Despite using observed forcing terms (Figure 5.1) SH74 responded insufficiently to sudden events of O(days). (3) SH74 predicted the timing of onset and breakdown of stratification inaccurately.

5.1.3 Discussion SH74

The lack of response to sudden events in both spring and autumn 2014 could be linked to a lack of surface forcing not currently included in SH74. A possible candidate mechanism is wave-driven mixing (e.g. Belcher *et al.*, 2012; D'Asaro, 2014). There are two ways by which surface waves can influence the surface boundary layer of the ocean. The most obvious one is wave breaking. While wave breaking is thought to be an important component affecting air-sea fluxes (Melville, 1996), its influence is restricted to a relatively shallow surface layer, as its vertical profile of dissipation decays within the length scale set by a few H_s away from the sea surface (D'Asaro, 2014). The second mechanism is caused by the interaction of the Stokes drift and vertically aligned vortices (which are created by a steady wind blowing over the sea surface) leading to instabilities, which is known as Langmuir turbulence (Langmuir, 1938; Craik and Leibovich, 1976; Thorpe, 2004). To investigate the influence of Langmuir turbulence on the surface mixed layer further, the turbulent Langmuir number, La_t, was calculated:

$$La_t = \left(\frac{w_*}{S_0}\right)^{1/2} \tag{5.1}$$

Where w_* [m s^{-1}] is the friction velocity (Equation 4.3) and S_0 [m s^{-1}] is the surface Stokes drift velocity. Webb and Fox-Kemper (2011) defined the surface Stokes drift as a function of H_s and T_p by:

$$S_0 = \frac{\pi^3}{g}\frac{H_s^2}{T_p^2} \tag{5.2}$$

La_t is a non-dimensional parameter proposed by McWilliams *et al.* (1997) to characterise surface regimes of turbulence, in the presence of both shear driven turbulence due to wind, and Langmuir turbulence due to waves. At $La_t \approx 0.3$ wind and waves are thought to be in equilibrium, and the sea state is often referred to as 'fully developed', i.e. the energy supplied to the ocean by the wind is balanced to the energy lost to wave field evolution and dissipation of TKE by breaking waves. Li *et al.* (2005) and Belcher *et al.* (2012) argue that at this equilibrium point, $La_t = 0.3$, Langmuir turbulence becomes important, whereas $La_t > 0.3$ implies the dominance of the wind forcing over wave driven turbulence. However, previous observational evidence has not been conclusive on the role of Langmuir turbulence deepening the surface mixed layer (e.g. Thorpe, 2004; D'Asaro, 2014; D'Asaro *et al.*, 2014).

During the entire observational period, La_t varied around an average of 0.30 ± 0.04 (1 std) at CCS. As can be seen from Figure 5.3, La_t displayed a weak seasonal signal, with monthly averaged values of $La_t > 0.3$ during the spring and summer months, compared to autumn and winter months when La_t was largely < 0.3. This change from the equilibrium state was most likely due to remotely generated swell propagating to the mooring site, something which was already noted in the seasonal signal of the wave conditions at CCS (Section 4.1.4).

While the long term average of $La_t = 0.30$ suggests that waves played an important role in deepening the surface mixed layer throughout the observational campaign, it is plausible to assume that the wind mixing efficiency, δ, already accounted for the wind and wave forcing during months wind and waves were in equilibrium, as it was empirically derived in such conditions (Simpson and Bowers, 1981). Hence for the majority

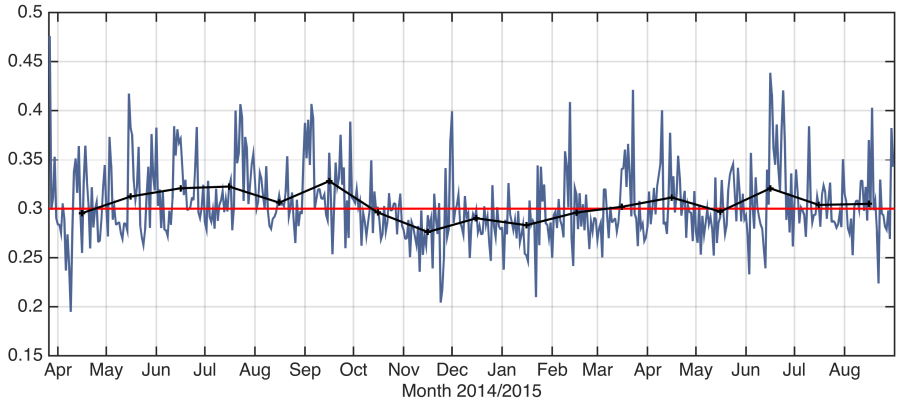

FIGURE 5.3: Turbulent Langmuir number, La_t, daily averaged (solid line), monthly averaged (black line with crosses). The red line marks $La_t = 0.3$, the equilibrium state of wind and waves.

of the stratified period 2014 and 2015, it seems reasonable to represent wind and wave forcing by just wind alone, as was done in the energetics model (Equation 2.16). In the autumn and winter months however, the relationship between wind and wave forcing broke down (Figure 5.3), due to remotely generated swell (Section 4.1.4). Here, $\frac{\partial \Phi}{\partial t}_{\text{wind}}$ might be insufficient and thus an additional source of mixing representing wave-driven turbulence may be required to fully represent the Φ budget at CCS.

The erroneously high levels of stratification predicted during both years suggests that either too much heat or insufficient levels of stirring were supplied to the water column. A simple way to allow less stratification to build up and hence improve the predictions, without including further sources of boundary driven PE, is by increasing the mixing efficiencies, thereby increasing the amount of available energy that supplies PE to the water column (Section 2.2.3).

To investigate whether it may be justified to increase the tidal mixing efficiency, e, the vertical extent of the bottom boundary layer, d, was compared to the depth of the main pycnocline. Here, only observed density and velocity measurements, presented in Chapter 4, were used. First, the depth of the main pycnocline was defined as the depth of the maximum value of N^2 [s^{-2}] at each time step (Equation 2.33). The combined boundary layer, d was calculated as the sum of the boundary thickness of clockwise and

anticlockwise motion, i.e. $d = d_+ + d_-$ (Prandle, 1982; Soulsby, 1983; Simpson and Sharples, 1994). The rotary current components of the barotropic velocity were calculated by splitting the results of a windowed FFT into positive (cyclonic) and negative (anticyclonic) frequency ranges (Thomson and Emery, 2014), similar to determining the rotary spectra of the depth averaged velocities (Section 4.2). Equation 2.59 was then used to calculate the individual boundary layers of the decomposed rotary currents using the local inertial frequency, f, at CCS, before they were combined to give d.

Figure 5.4 shows the vertical extent of the bottom boundary layer, d, compared to the depth of the main pycnocline (here depicted by the depth of maximum N^2). As could be expected from the earlier shown current record (Section 4.2), d is characterised by a strong spring-neap cycle that is modulated by the N_2 tidal constituent. The vertical extent of d only approaches the depth of the main pycnocline from summer 2014 onwards during strong peak tides until stratification is eroded in December. This suggest that the prevailing tidal currents at CCS are too weak to sufficiently erode any existing stratification. There is thus no physical basis to increase the tidal mixing efficiency, e, that modulates how effectively tidal mixing erodes any stratification within the water column, as tidal stirring potentially only provides a small fraction to the overall PE budget (Figure 5.4).

Clearly, tidal mixing keeps the bottom boundary layer vertically mixed throughout the year. However, an increase of PE in the water column only occurs if stratification is actively eroded, i.e. a contribution to the overall PE budget is only present if tidal stirring is actively eroding any existing stratification. The separation between the top of the bottom boundary layer d to the depth of maximum N^2 suggests that tidal stirring seems to only significantly supply PE to the water column once the pycnocline position has been sufficiently lowered towards the end of the stratified period (Figure 5.4). This had already been suggested during the introduction of the breakdown of stratification

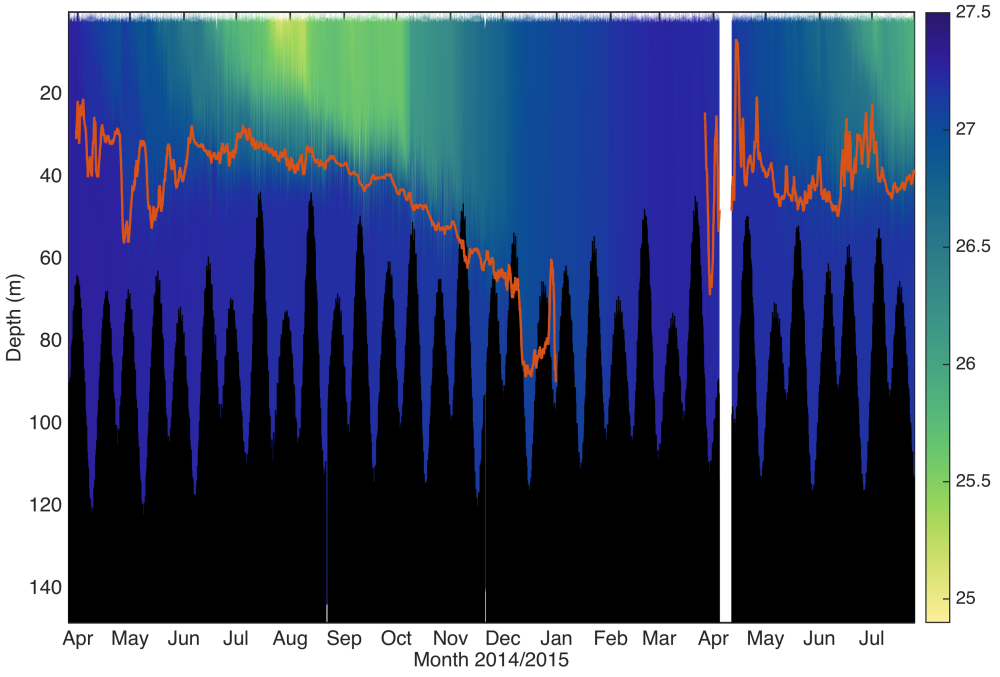

FIGURE 5.4: Observed vertical extent of bottom boundary layer, d (black) overlaid to observed potential density [kg m^{-3}]. Orange line marks depth of maximum N^2.

in autumn 2014 in Section 4.3.2. Considering the depth of the mooring site of $h \approx$ 145 metres and an average pycnocline depth of ∼50 metres, the tidal mixing efficiency, e, is therefore unlikely to be greater than originally proposed by Garrett *et al.* (1978); Simpson and Bowers (1981); Bowers and Simpson (1987). In fact, one could argue that the original fit of e, which was empirically derived based on observed frontal positions (Simpson and Bowers, 1981), is an over-estimation to predict the efficiency of tidal mixing away from areas of frontal movement, such as CCS. Here, the tidal mixing efficiency could potentially be lower. One of the reasons for this is that tidal fronts tend to occur in shallower water (80 - 100 metres), here the bottom boundary layer is sufficiently thick to actively erode stratification (Garrett *et al.*, 1978; Simpson, 1981). Furthermore, the lack of stratification on the mixed side of fronts does not restrict the vertical transfer of momentum, as is the case in stratified conditions. Stratification reduces the eddy viscosity, which in turn results in a decreased vertical extent of the boundary layer (Section 2.4.5).

This leaves the wind mixing efficiency, δ, to be increased to improve the fit. The efficiency values computed by Simpson and Bowers (1981) were derived from frontal positions observed in the Irish and Celtic Sea in summer 1987, which corresponds to the same area the observations presented in this thesis originated from. Instead of tuning δ to match the observations and thereby potentially fitting a result for the wrong reason, it was decided to look for alternative missing processes in the following sections.

5.1.4 Summary SH74

Using observed forcing terms (Figure 5.1), SH74 was able to predict the bulk sense of stratification, successfully replicating the general pattern of the seasonal cycle of Φ observed in 2014 and 2015 at CCS. This supports the hypothesis of Simpson and Hunter (1974); Simpson and Bowers (1984) that away from the influence of freshwater, stratification is to first order a vertical exchange process driven by the competition of buoyancy input versus stirring at the boundaries i.e. sea surface/bed. Considering the simplicity of this model, and how easily obtainable the main variables of net heat flux, wind and tidal speed are, this work confirms that SH74 can be a useful tool in determining the state of a water column with some confidence. However, its simplicity is also the reason for its main weakness. The main modes of failure within SH74 were found to be (1) higher than observed accumulation of strong stratification, (2) insufficient response to sudden meteorological forcing (3) poor timing of the onset and breakdown of stratification. By keeping this problem 0-dimensional, SH74 has no knowledge or memory of the vertical stratification, which in reality would lead to an adjustment of the PE sink and source terms. Without further investigating this problem in a 0D framework, the next section will deal with stratification at CCS using the 1-dimensional (1D) approach introduced as SB84 in Section 2.3.

5.2 1D approach - SB84

5.2.1 Model setup SB84

In order to test SB84 (Section 2.3) for the CCS location, SB84 was run to simulate the same 2 year period as SH74 (January 1st 2014 - December 31st 2015). To allow comparison between the performances of the two prescriptive models (SH74 and SB84), the same observed values of barotropic velocities, $\langle \boldsymbol{u} \rangle$, and meteorological forcing, i.e. w, Q_{sw}, Q_{u} (Equation 2.19), were used to force SB84, as were used to force SH74 earlier in this thesis (Section 5.1.1). Similarly, the same additional modelled and reanalysis data, respectively, were used outside of the observational date ranges of the ACP frame and the ODAS buoy deployment, explained in Section 5.1.1. This approach is thus different to the original setup of SB84 (Section 2.3.1), which parameterised Q_{u} as a function of modelled SST and fitted T_d (Equation 2.20) and used a sinusoidal fit to derive Q_{sw} (Equation 2.21). However, since w and the heat fluxes were taken or derived from observed values (Sections 3.5, 4.1), they were considered a preferable choice to the fitted alternatives proposed by Simpson and Sharples (2012).

The model grid was defined to have a depth $h = 145$ metres, with $n = 145$ vertical levels (bins) each 1 metre high (Δz) and time steps of $\Delta t = 24$ hours, and the model was thus forced with daily averaged values of tidal and meteorological forcing. The daily time steps were chosen as the emphasis of this research was on the seasonal cycle and hence SB84's performance replicating the diurnal heat cycle became less important. The variables in Equation 2.9 & 2.15 were kept constant as suggested by Simpson and Bowers (1984), i.e. k_b= 0.0025, $\rho_0 = 1027$ kg m^{-3}, $k_s = 6.4 \times 10^{-5}$ and $\rho_a = 1.3$ kg m^{-3}.

As described in Section 2.3 SB84 directly models the vertical temperature structure. It therefore requires an initial temperature profile, which was set to 9.65 °C based on the earliest and coldest measurements made in spring 2014. After the model run,

the density of the water column was computed using a fixed salinity of 35.5 g kg^{-1}, which corresponded to the average observed salinity at CCS (Section 4.3). While this simplification introduces a possible error by not accounting for salinity changes, these were observed to play only a minor role in defining density structure, as 99% of the variability in density was explained by the variability in temperature (Section 4.3).

The daily averaged forcing terms used to run SB84, are shown in Figure 5.5. While the shortwave heat flux, Q_{sw}, displayed a typical seasonal cycle, Q_u was particularly high at the end of 2015 (Figure 5.5a), most likely linked to the conditions associated with the mild winter 2015/2016 (McCarthy *et al.*, 2016). As expected, both δP_W (Figure 5.5b) and eP_T (Figure 5.5c) were closely linked to the observed wind speed (Section 4.1.1) and tidal velocities (Section 4.9). Similar to $\frac{\partial \Phi}{\partial t}_{\text{wind}}$ within SH74 (Figure 5.1), eP_T rarely exceeded δP_W.

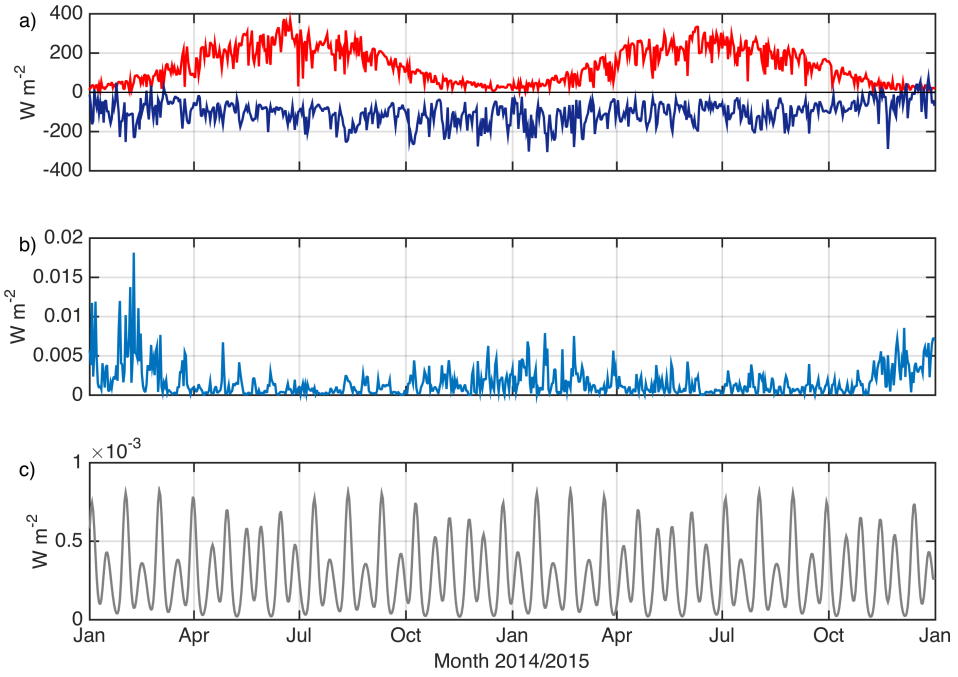

FIGURE 5.5: SB84 forcing terms [W m^{-2}] a) Q_{sw} (red) and Q_u (dark blue) b) δP_W (blue) c) eP_T (grey).

5.2.2 Results: SB84

Figure 5.6a shows the results from SB84 (Φ_{SB84}) alongside observations (Φ_{obs}) and model results from the previous 0D model, SH74 (Φ_{SH74}, Section 5.1.2). SB84 replicated the seasonal cycle of Φ_{obs} well ($R^2 = 0.88$ for the whole period), and was able to better predict the timing of onset and breakdown of stratification compared to SH74 (Figure 5.6a). Similar to SH74 (purple line Figure 5.6a), SB84 also overestimated stratification in both years, particularly during summer and early autumn. In fact, SB84 appeared to have suffered from similar problems as SH74 (Section 5.1.2), i.e. accumulation of additional stratification during spring and summer, and insufficient response to sudden meteorological forcing, albeit to a lesser degree.

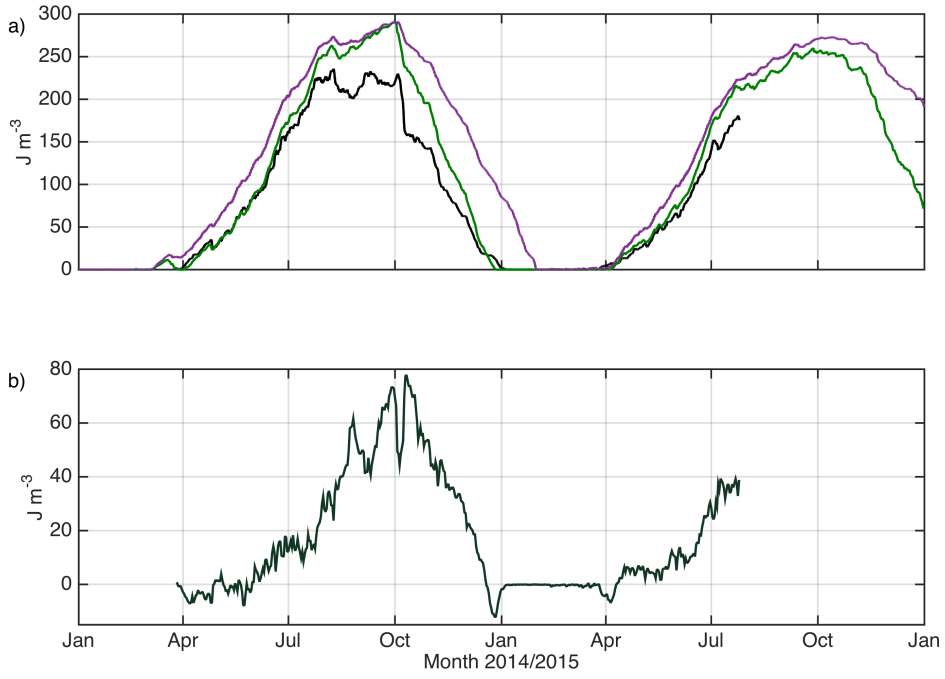

FIGURE 5.6: SB84 and SH74: a) Φ [J m^{-3}] observations (black), SH74 (purple) and SB84 (green) b) Φ_{SB84} - Φ_{obs} [J m^{-3}].

Surprisingly, both models predicted peak values of $\Phi_{SH74\ \&\ SB84} \sim 290$ J m^{-3} around October 1st 2014. Furthermore, SB84 also agreed with SH74 that stratification would not have been completely eroded by the end of 2015 (Figure 5.6a), although the final

value in SB84 in 2015 is less than half that of SH74 and is rapidly approaching mixed conditions, which seems a more plausible result. Here, SB84 predicted $\Phi \sim 75$ J m^{-3} at the end of 2015, which was comparable to levels of Φ_{obs} at the beginning of December 2014, and thus roughly one month away from complete breakdown of stratification in 2014 (see Section 4.3). Interestingly, SB84 predicted a brief period of stratification before the observational campaign even began in March 2014 (Figure 5.6a) that observations agree was mixed out prior to the deployment date. SH74 however erroneously predicted this event to be the onset for seasonal stratification in 2014.

Between April and June in both years, SB84 stratified at roughly the same rate as the observations (1.23 vs. 1.30 J m^{-3} d^{-1}), which is also evident by the near constant difference between Φ_{SB84} and Φ_{obs} during this time (Figure 5.6c). After this period, the difference between Φ_{SB84} and Φ_{obs} accumulated at 0.56 J m^{-3} d^{-1} during June 1st - September 30th 2014, and at 0.66 J m^{-3} d^{-1} during June 1st - July 25th 2015, which potentially explains the overestimation of Φ in the summers of both years.

Figure 5.7a-b shows the observed and predicted full depth temperature time series for comparison. SB84 replicated the overall temperature structure observed at CCS well (Figure 5.7c), however it was unable to vertically distribute the heat realistically. During both years, SB84 retained too much heat within the surface boundary layer compared to the observations (Figure 5.7a-c). During August 2014, SB84 predicted near-surface temperatures of up to 22.75°C compared to the maximum observed near-surface temperatures of $\sim$ 20.3°C. Similarly in July 2015, SB84 predicted peak temperatures of 20.3°C at the sea surface, almost 2°C higher than was observed during this time. The lack of vertical heat distribution can also be seen by the sharp thermocline predicted by SB84 (Figure 5.7b) and the lack of heat being transferred into the bottom boundary layer (Figure 5.7d). Between April and December 2014 the observed near bed temperature increased at 0.074°C d^{-1} compared to the predicted rate of 0.0027°C d^{-1}. The near bed temperature predictions only matched the observations in January 2015, when SB84 equilibrated surface and near-bed temperatures due to

complete breakdown of stratification. In contrast to the observed near bed temperatures, which only started to increase again in mid-April 2015, SB84 predicted near bed temperatures to start rising in March 2015. This discrepancy was only observed in 2015, as the initial profile was carefully tuned to match the March profiles in 2014.

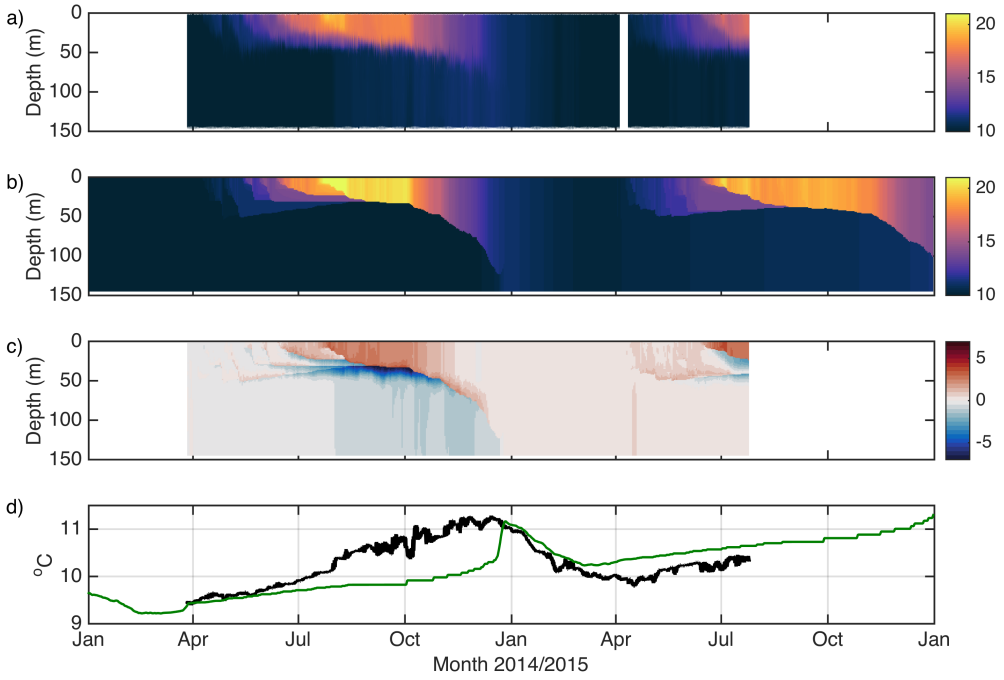

FIGURE 5.7: Temperature [°C]: a) observations b) SB84 results c) SB84 temperature difference to daily averaged observations [°C] d) near bed temperature: observations (black) and predictions (green)

Despite SB84 including an improved consideration of physical process controlling stratification than SH74, SB84 still overestimated stratification in both years (Figure 5.6). The most probable cause for this is its poor vertical heat distribution. While the observed thermocline is rather diffuse and several metres deep (Figure 5.7a), the modelled thermocline only spanned a maximum of 10 metres between August and the beginning of October 2014 (Figure 5.7b), which is also when the biggest difference in predicted and observed Φ (Figure 5.6b), and bed temperatures (Figure 5.7d) were noted.

The diffuse nature of the observed thermocline is often considered to be indicative of internal mixing processes (Rippeth, 2005; Green *et al.*, 2008; Simpson and Sharples, 2012), a potential PE source term currently unaccounted for in the boundary driven model, SB84. Internal mixing processes, especially those driven by internal waves, have been documented extensively in the Celtic Sea and other temperate shelf seas around the world (e.g. Holloway, 1994; Sharples *et al.*, 2001; MacKinnon and Gregg, 2003b; Moum *et al.*, 2008). Observations of vertical density structure (Section 4.3) and S^2 (Section 4.2) at CCS also suggested evidence of an active internal wave field at CCS, which will be further investigated in Section 6.1.

Whether the consideration of internal mixing processes within SB84 will improve the predictions will be further examined in Section 5.2.3.3, after the dominant boundary driven forcing terms are explored in more detail.

5.2.3 Discussion SB84

5.2.3.1 Importance of tidal mixing

Despite CCS seemingly behaving as described by the energetics model presented in Chapter 2, it was already noticed in Section 4.3.1 and Section 4.3.3 that the onset of stratification at CCS did not necessarily coincide with the lowest tidal speeds, as could be expected from the energetics balance (Equation 2.16). In fact, during the onset of stratification in spring 2014 (Section 4.3.1), tidal amplitudes were increasing to their fortnightly maxima, i.e. spring tides. This is in contrast to observations made in the North Sea, where the suggestion was made that stratification most likely to develop as tides reduced towards neaps, however these observations were made in a much shallower water column of depth $h = 60$ metres (Sharples *et al.*, 2006). Furthermore, it was shown in Section 5.1.3, that the boundary layer d might only supply PE towards the end of the year, when the pycnocline deepened sufficiently to overlap the bottom

boundary layer (Figure 5.4). This raised the hypothesis that the depth of the CCS site reduces the impact of the tide on stratification (Section 5.1.3).

To test this hypothesis, SB84 was forced with tidal velocities removed, and thus P_T (Equation 2.9) set to 0 J m^{-3}, while all other forcing terms were kept unchanged (Figure 5.5). The results of this run, SB84$_\mathrm{T}$, are shown in Figure 5.8. For comparison the results of SB84 (Φ_{SB84}) have also been overlaid. SB84$_\mathrm{T}$ replicated the seasonal cycle of Φ_{obs} surprisingly well ($R^2 = 0.64$ for the whole period). While the lack of tidal stirring input, P_T, was expected to lead to an increase in the overall magnitude of $\Phi_{\mathrm{SB84_T}}$, the timing of the onset of stratification in 2014 and 2015 was not affected (Figure 5.8a). The overall increase in magnitude of Φ however, which peaked at the end of each year, led to a delayed breakdown of stratification compared to the observed timing by $\sim$ 1 week in 2014. $\Phi_{\mathrm{SB84_T}}$ at the end of 2015 was predicted to be $\sim$ 50 J m^{-3} greater than Φ_{SB84}.

Compared to the observed vertical temperature structure (Figure 5.8b) and the earlier SB84 prediction (Figure 5.7b), the overall seasonal cycle was well replicated by SB84$_\mathrm{T}$ (Figure 5.8c). Like SB84, SB84$_\mathrm{T}$ also suffered from too much heat retention in the surface, which was only slightly greater than near-surface temperatures predicted by SB84, reaching 22.88°C compared to peak SB84 temperatures of 22.75°C (Section 5.2.2). While the lack of tidal stirring clearly affected the thickness of the thermocline, its main shape and location were replicated reasonably well by SB84$_\mathrm{T}$ compared to the observations (Figure 5.8d), which suggests that overall tidal stirring might not be a significant PE source at CCS.

To study the contribution of tidal stirring ($\int \frac{\partial \Phi}{\partial t}_{\mathrm{tide}} dt$) [J m^{-3}] to the overall Φ budget in more detail, daily values of all three forcing terms were derived as a difference in Φ of the vertical ρ profile before and after each term was applied using Equation 2.1. Similar to the buoyancy production term, $\boldsymbol{B}$ in the TKE equation (2.31), the $\int \frac{\partial \Phi}{\partial t}_{\mathrm{heat}} dt$ can

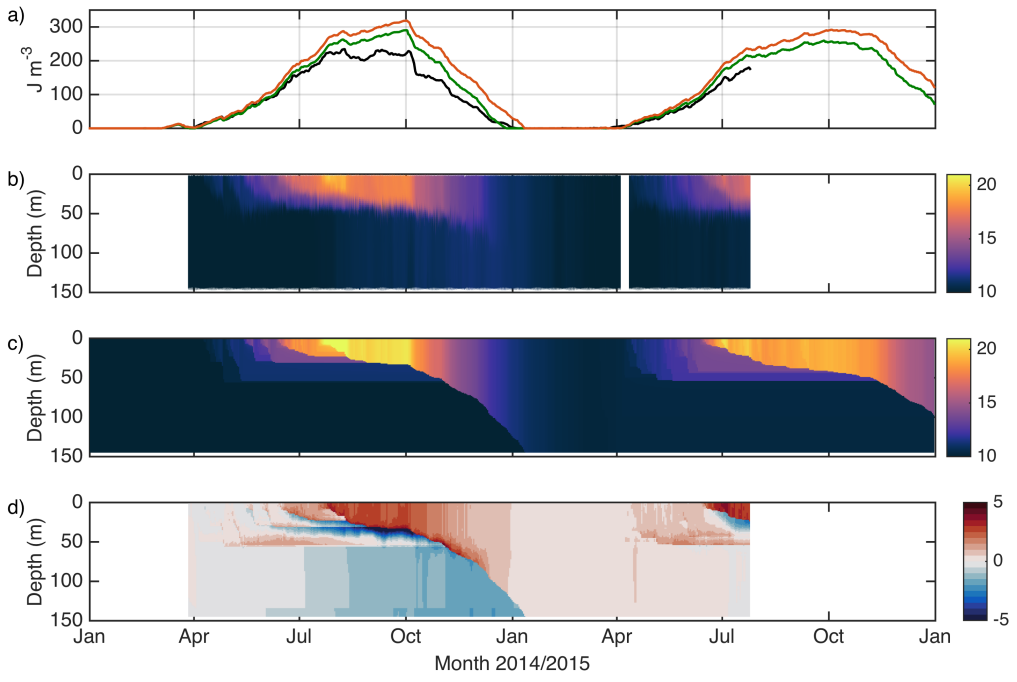

FIGURE 5.8: $SB84_T$ a) Φ [J m^{-3}] observations (black), SB84 (green). $SB84_T$ (orange). Temperature [°C] b) observations c) $SB84_T$ predictions. d) $SB84_T$ temperature difference to daily averaged observations [°C].

supply or reduce Φ, as it is either promoting stable stratification or convective overturning due to heat loss to the atmosphere. Whereas $\int \frac{\partial \Phi}{\partial t}_{\text{wind}} dt$ and $\int \frac{\partial \Phi}{\partial t}_{\text{tide}} dt$ are representative of the TKE production term, $\boldsymbol{P}$, and thus can only erode stratification and thereby reduce Φ. In agreement with the magnitude of the forcing terms (Figure 5.1), $\int \frac{\partial \Phi}{\partial t}_{\text{tide}} dt$ accounted for the smallest contribution to the overall Φ budget. In both years $\int \frac{\partial \Phi}{\partial t}_{\text{tide}} dt$ contributed only 5% to the overall Φ budget, while $\int \frac{\partial \Phi}{\partial t}_{\text{heat}} dt$ amounted to the largest contribution of 65% in 2014, which decreased to 58% in 2015. In correspondence with this shift, the contribution of $\int \frac{\partial \Phi}{\partial t}_{\text{wind}} dt$ increased from 29% during 2014 to 36% during 2016.

This result contradicts Simpson and Hunter (1974); Simpson *et al.* (1978) and Simpson and Bowers (1984) conclusion to some extent, who considered tidal mixing the dominant control on the vertical water column structure. However, their results particularly focused on frontal regions. As already mentioned in Section 5.1.3, frontal regions are

characterised by thick bottom boundary layers, where stratification is actively being eroded. Away from frontal regions in sufficiently deep water, such as at CCS, the effect of tidal mixing on the overall water column structure is shown here to be much reduced, due to the distance of the pycnocline from the bottom boundary layer for most of the stratified period (Figure 5.4). While CCS was clearly portraying characteristics of a seasonally-stratifying shelf sea site, with clearly defined upper and lower mixed layers separated by a seasonal pycnocline of O(20 metres) thickness, the controls on vertical density structure were largely analogous to that of the open-ocean (Kraus and Turner, 1967; Waniek, 2003) rather than the tidally dominated system described by Simpson and Hunter (1974); Simpson *et al.* (1978). In fact, it is only its relatively shallow depth that made CCS completely mix regardless of whether tidal mixing is present (Figure 5.7b) or not (Figure 5.8c), as surface forcing appears sufficiently strong to cause a complete breakdown of stratification within each seasonal cycle. While the positions of frontal regions are closely dependent on the parameter χ (Section 2.2), away from frontal regions surface forcing dominates, which is a clear shift from the often quoted paradigm of the water column structure in temperate shelf seas proposed by Simpson and Hunter (1974). This suggests that an additional third regime is required that connects the tidally dominated Simpson-Hunter (Simpson and Hunter, 1974) regime to the open-ocean Kraus-Turner (Kraus and Turner, 1967), regime.

5.2.3.2 Importance of wind mixing

To further study the importance of wind mixing, SB84 was also run with wind mixing term (Equation 2.15), $P_W = 0$ J m^{-3}, while the remaining forcing from tides and heat flux were kept unchanged to SB84 (Figure 5.5a, c). The results of this run, SB84$_{\mathrm{W}}$, are shown in Figure 5.9. For comparison the results of SB84 (Φ_{SB84}) have been overlaid.

Setting $P_W = 0$ J m^{-3} leads to complete failure in replicating the seasonal cycle of Φ_{obs} ($R^2 = 0$ for the whole period), which was expected considering that wind was the

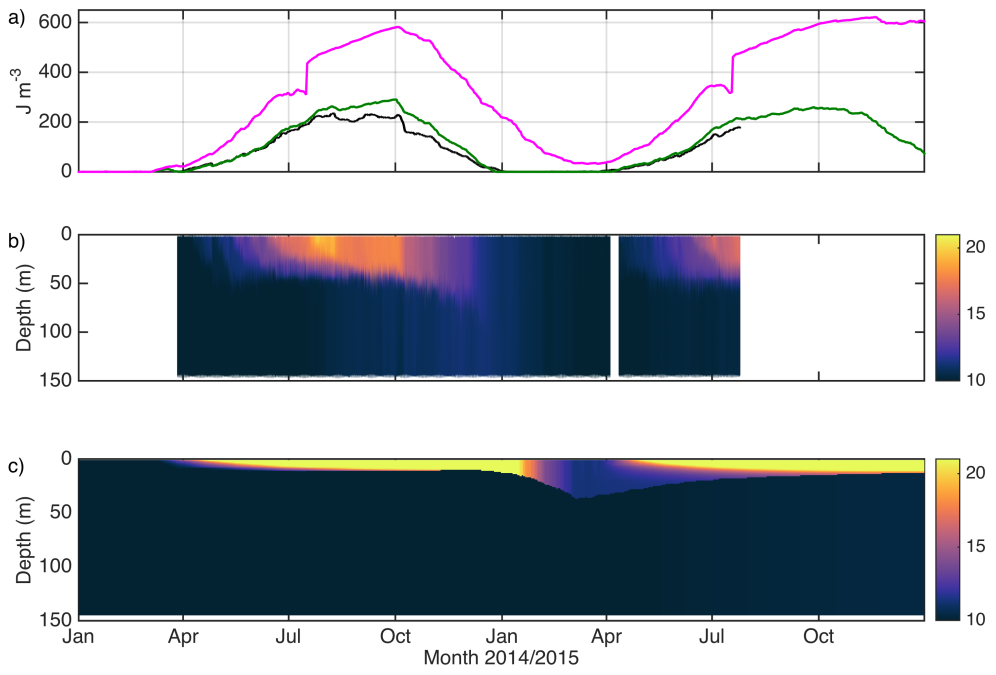

FIGURE 5.9: $SB84_W$ a) Φ [J m^{-3}] observations (black), SB84 (green). $SB84_W$ (pink). Temperature [°C] b) observations c) $SB84_W$ predictions.

second most important contributor to the overall Φ budget in SB84 (Section 5.2.3.1). While the overall shape of Φ_{SB84_W} displayed a seasonal signal (Figure 5.9c), the lack of P_W resulted in $SB84_W$ accumulating an unrealistic amount of heat in the near surface (>100°C), and the pycnocline only extended to a depth of 10 metres during summer 2014 and 2015. Two clear examples of this occur during July of both years, when a step-like increase in Φ was observed O(100) J m^{-3} (Figure 5.9c). This excess heat was retained within only the near surface layer, which promoted a prolonged period of increasing stratification that lasted for a number of months during both years, but is not replicated in the observations. Subsequently, stratification in $SB84_W$ never completely broke down and Φ_{SB84_W} only reached minimum values of 35 J m^{-3} by March 2015, before stratification was re-established in April 2015 (Figure 5.9a). Negative Q_{net} in early October then changed the polarity of $\frac{\Delta\Phi_{SB84_W}}{\Delta t}$ (not shown) in early October, in agreement with the observed start of the breakdown of stratification (Section 4.3.2). Negative Q_{net} resulted in loss of heat and eventual deepening of the

pycnocline to a maximum depth of 37 metres, which coincided with some of the coldest fully mixed conditions at CCS (Figure 5.9b). The poor timing and overestimated heat retention within $SB84_W$ certainly confirms that wind mixing is a key component driving vertical heat distribution, and thus SML deepening throughout the year. The previously discussed step-like increases during July introduced a greater amount of Φ that was observed as the winter minimum in $SB84_W$ (March 2015), suggesting that stratification resulting from the observed heat flux could not have been broken down without wind mixing.

As previously discussed in Section 4.3.2, autumn 2014 was characterised by the arrival of winter storms, which eventually led to the complete breakdown of stratification at CCS (Section 4.3.2). During the breakdown period 2014 strong negative heat fluxes rarely occurred in isolation from strong wind forcing, as the heat exchange with the atmosphere is intrinsically linked to the wind speed (see Equations 2.44 and 2.45). Following these observations, an attempt was made in Section 4.3.2.1 to determine wether the breakdown of stratification in 2014 was driven by shear driven processes caused by wind stress, or by convective mixing due to buoyancy reduction initiated by negative heat fluxes using the Obukhov length scale, L_{OB} (Equation 4.2) (Obukhov, 1946). This analysis suggested a potentially significant result that during the autumnal breakdown of stratification, wind was the dominant SML deepening mechanism. However, due to wind and convection both acting to erode the SML, it was difficult to distinguish their contribution conclusively. It was thus suggested to further study wind and convection during the breakdown of stratification in isolation using the SB84.

As demonstrated in Figure 5.9, setting $P_W = 0$ J m^{-3} led to complete failure, partly due to retention of legacy heat within the SB84 framework (Section 2.3.1). Furthermore, in order to return to colder sea water temperatures during winter, a heat loss to the atmosphere is clearly required. By only changing P_W or $\mathrm{Q_{net}}$ once stratification was observed to start breaking down, the contribution of each event was easier to study. Thus the model was run again with P_W (Equation 2.9) or $\mathrm{Q_{net}}$ (Equation 2.18) set to

0 J m^{-3} from Julian Day 274 (1^{st} October) onwards, which corresponds to the start of the breakdown of stratification in 2014 (Section 4.3.2), while the remaining forcing terms were kept unchanged (Figure 5.5). The results of those runs are referred to as $SB84_{WB}$ (breakdown solely driven by Q_{net}) and $SB84_{QB}$ (breakdown solely driven by wind), respectively, and are shown in Figure 5.10. For comparison the results of SB84 (Φ_{SB84}) have also been overlaid.

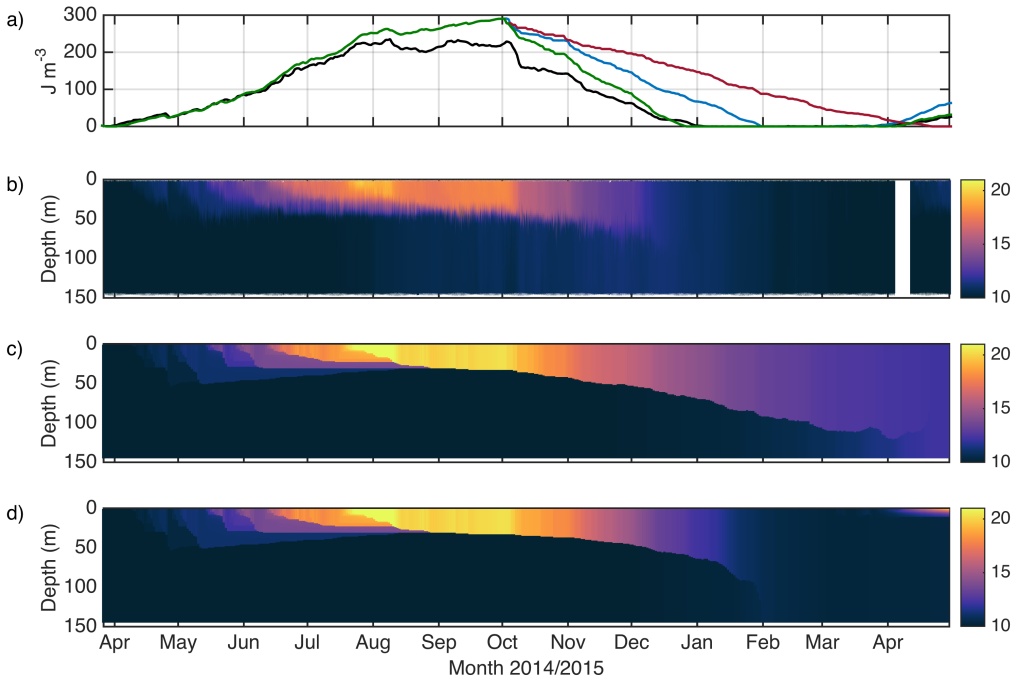

FIGURE 5.10: Onset and breakdown of stratification 2014 a) Φ [J m^{-3}] observations (black), SB84 (green). $SB84_{QB}$ (red) $SB84_{WB}$ (blue). Temperature [°C] b) observations c) $SB84_{WB}$ d) $SB84_{QB}$ predictions.

Figure 5.10a demonstrates that all variations of SB84 were identical until either P_W or Q_{net} was set to 0 J m^{-3} after and including Julian Day 274. $SB84_{QB}$ (red in Figure 5.10a) took the longest time to completely break down. Surface and bed temperatures did equilibrate at the end of April 2015 (Figure 5.10d), however temperatures were 2.5°C warmer than observed (Figure 5.10b), which is easily explained by the lack of heat loss to the atmosphere. If however, the breakdown was solely driven by Q_{net}, $SB84_{WB}$ retained too much heat in the surface layer (Figure 5.10c) compared to the

observations (Figure 5.10b), and thus breakdown was delayed until the end of January 2015 (blue in Figure 5.10a).

These results suggest that the presence of both convection and wind stirring are important to accurately reproduce vertical heat distribution and thus the timing of breakdown realistically. Particularly, convection can act to better connect surface mixing processes with the stratified interior by homogenising the surface boundary layer, supporting further breakdown of seasonal stratification. Further, the dependence of both Q_{sen} (Equation 2.44) and Q_{lat} (Equation 2.45) on the wind speed, w, ensures that Q_{net} can never act fully decoupled from the wind forcing.

5.2.3.3 Addition of an internal source of PE

At the end of Section 5.2.2, it was noted that one of the main reasons for SB84 to fail to reproduce the seasonal cycle in Φ was caused due its poor distribution of heat in the vertical. Without including any further boundary driven sources of PE or arbitrarily increasing mixing efficiencies, this poor distribution could be attributed to the lack of an internal source of PE. Observations of an active internal wave field had been previously observed in this study area (Pingree *et al.*, 1982; Palmer *et al.*, 2008; Inall *et al.*, 2011), and the newly collected observations also suggested the presence an active internal wave field at CCS (Section 4.3). It can therefore be hypothesised that this unrealistic distribution of heat in the vertical could be improved by the addition of an internal PE source.

In order to include an internal source of PE as a means of parameterising internal wave mixing within SB84, a few assumptions must be made. Firstly, it is assumed that the internal PE will be generated by shear driven mixing due to internal wave activity. Secondly, given the predominately low mode structure of internal waves that have previously been observed in the Celtic Sea (Palmer *et al.*, 2008; Hopkins *et al.*, 2014), and

other shelf seas (Sharples *et al.*, 2001; MacKinnon and Gregg, 2003a; van der Lee and Umlauf, 2011), any associated internal mixing would act on the main pycnocline, where N^2 is strongest. Furthermore, since mixing is prescribed within SB84 (Section 2.3), it was unsuitable to simply set a constant background eddy diffusivity and viscosity, which is considered the most basic approach to parameterising internal wave mixing (e.g. Section 2.4.3). However, in a similarly basic way, a constant source of PE was added internally, PE_{int}, supplying PE directly to the main pycnocline. Hereafter model runs of SB84 that included an internal PE source will be referred to as $SB84_{int}$.

During the initialisation of $SB84_{int}$, a fixed value of ε [W m^{-3}] is set, which is then multiplied by an internal mixing efficiency of 0.2, akin to the mixing efficiency, Γ, empirically derived by Osborn (1980). Before any mixing takes place in the model, the main pycnocline location is found at each time step by searching for the vertical level (bin) containing the maximum value of N^2 [s^{-2}] (Equation 2.33), and its two surrounding bins (one bin above and one below the bins containing maximum N^2). Similarly to the stirring input by tide and wind within SB84 (Section 2.3.1), the influence of PE_{int}, i.e. the number of bins which would be mixed, depend on the existing stratification (Φ) and the available energy, i.e. PE_{int}. The amount of PE gained by the water column at each time step is equivalent to the effective stirring energy input by internal mixing, PE_{int}. If less than the available PE is used for mixing at each time step, than this remaining PE is carried over to the next time step, unless the water column is already fully mixed.

To test the effectiveness of the addition of an internal PE source, $SB84_{int}$ was run using the same boundary forcing used for SB84 (Figure 5.5), and background values of ε [W m^{-3}] typically found within pycnoclines of temperate shelf seas. These range from $1 \times 10^{-6} - 2 \times 10^{-3}$ W m^{-3} (Sharples *et al.*, 2001; MacKinnon and Gregg, 2005b; Williams *et al.*, 2013; Palmer *et al.*, 2013). Figure 5.11 shows the results of a selection of runs using low, medium and high values of $\varepsilon_l = 5 \times 10^{-6}$ W m^{-3}, ε_m

$= 1 \times 10^{-5}$ W m^{-3} and $\varepsilon_h = 2 \times 10^{-5}$ W m^{-3}, marked as SB84$_{\text{int}_l}$, SB84$_{\text{int}_m}$, and SB84$_{\text{int}_h}$, respectively.

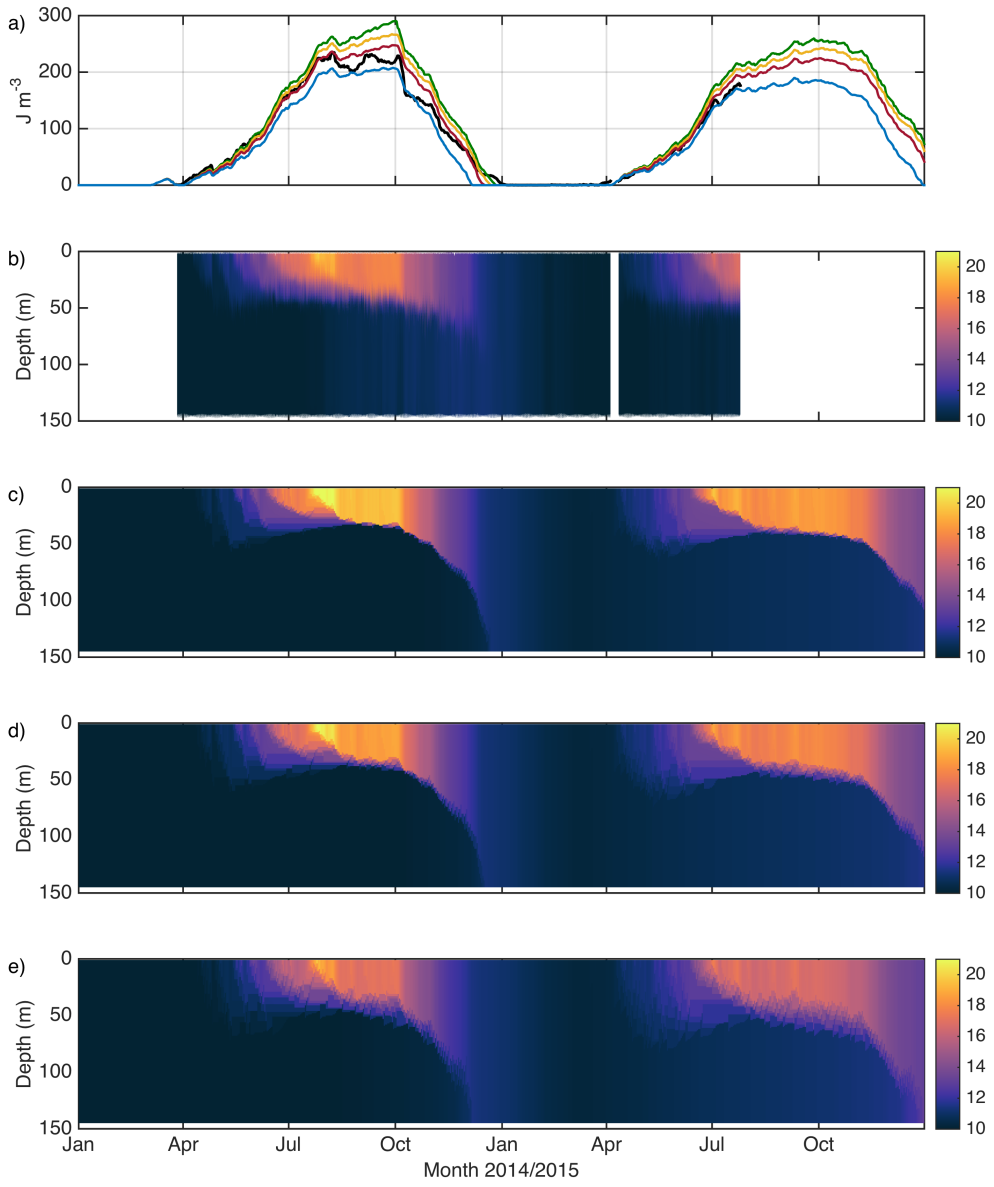

FIGURE 5.11: SB84$_{\text{int}}$: a) Φ [J m^{-3}] observations (black), SB84 (green), SB84$_{\text{int}_l}$ (yellow) SB84$_{\text{int}_m}$ (red) SB84$_{\text{int}_h}$ (blue). Temperature [°C]: b) observations c) SB84$_{\text{int}_l}$ d) SB84$_{\text{int}_m}$ e) SB84$_{\text{int}_h}$.

Figure 5.11a shows the performance of $SB84_{int}$ ($\Phi_{SB84_{int}}$) alongside the observed strength of stratification at CCS (Φ_{obs}) and the previous solely boundary-driven run, SB84 (Φ_{SB84}). The reduction in $\Phi_{SB84_{int}}$ was evident compared to Φ_{SB84} and further declined, as might be expected, with increasing levels of ε. The timing of the onset of stratification in both 2014 and 2015 was unaffected by the level of internal PE supplied. The breakdown of stratification in both years, however, was clearly tightly linked to values of ε. The best simulation producing a correlation coefficient of $R^2 = 0.98$ (for the whole period) was found using $\varepsilon_m = 1 \times 10^{-5}$ W m^{-3}. The correlation did differ slightly if the years were considered separately. While the best fit of $R^2 = 0.96$ was achieved using ε_m in 2014, the higher value of $\varepsilon_h = 2 \times 10^{-5}$ W m^{-3} in 2015 produced the best fit solution, with R^2=0.99. The impact of this higher value on the timing of the breakdown of stratification, which was shown to have the largest error, could not however be tested due to the length of the observations.

The values of ε, for which the best fits were achieved, were in the lower range of the observed pycnocline values of ε, which can reach one or two magnitudes higher. This is probably due to the fact that CCS is representative of a more quiescent site, away from topographic features that could enhance ε, such as observed around banks (e.g. Palmer *et al.*, 2013), or close to the shelf break (e.g. Sharples *et al.*, 2001; Green *et al.*, 2008). Furthermore, since this value is applied constantly, it should be considered a long-term average and thus does not include some of the higher, sporadic values typically associated with pycnocline turbulence in shelf seas.

The effects of adding a source of internal PE on the vertical temperature distribution are evident when comparing the results of $SB84_{int}$ to the observations (Figure 5.11b-e). Increasing ε leads to a more realistic vertical heat distribution in the summer months, which thus improves the predicted surface temperatures by distributing surface heat deeper into the water column (Figure 5.12a).

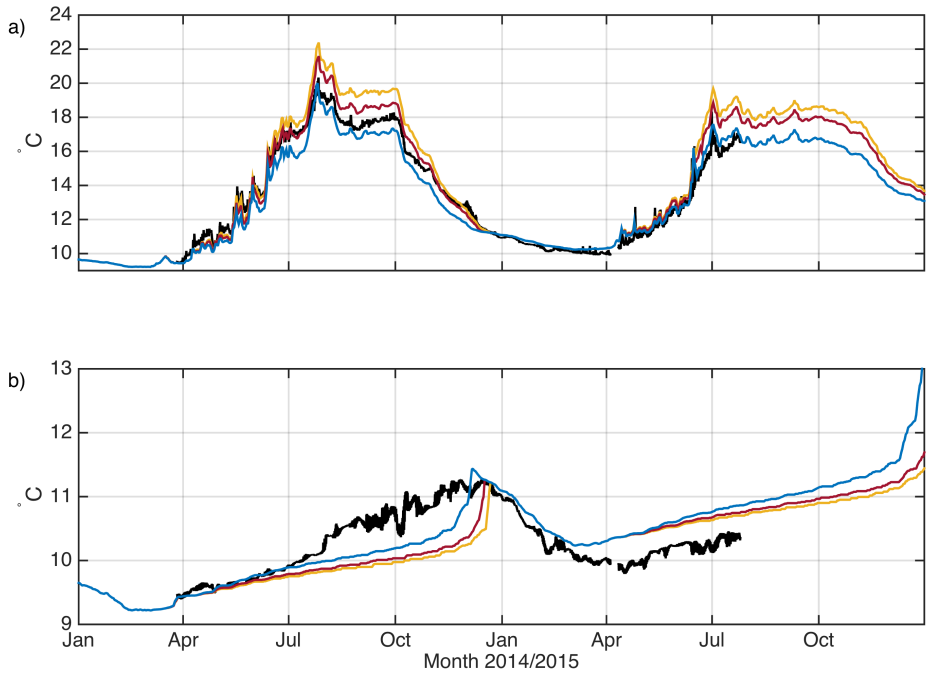

FIGURE 5.12: Temperature [°C] a) near-surface and b) near-bed, observations (black), $SB84_{int_l}$ (yellow) $SB84_{int_m}$ (red) $SB84_{int_h}$ (blue).

It is also apparent, however, that despite improved vertical heat distribution, there is still not enough heat being fluxed into the near-bed region in the summer months (Figure 5.11b). While at the same time, every increase in ε leads to the breakdown of stratification being advanced too quickly (Figure 5.11a), and the thermocline in spring being driven too deep (Figure 5.11d-e).

While the method used here to add internal mixing into the prescriptive mixing model SB84 is somewhat arbitrary it is analogous to the modifications to mixing efficiencies that Simpson and Bowers (1981) implemented when tuning SH74 to spring-neap adjustments (Section 2.2.4). It should thus be considered a first proof-of-concept of the need to include interior mixing in SB84 in order to replicate the vertical density structure more realistically. Furthermore, by supplying amounts of energy to midwater mixing, which are similar to those known to exist within shelf sea environments

(Sharples *et al.*, 2001; MacKinnon and Gregg, 2005b; Williams *et al.*, 2013; Palmer *et al.*, 2013), removes some of the arbitrariness of this method.

These results suggest that including a constant source of internal PE certainly improves the predictions of Φ by redistributing heat more realistically. However, they also suggest that a constant supply results in a seasonal discrepancy, which causes too little mixing during strongly stratified periods and too much mixing during periods with weak stratification. This in turn suggest that internal mixing at CCS has a seasonal cycle with the greatest effect in summer months and the least during transitional periods of stratification. This seasonality of internal mixing had been previously predicted to occur in the Clyde Sea (Simpson and Rippeth, 1993). Observational evidence presented by Cottier *et al.* (2004) revealed that the internal wave field in the Clyde Sea was tied to the state of the water column, as the energy within the internal wave field ceased when stratification was completely eroded. Cottier *et al.* (2004) did however not find any evidence of a clear seasonal cycle within the internal wave field, which strengthened during strongly stratified periods in the Clyde Sea. To investigate whether a seasonal cycle is evident within the internal wave field at CCS, the long-term observations of density and velocity structure will be further explored in the following Chapter 6.

5.2.4 Summary: SB84

Using observed forcing terms (Figure 5.5), SB84 provided an improved prediction of the seasonal cycle of Φ (Section 5.2.2), compared to SH74 (Section 5.1.2). While SB84 still overestimated Φ, it was able to improve on the SH74 predictions of the timing of the onset of stratification in 2014 and 2015 and breakdown of stratification in 2014. SB84 suffered from a poor vertical distribution of heat, which was attributed to the lack of an internal source of PE from a constantly energetic internal wave field at CCS. Exploiting the simplicity but also functionality of SB84, the importance of wind

and tidal stirring was then investigated in Section 5.2.3. Surprisingly, tidal mixing was found not to be a leading term controlling stratification at CCS, which suggests that away from shallow or frontal regions, the control on the vertical density structure is more analogous to that of the open-ocean than tidally dominated coastal regions (Section 5.2.3.1). Furthermore, by focusing on the 2014 autumn period, it was shown that both convection and wind driven mixing were important to fully break down stratification (Section 5.2.3.2). The final Section 5.2.3.3 explored the addition of an internal source of PE to improve the previously noted poor vertical heat distribution within SB84. While the addition of an additional source of turbulent mixing is shown to improve simulation of summer heat distribution and vertical structure, there appears to be a seasonal cycle in internal wave related turbulence indicated by over-mixing by the model during spring and winter/autumn months.

5.3 Summary: Prescriptive mixing models

In this chapter the prescriptive mixing models SH74 (Section 2.2) and SB84 (Section 2.3) were tested to replicate the observed stratification at CCS. Overall the heating-stirring based approaches were able to predict the general behaviour of the observed seasonal cycle of Φ. However, both models seemed to suffer from similar failures, namely an insufficient response to sudden events of O(days) and the overestimation of Φ. The latter failure was attributed to an underrepresentation of internal mixing when only boundary driven mixing terms are employed. While the results of SH74 first suggested that CCS behaves according to the classical balance between tidal mixing and solar heating (Simpson and Hunter, 1974), manipulation of SB84 identified CCS to be controlled predominantly by surface driven processes, analogous to an open-ocean environment (Kraus and Turner, 1967; Waniek, 2003). Manipulating SB84 further showed that both wind and convection are necessary to fully mix the water column in autumn. By adding a constant source of internal PE to represent a constant

level of internal wave mixing within SB84, it was shown that vertical heat distribution can be replicated realistically. However a seasonal discrepancy was identified, with too little mixing occurring during strongly stratified periods and an excess of mixing occurring during the transitional periods. The hypothesised seasonality within the internal wave field will be further explored in Chapter 6.

Chapter 6

Seasonality of internal waves and mixing

Introduction

This chapter aims to investigate the seasonality of internal waves and mixing at CCS using observational data and a combination of modelling tools.

Firstly the internal wave field at CCS is introduced using observations of vertical density and velocity structure (Section 6.1). The internal wave field was found to be active for the majority of the stratified period and dominated by internal tides and inertial oscillations. By evaluating the total amount of energy within the internal wave field an apparent seasonality with a super-imposed spring-neap variability was found. Here, peaks in energy were observed during summer and autumn months, while weaker levels occurred during the transitional periods of stratification. This result supported the hypothesis raised in Section 5.2.3, which suggested that seasonally varying levels of internal mixing were required to balance the energy budget according to SB84, which were attributed to the internal wave field.

The following Section 6.2 investigates the representation of internal wave seasonality and mixing in models. Initially three commonly used internal wave parameterisations were each included in the TC model to investigate their skill to represent realistic levels of internal mixing (Section 6.2.1). The results showed that each model predicted a seasonal cycle in internal mixing that was opposite to that suggested by energy within the internal wave field. Section 6.2.2 explores the implementation of a new parameterisation that is a modification of a suggested turbulence scaling that has previously been shown to be effective under similar forcing conditions to those observed at CCS. This new parameterisation successfully predicted the seasonality in internal mixing and improved on previous results of the prescriptive mixing model SB84, producing the most realistic representation of the observed seasonal cycle of Φ.

6.1 Observational evidence of internal wave seasonality

As already suggested by observations of vertical density structure (Section 4.3) and S^2 (Section 4.2), an active internal wave field was observed at CCS. Figure 6.1 presents the temperature observations [°C] from the 5 mooring deployments (Section 3.3). Internal waves with periods of $\approx$ 12 hours are visible during the stratified periods in 2014 and 2015. Wave heights typically ranged around 10- 20 metres in the spring and summer 2014 and 2015 (Figure 6.1a-b, e). Maximum wave heights of $\approx$ 40 metres were observed in late summer - autumn 2014 (Figure 6.1c).

The near-simultaneous occurrence of the onset of spring stratification and internal waves propagating past the mooring site is particularly evident when presenting the vertical temperature structure alongside Φ and focussing solely on the transitional period of stratification (Figure 6.2a-b, e-f). It is clear to see that during spring 2014 and 2015 (Figure 6.2a-b,e-f), internal waves were observed propagating past the mooring site soon after the initial onset of stratification. Pycnocline oscillations were however

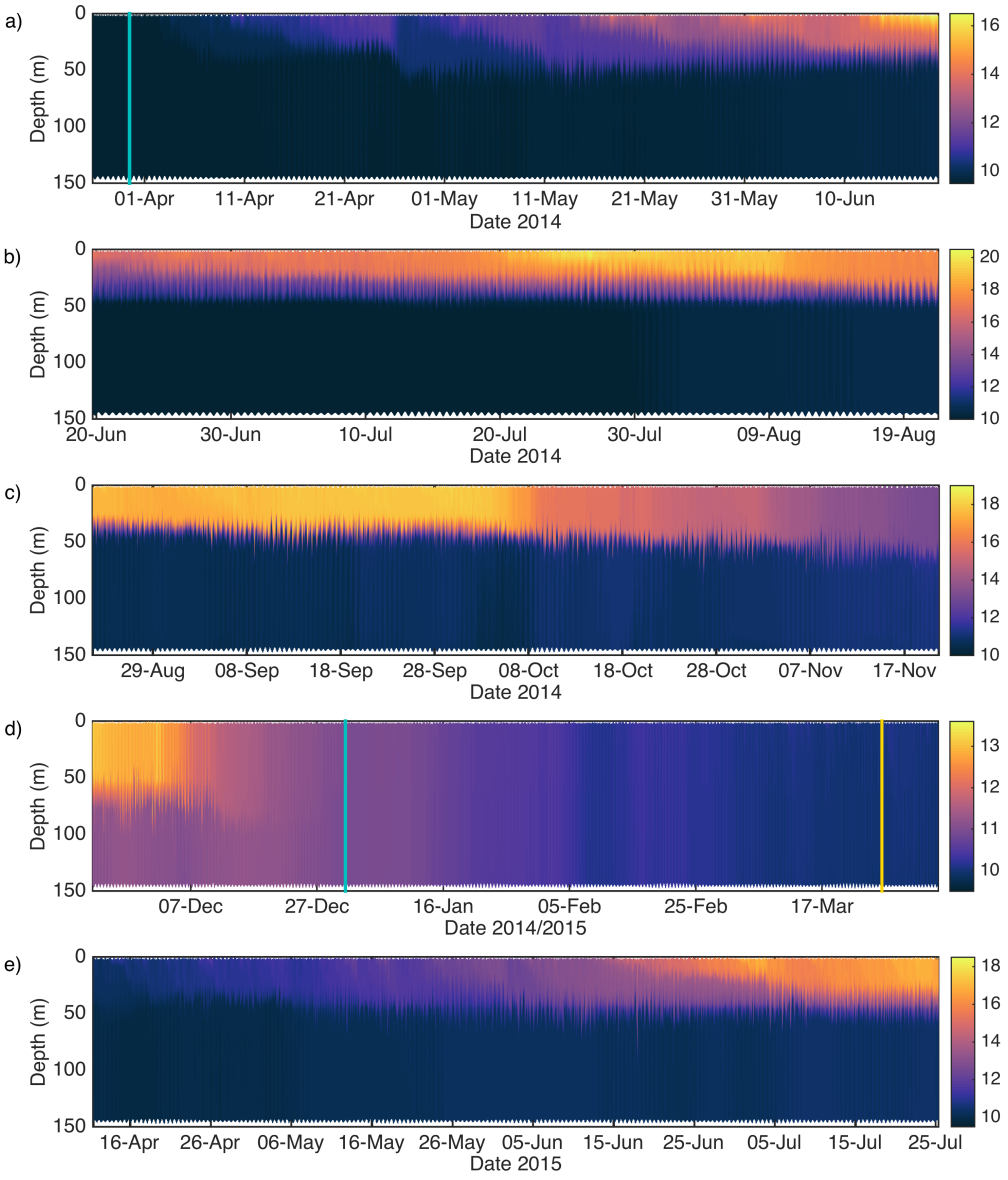

FIGURE 6.1: Internal wave field at CCS: a) - e) temperature observations [°C] of five mooring deployments. Note different temperature scales. Vertical blue line in a) marks the onset of stratification in 2014. The vertical blue and yellow lines in d) mark the breakdown of stratification in 2014 and the onset of stratification in 2015, respectively.

absent during the first 6 days of established stratification (Figure 6.2a, d-e). Since the CCS site was specifically chosen to be far away from topographic features and thus

representative of the background state, the seabed around CCS is not thought to be a generation zone of internal waves. Thus the observed internal wave field was most likely generated elsewhere and propagated to CCS. A likely source of these waves is the continental shelf break, which has often been identified as a major internal tide generation site (e.g. Huthnance, 1989; Green *et al.*, 2008). Assuming that the area between the shelf break and CCS was similarly stratified to CCS, the propagation time from the shelf break can be estimated using a simple two-layer approximation to calculate the phase speed c [m s^{-1}] of mode-1 internal waves:

$$c = \sqrt{(g'h)} \tag{6.1}$$

Where, g' is the reduced gravity

$$g' = g\frac{\Delta\rho}{\rho_0}. \tag{6.2}$$

due to the density difference $\Delta\rho$ between the two layers supporting the internal wave. Using the observed density profiles during the onset of stratification in 2014 and 2015, wave speeds of $c \approx 0.3$ m s^{-1} were likely. This would infer a propagation time of $\approx$ 5 days for an internal wave to travel from the shelf break to CCS. It is questionable however, whether shelf break generated internal tides are the only source of internal tides observed at CCS. While shelf break generated internal waves have been observed far into the shelf (Inall *et al.*, 2011) it has been shown that many other topographic features also generate energetic internal waves, that locally may be of greater importance (Marsden, 1986; Palmer *et al.*, 2013; Vlasenko *et al.*, 2014). Whether locally, shelf break or even more remotely generated waves make up the observed internal wave field at CCS (e.g. Nash *et al.*, 2012), is however beyond the scope of the work in this thesis. Here the focus lies on their local impact. The lack of internal wave activity in the very first days of established stratification could be considered an indication that the generation sites were not yet stratified due to their shallower depth and thus would not have allowed internal waves generation to occur.

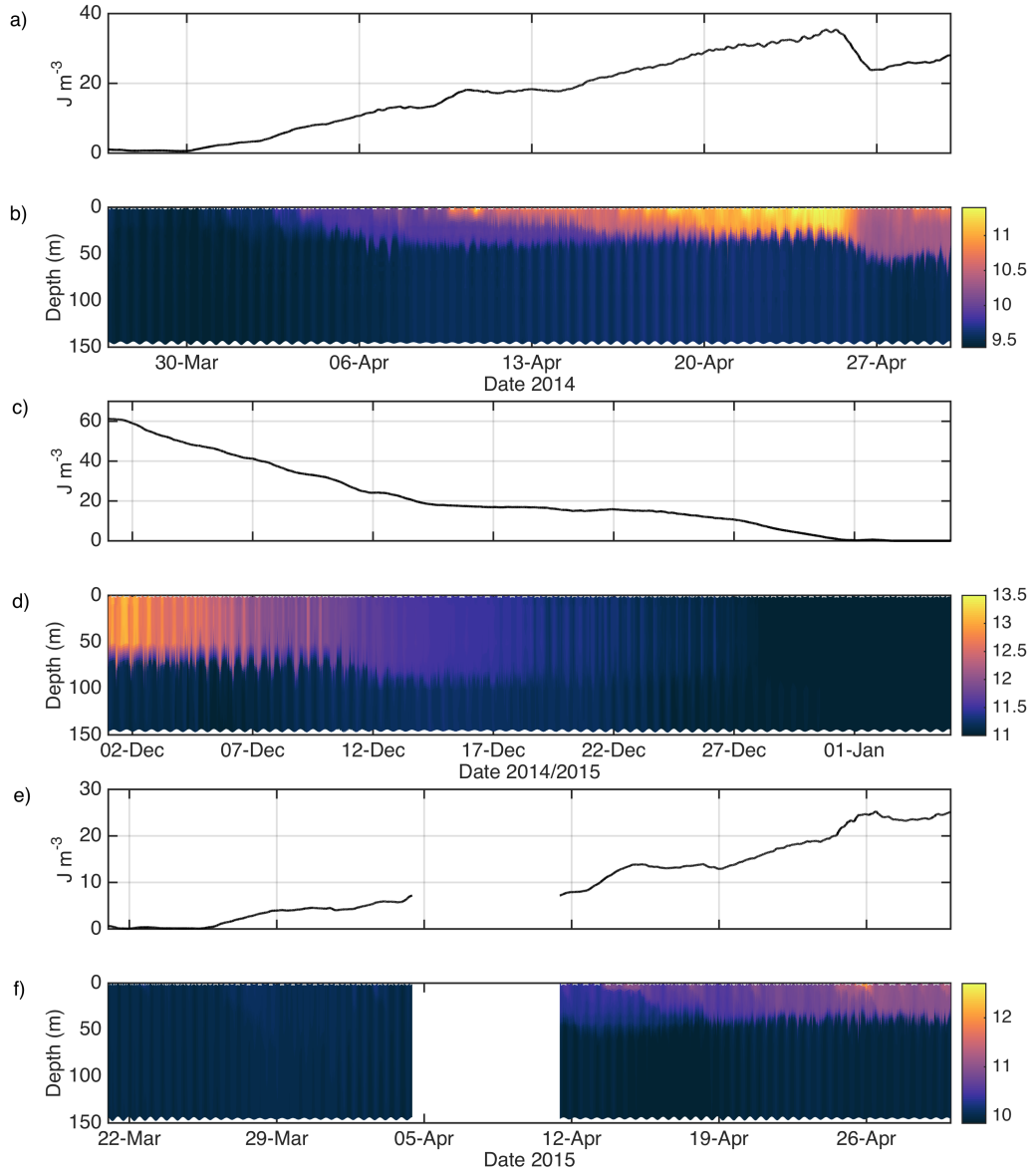

FIGURE 6.2: Internal wave field during transitional periods of stratification: a), c) and e) 25 hr running average of Φ [J m^{-3}] b), d) and f) temperature observations [°C]

At the end of the stratified period, internal waves were observed until mid-December 2014 (Figure 6.2c-d), the depth of the SML had deepened dramatically by 25 $\pm$ 3 metres (Section 4.3.2). After this event, internal wave activity was seen to dramatically reduce,

potentially indicating that internal waves were no longer being generated, despite the continued weak stratification at CCS.

In order to determine the dominant frequencies within the internal wave field a power spectral density (PSD) was calculated for the complex form $u + iv$ of the baroclinic velocity within the BML. This was done using a Welch's periodogram with a Hanning window of the size of 50% of the total data record of 8640 data points, which is equivalent to a window size of 30 days, and windows overlapping by 50%. The combined spectrum was dominated by peaks at the semi-diurnal and local near-inertial frequency (Figure 6.3). This is in agreement with previous studies that showed that the internal wave field in the Celtic Sea is dominated by internal tides (semi-diurnal periods) and inertial oscillations (local inertial period at CCS is $f = 15.76$ hours) (Palmer *et al.*, 2008; Inall *et al.*, 2011; Hopkins *et al.*, 2014). The spectrum also showed significant peaks at the frequencies of the M_2 overtides, M_4 and M_6.

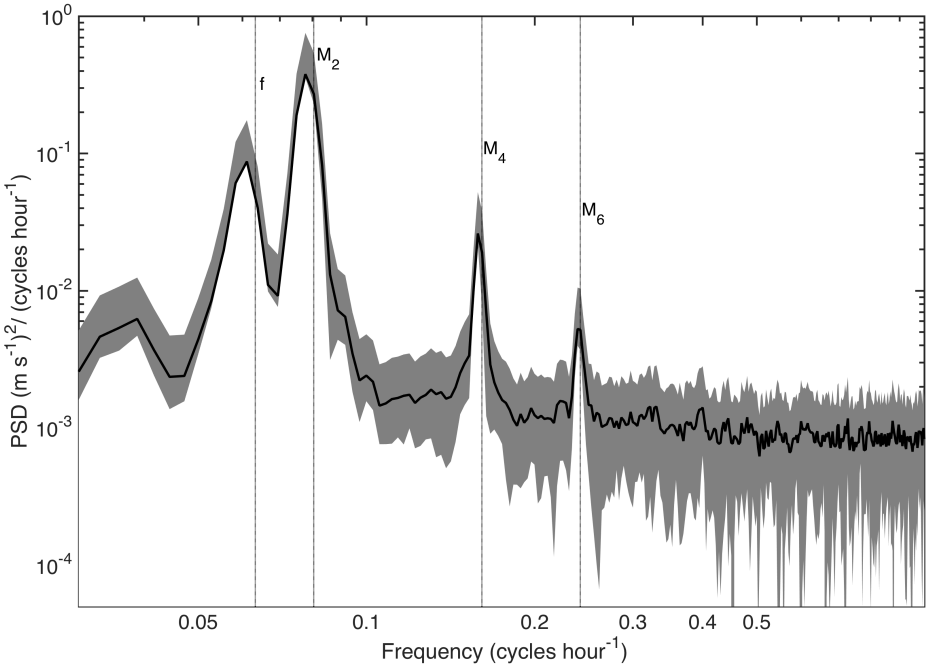

FIGURE 6.3: Total PSD spectra $[(\mathrm{m\,s^{-1}})^2/\ \mathrm{cycles\ hour^{-1}}]$ of baroclinic energy (black), with 90% confidence limit (grey). Vertical lines denote frequency of dominant frequencies.

To investigate the variability of the dominant wave periods, semi-diurnal and f, throughout the seasonal cycle at CCS, a wavelet analysis was performed on the baroclinic velocities during stratified periods ($\Phi \geq 2$ J m^{-3}). By decomposing a time series into time-frequency space, a wavelet power spectrum is able to show the dominant frequencies of the internal wave field and how their strength varies. Wavelet analysis essentially entails the convolution of a time series with a range of wavelet functions, which are based on a 'mother wavelet' that is being altered in frequency (dilated) and time (translated) along the time series. Here the Morlet Wavelet (Figure 6.4) was used as it is the standard 'mother wavelet' in geophysical applications (e.g. Farge, 1992; Jevrejeva *et al.*, 2003).

The wavelet analysis was performed following the methods described by Torrence and Compo (1998). Due to data gaps and mixed conditions in January - April 2015, a windowed analysis of five discrete segments was computed for each depth.

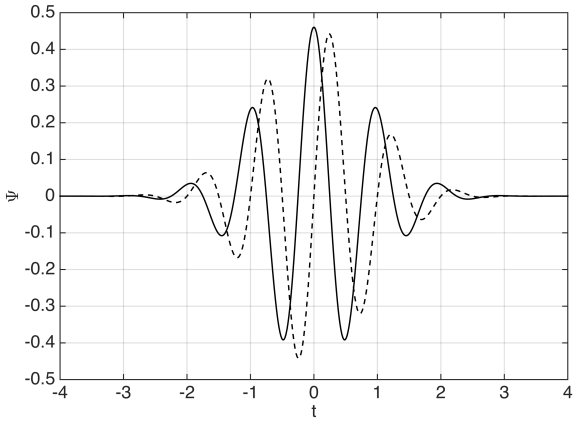

FIGURE 6.4: Real (solid) and imaginary (dashed) part of the Morlet Wavelet over time, t.

The depth average results are shown in Figure 6.5 and confirm the dominance of the semi-diurnal and the local inertial period throughout the observational period (Figure 6.5b). Increased amounts of power were also present at the periods of the diurnal tidal constituents and the M_2 overtides, reaching 0.07 m^2 s^{-2} and 0.1 m^2 s^{-2}, respectively.

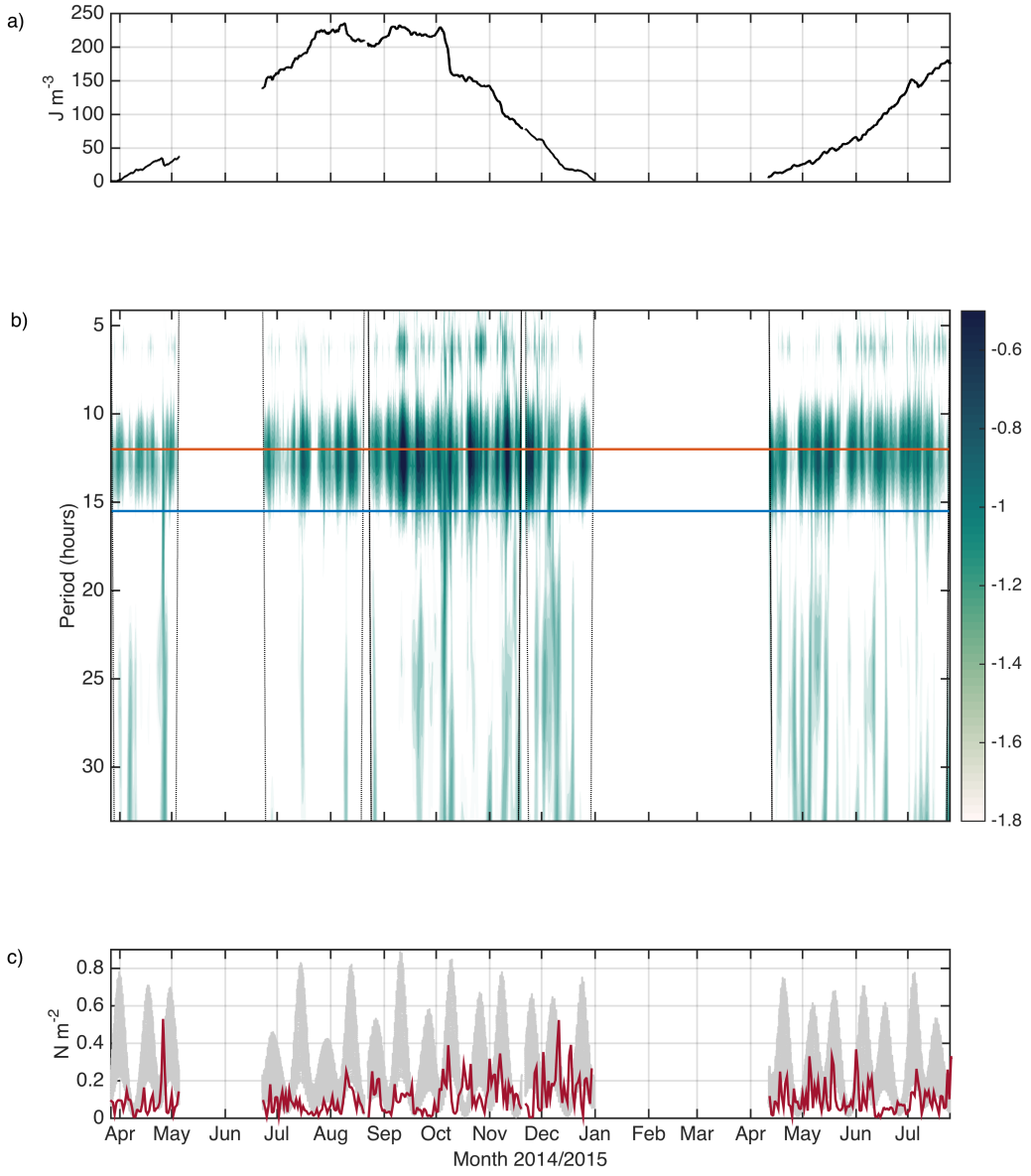

FIGURE 6.5: Wavelet analysis. a) Φ [J m^{-3}] b) Log_{10} of depth averaged wavelet power spectra [m^2 s^{-2}]. Dotted black lines mark the cone of influence of each segment, outside which the calculation becomes uncertain. Horizontal lines mark M_2 tidal (red) and inertial (blue) period c) daily average wind, τ_s, (red) and hourly averaged tidal, τ_b (grey) stresses [N m^{-1}] acting on the sea surface and bed, respectively.

The strongest power of 0.51 m^2 s^{-2} was observed at the semi-diurnal period during September 2014 (Figure 6.5). This peak occurred during strongly stratified conditions

(Φ = 230 J m^{-3}, Figure 6.5a) and the maximum tidal stresses (τ_b, Equation 2.8) observed during the observational campaign (Figure 6.5c). Power levels at the local inertial period reached maximum values of 0.26 m^2 s^{-2} in October 2014 (Figure 6.5b), which coincided with the sharp drop of 70 J m^{-3} over 6 days associated with the start of the breakdown of stratification in autumn 2014 (Section 4.3.2). In spring 2014, a local maximum in power levels at the local inertial frequency (0.1 m^2 s^{-2}) also coincided with a decrease in Φ of $\approx$ 11 J m^{-3} over a 36 hour period (Figure 6.5), associated with the storm in late April 2014 (Section 4.3.1). Generally, power levels at the local inertial frequency increased with increasing wind speeds in autumn and winter months 2014 (Section 4.1.1), but significantly decreased as stratification became weaker in December 2014.

While the results of the wavelet analysis provide a useful tool to observe the variability of the dominant wavebands at CCS, it fails to adequately separate between peaks of the internal tide (semi-diurnal period) and inertial oscillations (f period) distinctively. It is therefore a rather descriptive way of analysing the internal wave field. To analyse the seasonality more effectively the total depth integrated kinetic energy of the horizontal baroclinic velocities was calculated. This will hereafter be referred to as HKE_{tot}. HKE_{tot} is defined as:

$$HKE_{\text{tot}} = \int_0^h \frac{1}{2}\,\rho\left[\overline{u(z)^2} + \overline{v(z)^2}\right] \mathrm{dz} \tag{6.3}$$

Within this thesis HKE_{tot} was determined spectrally according to:

$$HKE_{\text{tot}} = \int_0^h \int_0^N E(fr)\ \mathrm{d}fr\ \mathrm{d}z \tag{6.4}$$

Where, $E(fr)$ is the power spectrum density of the horizontal kinetic energy. Rather than analysing the baroclinic velocities at fixed locations in the water column, baroclinic velocities were first interpolated into isopycnal coordinates thus providing a more

realistic representation of oscillations along density interfaces. To derive the time averaged u and v components of the flow, a windowed fast Fourier transform (FFT) of the complex baroclinic velocities in isopycnal space was then computed. To successfully separate the dominant semi-diurnal component, M_2 and the inertial frequency, f, the window size, win, had to be large enough according to:

$$win > \frac{2\Delta fr}{3} \tag{6.5}$$

Where $\Delta\ fr$ is the difference in frequency. At CCS the minimum window size required to separate M_2 (1/12.42 hours) and the local inertial frequency (1/15.76 hours) well was therefore $win_{\min} \geq 88$ hours.

The 25 hr moving average of HKE_{tot}, is shown in Figure 6.6b. HKE_{tot} displayed some evidence of a seasonal cycle with an apparent strong spring-neap variability, which includes some evidence of the N_2 modulation as observed in the barotropic tide (Figure 6.6c). Weakest energy levels were clearly observed during transitional periods of stratification in spring and late autumn 2014 and spring 2015. Strongest peaks were observed during summer and autumn periods (Figure 6.6a-b). Values during spring and summer 2015 were significantly higher compared to the values in spring 2014.

The observed seasonality in the internal wave energy is generally consistent with the theory of internal tide generation. Following Nash *et al.* (2006) the total rate of work of the barotropic tide interacting with topography is given by the product of Baines (1982) body force (F_{bt}) and the barotropically induced vertical velocity (v_{bt}), which Nash *et al.* (2006) combines as:

$$F_{bt}v_{bt} = \frac{N^2 v_{bt}^2}{\omega} \tag{6.6}$$

Which is indicative of the barotropic to baroclinic energy conversion. Here, v_{bt} is the result of the barotropic flow interacting with topography as it flows over a sloping

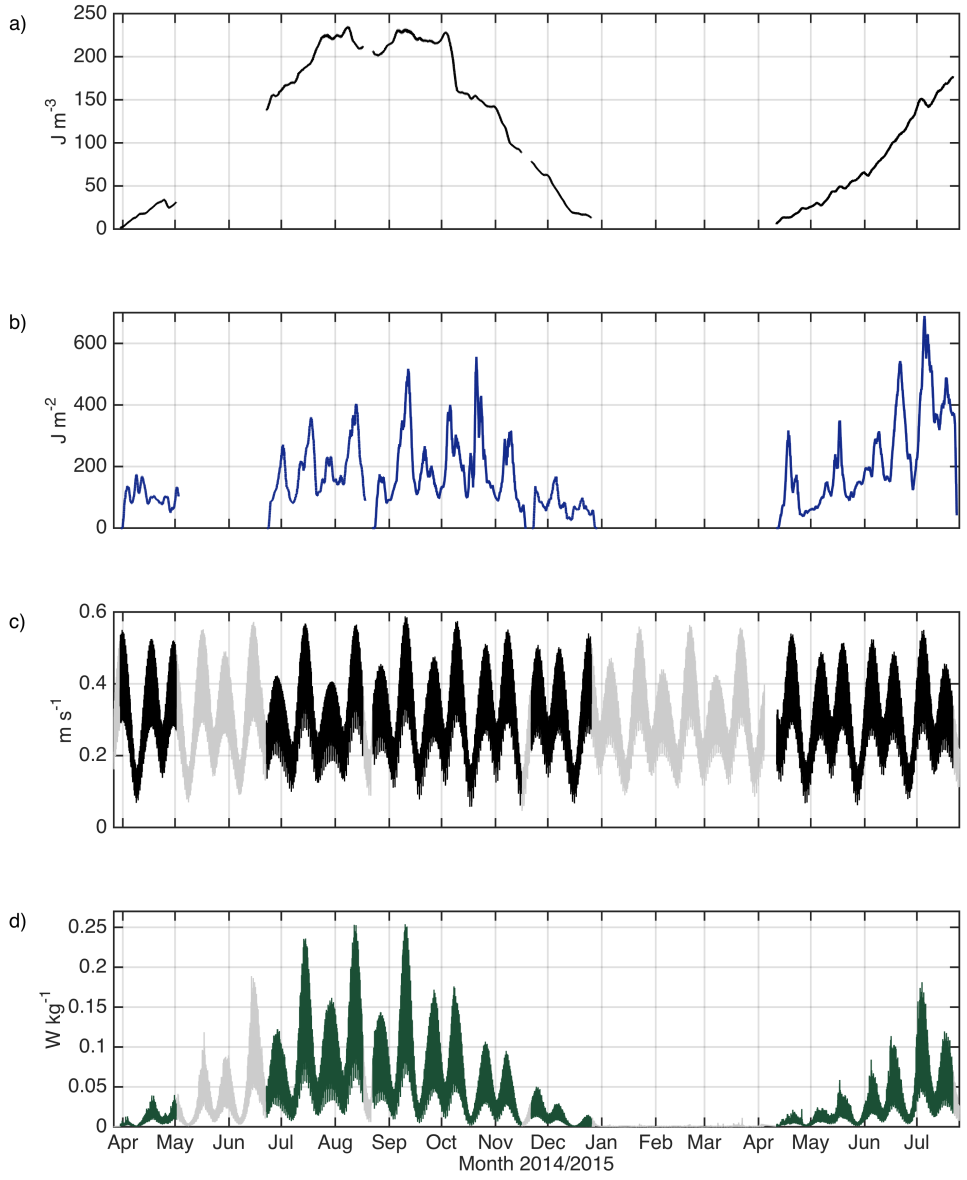

FIGURE 6.6: HKE_{tot} a) Φ [J m^{-3}] b) 25 hr running average of HKE_{tot} [J m^{-2}] c) $|\langle \boldsymbol{u} \rangle|$ full record (grey), period corresponding to available HKE_{tot} (black) d) depth averaged $F_{bt} v_{bt}$ [W kg^{-1}]. To aid the comparison, the full record of $|\langle \boldsymbol{u} \rangle|$ and $F_{bt} v_{bt}$ was plotted in grey, while periods when estimates of HKE_{tot} were also available, were highlighted in black and green, respectively.

bottom thereby inducing a vertical velocity:

$$v_{bt} = |\langle \boldsymbol{u} \rangle| s(z/H) \tag{6.7}$$

where s is the slope of the sea bed. As already mentioned, the location of the CCS site was specifically chosen to be away from any significant bathymetric features that could generate internal waves at CCS. However, power at the semi-diurnal period was present almost the entire stratified period (Figure 6.5), suggesting that a slope somewhere within a suitable propagation distance of CCS must have been sufficient to generate internal tides under the given conditions. Thus for the CCS location it is assumed that

$$v_{bt} \propto |\langle \boldsymbol{u} \rangle| \tag{6.8}$$

and thus a descriptive version of Equation 6.6 is used to indicate the likely relative energy level of the internal tide at CCS by

$$F_{bt} v_{bt} = \frac{N^2 |\langle \boldsymbol{u} \rangle|^2}{\omega} \qquad [\text{W kg}^{-1}] \tag{6.9}$$

Setting ω to the frequency of oscillation of the M_2 tidal constituent, $F_{bt}v_{bt}$ was calculated using observed values of N^2 [s^{-2}] (Equation 2.33, Figure 4.10d) and $|\langle \boldsymbol{u} \rangle|$ (Figure 6.6c). The depth averaged $F_{bt}v_{bt}$ [W kg^{-1}] is shown in Figure 6.6d. $F_{bt}v_{bt}$ (Equation 6.9) intuitively follows the seasonal cycle of N^2, modulated by the spring neap variability of $|\langle \boldsymbol{u} \rangle|$. While the general behaviour of the observed internal wave energy compared relatively well to the indicative barotropic to baroclinic energy conversion term, $F_{bt}v_{bt}$, a direct comparison highlighted that the timing of HKE_{tot} only occasionally matched that of $F_{bt}v_{bt}$. Given that internal tides are generated elsewhere, there is likely a lag associated with their propagation time to CCS. The lag itself is also subject to change due to varying phase speed (Equation 6.1) and generation site, as $|\langle \boldsymbol{u} \rangle|$ and stratification changes. Interestingly, the highest measured values of HKE_{tot} during 2014 were in autumn, in contrast to the behaviour of $F_{bt}v_{bt}$, which was generally reducing at this time.

Figure 6.7 presents the contributions to HKE_{tot} from the semi-diurnal internal tide (HKE_{t2}) and inertial oscillations (HKE_f). As was already noticed from the results of

the wavelet analysis (Figure 6.5), HKE_f increased as wind speeds increased in autumn 2014 (Section 4.1.1). While energy contribution from the semi-diurnal internal tide follows the overall pattern predicted by Equation 6.9 (Figure 6.6d), inertial oscillations potentially supplied the extra energy evident in autumn 2014. This suggests that wind, as well as being the primary control on SML depth (Section 4.3.2.1) also has a secondary role in supplying energy available to mixing via inertial oscillations.

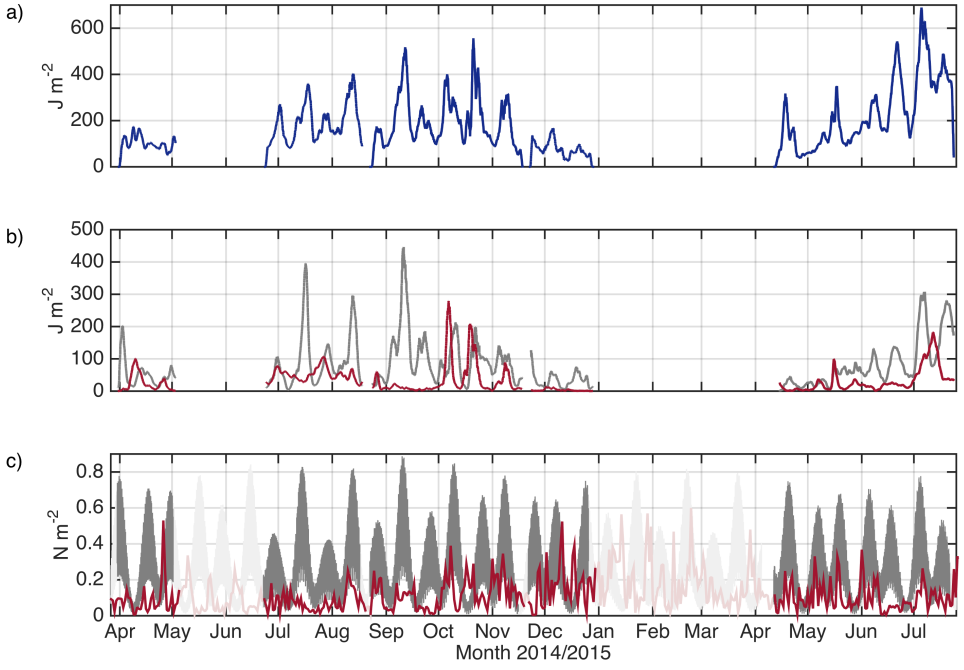

FIGURE 6.7: Contribution from semi-diurnal internal tide (HKE_{t2}) and inertial oscillations (HKE_f) a) HKE_{tot} [J m^{-2}] b) 25 hr moving average of depth integrated HKE_{t2} (grey) and HKE_f (red) [J m^{-2}] c) daily averaged wind, τ_s, (red) and hourly averaged tidal, τ_b (grey) stresses [N m^{-2}].

There is a clear difference in HKE_{tot} during both spring and summer periods 2014 and 2015. 2015 exhibited significantly higher levels of energy with peak values in June and July, which exceeded those of the observed maximum during autumn 2014 (Figure 6.7a). This is largely due to an apparent increase in semi-diurnal internal tidal energy (Figure 6.7b), which is seen to be greatly enhanced over 2014 levels, despite barotropic forcing remaining the same (Figure 6.6d). This could indicate differing

conditions at the generation sites producing varying internal wave production between 2014 and 2015 (e.g. Vlasenko *et al.*, 2013) or that differing levels of energy loss between generation and observation at CCS existed.

6.2 Representation of internal wave seasonality and mixing in models

The previous Section 6.1 confirmed a seasonality in baroclinic energy associated with the internal wave field at CCS. Since internal waves are often cited as a likely contributor to internal mixing, (e.g. Gregg, 1989; Munk and Wunsch, 1998; Inall *et al.*, 2000 this seasonality conforms to the hypothesis raised in Section 5.2.3, which suggested that seasonally varying levels of internal mixing were required to balance the energy budget according to SB84, which were attributed to the internal wave field.

In order to test how different internal wave parameterisations deal with the observed internal wave seasonality at CCS, the TC model, described in Section 2.4, was run for two years starting on 1st January 2014, using all three internal wave parameterisations that were introduced in Section 2.4.3.

6.2.1 TC model

6.2.1.1 Model setup: TC

The model grid was set to have a depth of $h = 146$ metres, with $n = 73$ bins each 2 metres high (Δz), at a latitude 49.4°N. Using this setup, and keeping $N_z^{\max} = K_z^{\max} = 1 \times 10^{-1}$ m^2, resulted in a time step of $\Delta t = 12.5$ seconds according to Equation 2.55. By carefully tuning the TC model to replicate the observed fully mixed temperature profile at the start of the observations, the initial temperature profile was found to be 10.7°C on 1st January 2014.

During the dates when meteorological observations recorded by the Met Office ODAS buoy (Section 3.5) were available, the TC model was forced using observed, daily averaged values of the parameters required to evaluate air sea fluxes (Equations 2.41 - 2.46). Outside of this date range, these variables were complemented using daily averaged values from the extended-range ERA-Interim product (Dee *et al.*, 2011). Daily averaged values of cloud cover, n_c [%], were also taken from the ERA-Interim product. The combined observed and reanalysis input variables of meteorological data are shown in Figure 6.8.

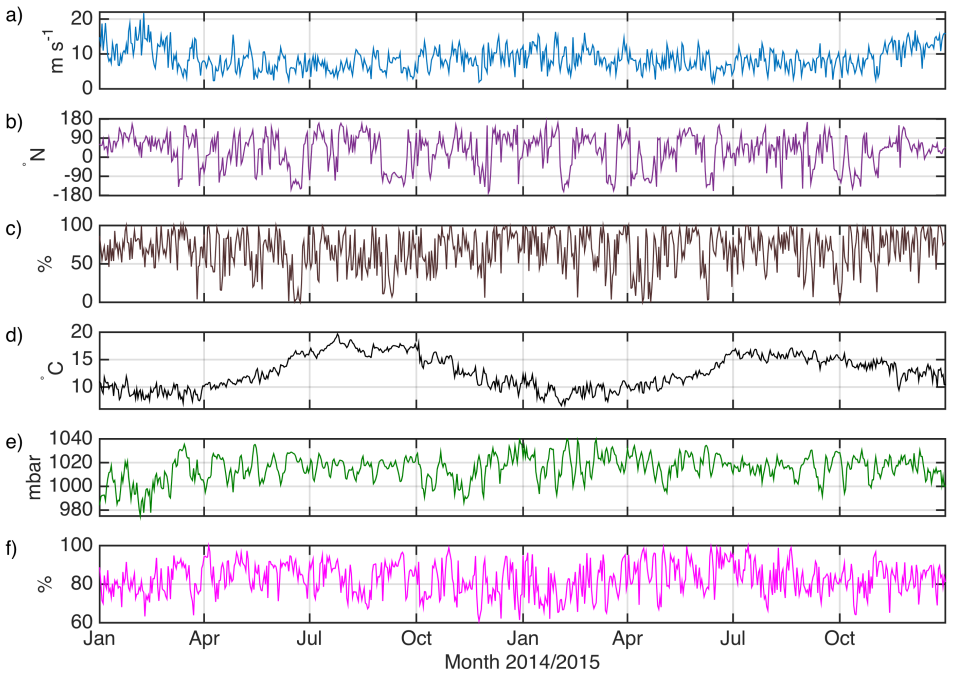

FIGURE 6.8: TC meteorological forcing. a) wind speed, w [m s^{-1}], b) wind direction [°N], c) cloud cover, n_c [%], d) air temperature, T_a [°C], e) air pressure, p_a [mbar] e) relative humidity, r_h [%].

In order to generate sea surface slopes (Equation 2.26), which are required to solve the equations of motions (Equations 2.24 and Equation 2.25), the model further required input of tidal parameters for the tidal constituents, M_2, S_2, N_2, O_1 and K_1. These were found by applying a least squares fit method of harmonic analysis to the earlier derived

barotropic ($\langle \boldsymbol{u} \rangle$) components of the observed velocities. The results of the harmonic analysis, which were used to force the model, are shown in Table 6.1.

Constituent	A_u [m s^{-1}]	ϕ_u [rad]	A_v [m s^{-1}]	ϕ_v [rad]
M_2	0.288	1.44	0.289	0.43
S_2	0.108	2.62	0.107	1.60
N_2	0.056	6.19	0.054	5.15
O_1	0.010	4.59	0.006	2.60
K_1	0.014	0.73	0.010	5.12

TABLE 6.1: Tidal parameters to force TC model

To validate the model, the hourly output data was then compared to the observed barotropic components of u and v (Figure 6.9) and found to have a good fit throughout.

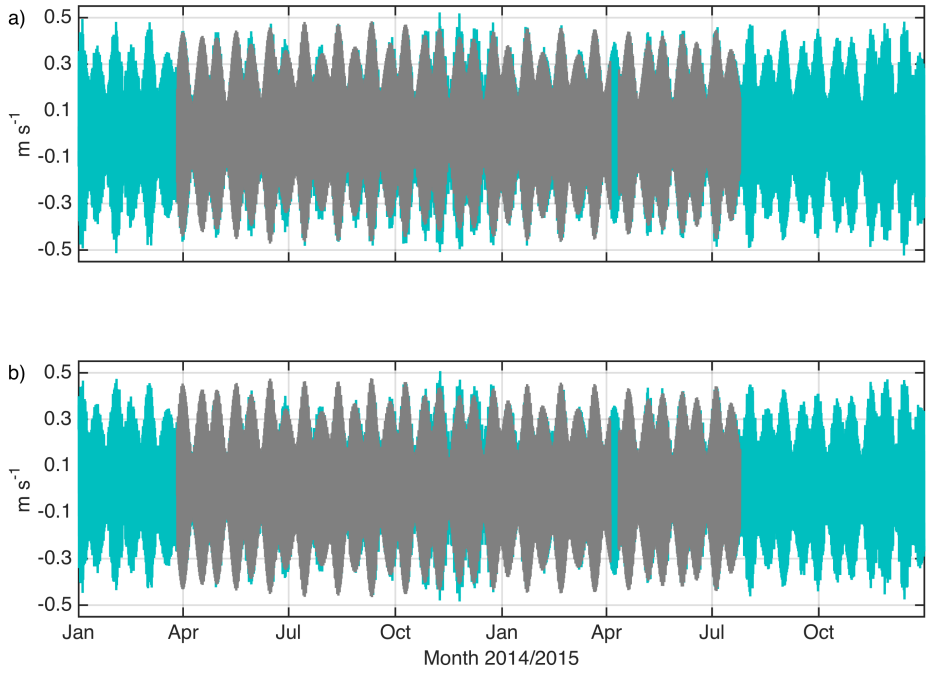

FIGURE 6.9: Model validation: Tides [m s^{-1}]. TC depth averaged velocities (cyan) vs. observed barotropic (grey) components of a) u and b) v.

To assess the modelled velocity components in a more quantitive way, the absolute root mean square error (RMSE), D (Equation 6.10), and relative RMSE, D/A_o, were

calculated for each tidal component, u and v, for all five tidal constituents (M_2, S_2, N_2, O_1 and K_1) following the methods by Cummins and Oey (1997):

$$D = \left[\frac{1}{2}\left(A_o^2 - A_m^2\right) - A_o A_m \cos\left(\phi_o - \phi_m\right)\right] \tag{6.10}$$

Here, A and ϕ denotes amplitudes and phases of a tidal constituents and the subscripts o and m depict the observational and model data, respectively. The results for the absolute and relative RMSE during the observational period are shown in Table 6.2.

Constituent	D_{u} [cm s^{-1}]	relative error$_{\mathrm{u}}$ [%]	D_{v} [cm s^{-1}]	relative error$_{\mathrm{v}}$ [%]
M_2	4.16	14.4	3.61	13.0
S_2	0.59	5.43	0.49	4.81
N_2	0.16	2.82	0.12	2.33
O_1	< 0.01	0.48	< 0.01	0.24
K_1	< 0.01	0.71	< 0.01	0.43

TABLE 6.2: Model performance. Absolute, D [cm s^{-1}], and relative RMSE [%].

Based on the results shown in Figure 6.9 and Table 6.2, it was concluded that the tidal velocities were reasonably well replicated by the TC model to continue forcing the model using the parameters found in Table 6.1.

Each of three runs of the TC model used the same boundary forcing to permit direct comparison of results base purely on the different methods to parameterise internal wave mixing. By using the same meteorological forcing as used in the prescriptive models, SH74 (Section 5.1.1) and SB84 (Section 5.2.1), and the well validated tidal velocities also allows direct comparison, between TC and prescriptive mixing models (Chapter 5).

Hereafter, the TC model results employing the background (Section 2.4.3.1), Kantha and Clayson (1994) (Section 2.4.3.2) and Canuto *et al.* (2001) (Section 2.4.3.3) internal wave mixing parameterisations will be referred to as TC_{BG}, TC_{KC} and TC_{CA}, respectively.

6.2.1.2 Results: TC model

Figure 6.10 presents the results of all TC variations alongside those of the observations and their differences to the observations. All TC models were able to replicate the overall seasonal cycle of Φ well ($R^2_{BG} = 0.96$, $R^2_{KC} = 0.96$ and $R^2_{CA} = 0.84$) and were able to correctly predict the timing of the onset of stratification ($\pm$ 1 day) during both years. While Φ_{BG} and Φ_{KC} appeared indistinguishable ($R^2 = 1.0$) from each other throughout 2014 and 2015, Φ_{CA} was predicted to be significantly lower overall. In contrast to the prescriptive models investigated in Chapter 5, all TC runs underestimated peak stratification values in the summer months in 2014 (Figure 6.10a-b). In 2015 however both TC_{BG} and TC_{KC} overestimated Φ until the end of the observational period in July 2015, at which point they were in good agreement. In 2014 Φ_{BG} and Φ_{KC} appeared to replicate the observations well up to July. Whereas TC_{CA} underestimated Φ throughout most of this period (green in Figure 6.10a-b). Comparing the same period in 2015, TC_{BG} and TC_{KC} significantly overestimate Φ, while the relatively higher mixing of the TC_{CA} produced an improved estimate for spring 2015.

The general underestimation of the predicted Φ in all TC models in 2014, potentially led to the breakdown of stratification being predicted 16 days (TC_{BG} and TC_{KC}), and 28 days (TC_{CA}) earlier than observed. It is also noted however, that similar to the prescriptive models in Chapter 5, all TC models suffered from an insufficient response to sudden events (of O(days)). An example of this is the onset of breakdown of stratification in autumn 2014 (Section 4.3.2). Between 3rd and 10th October 2014, stratification changed at an observed rate of -10.0 J m^{-3} d^{-1}. Over the same time

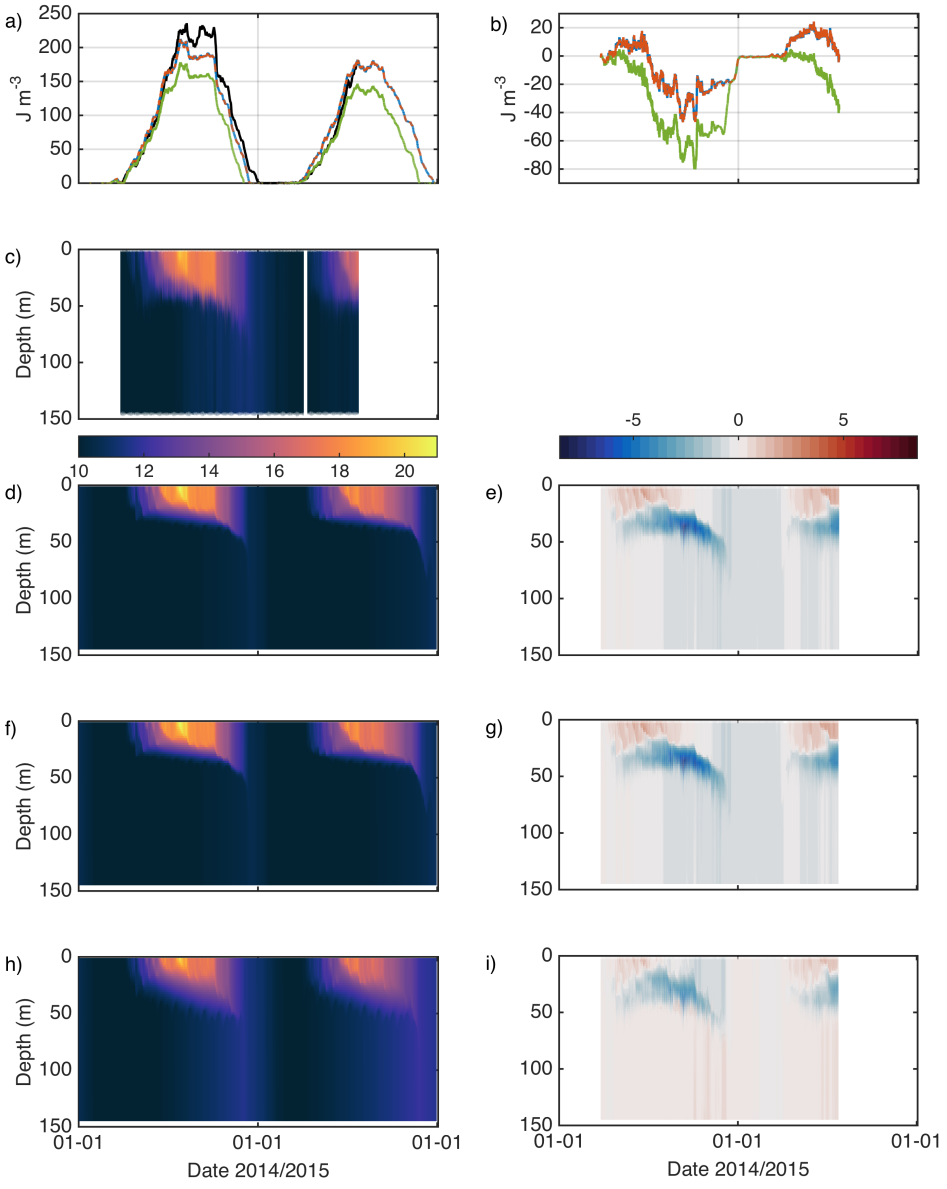

FIGURE 6.10: TC model vs observations a) Φ [J m^{-3}] observations (black), TC_{BG} (blue solid), TC_{KC} (red dashed), TC_{CA} (green) b) difference of modelled Φ to observations, same colours as a). Temperature [°C]: b) observations d) TC_{BG} f) TC_{KC} h) TC_{CA}. Temperature difference to observations c) [°C]: e) TC_{BG} g) TC_{KC} i) TC_{CA}.

period, both TC_{BG} and TC_{KC} only predicted a rate of -5.7 J m^{-3} d^{-1}, while TC_{CA} predicted a rate of -5.1 J m^{-3} d^{-1}. Interestingly, all TC variations also predicted a

brief, temporary period of stratification before the observational campaign began in March 2014. This had been previously also predicted by SB84 (Figure 5.6a).

Figure 6.10c-i shows the observed and predicted full depth temperature time series for comparison and their differences. All TC models replicated (Figure 6.10d, f, e) the overall temperature structure observed at CCS well. Again, the results of both TC_{BG} and TC_{KC} (Figure 6.10d, f) appeared indistinguishable from each other, which explains their close match in predicted Φ (Figure 6.10a-b). Unlike SB84, which struggled with heat retention at the surface, all TC models successfully predicted realistic SML temperatures, at most 3.6 °C higher than the observations (Figure 6.10e, g, i). Despite this, the distribution of heat with depth was poorly replicated compared to the observations (Figure 6.10e, g, i). This is also evident in the predicted SML depth and location of the seasonal thermocline being too shallow. This failure likely contributed significantly to the general underestimation of Φ in 2014 since the centre of mass was artificially raised in the water column (Section 2.1).

The temperature structure predicted by TC_{CA} (Figure 6.10h, i) showed clear evidence of enhanced internal mixing, due to a greater increase in bottom mixed layer temperature compared to TC_{BG} (Figure 6.10d, e) and TC_{KC} (Figure 6.10f, g), which was better aligned with the observations evident in the generally low temperature difference (maximum of 2.9°C) to the observations shown in Figure 6.10i. In addition, a more diffuse thermocline with greater levels of variability was predicted.

To investigate the different responses from the three internal wave parameterisations, the predicted levels of pycnocline mixing was examined (Figure 6.11). Each TC model predicted order magnitude variability in K_z over relatively short time scales. As might be expected from similar results in Φ and temperature, TC_{BG} and TC_{KC} only varied slightly from each other. Overall, TC_{CA} predicted higher levels of pycnocline mixing. Average values across the two seasons were, $K_z = 3.16 \pm 2.80 \times 10^{-4}$, $3.11 \pm 2.78 \times$

10^{-4} and $5.66 \pm 6.19 \times 10^{-4}$ m^2 s^{-1} for the three models TC_{BG}, TC_{CL} and TC_{CA}, respectively.

Pycnocline mixing within each model was also characterised by a clear seasonal cycle, with lowest values during summer months and highest during the transitional periods of stratification (Figure 6.11). This in direct contradiction to the missing mixing that was hypothesised to close the PE budget within SB84 (Section 5.2.3.3). Similarly, this contradicts the observational evidence that shows internal wave energy to be closed related to the seasonal cycle in Φ, with maximum in summer and autumn (Section 6.1). The enhanced mixing seen in all models during autumn and winter months is a potential cause of the breakdown of stratification being predicted too early (Figure 6.10).

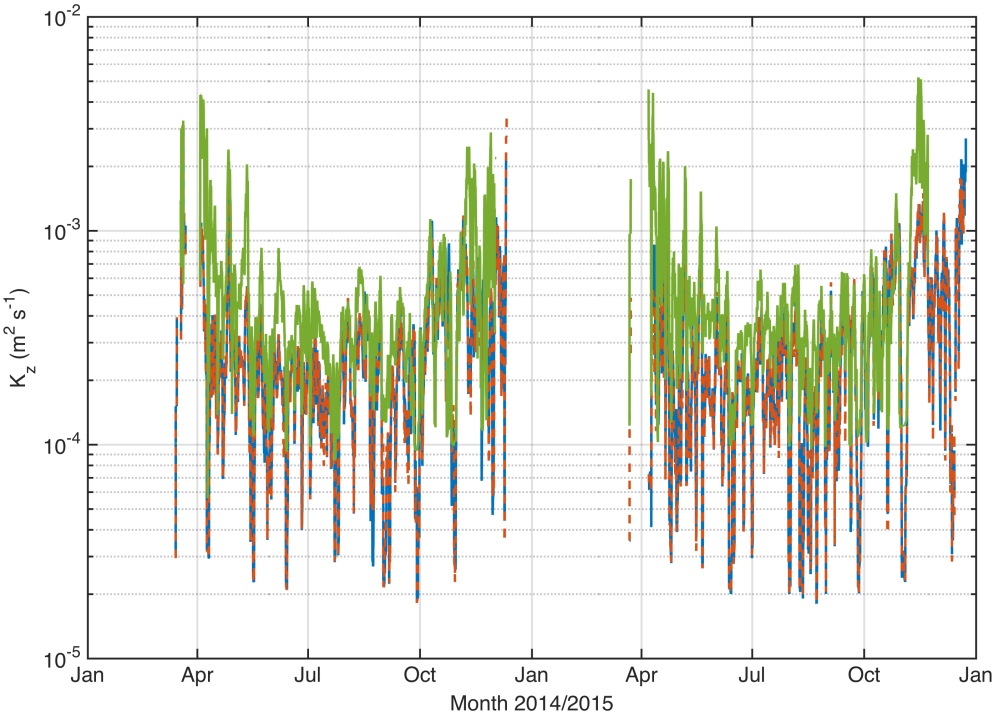

FIGURE 6.11: K_z [m^2 s^{-1}] within thermocline region as predicted from a) TC_{BG} (blue) TC_{KC} (red dashed) TC_{CA} (green).

To try to better understand the individual parameterisations' response to forcing conditions the predicted energy available for mixing, ε [W kg^{-1}], will be examined relative

to the buoyancy, $\boldsymbol{B}$, and shear production, $\boldsymbol{P}$, terms of the TKE equation (Equation 2.31), represented by N^2 and S^2 (Figure 6.12). This allows comparison of ε from each model in a non-dimensional stability space and permits a focus on turbulence within the pycnocline. To assist this only data with $N^2 > 10^{-6}$ s^{-2} were included in the analysis.

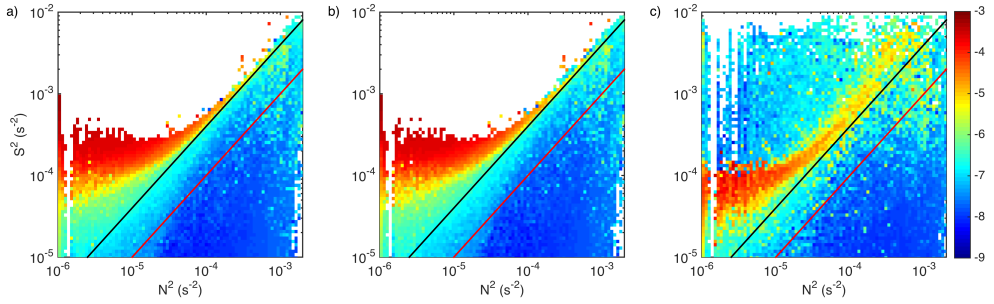

FIGURE 6.12: $\log_{10}\varepsilon$ [W kg^{-1}] in stability space, N^2 [s^{-2}] vs S^2 [s^{-2}] predicted from a) TC_{BG} b) TC_{KC} c) TC_{CA}. Overlaid are $Ri_{cr} = 1/4$ (black) and $Ri_g = 1$ (red) for reference.

Each model predicted a clear transition of ε at $Ri_g = 1/4$ (Section 2.36), which is as should be expected since this typically indicates the Ri_{cr} (critical gradient Richardson number) when shear driven instability is likely to occur (Section 2.4.1). Similar to Φ, the temperature structure (Figure 6.10) and K_z (Figure 6.11), the behaviour of ε in stability space predicted by TC_{BG} and TC_{KC} appeared indistinguishable (Figure 6.12a-b). Both schemes associated strongest levels of ε with weak stratification, which is likely due to boundary forcing acting on the periphery of the thermocline rather than any parameterisation effects designed to represent internal wave mixing. Within regions of stronger stratification ($N^2 > 10^{-4}$ s^{-2}) ε was observed to increase with reducing stability. However, the Ri_g was rarely seen to become sub-critical and thus turbulence was maintained within only 2-3 orders of magnitude above background levels.

The distribution of ε in stability space as predicted by TC_{CA} (Figure 6.12c) clearly differed from TC_{BG} and TC_{KC} (Figure 6.12a-b). Within less stratified regions (N^2 $<10^{-4}$ s^{-2}), peak values of ε were significantly lower in magnitude and, a greater range of Ri_g space was occupied. Within the more strongly stratified region (N^2 $>10^{-4}$ s^{-2}) there appeared to be more noise in the system. Similar to the TC_{BG} and TC_{KC}, ε increased with decreasing stability up to Ri_{cr}. Within this space, values were sometimes elevated by $\sim$ 1 order of magnitude. Again, an increased area within the sub-critical stability space was occupied, with strongest values of ε associated close to Ri_{cr}.

In summary, each TC model captured the general behaviour of the seasonality of stratification observed at CCS well. While TC_{BG} and TC_{KC} appeared to behave similarly, TC_{CA} predicted a significantly different temperature field and thus Φ (Figure 6.10). Comparing the rates of pycnocline mixing between the three parameterisations suggested that TC_{CA} predicted the highest overall values of K_z within the pycnocline (Figure 6.11). Most importantly however, all TC variations predicted a seasonal cycle of internal mixing. This cycle however was the inverse of that suggested to be missing by $SB84_{int}$ (Section 5.2.3.3) implied by the energy levels within the observed internal wave field. The response of TC_{BG} and TC_{KC} to predicted N^2 and S^2 goes some way to answering their failures in predicting turbulence due to internal waves (Figure 6.12a-b). Neither scheme introduces sufficient shear within pycnocline regions to drive the required criticality (indicated by Ri_{cr}) to produce internal mixing. This is contrary to high levels of pycnocline shear that were observed (Section 4.3), and are attributable to the internal wave field at CCS. TC_{CA} does appear to introduce enhanced levels of shear in pycnocline regions leading to sub-critical Ri_g and subsequently enhanced turbulence (Figure 6.12c). Despite this TC_{CA} still predicts the highest mixing at transitional stages of stratification.

6.2.2 Introducing internal wave seasonality and mixing into models

Within the deep open ocean internal wave energy is often described following the observed cascade of energy as described by Garrett and Munk (1979). A typical application of this method is described by Gregg (1989) to estimate the amount of energy available for mixing by internal waves, ε_{iw}, as

$$\varepsilon_{iw} = \varepsilon_0 \left\langle \frac{N^2}{N_0^2} \right\rangle \left\langle \frac{S^4}{S_{GM}^4} \right\rangle \tag{6.11}$$

Where N and S are the modelled buoyancy frequency and shear respectively, N_0 is a background N and S_{GM} is an estimate of shear following the Garrett and Munk (1979) cascade of energy. Within shallower, shelf sea environments however such parameterisations of internal wave mixing have been shown to fail as internal wave spectra have a greater level of variability. MacKinnon and Gregg (2003a) proposed a significant modification to the Gregg (1989) parameterisation based on observations of low frequency dominated internal wave mixing on the New England shelf. Here, ε becomes a function of low-frequency shear (S_{lf}) and buoyancy frequency (N_{lf}) according to:

$$\varepsilon_{MG} = \varepsilon_0 \left(\frac{N}{N_0} \right) \left(\frac{S_{lf}}{S_0} \right) \qquad [\text{W m}^{-3}] \tag{6.12}$$

where ε_0 is a background level of turbulence, N_0 and S_0 are reference buoyancy frequency and shear values.

Palmer *et al.* (2008, 2013) later showed that pycnocline turbulence in the summer stratified Celtic Sea, in a region away from direct forcing of internal wave generation, followed the MacKinnon and Gregg (2003a) scaling of turbulence relative to low frequency stratification and shear. In addition to this proposed scaling, it has been extensively observed on the NW European shelf (e.g. van Haren *et al.*, 1999; Rippeth *et al.*, 2009; Palmer *et al.*, 2013) and in comparable shelf sea systems (e.g. MacKinnon

and Gregg, 2005a,b) that the seasonal pycnocline exists in a state of 'marginal stability'. Under this state, local stratification (N) and shear (S) introduced by internal waves maintain a near constant, low level of stability that is characterised by a $Ri_g \approx 1$ (Equation 2.36).

To test whether the pycnocline at CCS was in a comparable state to these previous studies, Ri_g (Equation 2.36) was calculated using all available observed values of N^2 (Equation 2.33) and S^2 (Equation 2.32). Since only values within the pycnocline region were of interest, weakly stratified and highly turbulent areas, such as the surface and bottom boundary layer, were discarded, by setting $Ri_g(N^2 < 1 \times 10^{-4}\ \mathrm{s}^{-2}) =$ non-values (NaNs). The probability density function (PDF) of the Ri_g was then computed and is presented in Figure 6.13. The mode value was $Ri_g = 0.45$, which contributes to the growing body of evidence that the seasonal pycnocline in shelf seas is commonly maintained in this state of marginal stability.

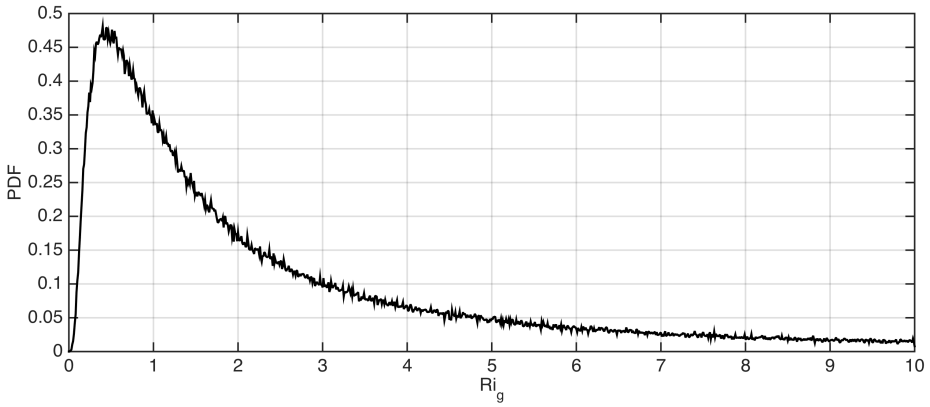

FIGURE 6.13: PDF of $Ri_g(N^2 > 1 \times 10^{-4}\ \mathrm{s}^{-2})$.

While the distribution of $Ri_{g\mathrm{CCS}}$ shows that higher stability states do exist, the distribution shows that a low stability state is often likely to occur. The tight relationship between N^2 and S^2 is therefore used to justify a further iteration to the MacKinnon and Gregg (2003a) parameterisation in an attempt to predict the supposed seasonality in pycnocline mixing, inferred by the $\mathrm{SB84_{int}}$ results presented in Section 5.2.3.3.

Assuming that $Ri_g = N^2/S^2 = 0.45$ at CCS, Equation 6.12 can be rewritten as

$$\varepsilon_{CCS} = \varepsilon_0 \left(\frac{N^2}{N_0^2 \sqrt{Ri_0}} \right) \qquad [\text{W m}^{-3}] \tag{6.13}$$

Where $Ri_0 = 0.45$ and $N_0 = S_0 = 6$ cph.

To test this newly suggested iteration on the MacKinnon and Gregg (2003a) parameterisation SB84 was rerun with the same forcing as SB84_{int} but with Equation 6.13 in place of the constant background value for internal mixing. Results from this new run of SB84 will hereafter be referred to as SB84_{MG}.

6.2.2.1 SB84_{MG} results

Figure 6.14 shows the results from SB84_{MG} alongside observations and model results from previous runs that included only boundary forces (SB84, Section 5.2.2) and a constant level of internal mixing ($\text{SB84}_{\text{int}_m}$, Section 5.2.3.3). To produce these results ε_0 was set to 8×10^{-8} W m^{-3} since this provided the optimal fit observed values ($R^2 = 0.99$). It is immediately evident that the SB84_{MG} parameterisation introduces a greater level of mixing than had previously been included in SB84, bringing spring and summer results more in line with the observations. SB84_{MG} also succeeded in better reproducing the observed summer variability, being the only iteration of the SB84 framework to not predict increasing Φ between August and October 2014.

The impact of the new parameterisation on the vertical structure was immediately evident (Figure 6.14e) as it produced a greater levels of pycnocline diffusion and so broke down the unrealistically tight interfaces that were particularly evident at the base of the pycnocline during summer months in SB84 (Figure 6.14c). While spring and summer conditions were best replicated in SB84_{MG} the model does still unfortunately overmix during autumn months, leading to breakdown being predicted too early, similar to results from SB84_{int} (Section 5.2.3.3).

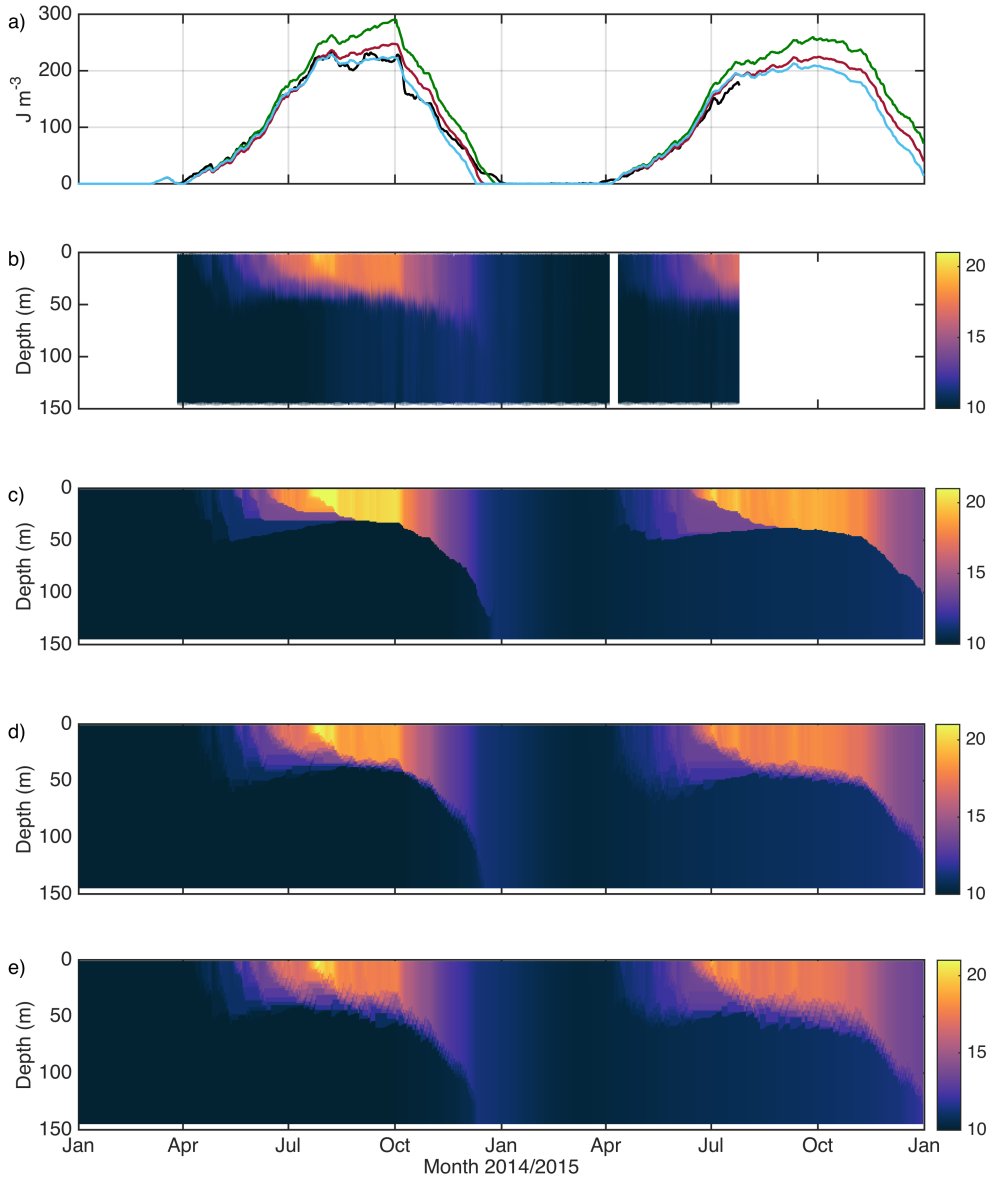

FIGURE 6.14: $SB84_{MG}$: a) Φ [J m^{-3}] observations (black), SB84 (green), $SB84_{int_m}$ (red) $SB84_{MG}$ (purple). Temperature [°C]: b) observations c) SB84 d) $SB84_{int_m}$ e) $SB84_{MG}$

Despite Equation 6.13 successfully managing to dampen internal mixing during autumn months (Figure 6.15) it is clear that mixing during these latter stages of stratification was still too high to accurately predict the full seasonal cycle. It is unlikely however

that this is solely due to inaccurate internal mixing alone since the initial run of SB84, which lacks any representation for internal mixing processes, still underestimated the timing of breakdown of stratification in 2014 (Section 5.2.2). Interestingly, the seasonal average of $\varepsilon_{\mathrm{CCS}}$ was 1.7×10^{-5} W m^{-3}, slightly increased compared to the best overall fit using a constant background $\varepsilon = 1 \times 10^{-5}$ W m^{-3} rate used in SB84$_{\mathrm{int}_m}$ (Section 5.2.3.3).

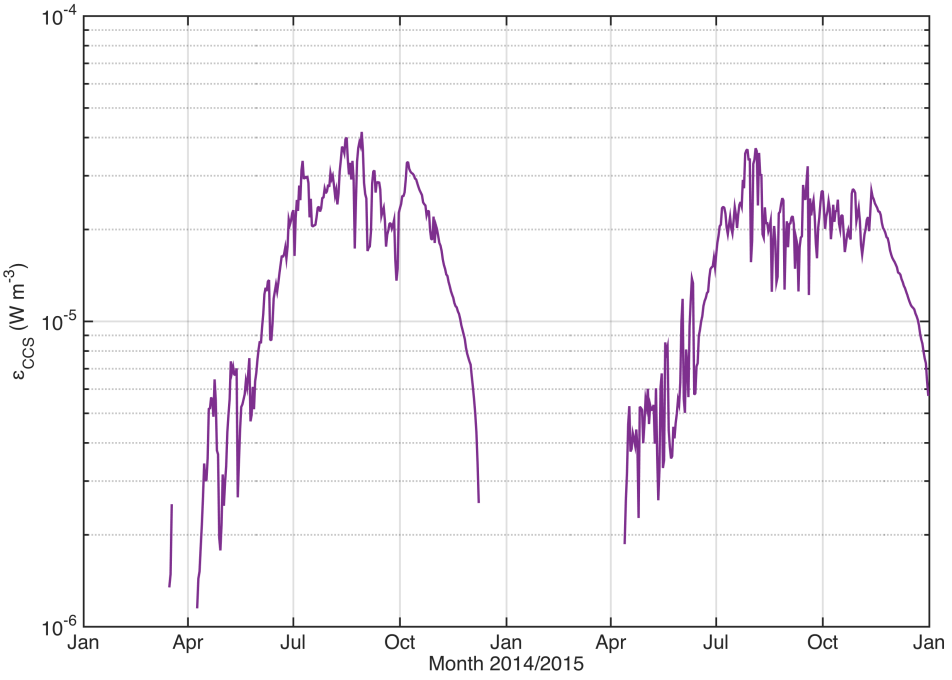

FIGURE 6.15: $\varepsilon_{\mathrm{CCS}}$ [W m^{-3}] as predicted by Equation 6.13 within SB84$_{\mathrm{MG}}$

6.3 Discussion

Results from the SB84 suggested a seasonally varying source of internal mixing was required to close the Φ budget at CCS, which is often assumed attributable to enhanced midwater shear driven by internal waves. Analysis of the active internal wave field at CCS support this hypothesis, revealing internal wave energy to peak through summer months and reducing during transitional periods of stratification. The TC model was

run with three commonly used internal wave parameterisations. Each produced a seasonal cycle in pycnocline mixing, however the seasonal cycle was the inverse of that expected, at a minimum during summer months and peaking during transitional periods of stratification (Figure 6.11). It was interesting to note, that both TC_{BG} and TC_{KC} produced similar results throughout. In contrast to this, TC_{CA} predicted more pycnocline mixing overall as the pycnocline regions were able to become sub-critical and therefore turbulence was introduced to the more stratified regions (Figure 6.12c).

In an attempt to address the inaccurate scaling of turbulence produced by the TC models a modification of a parameterisation proposed for stratified shelf seas was employed that was directly dependent on varying N^2. This parameterisation (Equation 6.13) includes two tuneable parameters prescribing a background level of turbulence, represented by ε_0 and a background criticality represented by Ri_0. This parameterisation is analogous to that proposed by MacKinnon and Gregg (2003a), but enables representation of internal wave shear via an assumption of persistent marginal stability. $\varepsilon_0 = 8 \times 10^{-8}$ W m^{-3} was chosen as optimal fit of $SB84_{MG}$ at CCS. This is significantly lower than suggested values of ε_0 proposed by (MacKinnon and Gregg, 2003a, 2005a) on the New England Shelf and by (Palmer *et al.*, 2008) during a previous study in the Celtic Sea, which ranged between 6.9×10^{-7} - 1.75×10^{-5} W m^{-3}. Within this new parameterisation however, ε_0 is scaled by the empirically derived Ri_g at CCS. It is possible that differences in ε_0 between studies are due to varying background states of criticality.

By prescribing the state of constant near-critical stability within the pycnocline, Equation 6.13 successfully introduces internal mixing directly relative to the seasonal cycle N^2, which is in direct contradiction to the TC solutions, which scaled mixing inversely with N^2 (Figure 6.11).

6.4 Summary: Seasonality of internal waves and mixing

The aim of this chapter was to investigate the seasonality of internal waves and mixing at CCS using observational data and a combination of modelling tools. The main findings of this chapter are summarised below.

An active internal wave field was observed throughout the majority of the stratified periods at CCS. Wave heights typically reached 10-20 metres during spring and summer 2014/2015, and during autumn 2014, internal waves occasionally reached heights of 40 metres. Analysis of the observed baroclinic velocities revealed that the internal wave field was dominated by semi-diurnal internal tides and inertial oscillations. By evaluating the total amount of energy within the internal wave field (HKE_{tot}) an apparent seasonality with a super-imposed spring-neap variability was found. Here, peaks in energy were observed during summer and autumn months, while weaker levels occurred during the transitional periods of stratification. The apparent spring-neap variability appeared to be further affected by an N_2 modulation, similar to observations of the barotropic velocities, which suggests a level of predictability of the internal wave field. The observed signal of HKE_{tot} was generally in good agreement to the barotropic forcing term $F_{bt}v_{bt}$, but showed a number of disparities. Firstly, a variable lag relative to $F_{bt}v_{bt}$ was observed. This suggests a variable internal wave field that is characterised by waves with different phase speeds and generation sites as a result of N^2 changing throughout the year. Secondly, high levels of HKE_{tot} were observed during autumn 2014. At this time the overall pattern of $F_{bt}v_{bt}$ was generally decreasing. This additional amount of energy was potentially supplied by inertial oscillations in good agreement with increasing wind speeds reported during this time. Thirdly, total energy levels within the internal wave field were significantly higher during spring and summer 2015 than spring and summer 2014. This was mostly due to an apparent increase in semi-diurnal internal tide energy (HKE_{t2}), but the reason for this was unknown.

To investigate the capabilities of three described, commonly used internal wave parameterisations to produce the suggested seasonality in internal mixing, they were each included in the TC model. Each TC model was able to replicate the overall seasonal cycle of stratification observed at CCS well. However, each parameterisation suffered from poor vertical heat distribution, which led to the SML and thermocline depth being predicted too shallow. By investigating rates of mixing (K_z) within the thermocline, a large variability was found to occur throughout the stratified periods. It was clear however, that each parameterisation predicted a strong seasonal cycle of thermocline mixing that peaked during the transitional regions of stratification, but were lowest during peak stratification in summer months. It was hypothesised that those high levels of K_z during autumn were responsible for the early breakdown of stratification predicted by the model. The seasonality predicted by each TC variation is in direct contradiction with the suggested seasonality of internal mixing implied by the $SB84_{int}$ results and supported by the energy levels within the observed internal wave field. By examining the predicted energy available for mixing, ε, provides some suggestions for the responses seen in the models. While TC_{BG} and TC_{KC} generally appeared to behave similarly, both failed at introducing sufficient levels of shear within pycnocline regions to drive the criticality required to produce internal mixing. Despite TC_{CA} correctly predicting sub-criticality to occur within pycnocline regions, it overmixed during the transitional periods of stratification.

In an attempt to address the inaccurate scaling of turbulence found within the TC models, an iteration of MacKinnon and Gregg (2003a) scaling of turbulence relative to low frequency stratification and shear was employed within the SB84 framework. The prescriptive mixing model SB84 does not include any of the dynamics (Section 2.3) required to simulate the transfer of energy via enhanced levels of shear from internal waves. The MacKinnon and Gregg (2003a) parameterisation was thus adjusted to take account of the criticality observed within the pycnocline region at CCS to enable the

representation of internal wave shear due to persistent marginal stability. The impact of the new parameterisation was immediately evident on the vertical structure of temperature, which removed previously unrealistically tight interfaces during summer months. At the same time internal mixing was reduced during the transitional periods of stratification and subsequently provides a seasonal cycle in internal mixing.

Chapter 7

Biogeochemical environment

Introduction

In this chapter a first attempt is made at investigating the biogeochemical environment in response to the evolution of the vertical density structure throughout the seasonal cycle, with a particular focus on the SML deepening period in autumn 2014. The focus of this chapter was to establish the role the autumn phytoplankton bloom plays within the seasonal cycle of primary production in a temperate shelf sea. While its significance has previously not been well quantified, it is shown that the autumn phytoplankton bloom can be as productive in fixing carbon as the spring phytoplankton bloom or the well-studied subsurface chlorophyll maximum (SCM) during summer months. This is done by combining observations of vertical density structure collected by the TS mooring, introduced in Section 4.3, with measurements of chl *a* and nitrate, which were collected during CTD profiles (Section 3.2 andSection 3.7) and by the Cefas SmartBuoy (Section 3.6).

7.1 Motivation

Autumnal phytoplankton blooms are considered characteristic features of the seasonal cycle of primary productivity in most temperate and subpolar oceans (Longhurst, 1995; Findlay *et al.*, 2006; Behrenfeld, 2010; Song *et al.*, 2010; Martinez *et al.*, 2011). The classical view suggests that autumn blooms are caused by the deepening of the surface mixed layer (SML) at the end of summer. Here the SML depth is increased by a combination of shear driven mixing due to wind stress acting on the sea surface, and convective overturning of the water column due to cooling of the sea surface. The increase in SML depth subsequently leads to replenishment of nutrients to the euphotic layer by entraining them from below the pycnocline. For a bloom to occur, light levels need to remain high enough during the deepening to support photosynthesis, despite the increase in SML depth resulting in phytoplankton receiving less light on average. The deepening of SML depth has also been linked to the dilution of grazers (thus reducing the prey predator encounter rate), which can further promote phytoplankton growth by decoupling phytoplankton biomass from grazing pressure by zooplankton (Smayda, 1957; Landry and Hassett, 1982; Martinez *et al.*, 2011; Behrenfeld, 2010).

Compared to the sub-surface chlorophyll maximum (SCM) in summer months or the spring phytoplankton bloom, autumn blooms are less well studied. Often this is due to their relatively small surface signature, short duration and spatial and temporal variability (Colebrook and Robinson, 1961; Hu *et al.*, 2011; Chiswell, 2011; Song *et al.*, 2011), although some of these characteristics can also be attributed to the spring bloom (Thomas *et al.*, 2003; Chiswell, 2011; Song *et al.*, 2011). While observations of its occurrence and strength have been documented extensively (e.g. Thomas *et al.*, 2003; Aiken *et al.*, 2004; Henson *et al.*, 2009; Chiswell, 2011; Chiswell *et al.*, 2013), its significance within the seasonal cycle of primary production is not well quantified. The full seasonal coverage provided by this study permits quantitative analysis of the autumn bloom period in terms of total seasonal productivity.

7.2 Biogeochemical observations

The seasonal cycle of primary production in the Celtic Sea is, like in other seasonally stratifying shelf sea regions, tightly coupled to the change in vertical water column structure (Tett *et al.*, 1993; Thomas *et al.*, 2003; Hu *et al.*, 2011; Sharples *et al.*, 2013). The long-term observations of surface chl *a* [mg m^{-3}] and nitrate [μmol l^{-1}] shown in Figure 7.1c & d demonstrated a clear response to the seasonal cycle of vertical density structure described in Section 4.3.

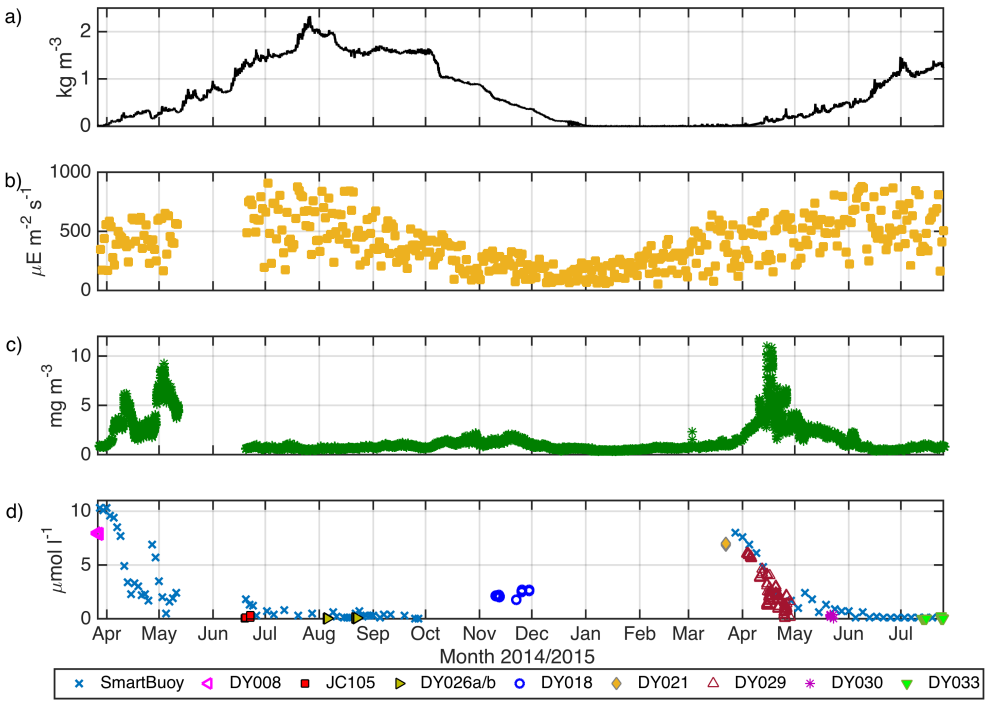

FIGURE 7.1: Combined physical and biogeochemical observations: a) top-bottom potential density difference [kg m^{-3}]. b) daily averaged photosynthetically active radiation (PAR) [μE m^{-2} s^{-1}]. c) surface chl *a* [mg m^{-3}]. In order to omit artefacts due to non-photochemical quenching only data when PAR < 10 μE m^{-2} s^{-1} were included here. d) nitrate concentration [μmol l^{-1}] in the surface mixed layer. Markers denote the SmartBuoy platform and CTD derived values during the process cruises (Table 3.1).

At the beginning of the observations in March 2014, before stratification was fully established, chl *a* concentrations were low (< 1 mg m^{-3}) and nitrate concentrations were high (~ 9 μmol l^{-1}) throughout the water column from the previous winter. As

spring stratification became established a phytoplankton bloom was initiated, which peaked on April 11$^{\text{th}}$ 2014 with surface chl *a* concentrations of up to 6.2 mg m^{-3}. Consequently the available nitrate in the SML became quickly depleted and concentrations dropped to $\sim$ 2.5 μmol l^{-1}. During stratified periods, the diapycnal transport of momentum, heat and tracers is restricted due to suppressed turbulent motions in the pycnocline. Thus the resupply of inorganic nutrients from the dark, nutrient rich bottom waters to the well-lit, nutrient depleted surface waters is inhibited. The resulting nutrient limitation, and potentially also an increased impact of grazers, led to a decrease in the surface population and the demise of the spring bloom. The secondary peak in surface nitrate concentration around April 26$^{\text{th}}$ 2014 was induced by a strong storm event (Section 4.3.1). Here, strong wind and waves deepened the SML by $\approx$ 20 metres over a 36 hour period (Figure 4.12a) and thereby entrained dissolved nutrients from the bottom mixed layer (BML), raising surface nitrate concentrations to 6.9 μmol l^{-1}. Subsequently a secondary phytoplankton bloom was initiated, with surface chl *a* concentrations of up to 9 mg m^{-3} that peaked on May 4$^{\text{th}}$ 2014.

On May 12$^{\text{th}}$ the Cefas SmartBuoy platform drifted away from its location and hence no surface nitrate and chl *a* observations were available from CCS until June 19$^{\text{th}}$ 2014. At this time the vertical profiles of density, nitrate and chl *a* resembled that of a typical shelf sea summer profile as also observed in other studies e.g. (Pingree *et al.*, 1976; Williams *et al.*, 2013; Townsend *et al.*, 2015). Compared to the spring phytoplankton bloom at the surface, the biomass peak had been shifted to the interior of the water column to the SCM. In all coincident, full depth profiles of CTD, nitrate and chl *a* at CCS, the SCM was located within the base of the pycnocline and in the vicinity of the nitracline. Here, turbulence from internal mixing mechanisms, for example internal waves, together with the strong nutrient gradient (the nitracline) caused an upward flux of nutrients that sustained this biomass peak (Holligan *et al.*, 1984; Williams *et al.*, 2013; Lee *et al.*, 2016). Peak concentrations of chl *a* within the sub-surface chlorophyll maximum (SCM) were variable (average 2.06 $\pm$ 0.92 mg chl *a* m^{-3}; *ns*=9), while chl *a*

concentrations within the SML were uniformly low (average 0.31 ± 0.1 mg chl *a* m^{-3}; *ns*=9).

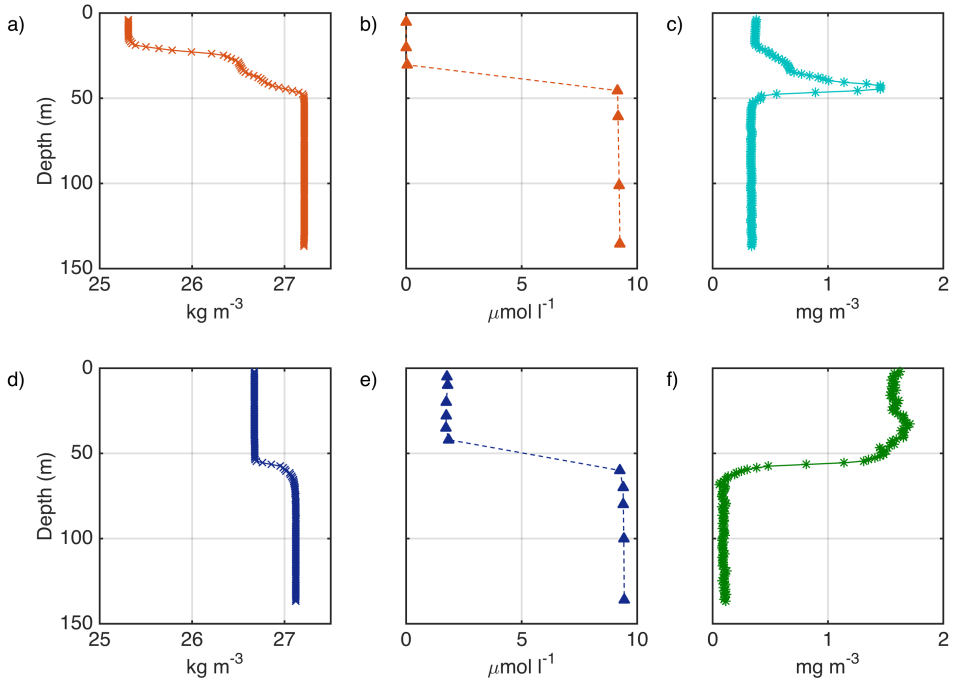

FIGURE 7.2: Vertical profiles during a)-c): summer (DY026a/b) and d)-f): autumn (DY018). a) & d) potential density [kg m^{-3}]. b) & e) nitrate [μmol l^{-1}]. c) & f) chl *a* [mg m^{-3}].

The breakdown of stratification commenced in early October 2014 due to increased wind mixing and surface cooling (Section 4.3.2). While this resulted in a deepening of the SML and sharpening of the pycnocline (Figure 7.2a, d), it also transformed the vertical structure of chlorophyll biomass and inorganic nutrients. Figure 7.2 illustrates the change in vertical structure between summer (Figure 7.2a-c) and autumn (Figure 7.2d-f) 2014: The deepening of the mixed layer resulted in entrainment of nutrients from below the pycnocline, which increased surface nitrate concentrations by 2.24 ± 0.36 μmol l^{-1} (Figure 7.1d). This increase was seen over the entire SML (Figure 7.2b & e). The deepening also led to the erosion of the SCM and instead a vertically homogenous profile of chlorophyll biomass was established above the pycnocline (Figure 7.2c & f). Simultaneously an increase in surface chl *a* concentrations of up to 2.2 mg m^{-3}

(Figure 7.1c) was observed, which could be indicative of an autumnal bloom driven by the resupply of nutrients replenished by SML deepening. Surface light levels were low during this period, and less than half of spring and summer photosynthetically active radiation (PAR) levels (Figure 7.1b).

Surface chl *a* concentrations dropped to winter background levels of < 1 mg m^{-3} around December 13 th 2014 and stayed low during the mixed winter period. While nitrate data were unusable between October 16th 2014 and March 20th 2015 due to problems with the preservative (T. Hull, personal communication, 29.04.2016), pre bloom nitrate concentrations of $\sim$7.5 μmol l^{-1} were observed during the DY021 March process cruise.

The phytoplankton spring bloom that followed the onset of stratification in 2015 (Section 4.3.3), was significantly stronger in magnitude compared to 2014, with peak surface chl *a* concentrations of up to 11 mg m^{-3}. In general, the 2015 bloom had more peaks and hence the main phytoplankton bloom event was less well defined compared to 2014. Following the spring phytoplankton bloom in 2015 chl *a* concentrations within the SML dropped back to low summer values (average 0.16 $\pm$ 0.05 mg chl *a* m^{-3}; *ns*=40). Peak chl *a* concentrations within the SCM were again variable (average 1.05 $\pm$ 0.41 mg chl *a* m^{-3}; *ns*=40).

7.3 Discussion

New observations of surface chl *a* and nitrate concentrations collected at CCS throughout the 17-month observational campaign were presented. These showed a clear response to the seasonal evolution of vertical density structure presented in Section 4.3. It was shown that the deepening of the SML depth in autumn 2014, replenished inorganic nutrient concentrations in the surface layer. At the same time, the erosion of the summer SCM peak by homogenising the vertical chlorophyll biomass profile over the

entire SML was observed. Thus it raised the question whether the observed increase in surface chl *a* was linked to in-situ growth due to replenishment of nutrients that was indicative of an autumn phytoplankton bloom, or simply a redistribution of the subsurface phytoplankton community, which was available before surface deepening began. In an attempt to answer this question the depth integrated chlorophyll biomass was computed.

Figure 7.3 shows the seasonal cycle of depth integrated chlorophyll biomass [mg m^{-2}] during the stratified periods of 2014 and 2015. These were calculated by taking the depth integral from the surface to the top of the BML depth for all available CTD profiles. In most vertical profiles of chl *a* evidence of photochemical quenching was found during daytime CTDs in the near surface. To avoid underestimating the depth integrated chlorophyll biomass values, chl *a* values were extrapolated from the SML depth to the near surface using nearest neighbour extrapolation for all daytime CTDs. This led to an average increase of 4% compared to using non-corrected profiles of chl *a*.

To estimate depth integrated biomass from surface chl *a* concentrations, recorded by the SmartBuoy, a homogeneous profile of chl *a* throughout the SML was assumed, as had been observed during DY018 (Figure 7.2f). The depth integral from the surface to the SML depth was then taken and hence this should be considered as a minimum estimate of chlorophyll biomass.

As might be expected, the highest observed values of 186 mg m^{-2} were found during the spring bloom cruise (DY029) in 2015. In contrast to this, the summer values (JC105, DY026a/b, DY030 and DY033) were relatively low, yet variable (average 21.33 $\pm$ 9.89 mg Chl *a* m^{-2}, n= 55), but similar in magnitude to values observed by Hickman *et al.* (2012) during a previous study in the Celtic Sea. As soon as the vertical water column structure began to break down in early October 2014 (Section 4.3.2), a sharp increase in integrated chlorophyll biomass of up to 90 mg m^{-2} compared to

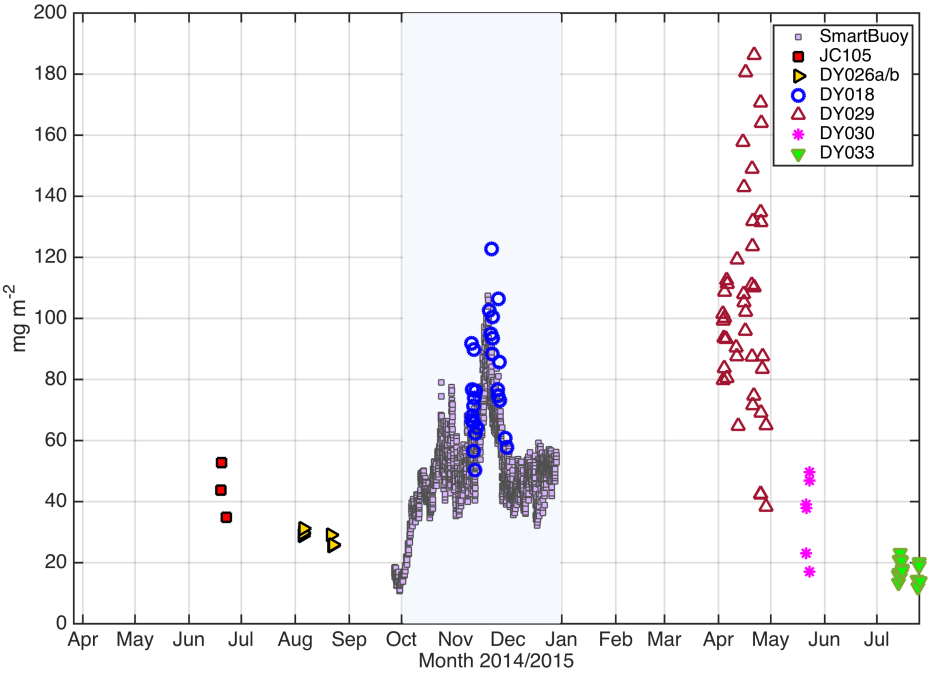

FIGURE 7.3: Depth integrated chl *a* biomass [mg m^{-2}]. Markers denote the SmartBuoy platform and CTD derived values during the stratified periods of observations. The shaded area denotes the time of active SML deepening (October 2nd - December 31st 2014). For comparison SmartBuoy data before the breakdown of stratification had started was also included.

summer values was observed (Figure 7.3). This increase is indicative of in-situ growth fuelled by the resupply of inorganic nutrients to the euphotic layer from depth, as opposed to a redistribution of chl *a*, and the availability of sufficient light to sustain an autumnal phytoplankton bloom. However, these relatively low light levels during this period (Figure 7.1b) resulted in primary production becoming light limited, as not all available inorganic nutrients in the SML were used up during the bloom (Figure 7.2e).

To further study this light limitation the SML depth was compared to the critical depth, z_{cr}, the depth where integrated losses and production balances. The concept of z_{cr} was developed by Sverdrup in 1953 as part of his critical depth theory (SCD) (Sverdrup, 1953), which predicts the onset of a phytoplankton bloom when the actively turbulent layer shoals above the critical depth (Franks, 2015). As a result phytoplankton are no longer light limited, growth outweighs losses, and a phytoplankton bloom can occur.

This concept has been usually applied to study the mechanisms triggering the onset of the spring phytoplankton bloom (Siegel *et al.*, 2002) but has recently received considerable debate regarding its validity (Behrenfeld, 2010; Taylor and Ferrari, 2011; Brody and Lozier, 2014). Interestingly, Chiswell (2011) & Chiswell *et al.* (2015) proposed that the SCD may actually apply in autumn and winter to determine the shut-off of primary production. One of the SCD's main assumption regards an actively turbulent surface layer that ensures equal light exposure, rather than a surface mixed layer that is defined by a fixed difference in temperature/density to a near surface value, (Franks, 2015). In contrast to most spring conditions, during autumn the SML $\simeq$ the 'actively turbulent layer', as the SML is being actively deepened, which homogenises the surface layer (Figure 7.2d-f). The SML depth was therefore here used as an indicator for the depth of the turbulent layer during autumn. Values for z_{cr} [metres] were calculated following Siegel *et al.* (2002):

$$\frac{1}{Kz_{cr}}\left(1 - e^{-Kz_{cr}}\right) = \frac{I_c}{I_0} \tag{7.1}$$

where $K = 0.1$ m^{-1} is the attenuation coefficient, I_c [mol m^{-2} d^{-1}] is the compensation irradiance, where integrated losses and production balances, and I_0 [mol m^{-2} d^{-1}] is the surface irradiance. Here z_{cr} was evaluated for for $I_c = 1.24$ mol m^{-2} d^{-1} a value obtained by Siegel *et al.* (2002) for an open ocean zonal average between 45-50° N, and $I_c = 3.03$ mol m^{-2} d^{-1} a value observed by Langdon (1988) for a coastal dinoflagellate. For comparison, values of z_{cr} calculated for the Celtic Sea by Pingree *et al.* (1976) were also included.

As might be expected, all variants of z_{cr} showed a clear seasonal cycle with deepest values during summer and shallowest during winter (Figure 7.4a), which is in good agreement with the magnitude of surface irradiance (Figure 7.1b). While the values calculated by Pingree *et al.* (1976) clearly show a stronger response to the seasonal cycle, the timings at which z_{cr} became shallower/deeper than the SML were similar to the values calculated within this thesis. Without knowledge of the observed turbulence

during the onset of spring stratification one cannot draw a conclusion from the SML depth versus z_{cr} to predict the onset of the spring phytoplankton bloom. The focus within this thesis is therefore solely on the autumn period (Figure 7.4b-c). During the first half of the autumn bloom period the SML $< z_{cr}$ (Figure 7.4b) and surface chl *a* concentrations were increasing (Figure 7.4c). During the second half of this period the SML approached z_{cr}, while surface chl *a* concentrations were steadily decreasing. SML $> z_{cr}$ around December 13th 2014 (Section 4.3.2), which coincided with surface chl *a* concentrations dropping to winter background levels of < 1 mg m^{-3} (Figure 7.1c). This observed relationship does suggest that the SCD might be applicable to winter conditions and can be used to predict the shut-down of the autumn bloom, based on SML depth and surface irradiance values.

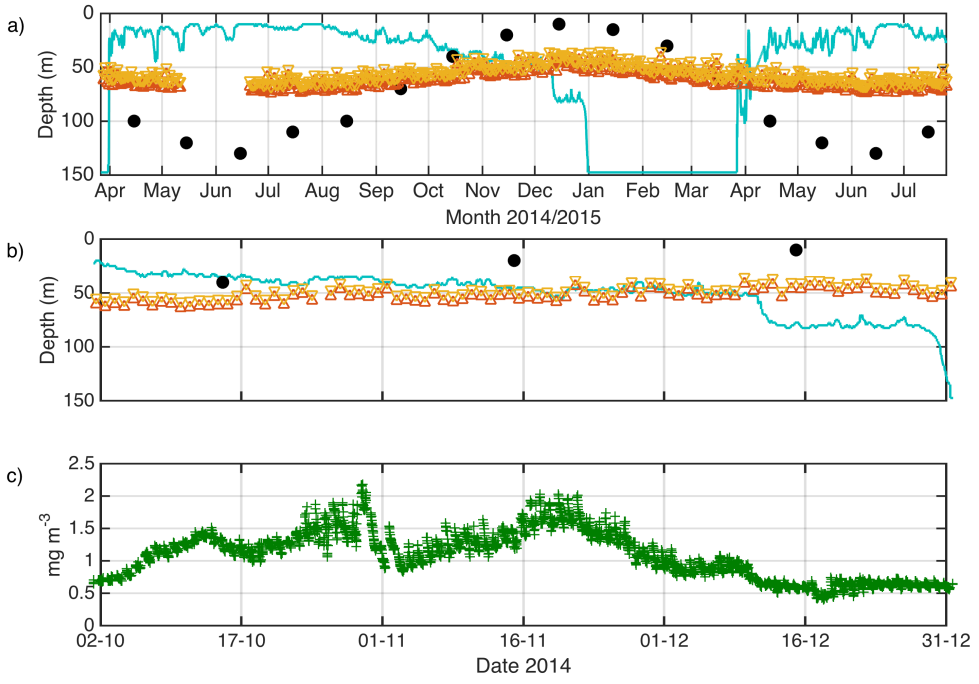

FIGURE 7.4: Critical depth hypothesis. a) Seasonal cycle of SML depth [metre] (turquoise) compared to calculated values of z_{cr} using $I_c = 1.24$ mol m^{-2} d^{-1} (orange), $I_c = 3.03$ mol m^{-2} d^{-1} (yellow) and z_{cr} by Pingree *et al.* (1976) (black) b) same as a) but focused on autumn phytoplankton bloom period. c) surface chl *a* [mg m^{-3}] during autumn phytoplankton bloom period.

In order to quantify the autumn bloom's magnitude within the seasonal cycle of primary production its potential contribution to the annual budget and rates of carbon fixation were calculated:
At first the average change in SML depth between summer (DY026) and autumn (DY018) was estimated as $\approx$ 32 metres, and the total new supply of nitrate due to SML deepening as 5.5 $\pm$ 0.1 μmol l^{-1}. The uptake of nitrate was then derived from the difference of the newly replenished nitrate concentration and the surface nitrate concentrations observed during the bloom event as 3.4 $\pm$ 0.1 μmol l^{-1} and a new SML depth of $\approx$ 52 metres (Figure 7.2e). Assuming the phytoplankton growth maintained a C:N Redfield ratio of 6.625 (Redfield, 1934) the autumn phytoplankton bloom potentially supported 14.1 $\pm$ 0.2 g C m^{-2}.

In order to put the autumn phytoplankton bloom into context with other events during the seasonal cycle the equivalent new production was calculated per season (Figure 7.5). To enable direct comparison to the autumn production the same fixed C:N ratio of 6.625 was used for all seasons. While it is well documented that the C:N ratio varies seasonally and for different species (e.g. Sterner and Elser, 2002), observed rates of C:N were not available for all seasons, and hence a fixed uptake ratio was used.

For spring values calculations of new primary production were based on the initial nitrate concentration in the SML prior to the bloom and the average depth of the SML during the spring bloom. During summer months surface nutrients were depleted (Figure 7.1d) and hence new primary production within the SCM depended on diapycnal nutrient fluxes from the BML, which is the product of the vertical diffusivity at the base of the pycnocline, K_z [m^2 s^{-1}], multiplied by the vertical nitrate gradient $\frac{\Delta \mathrm{Ni}}{\Delta z}$ [mmol m^{-4}]. Here, ΔNi is difference of nitrate within the SML and BML, and Δz is the thickness of the nitracline.

Due to the relatively low vertical resolution of discrete bottle samples, especially compared to physical data (Figure 7.2a-c), deducing the thickness of the nitracline from

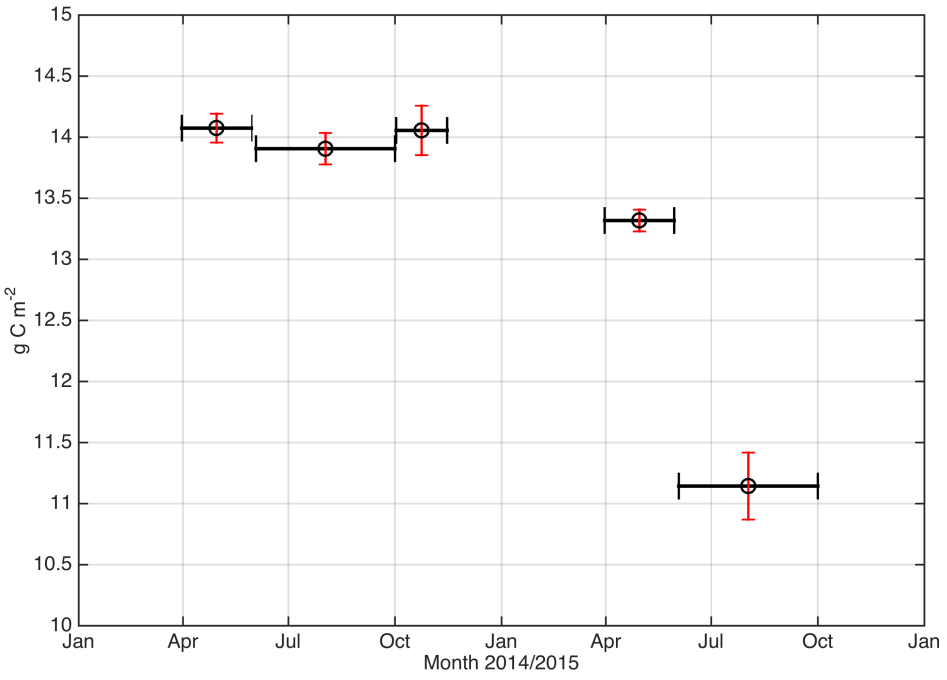

FIGURE 7.5: Seasonal cycle of carbon fixation. Circles denote amounts of g carbon m^{-2} fixed per season (spring 2014, summer 2014, autumn 2014, spring 2015, summer 2015). Red lines represent 1 standard deviation. Black bars show duration of each event.

discrete data points would have resulted in an underestimate of the nitrate gradient. Instead, following the methods by Sharples *et al.* (2001), the thickness of the nitracline was defined as the distance between the depth of the SCM peak and the BML depth. For K_z a typical background diffusivity (at the base of the pycnocline) of 1×10^{-5} m^2 s^{-1} (Townsend, 1991; Benitez-Nelson *et al.*, 2000; Sharples *et al.*, 2001, 2009) was used. As already mentioned by Townsend (1991), the amount of new production is extremely sensitive to the chosen value of K_z, and in reality the nitrate flux will vary with time in response to changes in tidal, wind and internal mixing (Sharples, 2008; Burchard and Rippeth, 2009; Williams *et al.*, 2013), e.g. Chapter 6. The error bounds presented here take, account of uncertainties in nitrate concentrations (1 standard deviation, DY026a,b *ns*=35, DY018 *ns*=26) within the SML & BML.

As can be seen from Figure 7.5 the estimate of carbon fixation during the autumn

phytoplankton bloom of 14.1 ± 0.2 g C m^{-2} was similar in magnitude to the spring and summer production 2014, each of these fixing 14.1 ± 0.1 and 13.9 ± 0.1 g C m^{-2}, respectively. Carbon fixation throughout 2014 also appeared to be greater than spring and summer production in the following year, during which spring and summer production each fixed 13.3 ± 0.1 and 11.1 ± 0.3 g C m^{-2} respectively. This suggest that the autumn phytoplankton bloom was between 6 and 20% stronger than the observed spring and summer seasons in 2015. In summary, the autumn phytoplankton bloom thus has the potential to be as productive as the well studied spring bloom and summer SCM.

A potential reason for this decreased production observed in 2015, is the decreased nitrate inventory at the start of the onset of stratification in 2015, which was 21% lower compared to 2014 levels (Figure 7.1d). Secondly, reduced levels of stratification in 2015 compared to 2014 (Section 4.3.4), led to $\frac{\Delta \mathrm{Ni}}{\Delta z}$ being 24% lower than observed during 2015.

7.4 Summary: Biogeochemical environment

This aim of this chapter was to provide a first attempt at investigating the biogeochemical response to the change in vertical density structure observed throughout the seasonal cycle at CCS. The focus of the chapter was on the effect the transition of vertical water column structure from summer to autumn had on the inorganic nutrients and chlorophyll biomass. SML deepening during this period eroded an established SCM, whilst replenishing surface concentrations of nitrate. A subsequent increase in surface chl *a* concentrations suggested in-situ growth, which was confirmed by examining depth integrated chlorophyll biomass. The presence of detectable nitrate concentrations within the surface layer also suggested that primary production had shifted to become light limited.

It was further investigated what role the autumn phytoplankton bloom plays within the seasonal cycle and estimated its contribution to the annual primary production. It was illustrated that the autumn phytoplankton bloom has the potential to be as productive as the well-studied spring phytoplankton bloom and the summer SCM and the capacity to significantly contribute to the drawdown of atmospheric CO_2.

Chapter 8

Summary and conclusions

This thesis has presented and examined new, high-resolution measurements of unprecedented detail spanning 17-months (March 2014 – July 2015) collected on the North-West European Shelf as part of the UK Shelf Sea Biogeochemistry programme. A long-term mooring array collected measurements of full-depth density (Wihsgott *et al.*, 2016) and velocity structure, meteorological and wave forcing, surface nitrate and surface chl *a* at the centre of the Celtic Sea (CCS), in a mean water depth of 145.4 metres. The observations at CCS captured a full seasonal cycle of stratification and its control on the seasonal cycle of primary production. The key strengths of this dataset were the combination of its length and its high sampling resolution. This provided an excellent opportunity to investigate the seasonality of key controls on the vertical density structure and its biogeochemical response in a temperate shelf sea. The length of the observations ensured that signals could be interpreted against a clear, long-term context, for instance allowing the assessment of the N_2 modulation of the spring-neap effects. While key events could be investigated in detail, the long-term record enabled putting them in context within the seasonal cycle.

An important result of this thesis showed that the controls on vertical density structure at CCS were largely analogous to that of open-ocean environments (Kraus and Turner,

1967), with tidal mixing only playing a minor role. While the tide keeps the bottom boundary layer mixed all year round it appeared to only erode stratification towards the end of the seasonal cycle as the pycnocline had been lowered sufficiently. This result contrasts with the well-known tidally controlled frontal systems described by Simpson and Hunter (1974); Simpson *et al.* (1978) and Simpson and Bowers (1984). Since a large proportion of continental shelf regions are away from tidal mixing fronts this is an important result as it highlights the need for an adjusted third regime that bridges the gap between open-ocean environments and frontal regions.

A second key result of this thesis was the observed seasonality in internal wave energy, which suggested seasonally varying levels of internal wave mixing due to enhanced levels of S^2 that varied relative to the seasonal cycle of N^2. By investigating the representation of this seasonality by three commonly used internal wave parameterisations it was shown that each predicted a seasonality that directly contradicted that observed within the internal wave energy. It was suggested that the reason for this was that the models scaled internal mixing inversely with N^2. In an attempt to provide realistic scaling of turbulence an adjusted iteration of the MacKinnon and Gregg (2003a) scaling of turbulence was employed, which proved successful in replicating the suggested seasonal cycle of internal wave mixing relative to N^2. This is an important result as it highlights the need of future internal wave mixing parameterisations to scale mixing due to enhanced levels of S^2 from internal waves relative to the seasonal cycle of N^2. This result is also important in relation to better representing the supply of nutrients to the SCM during the summer stratified period of temperate shelf seas.

The final significant result of this thesis shows that the autumn phytoplankton bloom is a highly productive event within the seasonal cycle of primary production. It was shown that in-situ growth due to replenishment of surface nutrients during the autumnal breakdown of stratification fuelled an autumn phytoplankton bloom. By putting the autumn phytoplankton bloom within the context of the seasonal cycle it was shown that is has the potential to be as productive as the well-studied spring phytoplankton

bloom and the summer sub-surface chlorophyll maximum and thus the capacity to significantly contribute to the drawdown of atmospheric CO_2. Improving our understanding of the significance these events play within the seasonal cycle is of fundamental importance to better represent global carbon budgets and predict the response of temperate shelf seas to future climate change.

To successfully predict the observed seasonal cycle of primary production in a biogeochemical model the findings of this thesis must be appropriately parameterised to ensure accurate internal mixing. This is necessary to produce a realistic vertical density structure, and subsequently accurate light and nutrient availability, but also to provide correct timing of onset and breakdown of stratification. The identified seasonality in internal wave behaviour and its implied mixing is likely to play a critical role in balancing the energy budget, and the performance of coupled physical-biogeochemical models will likely be improved by inclusion of the reported processes. Future work stemming from this research will be to extend the capability of the prescriptive model SB84 by including a suitable biogeochemical model to assess the impact of the suggested turbulence parameterisation on biogeochemical cycles. Additionally, further work is required to extend this parameterisation for inclusion in regional scale hydrodynamic models to assess its impact on shelf sea seasonal cycles.

Appendix A

TS mooring diagrams

Instrument type	Data channels used [units]
SBE 16*plus* SeaCAT CTD	Temperature [°C] Salinity/and or conductivity [S m^{-1}] Pressue [dbar]
SBE 37 MicroCAT CTD	Temperature [°C] Salinity/and or conductivity [S m^{-1}] Pressue [dbar]
Star Oddi Starmon mini underwater temperature logger	Temperature [°C]
Star Oddi DST Centi Temperature	Temperature [°C]
RBRsolo T — Temperature Logger	Temperature [°C]

TABLE A.1: Instrument types and data channels used during 5 TS mooring deployments.

Planned deployment depth [m]	Instrument	Serial #	Comments
10	SBE 16*plus*	4597	
15	Star Oddi DST	5753	
20	Star Oddi Starmon	3578	
25	Star Oddi DST	5768	
30	SBE 37	4998	
35	Star Oddi Starmon	3584	
37	Star Oddi DST	3278	
40	Star Oddi Starmon	3580	
42	Star Oddi DST	3654	
45	SBE 16*plus*	5309	
47	Star Oddi DST	3653	
49	SBE 37	7459	
54	Star Oddi Starmon	3890	
59	Star Oddi Starmon	3581	
64	Star Oddi Starmon	3891	
69	SBE 37	2010	
79	Star Oddi Starmon	3582	
89	Star Oddi Starmon	3583	
99	SBE 37	4550	Instrument stopped recording on June 5th 2014 at 05:20:01
109	Star Oddi DST	5284	
120	Star Oddi DST	5264	
129	SBE 16*plus*	4738	
145	SBE 16*plus*	4596	

TABLE A.2: **TS1**: Available instrument data from 1st TS mooring deployment. Colours denote instrument type specified in Table A.1.

Planned deployment depth [m]	Instrument	Serial #	Comments
10	SBE 16*plus*	4848	
15	Star Oddi DST	5286	
20	Star Oddi Starmon	3893	
25	Star Oddi DST	5763	
30	SBE 37	2506	
35	Star Oddi Starmon	3594	
37	Star Oddi DST	3614	
40	Star Oddi Starmon	3896	
42	Star Oddi DST	3271	
45	SBE 16*plus*	5310	
47	Star Oddi DST	3270	
49	SBE 37	7460	
54	Star Oddi Starmon	3897	
59	Star Oddi Starmon	3899	
64	Star Oddi Starmon	3901	
69	SBE 37	2081	
74	Star Oddi DST	3655	
79	Star Oddi Starmon	3903	
89	Star Oddi Starmon	3905	
99	SBE 37	7458	
109	Star Oddi DST	3269	
120	Star Oddi DST	5263	
129	SBE 16*plus*	4737	
145	SBE 16*plus*	4736	The bedframe containing the SBE 16*plus* was deployed 3 days after the TS mooring.

TABLE A.3: **TS2**: Available instrument data from 2nd TS mooring deployment. Colours denote instrument type specified in Table A.1.

Planned deployment depth [m]	Instrument	Serial #	Comments
10	SBE 16*plus*	4597	
15	Star Oddi DST	5753	
20	Star Oddi Starmon	3578	
25	Star Oddi DST	5768	
30	SBE 37	4998	
35	Star Oddi Starmon	3584	
37	Star Oddi DST	3278	
40	Star Oddi Starmon	3580	
42	Star Oddi DST	3654	
45	SBE 16*plus*	5309	
47	Star Oddi DST	3653	
49	SBE 37	7459	
54	Star Oddi Starmon	3890	
59	Star Oddi Starmon	3581	
64	Star Oddi Starmon	3891	
69	SBE 37	2010	
74	Star Oddi DST	3661	
79	Star Oddi Starmon	3582	
89	Star Oddi Starmon	3583	
99	SBE 37	4550	
109	Star Oddi DST	5284	
120	Star Oddi DST	5264	
129	SBE 16*plus*	4738	
145	SBE 16*plus*	4596	Pressure data were suspect after 13.11.2014 19:15:03 and have been reconstructed using harmonic analysis using M2, S2, N2 and K1 constituents, which were obtained form the remaining pressure record.

TABLE A.4: **TS3**: Available instrument data from 3rd TS mooring deployment. Colours denote instrument type specified in Table A.1.

Planned deployment depth [m]	Instrument	Serial #	Comments
10	SBE 16*plus*	4848	
15	RBR Solo	76789	
20	Star Oddi Starmon	3893	
25	RBR Solo	76790	
30	SBE 37	2506	Only data that was recorded from 26.11.2014 10:10:01 onward is available as some of the initial data had been overwritten.
35	Star Oddi Starmon	3594	
37	RBR Solo	76791	
40	Star Oddi Starmon	3896	
42	RBR Solo	76792	
45	SBE 16*plus*	5310	
47	Star Oddi DST	3613	
49	SBE 37	7460	
54	Star Oddi Starmon	3897	
59	Star Oddi Starmon	3899	
64	Star Oddi Starmon	3901	
69	SBE 37	2081	Only data that was recorded from 27.11.2014 13:45:01 onward is available as some of the initial data had been overwritten.
74	RBR Solo	76794	
79	Star Oddi Starmon	3903	
89	Star Oddi Starmon	3905	
99	SBE 37	7458	
109	RBR Solo	76795	
120	RBR Solo	76796	
129	SBE 16*plus*	4737	
145	SBE 16*plus*	4736	Due to recovery problems the bedframe stayed deployed during TS4 and TS5.

TABLE A.5: **TS4**: Available instrument data from 4th TS mooring deployment. Colours denote instrument type specified in Table A.1.

Planned deployment depth [m]	Instrument	Serial #	Comments
10	SBE 16*plus*	4597	
15	RBR Solo	76797	
20	Star Oddi Starmon	3578	
25	RBR Solo	76806	
30	SBE 37	4998	
35	Star Oddi Starmon	3584	
37	RBR Solo	76807	
40	Star Oddi Starmon	3580	
42	RBR Solo	76798	
45	SBE 16*plus*	5309	
47	Star Oddi Starmon	2836	
49	SBE 37	7459	
54	Star Oddi Starmon	3890	
59	Star Oddi Starmon	3581	
64	Star Oddi Starmon	3891	
69	SBE 37	2010	
74	RBR Solo	76799	
79	Star Oddi Starmon	3582	
89	Star Oddi Starmon	3583	
99	SBE 37	5434	
109	RBR Solo	76800	
120	RBR Solo	76801	
129	SBE 16*plus*	4738	
145	SBE 16*plus*	4596	Pressure data were suspect after 9.6.2015, 11:40:01 and have been reconstructed using harmonic analysis using M2, S2, N2 and K1 constituents, which were obtained form the remaining pressure record.

TABLE A.6: **TS5**: Available instrument data from 5th TS mooring deployment. Colours denote instrument type specified in Table A.1.

Bibliography

Aiken, J., Fishwick, J., Moore, G., and Pemberton, K. (2004). The annual cycle of phytoplankton photosynthetic quantum efficiency, pigment composition and optical properties in the western English Channel. *Journal of the Marine Biological Association of the United Kingdom*, *84*(2), 301–313.

Baines, P. G. (1982). On internal tide generation models. *Deep Sea Research Part A. Oceanographic Research Papers*, *29*(3), 307–338.

Barker, L., Hannaford, J., Muchan, K., Turner, S., and Parry, S. (2016). The winter 2015/2016 floods in the UK: a hydrological appraisal. *Weather*, *71*(12), 324–333.

Bascom, W. (1964). *Waves and beaches; the dynamics of the ocean surface*. Anchor Books.

Bauer, J. E., Cai, W.-J., Raymond, P. A., Bianchi, T. S., Hopkinson, C. S., and Regnier, P. A. G. (2013). The changing carbon cycle of the coastal ocean. *Nature*, *504*(7478), 61–70.

Behrenfeld, M. J. (2010). Abandoning Sverdrup's Critical Depth Hypothesis on phytoplankton blooms. *Ecology*, *91*(4), 977–989.

Belcher, S. E., Grant, A. L. M., Hanley, K. E., Fox-Kemper, B., Van Roekel, L., Sullivan, P. P., Large, W. G., Brown, A., Hines, A., Calvert, D., Rutgersson, A., Pettersson, H., Bidlot, J.-R., Janssen, P. A. E. M., and Polton, J. A. (2012). A global perspective on Langmuir turbulence in the ocean surface boundary layer. *Geophysical Research Letters*, *39*(18).

Benitez-Nelson, C. R., O. Buesseler, K., and Crossin, G. (2000). Upper ocean carbon export, horizontal transport, and vertical eddy diffusivity in the southwestern Gulf of Maine. *Continental Shelf Research*, *20*(6), 707–736.

Bianchi, A. A., Bianucci, L., Piola, A. R., Pino, D. R., Schloss, I., Poisson, A., and Balestrini, C. F. (2005). Vertical stratification and air-sea CO2 fluxes in the Patagonian shelf. *Journal of Geophysical Research: Oceans*, *110*(C7).

Birchill, A. J., Milne, A., Woodward, E. M. S., Harris, C., Annett, A., Rusiecka, D., Achterberg, E. P., Gledhill, M., Ussher, S. J., Worsfold, P. J., Geibert, W., and Lohan, M. C. (2017). Seasonal iron depletion in temperate shelf seas. *Geophysical Research Letters*, *44*(17), 8987–8996.

Borges, A. V., Delille, B., and Frankignoulle, M. (2005). Budgeting sinks and sources of CO_2 in the coastal ocean: Diversity of ecosystems counts. *Geophysical Research Letters*, *32*(14), 1–4.

Bowers, D. G. and Simpson, J. H. (1987). Mean position of tidal fronts in European-shelf seas. *Continental Shelf Research*, *7*(1), 35–44.

Brady, D. K., Graves, W. L., and Geyer, J. C. (1969). Surface heat exchange at power plant cooling lakes. In *Cooling water discharge project report*, Volume 69. New York: Johns Hopkins Univ., Dept. of Geography and Environmental Engineering, Baltimore, MD.

Brody, S. R. and Lozier, M. S. (2014). Changes in dominant mixing length scales as a driver of subpolar phytoplankton bloom initiation in the North Atlantic. *Geophysical Research Letters*, *41*(9), 3197–3203.

Burchard, H., Petersen, O., and Rippeth, T. P. (1998). Comparing the performance of the Mellor-Yamada and the - two-equation turbulence models. *Journal of Geophysical Research: Oceans*, *103*(C5), 10543–10554.

Burchard, H. and Rippeth, T. P. (2009). Generation of Bulk Shear Spikes in Shallow Stratified Tidal Seas. *Journal of Physical Oceanography*, *39*(4), 969–985.

Cai, W.-J. (2011). Estuarine and Coastal Ocean Carbon Paradox: CO_2 Sinks or Sites of Terrestrial Carbon Incineration? *Annual Review of Marine Science*, *3*(1), 123–145.

Cai, W.-J., Dai, M., and Wang, Y. (2006). Air-sea exchange of carbon dioxide in ocean margins: A province-based synthesis. *Geophysical Research Letters*, *33*(12).

Canuto, V. M., Howard, A., Cheng, Y., and Dubovikov, M. S. (2001). Ocean Turbulence. Part I: One-Point Closure Model—Momentum and Heat Vertical Diffusivities. *Journal of Physical Oceanography*, *31*(6), 1413–1426.

Chiswell, S. M. (2011). Annual cycles and spring blooms in phytoplankton: don't abandon Sverdrup completely. *Marine Ecology Progress Series*, *443*, 39–50.

Chiswell, S. M., Bradford-Grieve, J., Hadfield, M. G., and Kennan, S. C. (2013). Climatology of surface chlorophyll a, autumn-winter and spring blooms in the southwest Pacific Ocean. *Journal of Geophysical Research: Oceans*, *118*(2), 1003–1018.

Chiswell, S. M., Calil, P. H. R., and Boyd, P. W. (2015). Spring blooms and annual cycles of phytoplankton: a unified perspective. *Journal of Plankton Research*, *37*(3), 500–508.

Colebrook, J. M. and Robinson, G. A. (1961). The seasonal cycle of the plankton in the North Sea and the north-eastern Atlantic. *Journal du Conseil*, *26*(2), 156–165.

Cottier, F., Inall, M., and Griffiths, C. (2004). Seasonal variations in internal wave energy in a Scottish sea loch. *Ocean Dynamics*, *54*(3-4), 340–347.

Craik, A. D. D. and Leibovich, S. (1976). A rational model for Langmuir circulations. *Journal of Fluid Mechanics*, *73*(3), 401–426.

Cummins, P. F. and Oey, L.-Y. (1997). Simulation of barotropic and baroclinic tides off northern British Columbia. *Journal of Physical Oceanography*, *27*(5), 762–781.

D'Asaro, E. A. (2014). Turbulence in the Upper-Ocean Mixed Layer. *Annual Review of Marine Science*, *6*(1), 101–115.

D'Asaro, E. A., Thomson, J., Shcherbina, A. Y., Harcourt, R. R., Cronin, M. F., Hemer, M. A., and Fox-Kemper, B. (2014). Quantifying upper ocean turbulence driven by surface waves. *Geophysical Research Letters*, *41*(1), 102–107.

De Boer, G. J., Pietrzak, J. D., and Winterwerp, J. C. (2008). Using the potential energy anomaly equation to investigate tidal straining and advection of stratification in a region of freshwater influence. *Ocean Modelling*, *22*(1), 1–11.

de Boyer Montégut, C., Madec, G., Fischer, A. S., Lazar, A., and Iudicone, D. (2004). Mixed layer depth over the global ocean: An examination of profile data and a profile-based climatology. *Journal of Geophysical Research: Oceans*, *109*(C12), C12003.

Dee, D. P., Uppala, S. M., Simmons, A. J., Berrisford, P., Poli, P., Kobayashi, S., Andrae, U., Balmaseda, M. A., Balsamo, G., Bauer, P., Bechtold, P., Beljaars, A. C. M., van de Berg, L., Bidlot, J., Bormann, N., Delsol, C., Dragani, R., Fuentes, M., Geer, A. J., Haimberger, L., Healy, S. B., Hersbach, H., Hólm, E. V., Isaksen, L., Kållberg, P., Köhler, M., Matricardi, M., McNally, A. P., Monge-Sanz, B. M., Morcrette, J. J., Park, B. K., Peubey, C., de Rosnay, P., Tavolato, C., Thépaut, J. N., and Vitart, F. (2011). The ERA-Interim reanalysis: configuration and performance of the data assimilation system. *Quarterly Journal of the Royal Meteorological Society*, *137*(656), 553–597.

Doney, S. C. and Schimel, D. S. (2007). Carbon and Climate System Coupling on Timescales from the Precambrian to the Anthropocene. *Annual Review of Environment and Resources*, *32*(1), 31–66.

D'Ortenzio, F., Iudicone, D., de Boyer Montegut, C., Testor, P., Antoine, D., Marullo, S., Santoleri, R., and Madec, G. (2005). Seasonal variability of the mixed layer depth in the Mediterranean Sea as derived from in situ profiles. *Geophysical Research Letters*, *32*(12).

Dunne, J. P., Sarmiento, J. L., and Gnanadesikan, A. (2007). A synthesis of global particle export from the surface ocean and cycling through the ocean interior and on the seafloor. *Global Biogeochemical Cycles*, *21*(4), 1–16.

Edinger, J. E., Brady, D. K., and Geyer, J. C. (1974). *Heat exchange and transport in the environment. Report No. 14.* Johns Hopkins Univ., Baltimore, MD (USA). Dept. of Geography and Environmental Engineering.

Edinger, J. E., Duttweiler, D. W., and Geyer, J. C. (1968). The response of water temperatures to meteorological conditions. *Water Resources Research*, *4*(5), 1137–1143.

Egbert, G. D. and Ray, R. D. (2000). Significant dissipation of tidal energy in the deep ocean inferred from satellite altimeter data. *Nature*, *405*(6788), 775–778.

Elliott, A. J. and Clarke, T. (1991). Seasonal stratification in the northwest European shelf seas. *Continental Shelf Research*, *11*(5), 467–492.

Farge, M. (1992). Wavelet transforms and their applications to turbulence. *Annual Review of Fluid Mechanics*, *24*(1), 395–458.

Findlay, H. S., Yool, A., Nodale, M., and Pitchford, J. W. (2006). Modelling of autumn plankton bloom dynamics. *Journal of Plankton Research*, *28*(2), 209–220.

Flather, R. A. (1976). A tidal model of the northwest European continental shelf. *Mem. Soc. R. Sci. Liege*, *10*(6), 141–164.

Franks, P. J. S. (2015). Has Sverdrup's critical depth hypothesis been tested? Mixed layers vs. turbulent layers. *ICES Journal of Marine Science: Journal du Conseil*, *72*(6), 1897–1907.

Galperin, B., Kantha, L. H., Hassid, S., and Rosati, A. (1988). A Quasi-equilibrium Turbulent Energy Model for Geophysical Flows. *Journal of the Atmospheric Sciences*, *45*(1), 55–62.

Garratt, J. R. (1977). Review of Drag Coefficients over Oceans and Continents. *Monthly Weather Review*, *105*(7), 915–929.

Garrett, C. and Kunze, E. (2007). Internal Tide Generation in the Deep Ocean. *Annual Review of Fluid Mechanics*, *39*(1), 57–87.

Garrett, C. and Munk, W. (1979). Internal Waves in the Ocean. *Annual Review of Fluid Mechanics*, *11*(1), 339–369.

Garrett, C. J. R., Keeley, J. R., and Greenberg, D. A. (1978). Tidal Mixing versus Thermal Stratification in the Bay of Fundy and Gulf of Maine. *Atmosphere-Ocean*, *16*(4), 403–423.

Geernaert, G. L. (1987). On the importance of the drag coefficient in air-sea interactions. *Dynamics of Atmospheres and Oceans*, *11*(1), 19–38.

Gill, A. E. (1982). *Atmosphere-Ocean Dynamics. International Geophysics Series*, Volume 30. Academic Press, New York.

Green, J. M., Simpson, J. H., Legg, S., and Palmer, M. R. (2008). Internal waves, baroclinic energy fluxes and mixing at the European shelf edge. *Continental Shelf Research*, *28*(7), 937 – 950.

Gregg, M. C. (1989). Scaling Turbulent Dissipation in the Thermocline. *Journal of Geophysical Research: Oceans (1978–2012)*, *94*(C7), 9686–9698.

Henson, S. A., Dunne, J. P., and Sarmiento, J. L. (2009). Decadal variability in North Atlantic phytoplankton blooms. *Journal of Geophysical Research: Oceans*, *114*(C4).

Hickman, A. E., Moore, C. M., Sharples, J., Lucas, M. I., Tilstone, G. H., Krivtsov, V., and Holligan, P. M. (2012). Primary production and nitrate uptake within the seasonal thermocline of a stratified shelf sea. *Marine Ecology Progress Series*, *463*, 39–57.

Hofmeister, R., Burchard, H., and Bolding, K. (2009). A three-dimensional model study on processes of stratification and de-stratification in the Limfjord. *Continental Shelf Research*, *29*(11), 1515–1524.

Holligan, P. M. (1981). Biological Implications of Fronts on the Northwest European Continental Shelf. *Philosophical Transactions of the Royal Society of London. Series A, Mathematical and Physical Sciences*, *302*(1472), 547.

Holligan, P. M. (1989). Primary Productivity in the Shelf Seas of North-West Europe. *Advances in Botanical Research*, *16*, 193–252.

Holligan, P. M., Williams, P. J. l., Purdie, D., and Harris, R. P. (1984). Photosynthesis, respiration and nitrogen supply of plankton populations in stratified, frontal and tidally mixed shelf waters. *Marine ecology. Progress series*, *17*(2), 201–213.

Holloway, P. E. (1994). Observations of Internal Tide Propagation on the Australian North West Shelf. *Journal of Physical Oceanography*, *24*(8), 1706–1716.

Holt, J. T. and James, I. D. (2001). An s coordinate density evolving model of the northwest European continental shelf: 1. Model description and density structure. *Journal of Geophysical Research: Oceans*, *106*(C7), 14015–14034.

Holte, J. and Talley, L. (2009). A New Algorithm for Finding Mixed Layer Depths with Applications to Argo Data and Subantarctic Mode Water Formation. *Journal of Atmospheric and Oceanic Technology*, *26*(9), 1920–1939.

Hopkins, J. E., Stephenson, G. R., Green, J. M., Inall, M. E., and Palmer, M. R. (2014). Storms modify baroclinic energy fluxes in a seasonally stratified shelf sea: Inertial-tidal interaction. *Journal of Geophysical Research: Oceans*, *119*(10), 6863–6883.

Howard, L. N. (1961). Note on a paper of John W. Miles. *Journal of Fluid Mechanics*, *10*(04), 509–512.

Hu, S., Chen, C., Ji, R., Townsend, D. W., Tian, R., Beardsley, R. C., and Davis, C. S. (2011). Effects of surface forcing on interannual variability of the fall phytoplankton bloom in the Gulf of Maine revealed using a process-oriented model. *Marine Ecology Progress Series*, *427*, 29–49.

Hull, T., Greenwood, N., Kaiser, J., and Johnson, M. (2016). Uncertainty and sensitivity in optode-based shelf-sea net community production estimates. *Biogeosciences*, *13*(4), 943–959.

Huthnance, J. M. (1989). Internal tides and waves near the continental shelf edge. *Geophysical Astrophysical Fluid Dynamics*, *48*(1-3), 81–106.

Hydes, D. J., Aoyama, M., Aminot, A., Bakker, K., Becker, S., Coverly, S., Daniel, A., Dickson, A., Grosso, O., Kerouel, R., Van Ooijen, J., Sato, K., Tanhua, T., Woodward, E. M. S., and Zhang, J. (2010). Determination of dissolved nutrients (N, P, Si) in seawater with high precision and inter-comparability using gas-segmented continuous flow analysers. In *The GO-SHIP Repeat Hydrography Manual : A Collection*

of Expert Reports and guidelines. IOCCP Report No 14, ICPO Publication Series No. 134, version 1. 2010 (UNESCO/IOC).

Inall, M. E., Aleynik, D., Boyd, T., Palmer, M. R., and Sharples, J. (2011). Internal tide coherence and decay over a wide shelf sea. *Geophysical Research Letters*, *38*(23), L23607.

Inall, M. E., Rippeth, T. P., and Sherwin, T. J. (2000). Impact of nonlinear waves on the dissipation of internal tidal energy at a shelf break. *Journal of Geophysical Research: Oceans*, *105*(C4), 8687–8705.

International Association of Geomagnetism and Aeronomy, W. G. V.-M. P. m., Finlay, C. C., Maus, S., Beggan, C. D., Bondar, T. N., Chambodut, A., Chernova, T. A., Chulliat, A., Golovkov, V. P., Hamilton, B., Hamoudi, M., Holme, R., Hulot, G., Kuang, W., Langlais, B., Lesur, V., Lowes, F. J., Lühr, H., Macmillan, S., Mandea, M., McLean, S., Manoj, C., Menvielle, M., Michaelis, I., Olsen, N., Rauberg, J., Rother, M., Sabaka, T. J., Tangborn, A., Tøffner-Clausen, L., Thébault, E., Thomson, A. W. P., Wardinski, I., Wei, Z., and Zvereva, T. I. (2010). International Geomagnetic Reference Field: the eleventh generation. *Geophysical Journal International*, *183*(3), 1216–1230.

Ivanoff, A. (1977). Oceanic absorption of solar energy. In E. B. Kraus (Ed.), *Modelling and Prediction of the Upper Layers of the Ocean*, 47–71. Oxford Pergamon Presk.

James, I. D. (1977). A model of the annual cycle of temperature in a frontal region of the Celtic Sea. *Estuarine and Coastal Marine Science*, *5*(3), 339–353.

Jevrejeva, S., Moore, J. C., and Grinsted, A. (2003). Influence of the Arctic Oscillation and El Niño-Southern Oscillation (ENSO) on ice conditions in the Baltic Sea: The wavelet approach. *Journal of Geophysical Research: Atmospheres*, *108*(D21).

Kantha, L. H. and Clayson, C. A. (1994). An improved mixed layer model for geophysical applications. *Journal of Geophysical Research: Oceans*, *99*(C12), 25235–25266.

Kendon, M. and McCarthy, M. (2015). The UK's wet and stormy winter of 2013/2014. *Weather*, *70*(2), 40–47.

Kirkwood, D. (1996). *Nutrients: Practical notes on their determination in sea water.* Number 17. International Council for the Exploration of the Sea.

Kraus, E. B. and Turner, J. S. (1967). A one-dimensional model of the seasonal thermocline II. The general theory and its consequences. *Tellus*, *19*(1), 98–106.

Kröger, S., Parker, E. R., Metcalfe, J. D., Greenwood, N., Forster, R. M., Sivyer, D. B., and Pearce, D. J. (2009). Sensors for observing ecosystem status. *Ocean Science*, *5*(4), 523–535.

Kunze, E., Rosenfeld, L. K., Carter, G. S., and Gregg, M. C. (2002). Internal Waves in Monterey Submarine Canyon. *Journal of Physical Oceanography*, *32*(6), 1890–1913.

Lacombe, H., Tchernia, P., Charcot, J., Ribet, M., Bonnot, J., Frassetto, R., and Swallow, J. C. (1970). Observation of formation of deep water in the Mediterranean Sea, 1969. *Nature*, *227*, 1037–1040.

Landry, M. R. and Hassett, R. P. (1982). Estimating the Grazing Impact of Marine Micro-zooplankton. *Marine Biology*, *67*(3), 283–288.

Langdon, C. (1988). On the causes of interspecific differences in the growth-irradiance relationship for phytoplankton. II. A general review. *Journal of Plankton Research*, *10*(6), 1291–1312.

Langmuir, I. (1938). Surface motion of water induced by wind. *Science*, *87*(2250), 119–123.

Lee, K., Matsuno, T., Endoh, T., Ishizaka, J., Zhu, Y., Takeda, S., and Sukigara, C. (2016). A role of vertical mixing on nutrient supply into the subsurface chlorophyll maximum in the shelf region of the East China Sea. *Continental Shelf Research*, *143*, 139–150.

Li, M., Garrett, C., and Skyllingstad, E. (2005). A regime diagram for classifying turbulent large eddies in the upper ocean. *Deep Sea Research Part I: Oceanographic Research Papers*, *52*(2), 259–278.

Linden, P. F. (1979). Mixing in Stratified Fluids. *Geophysical & Astrophysical Fluid Dynamics*, *13*(1), 3–23.

LinkQuest Inc. (2013). FlowQuest 150 Long-range Acoustic Current Profiler Data Sheet. `http://www.link-quest.com/html/FlowQuest150.pdf`. Online; accessed: 15.03.2017.

Liu, K.-K. (2010). Biogeochemistry of Continental Margins in a Global Context. In K.-K. Liu, L. Atkinson, R. Quiñones, and L. Talaue-McManus (Eds.), *Carbon and nutrient fluxes in continental margins: a global synthesis*, Volume 3–24 of *IGBP Book Series*, Chapter 1, 741. Berlin: Springer Science & Business Media.

Loder, J. W. and Greenberg, D. A. (1986). Predicted positions of tidal fronts in the Gulf of Maine region. *Continental Shelf Research*, *6*(3), 397–414.

Longhurst, A. (1995). Seasonal cycles of pelagic production and consumption. *Progress in Oceanography*, *36*(2), 77–167.

MacKinnon, J. A. and Gregg, M. C. (2003a). Mixing on the Late-Summer New England Shelf—Solibores, Shear, and Stratification. *Journal of Physical Oceanography*, *33*(7), 1476–1492.

MacKinnon, J. A. and Gregg, M. C. (2003b). Shear and Baroclinic Energy Flux on the Summer New England Shelf. *Journal of Physical Oceanography*, *33*(7), 1462–1475.

MacKinnon, J. A. and Gregg, M. C. (2005a). Near-Inertial Waves on the New England Shelf: The Role of Evolving Stratification, Turbulent Dissipation, and Bottom Drag. *Journal of Physical Oceanography*, *35*(12), 2408–2424.

MacKinnon, J. A. and Gregg, M. C. (2005b). Spring Mixing: Turbulence and Internal Waves during Restratification on the New England Shelf. *Journal of Physical Oceanography*, *35*(12), 2425–2443.

Marsden, R. (1986). The internal tide on Georges Bank. *Journal of Marine Research*, *44*(1), 35–50.

Marshall, J. and Schott, F. (1999). Openocean convection: Observations, theory, and models. *Reviews of Geophysics*, *37*(1), 1–64.

Martinez, E., Antoine, D., D'Ortenzio, F., and De Boyer Montegut, C. (2011). Phytoplankton spring and fall blooms in the North Atlantic in the 1980s and 2000s. *Journal of Geophysical Research: Oceans*, *116*(C11), 1–11.

Matthews, T., Murphy, C., Wilby, R. L., and Harrigan, S. (2014). Stormiest winter on record for Ireland and UK. *Nature Clim. Change*, *4*(9), 738–740.

McCarthy, M., Spillane, S., Walsh, S., and Kendon, M. (2016). The meteorology of the exceptional winter of 2015/2016 across the UK and Ireland. *Weather*, *71*(12), 305–313.

McDougall, T. J. and Barker, P. M. (2011). Getting started with TEOS-10 and the Gibbs Seawater (GSW) Oceanographic Toolbox. *SCOR/IAPSO WG*, *127*, 1–28. ISBN 978-0-646-55621-5.

McDougall, T. J., Jackett, D. R., Millero, F. J., Pawlowicz, R., and Barker, P. M. (2012). A global algorithm for estimating Absolute Salinity. *Ocean Science*, *8*(6), 1123–1134.

McWilliams, J. C., Sullivan, P. P., and Moeng, C.-H. (1997). Langmuir turbulence in the ocean. *Journal of Fluid Mechanics*, *334*, 1–30.

Mellor, G. L. and Yamada, T. (1974). A hierarchy of turbulence closure models for planetary boundary layers. *Journal of the Atmospheric Sciences*, *31*(7), 1791–1806.

Mellor, G. L. and Yamada, T. (1982). Development of a turbulence closure model for geophysical fluid problems. *Reviews of Geophysics*, *20*(4), 851–875.

Melville, W. K. (1996). The role of surface-wave breaking in air-sea interaction. *Annual review of fluid mechanics*, *28*(1), 279–321.

Met Office (2014). Wetterzentrale: Met Office Reanalysis Synoptic Chart. `http://www.wetterzentrale.de/reanalysis.php?jaar=2014&maand=8&dag=17&uur=000&var=45&map=1&model=bra`.

Mignot, J., Boyer Montégut, C. d., and Tomczak, M. (2009). On the porosity of barrier layers. *Ocean Science*, *5*(3), 379–387.

Miles, J. W. (1961). On the stability of heterogeneous shear flows. *Journal of Fluid Mechanics*, *10*(04), 496–508.

Moum, J. N., Nash, J. D., and Klymak, J. M. (2008). Small-scale processes in the coastal ocean. *Oceanography*, *21*(4), 22–33.

Muller-Karger, F. E., Varela, R., Thunell, R., Luerssen, R., Hu, C., and Walsh, J. J. (2005). The importance of continental margins in the global carbon cycle. *Geophysical Research Letters*, *32*(1), L01602.

Munk, W. and Wunsch, C. (1998). Abyssal recipes II: energetics of tidal and wind mixing. *Deep-Sea Research Part I*, *45*(12), 1977–2010.

Nash, J. D., Kelly, S. M., Shroyer, E. L., Moum, J. N., and Duda, T. F. (2012). The unpredictable nature of internal tides on continental shelves. *Journal of Physical Oceanography*, *42*(11), 1981–2000.

Nash, J. D., Kunze, E., Lee, C. M., and Sanford, T. B. (2006). Structure of the Baroclinic Tide Generated at Kaena Ridge, Hawaii. *Journal of Physical Oceanography*, *36*(6), 1123–1135.

National Oceanography Centre (2014). POLPRED (Version 2.4.1.0) [Computer programme]. Available from: `http://noc.ac.uk/using-science/products/software/polpred/polpred`.

Naveira Garabato, A. C., Polzin, K. L., King, B. A., Heywood, K. J., and Visbeck, M. (2004). Widespread Intense Turbulent Mixing in the Southern Ocean. *Science*, *303*(5655), 210–213.

NEODAAS (2015). NERC Earth Observation Data Acquisition and Analysis Service. `https://www.neodaas.ac.uk/`. Accessed: 25.08.2015.

Nielsen, M. H. and St. John, M. (2001). Modelling Thermal Stratification in the North Sea: Application of a 2-D Potential Energy Model. *Estuarine, Coastal and Shelf Science*, *53*(5), 607–617.

Nikurashin, M. and Ferrari, R. (2013). Overturning circulation driven by breaking internal waves in the deep ocean. *Geophysical Research Letters*, *40*(12), 3133–3137.

Obukhov, A. M. (1946). Turbulentnost'v temperaturnojneodnorodnoj atmosfere (Turbulence in an Atmosphere with a Non-uniform Temperature). *Trudy Inst. Theor. Geofiz. AN SSSR*, *1*, 95–115.

Osborn, T. R. (1980). Estimates of the Local Rate of Vertical Diffusion from Dissipation Measurements. *Journal of Physical Oceanography*, *10*(1), 83–89.

Painter, S. C., Finlay, M., Hemsley, V. S., and Martin, A. P. (2016). Seasonality, phytoplankton succession and the biogeochemical impacts of an autumn storm in the northeast Atlantic Ocean. *Progress in Oceanography*, *142*, 72–104.

Palmer, M. R., Inall, M. E., and Sharples, J. (2013). The physical oceanography of Jones Bank: A mixing hotspot in the Celtic Sea. *Progress in Oceanography*, *117*(0), 9–24.

Palmer, M. R., Polton, J. A., Inall, M. E., Rippeth, T. P., Green, J. A. M., Sharples, J., and Simpson, J. H. (2013). Variable behavior in pycnocline mixing over shelf seas. *Geophysical Research Letters*, *40*(1), 161–166.

Palmer, M. R., Rippeth, T. P., and Simpson, J. H. (2008). An investigation of internal mixing in a seasonally stratified shelf sea. *Journal of Geophysical Research: Oceans*, *113*(C12).

Pingree, R. D. (1975). The advance and retreat of the thermocline on the continental shelf. *Journal of the Marine Biological Association of the United Kingdom*, *55*(04), 965–974.

Pingree, R. D. and Griffiths, D. K. (1978). Tidal fronts on the shelf seas around the British Isles. *Journal of Geophysical Research: Oceans*, *83*(C9), 4615–4622.

Pingree, R. D., Holligan, P. M., and Mardell, G. T. (1978). The effects of vertical stability on phytoplankton distributions in the summer on the northwest European Shelf. *Deep Sea Research*, *25*(11), 1011–1028.

Pingree, R. D., Holligan, P. M., Mardell, G. T., and Head, R. N. (1976). The influence of physical stability on spring, summer and autumn phytoplankton blooms in the Celtic Sea. *Journal of the Marine Biological Association of the United Kingdom*, *56*(04), 845–873.

Pingree, R. D., Mardell, G. T., Holligan, P. M., Griffiths, D. K., and Smithers, J. (1982). Celtic Sea and Armorican current structure and the vertical distributions of temperature and chlorophyll. *Continental Shelf Research*, *1*(1), 99–116.

Polzin, K. L., Toole, J. M., Ledwell, J. R., and Schmitt, R. W. (1997). Spatial Variability of Turbulent Mixing in the Abyssal Ocean. *Science*, *276*(5309), 93–96.

Prandle, D. (1982). The vertical structure of tidal currents and other oscillatory flows. *Continental Shelf Research*, *1*(2), 191–207.

Pugh, D. T. (1996). *Tides, Surges and Mean Sea-Level*. John Wiley & Sons Ltd.

Ranasinghe, R. and Pattiaratchi, C. (1999). Circulation and mixing characteristics of a seasonally open tidal inlet: a field study. *Marine and Freshwater Research*, *50*(4), 281–290.

RBR (2015). RBRsolo T Temperature Logger fact sheet. `http://www.rbr-global.com/products/small-single-channel-loggers/temperature-rbrsolo-t`. Online; accessed: 18.08.2015.

RD Instruments (2011). Acoustic Doppler Current Profilers, Principles of Operation: A Practical Primer. `http://www.comm-tec.com/Docs/Manuali/RDI/BBPRIME.pdf`. Online; accessed: 16.03.2017.

Redfield, A. C. (1934). *On the proportions of organic derivatives in sea water and their relation to the composition of plankton,*. James Johnstone Memorial Volume. University Press of Liverpool.

Regnier, P., Friedlingstein, P., Ciais, P., Mackenzie, F. T., Gruber, N., Janssens, I. A., Laruelle, G. G., Lauerwald, R., Luyssaert, S., Andersson, A. J., Arndt, S., Arnosti, C., Borges, A. V., Dale, A. W., Gallego-Sala, A., Godderis, Y., Goossens, N., Hartmann, J., Heinze, C., Ilyina, T., Joos, F., LaRowe, D. E., Leifeld, J., Meysman, F.

J. R., Munhoven, G., Raymond, P. A., Spahni, R., Suntharalingam, P., and Thullner, M. (2013). Anthropogenic perturbation of the carbon fluxes from land to ocean. *Nature Geosci*, *6*(8), 597–607.

Rippeth, T. P. (2005). Mixing in seasonally stratified shelf seas: a shifting paradigm. *Philosophical Transactions of the Royal Society A: Mathematical, Physical and Engineering Sciences*, *363*(1837), 2837–2854.

Rippeth, T. P. and Inall, M. E. (2002). Observations of the internal tide and associated mixing across the Malin Shelf. *Journal of Geophysical Research: Oceans*, *107*(C4), 3–1–3–14.

Rippeth, T. P., Palmer, M. R., Simpson, J. H., Fisher, N. R., and Sharples, J. (2005). Thermocline mixing in summer stratified continental shelf seas. *Geophysical Research Letters*, *32*(5), L05602.

Rippeth, T. P., Simpson, J. H., Player, R. J., and Garcia, M. (2002). Current oscillations in the diurnal–inertial band on the Catalonian shelf in spring. *Continental Shelf Research*, *22*(2), 247–265.

Rippeth, T. P., Wiles, P., Palmer, M. R., Sharples, J., and Tweddle, J. (2009). The diapcynal nutrient flux and shear-induced diapcynal mixing in the seasonally stratified western Irish Sea. *Continental Shelf Research*, *29*(13), 1580–1587.

Rumyantseva, A., Lucas, N., Rippeth, T., Martin, A., Painter, S. C., Boyd, T. J., and Henson, S. (2015). Ocean nutrient pathways associated with the passage of a storm. *Global Biogeochemical Cycles*, *29*(8), 1179–1189.

Sandstrom, H. and Elliott, J. A. (1984). Internal tide and solitons on the Scotian Shelf: A nutrient pump at work. *Journal of Geophysical Research: Oceans*, *89*(C4), 6415–6426.

Sea-Bird Electronics (2015a). SBE 16plus V2 SeaCAT C-T (P) Recorder Specifications. `http://www.seabird.com/sbe16plusv2-seacat-CTD`. Online; accessed: 18.08.2015.

Sea-Bird Electronics (2015b). SBE 37-SI MicroCAT C-T (P) Recorder Specifications. `http://www.seabird.com/sbe37si-microcat-ctd`. Online, accessed: 18.08.2015.

Sharples, J. (1999). Investigating the seasonal vertical structure of phytoplankton in shelf seas. *Marine Models*, *1*(1–4), 3–38.

Sharples, J. (2008). Potential impacts of the spring-neap tidal cycle on shelf sea primary production. *Journal of Plankton Research*, *30*(2), 183–197.

Sharples, J., Ellis, J. R., Nolan, G., and Scott, B. E. (2013). Fishing and the oceanography of a stratified shelf sea. *Progress in Oceanography*, *117*(0), 130–139.

Sharples, J., Moore, C. M., and Abraham, E. R. (2001). Internal tide dissipation, mixing, and vertical nitrate flux at the shelf edge of NE New Zealand. *Journal of Geophysical Research: Oceans*, *106*(C7), 14069–14081.

Sharples, J., Moore, C. M., Hickman, A. E., Holligan, P. M., Tweddle, J. F., Palmer, M. R., and Simpson, J. H. (2009). Internal tidal mixing as a control on continental margin ecosystems. *Geophysical Research Letters*, *36*(23), L23603.

Sharples, J., Moore, M. C., Rippeth, T. P., Holligan, P. M., Hydes, D. J., Fisher, N. R., and Simpson, J. H. (2001). Phytoplankton distribution and survival in the thermocline. *Limnology and Oceanography*, *46*(3), 486–496.

Sharples, J., Ross, O. N., Scott, B. E., Greenstreet, S. P. R., and Fraser, H. (2006). Inter-annual variability in the timing of stratification and the spring bloom in the North-western North Sea. *Continental Shelf Research*, *26*(6), 733–751.

Sharples, J. and Simpson, J. H. (1996). The Influence of the Springs-Neaps Cycle on the Position of Shelf Sea Fronts. In D. G. Aubrey and C. Friedrichs (Eds.), *Buoyancy Effects on Coastal and Estuarine Dynamics*, Coastal and Estuarine Dynamics, Chapter 6, 71–82. American Geophysical Union.

Sharples, J., Tweddle, J. F., Green, J. A. M., Palmer, M. R., Kim, Y., Hickman, A. E., Holligan, P. M., Moore, C. M., Rippeth, T. P., and Simpson, J. H. (2007). Spring - neap modulation of internal tide mixing and vertical nitrate fluxes at a shelf edge in summer. *Limnol. Oceanogr*, *52*(5), 1735–1747.

Shroyer, E. L., Moum, J. N., and Nash, J. D. (2011). Nonlinear internal waves over New Jersey's continental shelf. *Journal of Geophysical Research: Oceans*, *116*(C3).

Siegel, D. A., Doney, S. C., and Yoder, J. A. (2002). The North Atlantic Spring Phytoplankton Bloom and Sverdrup's Critical Depth Hypothesis. *Science*, *296*(5568), 730.

Sieracki, M. E., Verity, P. G., and Stoecker, D. K. (1993). Plankton community response to sequential silicate and nitrate depletion during the 1989 North Atlantic spring bloom. *Deep Sea Research Part II: Topical Studies in Oceanography*, *40*(1), 213–225.

Simpson, J. (1994). Introduction to the North Sea project. In *Understanding the North Sea system*, 1–4. Springer.

Simpson, J. H. (1981). The shelf-sea fronts: implications of their existence and behaviour. *Philosophical Transactions of the Royal Society of London. Series A, Mathematical and Physical Sciences*, *302*(1472), 531–546.

Simpson, J. H. (1997). Physical processes in the ROFI regime. *Journal of marine systems*, *12*(1-4), 3–15.

Simpson, J. H. (1998). TIDAL PROCESSES IN SHELF SEAS. In K. H. Brink and A. R. Robinson (Eds.), *The Sea*, Volume 10, Chapter 5, 113–150. John Wiley & Sons, Inc.

Simpson, J. H., Allen, C. M., and Morris, N. C. G. (1978). Fronts on the Continental Shelf. *Journal of Geophysical Research: Oceans*, *83*(C9), 4607–4614.

Simpson, J. H. and Bowers, D. (1979). Shelf sea fronts' adjustments revealed by satellite IR imagery. *Nature*, *280*(5724), 648–651.

Simpson, J. H. and Bowers, D. G. (1981). Models of stratification and frontal movement in shelf seas. *Deep Sea Research Part A. Oceanographic Research Papers*, *28*(7), 727–738.

Simpson, J. H. and Bowers, D. G. (1984). The role of tidal stirring in controlling the seasonal heat cycle in shelf seas. *Annales Geophysicae*, *2*(4), 411–416.

Simpson, J. H. and Bowers, D. G. (1990). Data Bank Oceanography: Testing Models of the Seasonal Heating Cycle in Shelf Seas. In H. Wang, J. Wang, and H. Dai (Eds.), *Physics of Shallow Seas*, 291–304. China Ocean Press.

Simpson, J. H., Brown, J., Matthews, J., and Allen, G. (1990). Tidal straining, density currents, and stirring in the control of estuarine stratification. *Estuaries and Coasts*, *13*(2), 125–132.

Simpson, J. H., Burchard, H., Fisher, N. R., and Rippeth, T. P. (2002). The semi-diurnal cycle of dissipation in a ROFI: model-measurement comparisons. *Continental Shelf Research*, *22*(11–13), 1615–1628.

Simpson, J. H., Hughes, D. G., and Morris, N. C. G. (1977). The relation of seasonal stratification to tidal mixing on the continental shelf. *Deep-Sea Research*, *24*(suppl), 327–340.

Simpson, J. H. and Hunter, J. R. (1974). Fronts in the Irish Sea. *Nature*, *250*, 404–406.

Simpson, J. H. and James, I. D. (1986). Coastal and Estuarine Fronts. In *Baroclinic Processes on Continental Shelves*, 63–93. American Geophysical Union.

Simpson, J. H. and Rippeth, T. P. (1993). The Clyde Sea: a Model of the Seasonal Cycle of Stratification and Mixing. *Estuarine, Coastal and Shelf Science*, *37*(2), 129–144.

Simpson, J. H. and Sharples, J. (1994). Does the Earth's rotation influence the location of the shelf sea fronts? *Journal of Geophysical Research: Oceans*, *99*(C2), 3315–3319.

Simpson, J. H. and Sharples, J. (2012). *Introduction to the physical and biological oceanography of shelf seas*. Cambridge University Press.

Simpson, J. H. and Tinker, J. P. (2009). A test of the influence of tidal stream polarity on the structure of turbulent dissipation. *Continental Shelf Research*, *29*(1), 320–332.

Smayda, T. J. (1957). Phytoplankton Studies in Lower Narragansett Bay. *Limnology and Oceanography*, *2*(4), 342–359.

Smith, S. D. and Banke, E. G. (1975). Variation of the sea surface drag coefficient with wind speed. *Quarterly Journal of the Royal Meteorological Society*, *101*(429), 665–673.

Song, H., Ji, R., Stock, C., Kearney, K., and Wang, Z. (2011). Interannual variability in phytoplankton blooms and plankton productivity over the Nova Scotian Shelf and in the Gulf of Maine. *Marine Ecology Progress Series*, *426*, 105–118.

Song, H., Ji, R., Stock, C., and Wang, Z. (2010). Phenology of phytoplankton blooms in the Nova Scotian Shelf–Gulf of Maine region: remote sensing and modeling analysis. *Journal of Plankton Research*, *32*(11), 1485–1499.

Soulsby, R. L. (1983). The bottom boundary layer of shelf seas. In B. Johns (Ed.), *Physical Oceanography of Coastal and Shelf Seas*, 189–266. New York: Elsevier.

Souza, A. and Simpson, J. (1996). The modification of tidal ellipses by stratification in the Rhine {ROFI}. *Continental Shelf Research*, *16*(8), 997 – 1007.

Star Oddi (2015a). DST centi-T temperature depth recorder fact sheet. `http://www.star-oddi.com/products/4/temperature-depth-recorder/default.aspx`. Online; accessed: 18.08.2015.

Star Oddi (2015b). Starmon mini - underwater temperature recorder fact sheet. `http//www.star-oddi.com/products/34/subsea-temperature-recorder/default.aspx`. Online; accessed: 18.08.2015.

Sterner, R. W. and Elser, J. J. (2002). *Ecological stoichiometry: the biology of elements from molecules to the biosphere*. Princeton University Press.

Stigebrandt, A. (1988). A note on the locus of a shelf front. *Tellus A*, *40A*(5), 439–442.

Stigebrandt, A. and Aure, J. (1989). Vertical Mixing in Basin Waters of Fjords. *Journal of Physical Oceanography*, *19*(7), 917–926.

Stocker, T. (2014). *Climate change 2013: the physical science basis: Working Group I contribution to the Fifth assessment report of the Intergovernmental Panel on Climate Change*. Cambridge University Press.

Sverdrup, H. U. (1953). On Conditions for the Vernal Blooming of Phytoplankton. *Journal du Conseil*, *18*(3), 287–295.

Taylor, J. R. and Ferrari, R. (2011). Shutdown of turbulent convection as a new criterion for the onset of spring phytoplankton blooms. *Limnology and Oceanography*, *56*(6), 2293–2307.

Tett, P. B., Joint, I. R., Purdie, D. A., Baars, M., Oosterhuis, S., Daneri, G., Hannah, F., Mills, D. K., Plummer, D., Pomroy, A. J., Walne, A. W., Witte, H. J., Howarth, M. J., and Lankester, R. (1993). Biological Consequences of Tidal Stirring Gradients in the North Sea [and Discussion]. *Philosophical Transactions of the Royal Society of London. Series A: Physical and Engineering Sciences*, *343*(1669), 493.

Thomas, A. C., Townsend, D. W., and Weatherbee, R. (2003). Satellite-measured phytoplankton variability in the Gulf of Maine. *Continental Shelf Research*, *23*(10), 971–989.

Thomas, H., Bozec, Y., Elkalay, K., and De Baar, H. J. W. (2004). Enhanced open ocean storage of CO_2 from shelf sea pumping. *Science*, *304*(5673), 1005–1008.

Thomson, R. E. and Emery, W. J. (2014). *Data Analysis Methods in Physical Oceanography*. Elsevier.

Thorpe, S. A. (2004). LANGMUIR CIRCULATION. *Annual Review of Fluid Mechanics*, *36*(1), 55–79.

Torrence, C. and Compo, G. P. (1998). A Practical Guide to Wavelet Analysis. *Bulletin of the American Meteorological Society*, *79*(1), 61–78.

Townsend, D. W. (1991). Influences of Oceanographic Processes on the Biological Productivity of the Gulf of Maine. *Reviews in Aquatic Sciences*, *5*(3), 211–230.

Townsend, D. W., Pettigrew, N. R., Thomas, M. A., Neary, M. G., McGillicuddy, J., Dennis, J., and O'Donnell, J. (2015). Water masses and nutrient sources to the Gulf of Maine. *Journal of Marine Research*, *73*(3-4), 93–122.

Townsend, D. W., Rebuck, N. D., Thomas, M. A., Karp-Boss, L., and Gettings, R. M. (2010). A changing nutrient regime in the Gulf of Maine. *Continental Shelf Research*, *30*(7), 820–832.

Turner, J. (1973). *Buoyancy Effects in Fuids*. Cambridge University Press.

van Aken, H. M. (1986). The onset of seasonal stratification in shelf seas due to differential advection in the presence of a salinity gradient. *Continental Shelf Research*, *5*(4), 475 – 485.

van der Lee, E. M. and Umlauf, L. (2011). Internal wave mixing in the Baltic Sea: Near-inertial waves in the absence of tides. *Journal of Geophysical Research: Oceans*, *116*(C10).

van Haren, H., Maas, L., Zimmerman, J. T. F., Ridderinkhof, H., and Malschaert, H. (1999). Strong inertial currents and marginal internal wave stability in the central North Sea. *Geophysical Research Letters*, *26*(19), 2993–2996.

Vlasenko, V., Stashchuk, N., Inall, M. E., and Hopkins, J. E. (2014). Tidal energy conversion in a global hot spot: On the 3-D dynamics of baroclinic tides at the Celtic Sea shelf break. *Journal of Geophysical Research: Oceans*, *119*(6), 3249–3265.

Vlasenko, V., Stashchuk, N., Palmer, M. R., and Inall, M. E. (2013). Generation of baroclinic tides over an isolated underwater bank. *Journal of Geophysical Research: Oceans*, *118*(9), 4395–4408.

Waniek, J. J. (2003). The role of physical forcing in initiation of spring blooms in the northeast Atlantic. *Journal of Marine Systems*, *39*(1), 57–82.

Waterhouse, A. F., MacKinnon, J. A., Nash, J. D., Alford, M. H., Kunze, E., Simmons, H. L., Polzin, K. L., St. Laurent, L. C., Sun, O. M., Pinkel, R., Talley, L. D., Whalen, C. B., Huussen, T. N., Carter, G. S., Fer, I., Waterman, S., Naveira Garabato, A. C., Sanford, T. B., and Lee, C. M. (2014). Global patterns of diapycnal

mixing from measurements of the turbulent dissipation rate. *Journal of Physical Oceanography*, *44*, 1854–1872.

Webb, A. and Fox-Kemper, B. (2011). Wave spectral moments and Stokes drift estimation. *Ocean Modelling*, *40*(3), 273–288.

Wihsgott, J. U., Hopkins, J. E., Sharples, J., Jones, E., and Balfour, C. (2016). Long-term mooring observations of full depth water column structure spanning 17 months, collected in a temperate shelf sea (Celtic Sea). `https://www.bodc.ac.uk/data/published_data_library/catalogue/10.5285/389fe406-ebd9-74f1-e053-6c86abc032a4/`. Available from British Oceanographic Data Centre, Natural Environment Research Council.

Wihsgott, J. U., Hopkins, J. E., Sharples, J., Jones, E., and Balfour, C. (2018). Long-term, full depth observations of horizontal velocitites spanning 17 months, collected in a temperate shelf sea (Celtic Sea) on the NW European Shelf. `https://dx.doi.org/10.5285/631ddd2a-48df-143b-e053-6c86abc0d49f`. Available from British Oceanographic Data Centre, Natural Environment Research Council.

Williams, C., Sharples, J., Green, M., Mahaffey, C., and Rippeth, T. (2013). The maintenance of the subsurface chlorophyll maximum in the stratified western Irish Sea. *Limnology and Oceanography: Fluids and Environments*, *3*(1), 61–73.

Williams, C., Sharples, J., Mahaffey, C., and Rippeth, T. (2013). Wind-driven nutrient pulses to the subsurface chlorophyll maximum in seasonally stratified shelf seas. *Geophysical Research Letters*, *40*(20), 5467–5472.

Wollast, R. (1998). Evaluation and comparison of the global carbon cycle in the coastal zone and in the open ocean. In K. H. Brink and A. R. Robinson (Eds.), *The Sea*, Volume 10, Chapter 9, 213–252. John Wiley & Sons, Inc.

Woodward, E. M. S. and Rees, A. P. (2001). Nutrient distributions in an anticyclonic eddy in the northeast Atlantic Ocean, with reference to nanomolar ammonium concentrations. *Deep Sea Research Part II: Topical Studies in Oceanography*, *48*(4), 775–793.

Wunsch, C. and Ferrari, R. (2004). Vertical Mixing, Energy, and the General Circulation of the Oceans. *Annu. Rev. Fluid Mech.*, *36*, 281–314.

Yanagi, T. and Tamaru, H. (1990). Temporal and spatial variations in a tidal front. *Continental Shelf Research*, *10*(7), 615–627.

Young, I. R. (1999). Seasonal variability of the global ocean wind and wave climate. *International Journal of Climatology*, *19*(9), 931–950.

Zhang, G. J. and Mcphaden, M. J. (1995). The Relationship between Sea Surface Temperature and Latent Heat Flux in the Equatorial Pacific. *Journal of Climate*, *8*(3), 589–605.